Delft University of Technology

Master of Science Thesis

To obtain the M.Sc. degree in Aerospace Engineering

Simulated Shadowgraphy of Transonic Wing-Bound Shock Waves

Author:
T.S. Onnink

29 August, 2016

Faculty of Aerospace Engineering
Department of Aerodynamics, Wind Energy, Flight Performance and Propulsion

Graduation work performed at the University of Bristol

Confidentiality

Dear reader,

This research was conducted for a commercial party, that requires confidentiality till the first of september of 2018. Contents of this thesis may not be made public before this date.

Kind regards,

Tom Onnink

Summary

The aim of this study was to assess the feasibility of extracting quantitative information about the shock waves on wings of aircraft flying at transonic speeds from in-flight shadowgraphs by means of a comparison with simulated shadowgraphs. The first step of this feasibility study was to obtain or create realistic transonic flow fields over a representative airfoil or wing profile. The transonic small disturbance potential flow equations were used to calculate the required two-dimensional flow fields. Secondly, an iterative ray tracing scheme was used to determine how light was deflected when it traveled through the calculated flow fields. Using the calculated light trajectories, simulated shadowgraphs were created. Finally, these simulated shadowgraphs were analyzed to determine if quantitative information about the shock wave could be extracted from the shadowgraph.

Flow fields, corresponding to a typical super critical airfoil and a thin parabolic arc airfoil, with varying upstream Mach numbers have been used for the shadowgraph simulation. Simulated shadowgraphs of the transonic flow fields with shock waves in them have been created for varying light angles. The simulated shadowgraphs have been analyzed and it was found that a unique combination of shadowgraph characteristics could be found for constant light angles. These shadowgraph characteristics consisted of the radiant flux values corresponding to the shadow and the bright spot of the shadowgraph and the distance between the shadow and the bright spot. When the distance between the shadow and the bright spot, the light angle, and the radiant flux of either the shadow or the bright spot are known, the shadowgraph in question could be coupled to a certain flow field, hence revealing quantitative information about the shock wave position and the shock wave strength and curvature. It should be noted that knowledge of the light angle is of the utmost importance when trying to extract data about a shock wave from these simulated shadowgraphs. During this study, the light angle was treated as a known parameter. However, in real life, the light angle has to be determined using the method that was presented by Fischer et al. [1]. It should be noted that this study has analyzed two-dimensional flow fields around airfoils and that the simulated shadowgraphs were one-dimensional.

It can be concluded that it is theoretically feasible to extract quantitative information about a wing bound shock wave from an in-flight shadowgraph formed on the airfoil surface by means of a comparison with simulated shadowgraphs. However, simplifications made during this study, measurement inaccuracies, and the fact that this study has not investigated three-dimensional flow fields makes the application of the relation that was found to real-life experiments questionable at this time. Furthermore, it is recommended to further refine the theoretical relation that has been found. This can be achieved by using more realistic flow models that include the boundary layer and by improving the shadowgraph simulation by taking the circle of confusion of the sunlight into account.

Acknowledgements

First I would like to thank Dr. Ir. Raf Theunissen, the University of Bristol, and the local commercial partner, for giving me the opportunity to perform the work for my M.Sc. thesis at the University of Bristol. This opportunity gave me the chance the work with different new people and it allowed me to live in the beautiful and vibrant city that is Bristol for a year.

Secondly, I would like to thank Dr. Ir. Raf Theunissen again for his advise, the brainstorm session, encouragements, and enthusiasm.

I would also like to thank Dr. Ir. Ferry Schrijer for the remarks, comments, and providing insightful literature during the thesis research work.

Furthermore, it would like the thank all the friends in Bristol for making this year truly amazing. I would like to thank Alex and Eamon for sticking with me through the good and the bad times. Dan, Matt, and the programming group for the good football matches. Jade for allowing me to speak Dutch from time to time. Jamie for all the delicious food. Beth for always being calm, kind, and good listener. Nick, Becka, and other Jamie for jamming with me from time to time.

Most of all, I would like to thank my parents for their unconditional support this year.

Contents

List of Figures

Nomenclature

Latin Symbols

A	Matrix used in the ray tracing Runge-Kutta scheme	$[-]$
A	Spars matrix to solve transonic equation	$[-]$
A_r	Halve of the projected area of a light beam on the surface for a 2D simulation (since surface is 1D in this case, speaking of a length instead of an area is more correct)	$[m^2]$
a_0	Speed of sound at stagnation conditions	$[m/s]$
a_{cr}	Speed of sound at critical conditions	$[m/s]$
a_{temp}	Temperature gradient, $a_{temp} = -0.0065$ for troposphere	$[K/m]$
B	Matrix used in the ray tracing Runge-Kutta scheme	$[-]$
B	Term in transonic equation: $B\phi_{xx} + \phi_{\tilde{y}\tilde{y}}$	$[-]$
C	Matrix used in the ray tracing Runge-Kutta scheme	$[-]$
C_1	Constant for the Murman-Cole-Krupp method	$[-]$
C_2	Constant for the Murman-Cole-Krupp method	$[-]$
$\bar{C}_p$	Reduced pressure coefficient	$[-]$
C_p	Pressure coefficient	$[-]$
c	Chord length	$[m]$
c	Speed of light	$[m/s]$
c_0	Speed of light in vacuum	$[m/s]$
$\mathbf{D}$	Ray equation operator for ray tracing scheme	$[-]$
D	Diameter of light source	$[m]$
D	Doublet strength	$[m^3/s]$
d	Height of the schlieren object	$[m]$
$d\theta_{ray}$	Angle spacing between light rays from a point light source	$[rad]$
dx_p	Width of pixel in the x-direction	$[-]$
E_e	Electric field	$[N/C]$ or $[V/m]$
E_e	Irradiance	$[W/m^2]$
$F(x)$	Body contour function of airfoil	$[-]$
$F'(x)$	Derivative of F(x) w.r.t. the x-axis	$[-]$
f	Column vector to solve transonic equation	$[-]$
f	Focal length of lens or mirror	$[m]$
f	Frequency of light	$[1/s]$
g	Distance between schlieren object and screen	$[m]$
g	Standard gravity or gravitational acceleration at sea level, $g = 9.81$	$[m/s^2]$

$H(x)$	Unit step or heaviside step function, $H(x) \begin{cases} = 0 & x < 0 \\ = 1 & x \geq 0 \end{cases}$	$[-]$
h	Distance between light source and screen	$[m]$
h	Flight altitude	$[m]$
h	Planck's constant	$[J \cdot s]$
I_e	Radiant intensity	$[W/sr]$
I_e	Radiant intensity	$[W/sr]$
H	Momentum shape factor, also known as shape factor	$[-]$
K	Transonic similarity parameter	$[-]$
k	Gladstone-Dale coefficient	$[m^3/kg]$
l	Distance from schlieren object to shadowgraph screen	$[m]$
M	Mach number	$[-]$
M^*	Characteristic Mach number	$[-]$
M_∞	Freestream Mach number	$[-]$
m	Magnification of the shadow with respect to the schlieren object	$[-]$
n	Index of refraction	$[-]$
n_0	Refractive index of fluid medium at reference conditions	$[-]$
n_i	Index of refraction of medium of incident light	$[-]$
n_r	Number of rays for the shadowgraph simulation	$[-]$
$n_{r,ext}$	Number of extra rays for the shadowgraph simulation	$[-]$
n_t	Index of refraction of medium of transmitted light	$[-]$
p	Pressure	$[Pa]$
p	Variable, Bohning-Zierep Model	$[-]$
$p^{(1)}$	Expansion variable	$[m/s]$
p_∞	Freestream pressure	$[Pa]$
p_t	Total pressure	$[Pa]$
q_n	Variable depending on eigenvalue, Bohning-Zierep Model	$[-]$
$\mathbf{R}$	Location vector of a light ray for the ray tracing scheme	$[-]$
R	Reflectance	$[-]$
R	Specific gas constant for dry air, $R = 287.05$	$[J/kgK]$
$R(x)$	Unit ramp function, $R(x) \begin{cases} = 0 & x < 0 \\ = x & x \geq 0 \end{cases}$	$[-]$
$\mathbf{r}$	Position vector: $r = xi + yj + zk$	$[-]$
r	Amplitude reflection coefficient	$[-]$
r	Distance travelled by ray	$[m]$
r_c	Vortex core radius	$[m]$
$\mathbf{T}$	Direction or optical ray vector of a light ray for the ray tracing scheme	$[-]$
T	Temperature	$[K]$
T	Transmittance	$[-]$
T	Travel time of light	$[s]$
T_∞	Freestream temperature	$[K]$
T_t	Total temperature	$[K]$

t	Amplitude transmission coefficient	$[-]$
t	New distance variable used for ray tracing scheme	$[m]$
u	Velocity in the x-direction	$[m/s]$
$u^{(1)}$	Expansion variable	$[m/s]$
u^*	Critical perturbation velocity	$[-]$
u_∞	Freestream velocity in the x-direction	$[m/s]$
v	Velocity in the y-direction	$[m/s]$
$v^{(1)}$	Expansion variable	$[m/s]$
v_θ	Tangential velocity	$[m/s]$
w_g	Multiplication factor altering the width of the standard deviation of the Gaussian distribution	$[-]$
$\mathbf{X}_p$	Vector with all x-locations of the pixel centers	$[-]$
$\mathbf{X}_w$	Vector with all x-locations of the light ray-airfoil intersections	$[-]$
y_0	Thickness or height of the inner boundary layer, Bohning-Zierep Model	$[-]$
$\tilde{y}$	Scaled y-coordinate	$[m]$

Greek Symbols

α	Exponent of velocity power law distribution ($M = y^\alpha$), Bohning-Zierep Model	$[-]$
β	Variable, Bohning-Zierep Model	$[-]$
Γ_∞	Circulation (vortex strength)	$[m^2/s]$
γ	Ratio of specific heats, $\gamma = C_p/C_v = 1.4$	$[-]$
Δa	Displacement distance of refracted ray on screen	$[m]$
Δx	Distance between mesh points (x-direction)	$[m]$
$\Delta\tilde{y}$	Distance between mesh points (y-direction)	$[m]$
δ	Airfoil thickness ratio	$[-]$
δ	Boundary layer thickness	$[m]$
δ	True size of smallest resolvable feature in a schlieren object	$[m]$
δ^*	Displacement thickness	$[-]$
$\delta\epsilon$	Incremental change in the angular deflection	$[rad]$
Δt	Incremental value of t or extrapolation distance	$[m]$
ϵ	Angular ray deflection or refraction angle.	$[rad]$
ϵ_{rf}	Error of the radiant flux value	$[-]$
ζ	Variable, Bohning-Zierep Model	$[-]$
θ	Momentum thickness	$[-]$
θ_i	Angle of incidence	$[rad]$
θ_r	Angle of reflection	$[rad]$
θ_{ray}	Light angle of a light ray	$[rad]$
θ_s	Angle between surface normal and incoming or outgoing light ray	$[rad]$
θ_t	Angle of refraction	$[rad]$
λ	wavelength of the light	$[m]$
λ_0	wavelength of the light in vacuum	$[m]$

λ_n	Eigenvalue of boundary value problem, Bohning-Zierep Model	$[-]$
μ	Dynamic viscosity	$[kg/m \cdot s]$
ξ	Photon energy	$[J]$
ρ	Density	$[kg/m^3]$
ρ_∞	Freestream density	$[kg/m^3]$
ρ_t	Total density	$[kg/m^3]$
σ	Standard deviation	$[-]$
σ_n	Variable depending on eigenvalue, Bohning-Zierep Model	$[-]$
Φ	Column vector of all ϕ values on a vertical line	$[m^2/s]$
Φ_e	Radiant flux	$[W]$
Φ_p	Radiant flux measured by a pixel	$[W]$
ϕ	Potential function for Bohning-Zierep model	$[-]$
ϕ	Velocity potential in scaled coordinate system	$[m^2/s]$
$\widehat{\phi}$	Intermediate ϕ value	$[m^2/s]$
$\bar{\psi}$	Variable depending on Mach number, Bohning-Zierep Model	$[-]$
ω	Relaxation parameter	$[-]$

Subscripts

$_b$	Backward difference scheme
$_c$	Centered difference scheme
$_G$	Grundfeld or mean part of dimensionless parameter, i.e. first term of: $u = u_G + u_S$
$_i$	Index
$_j$	Index
$_S$	Störgrößen or disturbance part of dimensionless parameter, i.e. second term of: $u = u_G + u_S$

Superscripts

*	Value at critical conditions, i.e. $M = 1$
$^-$	Average: $\bar{u} = \sum u_i/N$
^{n}	Number of current iteration through flow field

Abbreviations

BOSCO	Background-Oriented Schlieren using Celestial Objects
BOS	Background-Orientated Schlieren
CCD	Charge Coupled Device
CFD	Computational Fluid Dynamics
CISS	Constructed Interferograms, Schlieren, and Shadowgraphs

OPL	Optical Path Length
PIV	Particle Image Velocimetry
RpP	Rays per Pixel, average amount of rays per pixel for simulation
SWBLI	Shock Wave-Boundary Layer Interaction

1. Introduction

In order to create low pressures and to generate lift, air is locally accelerated over the wing surface. Depending on the flight speed and wing geometry, local regions of supersonic flow can be formed. This is called transonic flow as the flow around the wing is partly subsonic and partly supersonic. Depending on the back pressure or the change in the surface slope, shock waves can occur on the wing. These shock waves usually 'hit' the surface on which a boundary layer is present. The complex interaction between such a shock wave and the boundary layer determines the shock pattern, boundary layer characteristics, flow separation, etc. [37]. This is known as Shock Wave-Boundary Layer Interaction (SWBLI). When these shock waves occur on a wing, drag increases significantly due to wave drag, increased viscous drag caused by boundarly layer thickening, and potentially flow separation [35, 38, 39]. In the 1940's it was believed that the sound barrier could not be passed due to the enormous increase in drag due to these phenomena when the drag divergence Mach number was passed. However, in 1947 the sound barrier was broken and more research was done on flight at speeds close to a Mach number of one [40]. In the 1950's and 1960's, this research led to the development of supercritical airfoils. These airfoils have a more blunt nose and a flatter upper surface in comparison to the, at the time more conventional, NACA-6 airfoils. The new geometry caused the air to hardly accelerate over the nearly flat middle part of the upper surface. The supersonic flow was terminated by a weaker shock wave to realize the recompression over the airfoil, leading to higher critical and drag divergence Mach numbers. At the time, these supercritical wings could be used to achieve two things: either flight at higher velocities could be realized with the same fuel-economics or flight at the same speed with better fuel-economics, reduced structural weight, and a longer range could be achieved. The second option was chosen as this made flight cheaper and more profitable for airliners because enormous fuel savings were achieved [40, 41].

Till this day, shock waves still regularly occur on supercritical wings during flight and are often observed during cruise flight of commercial aircraft, as shown by Settles [7] or a quick Google search on 'wing shock shadows'. However, it is not clear from these shadow pictures of the wing bound shock waves whether the desired weak shock wave, for which the wing is designed, is present or a different less desirable shock wave. These non-desired shocks could occur on the supercritical wings as the airfoils have shown different behaviour at off-design points and SWBLI is a very dynamic process [35, 42]. When such a non-desired shock wave occurs, the drag of the wing increases, making flight less efficient. As sustainability has become an important issue and regulations call for more fuel-efficient flight, further investigation of these wing bound shock waves which influence the efficiency of an aircraft is necessary as a better understanding of these shock waves could lead to mitigation of these shocks, which would result in more efficient flight.

A further investegation of these wing bound shock waves that occur on the wings of commercial aircraft during transonic cruise flight may be performed in a laboratory environment. According to Crowder, there are numerous advantages to wind tunnel testing, like a precisely controlled environment and ease of measurements. However, both Crowder and Weinstein agree that aerodynamic testing on full-scale models in their real environment would present significant advantages [43, 44]. This is because wind tunnel tests often involve small-scale models which suffer from the compromise between Reynolds number and Mach number matching. Wind tunnel tests are further limited by boundary constraint, the mounting of the model, and the simulation of propulsion effects. When investigating SWBLI, mismatches between the Reynolds number and Mach number will affect either or both the shock wave and the boundary layer, and, as a result, the interaction between the two. Therefore, in-flight full-scale experiments would be ideal to gain a further understanding of the SWBLI that occurs when a plane flies at transonic speeds. Dolling, who summarized what has been done in the field of SWBLI in 2001, also mentioned that real flight experiments are needed to deepen the understanding of shock dynamics and to validate tools that predict the SWBLI behavior [42]. During the more recent UFAST project, which focused on the unsteady effects in shock wave induced separation, real experiments were closely coupled to numerical investigations to identify and overcome the weaknesses of both methods [45]. Both these studies highlight the need for full-scale experiments as well.

During real flight, shock waves on wings or around aircraft have been visualized utilizing either the shadowgraphy or the schlieren technique. In 1948, U.S. Air Force pilot Major Frederick A. Borsodi, was one of the first to discover shock shadowgraphs on the upper skin surface of the wing of his jet fighter as he carried out a high velocity dive test [6]. Since this in-flight discovery, shadowgraphy has proven to be a useful qualitative tool to reveal the presence of shock waves during flight. In 1998, experiments were carried out by NASA [1] to determine the optimal sun angles and aircraft orientation needed to produce the best shadowgraphs. However, the use of in-flight shadowgraphy to obtain useful quantitative information about wing-bound shock waves does not seem to have been studied in detail yet. Shock waves on aircraft, flying above Mach 1, have also been observed against a non-uniform background sky, as the background becomes visualy distorted as the light that travels through the shocks refracts [44]. Using an astronomic telescope, an opaque mask with a slit, film, and the sun as a light source, Weinstein [44, 46] was able to create schlieren images of supersonic aircraft using the same principles of light refraction. He called this technique 'schlieren for aircraft in flight'. A few years later a new schlieren technique called Background-Orientated Schlieren (BOS) was developed [20]. Recently, NASA has been able to capture images of shock waves around supersonic aircraft with both ground-to-air and air-to-air pictures using this BOS-technique [24, 25]. Other techniques to visualize flow, which were commonly used in full-scale in-flight experiments in the late 20th century, are flow tufts, flow cones, oil and or dyes [43, 47]. The problem with these methods is that they only visualize the flow near a surface, hence not visualizing the full extent of the shock. Smoke generators could be used to visualize the flow, but the smoke injection system could affect the flow as it is an intrusive technique. As both shadowgraphy and schlieren are line of sight techniques, the entire flow field can be imaged, making these techniques most suited to use in the further experimentation of the mentioned shock waves. However, both these techniques integrate information about the three-dimensional flow field along the light path, which makes it very challenging to extract three-dimensional information from the measurements.

The aim of this study is to assess the feasibility of using either a schlieren or shadowgraphy technique to extract quantitative information about the shock waves occurring on the wings of commercial aircraft during transonic cruise flight. The quantitative information of interest is the shock position, strength, and curvature. This study should determine whether one of these techniques can be used for this goal. If it is found that one of the techniques is useful to this end, this study should pave the way for further studies that will focus on the application of the technique to further investigate the wing bound shock waves in order to deepen the understanding of this phenomenon.

The theoretical background on which most of the work in this report is based, is shortly introduced in chapter 2. First, the basics of light propagation are shortly introduced. Secondly, the shadowgraphy and the BOS version of the schlieren technique are discussed. The reviewed literature, research questions, and the research objective are presented in chapter 3. The shock wave-boundary layer interaction and the transonic flow solver, which is based on the transonic small disturbance potential flow equations, are treated in chapter 4. Both the ray tracing scheme, used for the shadowgraph simulation, and the iterative method of simulating the shadowgraphs to reduce computational time are discussed in chapter 5. The simulated shadowgraphs are presented and analyzed in chapter 6. This chapter also presents the relation that is found between the shadowgraph characteristics and the wing bound shock waves, and the limitations of the studied shadowgraph simulation method are discussed. Finally, the conclusion and the recommendations are presented in chapter 7.

2. Light Propagation and the Shadowgraphy Technique

Before the shadowgraphy and schlieren techniques can be discussed, some introductory elements regarding light propagation are treated first. Most emphasis is put on the index of refraction and the deflection and reflection of light. Secondly, some basic concepts of the shadowgraphy and schlieren technique are explained. The direct shadowgraphy technique is discussed in more detail to illustrate how different light sources affect the formation of a shadowgraph and to explain what the sensitivity limits are for shadowgraphy. Lastly, the BOS technique is shortly introduced and some fundamental differences between the shadowgraphy and the schlieren technique are addressed.

2.1 Light Propagation

When light travels from a star through space, all the energy contained in the light travels forward with the speed of light. The speed of light c is constant and it equals the product of the wavelength of light λ and the frequency of the light f, i.e. $c = f \cdot \lambda$. Hence, light can have different frequencies and wavelengths but it always travels at the same speed. In a vacuum, no scattering occurs, hence the beam of light cannot be seen from the side. However, the beam of light does spread out a little. Light from stars, both close and far away from earth, can be observed even though the light has been traveling for thousands or millions of years. It can therefore be said that the photons, carrying the energy of the light, are timeless [2]. Photons are defined as massless elementary particles that are used for the transport of energy and the electromagnetic interactions. It has been well established that light is absorbed and emitted in discrete bursts, hence as the particles known as photons [48]. In 1905 Einstein's work on the photoelectric effect established that the electromagnetic field itself is quantized. Each photon has an energy ξ that equals the product of Planck's constant h and the frequency of the radiation field, i.e. $\xi = hf$. It should be noted that the frequency of the radiation field equals the frequency of the photon and that the energy of electromagnetic waves depends on the frequency.

When a photon hits a molecule or an atom, the photon and its energy are absorbed. If the frequency of the photon matches the resonance frequency of the absorbing particle, the particle can be raised to an exited state. If the pressure is about 100 Pa or higher, the absorbed energy will be converted into atomic motion, leading to collisions, which in turn result in thermal energy. This all happens before a photon can be re-emitted by the particle. This kind of absorption is called dissipative absorption. When the frequency of a photon does not match the resonance frequency of particle, the atom or molecule behaves like a oscillator according to Hecht [2]. When the frequency of the electromagnetic field is lower than the resonance frequency, the energy is too low to raise the particle into an exited state. However, the electron cloud is still driven into oscillation, but this time without atomic transition. Since the electron cloud vibrates with respect to the positive nucleus, a oscillating dipole is formed which immediately radiates at the same frequency. Hence, a photon is absorbed and another photon with the same frequency is immediately emitted again. This is called elastically scattering of light. As molecules are randomly oriented, photons are scattered in every direction. The number of photons being emitted is so immense that it appears as if each molecule scatters photons in spherical wavelets. This scattering by particles smaller than a wavelength, the molecules in this case, is called Rayleigh scattering. It should be noted that the scattering process is weak, thus a light beam is hardly attenuated unless it passes through an enormous volume of these particles.

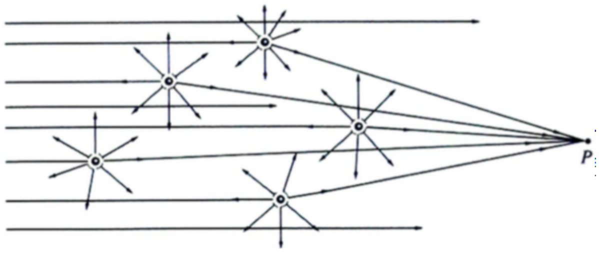

Figure 2.1: Scattering in the forward direction [2]

This Rayleigh scattering takes place in mediums with a very low density, for example the upper atmosphere. However, the Rayleigh scattering is suppressed when light travels through media with higher densities by means of interference. The total path length of light arriving at a forward point is not altered much when light is scattered in the forward direction, as shown by Figure 2.1. This means that all the wavelets arriving at this forward point are more or less in-phase, resulting in constructive interference that is unique for forward propagation of light. However, this is not the case for other directions. For Rayleigh scattering, the scattering molecules are roughly a wavelength or more separated and they emit wavelets that are essentially independent in all directions except forward. As a result, destructive interference does not always occur, allowing for laterally scattered light to leak out of the light beam travelling through a medium with a very low density. For media with an increased density, every space with the length of a wavelength of visible light, is filled with an enormous amount of molecules. Wavelets arriving at a random point in any direction, except the forward, cannot be assumed to have random phases anymore since the molecules are packed so close together. At one standard atmosphere the molecules are approximately 3 nm apart and for liquids and solids this spacing is decreased even further, thus interference is of importance [2]. With the exception of the forward direction, destructive interference dominates in all directions, resulting in little to no light being scattered in the lateral or backward direction. Hence, the amount of non-forward scattered light decreases with increasing density and uniformity of a medium.

2.1.1 Index of Refraction

Even though photons only exist at the velocity c_0, the velocity of light traveling through a medium can be different from c_0. Light traveling through a homogeneous medium is scattered and re-scattered. Each time the light is scattered a phase shift into the light field occurs, ultimately resulting in a different propagation velocity of the light through this medium. The index of refraction of a medium corresponds to this change in velocity, i.e. $n = c_0/c$

It was already mentioned that all the scattered wavelets constructively interfere in the forward direction to form a so called secondary wave. This secondary wave will combine with what is left of the primary wave, the original light that has not been scattered yet, to form a transmitted wave. Both the primary and secondary wave travel through the void of the medium with a velocity of c_0. However, the index of refraction of the medium may be larger than one. This is caused by the phase lag or lead of the secondary wave. The electron-oscillator can vibrate nearly completely in-phase with the driving force, the electromagnetic field, if the driving frequency is relatively low. As the frequency of the driving force increases, the oscillator will start to fall behind in phase. At resonance, the phase lag of the oscillator is 90°. This phase lag will further increase to 180° when the frequency of the driving force is increased to well above the resonance frequency [2]. In addition, the scattered wavelets forming the secondary wave lag the oscillator by a further 90°. Hence, the secondary wave lags the primary wave by a phase between 90° and 180° for driving frequencies below the resonance, and leads the primary wave by a phase between 90° and 180° for driving frequencies above the resonance. The transmitted wave will have a different phase compared to the primary wave, depending on the amplitudes and relative phases of the primary and secondary waves. If the secondary wave lags the primary wave, the transmitted wave will also lag the primary wave and vice versa. The transmitted wave is scattered over and over again as it travels through a medium, thus constantly retarding or advancing its phase with respect to the original wave. Since the speed of a wave is defined as the velocity of its wavefront, the speed is altered by changes in the phase. Hence, phase lag results in $c < c_0$ and phase lead results in $c > c_0$, corresponding to $n > 1$ and $n < 1$ respectively. It should be noted that the index of refraction depends on the wavenumber of light as the phase lag or lead is determined by the driving frequency.

2.1.2 Reflection and Refraction

When a beam of light, travelling through air, strikes the surface of a transparent material such as glass, the wavefront will encounter a very ordered array of closely spaced atoms. The separation of the atoms in the glass is thousand times smaller than the wavelength of the visible light. When the light is transmitted through such a dense medium, destructive interference cancels light propagation in all directions but the forward one. However, at the air-glass interface which is discontinuous, the light strikes the surface and some light is backscattered. This phenomena is called reflection. When the transition between two media is gradual, meaning the transition takes place over a length of at least one wavelength, the reflection is low. When the transition is over a length less than a quarter of a wavelength, the transition behaves likes a discontinuity. In principle, each molecule in the glass scatters light backwards, hence contributing to the reflection. In practice its is found that only a thin layer, approximately $\lambda/2$ thick, near the surface causes the reflection [2].

When a beam of light travels from a lower to a higher optically dense medium and light is reflected off the interface, this is called external reflection. When light travels from a more to a less optically dense medium and light is reflected off the interface, it is called internal reflection. Stokes relations for reflection and refraction show that there is a 180° phase difference between internally and externally reflected waves [2].

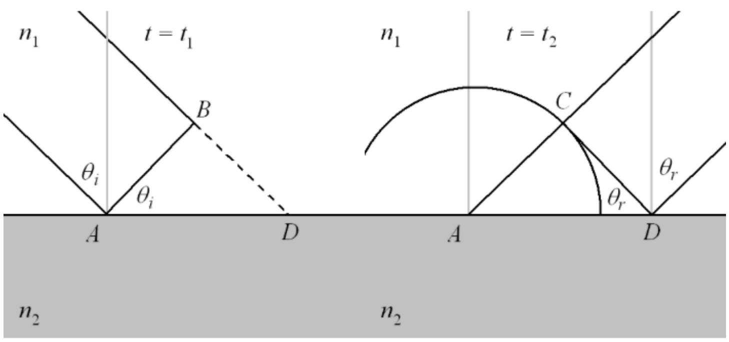

Figure 2.2: Reflection of a plane wave [3]

The law of reflection states that the angle of incidence θ_i equals the angle of reflection θ_r, which can be deduced in the following manner: Figure 2.2 shows the lines AB and CD, which lie along an incoming and outgoing wavefront respectively. If $AC = BD$, the wavelet emitted from point A will reach point C in-phase with the wavelet emitted from point D. $AC = BD$ is the condition for all the wavelets emitted from the surface to overlap in-phase in order to form a single reflected plane wave. Since the waves both travel at the same speed, $AC = c(t_2 - t_1) = BD$. Both triangles ABD and ACD share the same side AD and both angles

$\angle ABD$ and $\angle ACD$ are 90°, since a light ray is perpendicular to a wavefront. Hence the sine rule can be applied, which results in the first part of the law of reflection, as can be seen in Equation 2.1. The law of reflection also states that the incident ray, the reflected ray, and the surface normal all lie in one plane, namely the plane of incidence.

$$\frac{sin(\theta_i)}{\overline{BD}} = \frac{sin(\theta_r)}{\overline{AC}} \quad \rightarrow \quad \theta_i = \theta_r, \text{ for } \quad \overline{AC} = \overline{BD} \tag{2.1}$$

Depending on the smoothness of the surface, specular reflection or diffuse reflection can occur. When the surface roughness is small compared to λ, scattered wavelets will arrive approximately in-phase for $\theta_i = \theta_r$, resulting in specular reflection. When the surface roughness is large compared to λ, the law of reflection still holds, but each light ray will be reflected in a different direction due to the angles of the surface, resulting in diffusive reflection. Most surface reflection lies in between these two extreme cases of reflection.

As mentioned before, light is not only reflected from an interface between two media with a different index of refraction, but part of the light is also transmitted. Depending on the two media, light can sometimes be seen to bend when it crosses the interface, which is called refraction. When light hits an interface surface under an angle, the wavefront passing the surface slows down due to phase retardation, at least that is the case when $n_i < n_t$. Part of the wavefront that has not passed the surface will travel at a higher velocity, resulting in a refracted wavefront when the entire wavefront has passed the surface. This can be compared, in a non precise but illustrative manner, to a car where the inside wheels turn slower than the outside wheels, resulting in the car making a turn.

The first part of the law of refraction, better known as Snell's law, specifies the relation between the indices of refraction and the angles of incidence and refraction θ_t. Figure 2.3 shows an incoming wavefront AB and a transmitted wavefront ED. In this case $n_1 < n_2$, hence $c_1 > c_2$ since $c = c_0/n$. As a result $AE < BD$, which means the direction of the wavefront has changed. Since both triangles ABD and AED have the common side AD and both angles $\angle ABD$ and $\angle AED$ are 90°, the sine rule can be used. Equation 2.2 shows how this sine rule results in Snell's law (last equation) by using $AE = c_2(t_2 - t_1)$ and $BD = c_1(t_2 - t_1)$ and $c = c_0/n$. The law of refraction also states that the incident, reflected, and refracted rays all lie in the plane of incidence.

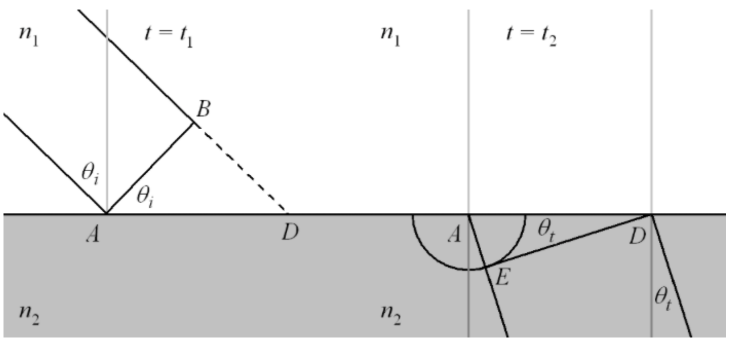

Figure 2.3: Refraction of a plane wave when $n_1 < n_2$ [3]

$$\frac{sin(\theta_i)}{\overline{BD}} = \frac{sin(\theta_t)}{\overline{AE}} \quad \Rightarrow \quad \frac{sin(\theta_i)}{c_1(t_2 - t_1)} = \frac{sin(\theta_t)}{c_2(t_2 - t_1)} \quad \Rightarrow \quad n_1 sin(\theta_i) = n_2 sin(\theta_t) \tag{2.2}$$

Snell's law states that a ray entering a higher index of refraction medium bends towards the surface normal and a ray entering a lower index of refraction medium bends away from the surface normal. It should also be noted that the cross section of a light beam entering a higher index of refraction medium becomes larger. The wavelength of light is decreased when entering a higher index of refraction medium, hence $\lambda = \lambda_0/n$. Color, therefore, is related to the frequency of light, which corresponds to the energy of light, rather than the wavelength of light. Usually when wavelengths and colors are treated, the vacuum wavelengths for these colors are used [2].

2.1.3 Optical Path Length

The optical path length (OPL) is defined in Equation 2.3 for light travelling from point S to point P. The optical path length relates the distance travelled by light through non vacuum media to the corresponding length travelled in vacuum. **Fermat's Principle** states that: *Light, in going from point S to P, traverses the route having the smallest optical path length* [2]. Both Snell's law and $\theta_i = \theta_r$ can be derived from this statement.

$$OPL = \int_S^P n(s)ds \tag{2.3}$$

As Fermat's principle of least time had some serious failings it was altered to the following more modern form: *A light ray in going from point S to point P must traverse an optical path length that is stationary with respect to variations of that path* [2]. If the OPL is a function of x, then the point where the slope of $OPL(x)$ is zero, i.e. the minimum, corresponds to the actual light path.

2.1.4 Fresnel Equations

When studying reflection and refraction using the electromagnetic theory, the radiant flux densities corresponding to incident, reflected, and refracted light can be quantified. Fresnel used this theory to derive equations that relate the reflected and transmitted light intensity to the incident light intensity. The complete derivation will not be given here but can be found in the book Optics by E. Hecht in chapter 4.6 [2]. This derivation makes use of the wavefront continuity requirement, which states that each point of the incident wavefront is also a point on the corresponding reflected and transmitted wavefronts. The law of reflection and refraction, no matter the kind of wave, can be directly derived from the wavefront continuity requirement, as shown by Sommerfield [49].

The Fresnel equations apply to all linear, isotropic, homogeneous media, and are presented in Equation 2.4 to Equation 2.7. The last form of these equations is obtained using Snell's Law to simplify the expressions. The minus and plus signs correspond to the directions of the electric fields E_e, which were assumed when deriving these equations. These equations represent the amplitude reflection coefficients r and the amplitude transmission coefficients t for light perpendicular $\perp$ and parallel $\|$ to the interface. Using the Fresnel equations, the reflectance R and transmittance T can be determined. The reflectance is defined as the ratio of the reflected to the incident radiant intensity I_e. The transmittance is defined as the ratio between the transmitted radiant intensity to the incident radiant intensity. The expressions for reflectance and transmittance are presented in Equation 2.8 and Equation 2.9. Furthermore, $R_\perp + T_\perp = 1$ and $R_\| + T_\| = 1$ in order to conserve energy. When working with unpolarized light the average of the two reflectance and transmittance values can be used to determine the total reflectance and total transmittance.

$$r_\perp = \left(\frac{E_{e,0r}}{E_{e,0i}}\right)_\perp = \frac{n_i cos(\theta_i) - n_t cos(\theta_t)}{n_i cos(\theta_i) + n_t cos(\theta_t)} = -\frac{sin(\theta_i - \theta_t)}{sin(\theta_i + \theta_t)} \tag{2.4}$$

$$t_\perp = \left(\frac{E_{e,0t}}{E_{e,0i}}\right)_\perp = \frac{2n_i cos(\theta_i)}{n_i cos(\theta_i) + n_t cos(\theta_t)} = +\frac{2sin(\theta_t)cos(\theta_i)}{sin(\theta_i + \theta_t)} \tag{2.5}$$

$$r_\parallel = \left(\frac{E_{e,0r}}{E_{e,0i}}\right)_\parallel = \frac{\frac{n_t}{\mu_t}cos(\theta_i) - \frac{n_i}{\mu_i}cos(\theta_t)}{\frac{n_i}{\mu_i}cos(\theta_i) + \frac{n_t}{\mu_t}cos(\theta_t)} = -\frac{tan(\theta_i - \theta_t)}{tan(\theta_i + \theta_t)} \tag{2.6}$$

$$t_\parallel = \left(\frac{E_{e,0t}}{E_{e,0i}}\right)_\parallel = \frac{2\frac{n_i}{\mu_i}cos(\theta_i)}{\frac{n_i}{\mu_i}cos(\theta_t) + \frac{n_t}{\mu_t}cos(\theta_i)} = +\frac{2sin(\theta_t)cos(\theta_i)}{sin(\theta_i + \theta_t)cos(\theta_i - \theta_t)} \tag{2.7}$$

$$R = \frac{I_{e,r}}{I_{e,i}} \quad \rightarrow \qquad R_\perp = r_\perp^2 \qquad \text{and} \qquad R_\parallel = r_\parallel^2 \tag{2.8}$$

$$T = \frac{I_{e,t}cos(\theta_t)}{I_{e,i}cos(\theta_i)} \quad \rightarrow \qquad T_\perp = \frac{n_t cos(\theta_t)}{n_i cos(\theta_i)}t_\perp^2 \qquad \text{and} \qquad T_\parallel = \frac{n_t cos(\theta_t)}{n_i cos(\theta_i)}t_\parallel^2 \tag{2.9}$$

2.1.5 Geometrical Optics of Light Refraction

The variational principle of light, also known as the Fermat's principle can be used to derive an expression for the deflection of light rays that travel through a medium with a changing index of refraction, as shown below:

The traveling time of light is defined in Equation 2.10, where ds stands for the infinitesimal arc length. It can be noted that this expression equals the optical path length divided by the local propagation speed of light. The index of refraction depends on arc length.

$$T = \int \frac{ds}{c} = \frac{1}{c_0}\int n(\vec{x}(s))ds \tag{2.10}$$

In order to find which path corresponds to an extreme, the path of the light ray is varied by changing $\vec{x}(s)$ to $\vec{x}(s)+\delta\vec{x}(s)$. The start and end points of the ray trajectory remain unchanged. The first order variation of the traveling time becomes:

$$\begin{aligned} \delta T =& \frac{1}{c_0}\int(\delta n ds + n\delta ds) \\ \text{where:}\quad & \delta n = \Delta n \cdot \delta\vec{x} \\ & \delta ds = \sqrt{(d\vec{x}+d\delta\vec{x})^2} - \sqrt{(d\vec{x})^2} = ds\frac{d\vec{x}}{ds}\cdot\frac{d\delta\vec{x}}{ds} \end{aligned} \tag{2.11}$$

$$\delta T = \frac{1}{c_0}\int\left(\Delta n\cdot\delta\vec{x} + n\frac{d\vec{x}}{ds}\cdot\frac{d\delta\vec{x}}{ds}\right)ds = \frac{1}{c_0}\int\left[\Delta n + \frac{d}{ds}\left(n\frac{d\vec{x}}{ds}\right)\right]\cdot\delta\vec{x}ds \tag{2.12}$$

It should be noted that higher order $\delta\vec{x}$ terms are ignored. The last term in Equation 2.12 is obtained using the integration by parts method and realizing that $\delta\vec{x}$ goes to zero at the end points. By setting the variation of the traveling time to zero, i.e. $\delta T = 0$, the extreme corresponding to the true light path is found. This results in Equation 2.13, which is the equation for the light ray deflection.

$$\Delta n = \frac{d}{ds}\left(n\frac{d\vec{x}}{ds}\right) \tag{2.13}$$

2.1.6 Surface Reflection

When light strikes a surface it can reflect in a specular of diffuse manner, as already mentioned in subsection 2.1.2. The reflection of light of surfaces can be approached from a physical optics or geometric optics perspective. While the later is an approximation of the former, geometrical optics are simpler mathematically speaking. According to Nayar et al. [50], the simpler mathematical form of the geometrical optics often render them more useful in comparison to the physical optic models. However, geometrical optic models are usually only valid when the surface roughness or imperfections are much larger than the wavelength of the incident light. When the surface roughness is large compared to λ, the law of reflection still holds, but each light ray will be reflected in a different direction due to the angles of the surface.

Another aspect of surface reflection is the subsurface scattering of light [4]. Due to the scattering of light in the material that is reflecting the light, the surface position of the incident ray and the reflected ray are not necessarily the same, as can be seen in Figure 2.4. The approximation that light enters and leaves a material at the same position is valid for metals according to Jensen et al. [4]. However, the wing of an aircraft is usually painted and has a coating layer.

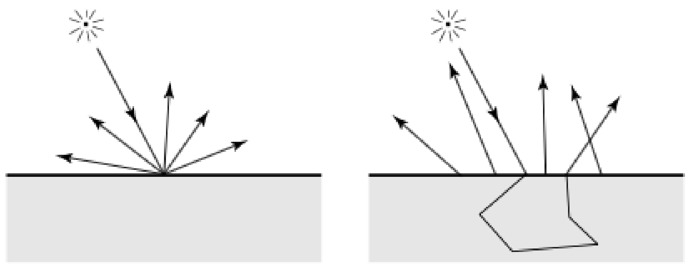

Figure 2.4: Scattering of light (a) in one point (b) with subsurface light scattering [4]

For diffuse reflection the Lambertian model can be used, which is a simple mathematical model describing diffuse reflection. Jensen et al. [4] refer to multiple studies which used the Lambertian model, concluding that it describes the diffuse reflection reasonably well. The Lambertian model describes Lambertian reflectance for which the brightness of a ideal diffuse reflecting surface is the same in every direction, hence not depending on the observer's angle with the surface. This is mathematically described by Lambert's cosine law, also known as the cosine emission law, which is presented by Equation 2.14 [51, 52]. I_e represents the radiant intensity and θ_s is the angle between the surface normal and the light ray that is reflected off the surface. It should be noted that this equation only relates the reflected radiant intensity in one direction to the maximum reflected radiant intensity. Hence, the calculated reflected radiant intensity should be divided by the total reflected radiant intensity in all directions. The term by which the reflected radiant intensity should be divided is $(\pi\ sr)$, as the maximum intensity $I_{e,0}$ is $(1/\pi\ sr)$ of the incident radiant intensity. However, if one is only interested in how strong the reflection under one angle is in comparison to another angle, the constant $(1/\pi\ sr)$ can be dropped. All surfaces that follow Lambert's law are called Lambertian.

$$I_e(\theta_s) = I_{e,0} cos(\theta_s) \tag{2.14}$$

It should be noted that a wing surface is usually made of metal, which is covered in a coating and might be painted. Hence, the wing surface is most likely not a perfectly diffuse reflector, meaning that part of the reflection will be specular. To describe this specular part of the reflection, another model will be needed. According to Jensen et al. [4] the Beckmann-Spizzichino model (physical optics) or the Torrance-Sparrow model (geometrical optics) could be used. However, both these models are significantly more computationally expensive than the Lambertian model, and they require knowledge of the reflective surface in terms of surface roughness and the surface material.

2.2 Shadowgraphy and BOS Basics

Light traveling through the atmosphere bends as a result of the inhomogeneities in the air caused by turbulence, thermal convection, weather related phenomena, etc. The bending of light is caused by changes in the refractive index in air as a result of changes in density. These disturbances in air or other gasses can be studied by means of shadowgraphy, schlieren, or interferometry techniques as these techniques visualize changes in the index of refraction. This section describes how the shadowgraphy technique and BOS technique work, and how these techniques can be used to visualize shock waves on wings. First, some basic principles of the schlieren and shadowgraphy technique and some definitions will be presented. Secondly, the direct shadowgraphy technique will be explained in more detail. Thirdly, the BOS technique will be discussed. This section will be concluded by a short comparison between the shadowgraphy and the schlieren techniques.

2.2.1 Basic Concepts & Definitions

According to Goldstein and Kuehn, the index of refraction of a homogeneous medium is often only a function of the density [53]. The Lorenz-Lorentz relation, presented in Equation 2.15 [53], relates the density of a transparent homogeneous medium to its index of refraction. When $n \cong 1$, this relation can be reduced to the Gladstone-Dale equation, presented in Equation 2.16, which is used to calculate the index of refraction for gasses [5, 53]. The Gladstone-Dale coefficient k for air is approximately $0.23 * 10^{-4} m^3/kg$ and it depends on the wavelength of the light. To be precise, k increases slightly with increasing λ, meaning that the weakest disturbances in a flow are most detectable using the red end of the color spectrum.

$$\frac{1}{\rho}\frac{n^2-1}{n^2+2} = constant \tag{2.15}$$

$$n - 1 = k\rho \tag{2.16}$$

When the deflection of the light rays is measured with either the shadowgraphy or schlieren technique, the z-axis of a Cartesian coordinate system is aligned with the light propagation direction of the undisturbed rays that pass through a region with inhomogeneities. The deflections will take place in the xy-plane, perpendicular to the normal z-direction. When the deflection is assumed to be small, the beam displacement with respect to the normal axis is small as well, thus $ds = dz$. For gradual bending of light rays, meaning no discontinuities in the index of refraction, dn/ds is very small for most disturbances in air. Using these assumptions, Equation 2.13 can be rewritten to Equation 2.17 for ray curvature. Integrating these equations once yields an expression for the angular ray deflection ϵ, as can be seen in Equation 2.18.

$$\frac{\partial^2 x}{\partial z^2} = \frac{1}{n}\frac{\partial n}{\partial x}, \qquad \frac{\partial^2 y}{\partial z^2} = \frac{1}{n}\frac{\partial n}{\partial y} \tag{2.17}$$

$$\epsilon_x = \frac{1}{n}\int \frac{\partial n}{\partial x}\partial z, \qquad \epsilon_y = \frac{1}{n}\int \frac{\partial n}{\partial y}\partial z \tag{2.18}$$

When Toepler invented the schlieren technique he named it after the optical inhomogeneities in glass which are called 'schlieren' in German. Throughout this study the definition of a 'schliere' or 'schlieren object' will be used as the name for the gradient disturbances of inhomogeneous transparent media [54]. Settles described them as follows: "They are relatively-small refractive differences within the overall background and by definition they bend light rays in any direction other than the normal direction z." [5, 55] A schlieren object can have refractive index gradients in up to three dimensions. However, the basic schlieren and shadowgraphy technique cannot fully characterize these three dimensional gradients as they are two dimensional optical methods. If only one or two index of refraction gradients are present, these should be aligned with the x and y axes in order to visualize them most clearly.

2.2.2 Direct Shadowgraphy

The simplest form of the shadowgraphy technique is called the direct shadowgraphy method and consists of only a light source, schlieren object, and a screen on which the light is projected. This technique was also called the simple shadowgraphy method by Schardin due to its simplicity [55]. Figure 2.5 shows how light from the light source shines on the screen while some of the light passed through a schlieren object before reaching the screen. Without the presence of the schlieren object, the screen would be uniformly illuminated. However, the schlieren object bends the light rays. Figure 2.5 shows a light ray that has been deflected by the angle ϵ while passing through the schlieren object. When the light ray reaches the screen, it will have been displaced by a distance Δa. In a very simplistic case where only this light ray is deflected, extra illumination would occur at the point where the ray strikes the screen, whereas the point were the ray used to strike the screen when no schlieren object was present would experience a lower illumination level. As a results of the bending of light, regions of higher and lower illumination levels will be formed on the screen, which are visible as bright and dark regions.

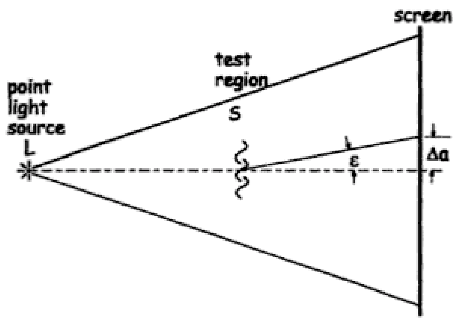

Figure 2.5: Diagram of the most simple direct shadowgraphy [5]

Another form of direct shadowgraphy is the method where parallel light is used. This is usually done by the addition of a lens to the system, as can be seen in Figure 2.6. The example shown in Figure 2.6, originally presented by Settles, uses a spherical schlieren object with a higher index of refraction than its surroundings [5]. The light refraction is strongest at the spherical boundary when the incoming rays are nearly tangent to the boundary surface, i.e. the rays have a large angle of incidence. This results in a a dark ring surrounding a light ring. This light ring is created by the refracted light that would previously strike the screen at the location of the dark ring. According to Settles, the outer diameter of the dark band should correspond to the actual diameter of the schlieren object in ideal conditions [5].

The biggest drawback of a shadowgraph is that it is a shadow and not an image. Hence, there is not always an one-to-one relation between the object and the shadow. Only dark regions can represent the schlieren object in an undistorted manner as these are the regions where the deflected rays originate [56]. The bright spots on a shadowgraph can be misleading as they

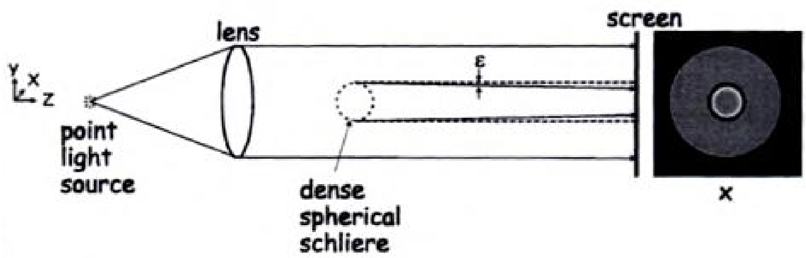

Figure 2.6: Diagram of simple direct shadowgraphy in parallel light [5]

represent where the deflected light ends up. As light rays can cross or overlap before forming a shadowgraph, caustics may be formed. Therefore, bright spots, that are near part of an object in the shadowgraph, might not be related to that part of the object in the shadowgraph. This is also where the difference lies between direct shadowgraphy with diverging or parallel light. As mentioned before, for parallel light, a dark region can reveal the size of a schlieren object, under ideal conditions. However, for diverging light, a magnification occurs. Hence, the distances between the light source, schlieren object, and the screen have to be known to couple the size of the dark zones to the schlieren object. When a schlieren object has a large depth along the optical axis (z-axis), near and far features in the shadowgraph suffer from different magnification factors when divergent light is used. This does not happen while using parallel light. Hence, direct shadowgraphy with divergent light usually has a simpler set-up, but the shadowgraphs might be harder to interpret in comparison to direct shadowgraphy with parallel light.

In order to make some deflection more visible, i.e. increasing Δa for the same ϵ, the distance between the schlieren object and the screen can be varied [5, 7]. For increasing distances between the two, the deflection of light rays increases. This can be used to make some 'weaker' phenomena more visible. However, the chance of light rays crossing, overlapping, and intersecting before striking the screen increases with increasing distance between the schlieren object and the screen. It can thus be concluded that, depending on the schlieren object of interest, an appropriate distance between the object and the screen needs to be chosen.

The following two subsections will discuss the sensitivity of direct shadowgraphy while using diverging or parallel light. These subsections will illustrate how different light sources effect what is visible in a shadowgraph by discussing the smallest resolvable size of a feature of a schlieren object. These limits will be treated from a geometrical and diffraction standpoint. These details are discussed here to clearly illustrate some limiting factors for shadowgraphy as well as to show the difference between parallel light and divergent light cases that is caused by the magnification.

Direct Shadowgraphy in Diverging Light

The notation used for the geometric-optical theory [55, 56] is presented in Figure 2.7. The magnification of the shadow with respect to the schlieren object m is defined in Equation 2.19, where g is the distance between the schlieren object and the screen and h is the distance between the light source and the screen. The light ray c, that is refracted through angle ϵ, will follow a new trajectory c', which strikes the screen at a distance Δa from the original trajectory c. This distance Δa is defined in Equation 2.20.

$$m = \frac{h}{h-g} \tag{2.19}$$

$$\epsilon \cdot g = \Delta a \tag{2.20}$$

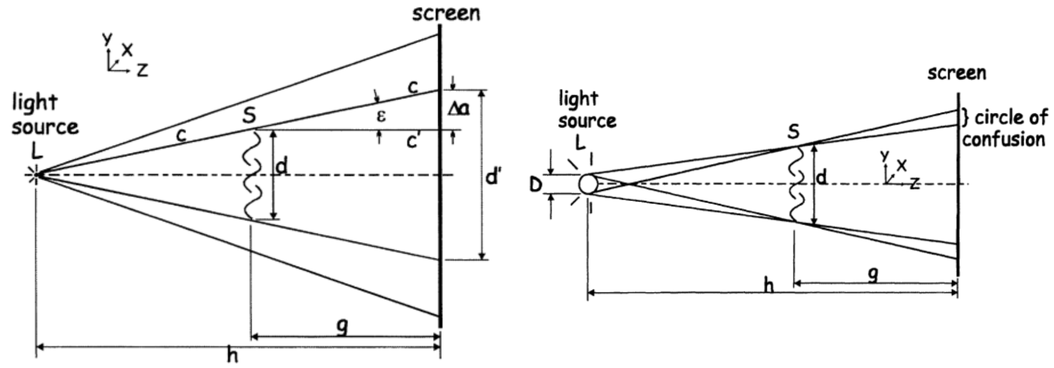

Figure 2.7: Diagrams of direct shadowgraphy with diverging light [5]

Schardin formulated the contrast in the shadowgram such that it equals the ray displacement relative to the size of the shadow, as can be seen in Equation 2.21 [55], where E_e stands for the irradiance. The sensitivity of a shadowgraph is determined by the contrast because more features of a schlieren object are visible in the shadowgraph when the contrast is increased. The ϵ/d term in the equation represents the strength of the schlieren object, where d stands for the height of the schlieren object. The $g(h-g)/h$ term represents the effect of the optical geometry on the sensitivity. By differentiation it was found that the sensitivity is maximized for $g/h = 1/2$. Schardin stated that h should be as large as possible and that the schlieren object should be halfway between the light source and the screen to obtain the highest sensitivity [55]. Hannes, a student of Schardin, stated that the strength of the refraction, ϵ/d, should be written as $\partial\epsilon/\partial y$ [57]. This clarifies that the spatial derivative of the refraction angle, $\partial\epsilon/\partial y \propto \partial^2 n/\partial y^2$, is sensed by shadowgraphy instead of the refraction angle itself. Hence, Equation 2.21 turns into Equation 2.22. However, Weinberg warns that this relation oversimplifies the difficulty of representing an object by its shadow due to the crossing of light rays [56]. Hence, Equation 2.22 is only approximately true when superposition of light from different regions does not occur.

$$\frac{\Delta E_e}{E_e} = \frac{\Delta a}{d'} = \frac{\epsilon}{d} \cdot \frac{g(h-g)}{h} \tag{2.21}$$

$$\frac{\Delta E_e}{E_e} = \frac{\partial\epsilon}{\partial y} \cdot \frac{g(h-g)}{h} \tag{2.22}$$

Next, geometrical blur is considered. Geometrical blur is caused by the size of the light source, namely its diameter D. As a result of the light source not being a point source, a circle of confusion with a diameter of $gD/(h-g)$ is present, as shown in Figure 2.7. When using the sun as a light source, the circle of confusion has an angle of approximately $1/2°$, resulting in a circle of confusion with a diameter of $g \cdot tan(1/2°)$ [7]. Among others, Schardin, Weinberg, and Hannes, recognized that the smallest feature δ one wants to resolve in a shadowgraph determines the allowable level of blur [55–57]. By dividing the diameter of the circle of confusion by the magnification, defined in Equation 2.19, the relative blur size is obtained, which is $(gD/(h-g))/(h/(h-g)) = gD/h$. This relative blur size is defined in such a way that it represents the size of the blur at the location of the schlieren object, enabling a one-to-one comparison with δ. Hence, if a schlieren object of true size δ needs to be resolved, the relative blur size has to be smaller than δ, i.e. $gD/h < \delta$. The usable sensitivity, according to Weinberg, is formulated in Equation 2.23 [56]. Weinberg derived this formula from Equation 2.22 while assuming peak sensitivity ($m = 2$). When this assumption is not made, the second definition can be used where m is still present. For the smallest resolvable feature $\delta = gD/h$, hence g in

Equation 2.23 is replaced by $g = \delta h/D$ to obtain Equation 2.22. Basically, ϵ has to compete with the blur angle for the phenomena of interest to be visible.

$$\frac{\Delta E_e}{E_e} = \frac{\partial \epsilon}{\partial y} \cdot \frac{\delta h}{2D} = \frac{\partial \epsilon}{\partial y} \cdot \frac{\delta h}{mD} \tag{2.23}$$

The above mentioned geometric considerations suggest that both the resolution and sensitivity can be improved by reducing the diameter of the light source. However, the wave nature of light limits this reduction of D as diffraction fringes appear. Weinberg derived Equation 2.24 and Equation 2.25 for the minimum refraction angle ϵ_{min} and the minimum schlieren object δ_{min} resolvable above the diffraction blur [56]. Weinberg also derived Equation 2.26 for the minimum useful D, evaluated at the onset of diffraction fringing in the shadowgram.

$$\epsilon_{min} = 1.33\sqrt{\lambda h/g(h-g)} \tag{2.24}$$

$$\delta_{min} = 1.33\sqrt{\lambda g(h-g)/h} \tag{2.25}$$

$$D_{min} = 1.33\sqrt{\lambda h(h-g)/g} \tag{2.26}$$

Direct Shadowgraphy in Parallel Light

For direct shadowgraphy in parallel light the sensitivity is defined in Equation 2.27. The first definition in Equation 2.27 is given by Schardin and the second definition is given by Hannes [55, 57]. It can be noted that the magnification term has been dropped in Equation 2.27 as no magnification occurs when using parallel light, as can be seen in Figure 2.8, which shows a generic setup for direct shadowgraphy in parallel light.

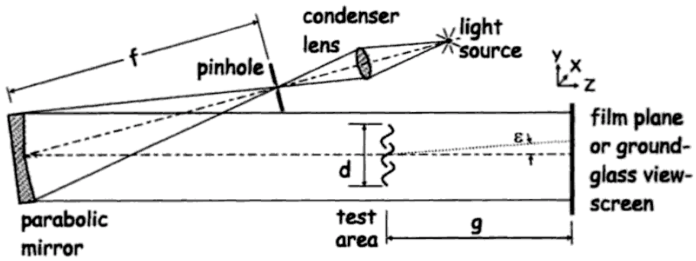

Figure 2.8: Setup for direct shadowgraphy in parallel light [5]

$$\frac{\Delta E_e}{E_e} = \frac{\Delta a}{d} = \frac{\epsilon g}{d} \qquad \text{or} \qquad \frac{\Delta E_e}{E_e} = \frac{\partial \epsilon}{\partial y} \cdot g \tag{2.27}$$

The geometric blur is defined by the aperture angle, which is D/f for the parallel light arrangement, where f represents the focal length of the mirror or lens used to create the parallel light. The diameter of the circle of confusion is gD/f in this case. In order to resolve a schlieren object of size δ, $gD/f < \delta$. Hence, the maximum usable sensitivity is once again determined by substituting $g = \delta f/D$ into the shadowgraph contrast equation, which results in Equation 2.28 [56].

$$\frac{\Delta E_e}{E_e} = \frac{\partial \epsilon}{\partial y} \cdot \frac{\delta f}{D} \tag{2.28}$$

The minimum resolvable refraction angle and schlieren object due to diffraction blur for parallel light are defined in Equation 2.29 and Equation 2.30. The minimum useful light source diameter for parallel light is formulated in Equation 2.31. It should be noted that the factor 1.33 comes from an arbitrary definition of diffraction blur, namely the distance by which the first bright fringe extends beyond shadow edge. Hence, these formulas should thus be used as a indication according to Weinberg [56].

$$\epsilon_{min} = 1.33\sqrt{\lambda/g} \tag{2.29}$$

$$\delta_{min} = 1.33\sqrt{\lambda g} \tag{2.30}$$

$$D_{min} = f\sqrt{\lambda/g} \tag{2.31}$$

2.2.3 Background-Orientated Schlieren

The basic schlieren technique usually uses a light source in combination with a pair of lenses or mirrors to create a beam of parallel light. The schlieren object is placed in this parallel light, in between the pair of lenses or mirrors, causing some of the light to bend. The light that has passed through the schlieren object passes the second lens or mirror and converges to the focal point of that lens or mirror before being projected on a screen or surface. The light that was bent by the schlieren object will not go through the focal point of the mirror or lens. Since a schlieren knife, a object that blocks part of the light, is placed at the focal point of the second lens or mirror, part of the deflected rays will be blocked by this schlieren knife. This will result in regions of higher and lower light intensity on the screen. For example, when a horizontal schlieren knife is placed on the lower side of the focal point, rays that were bend down will be blocked while rays that were bend up will be able to pass the schlieren knife.

The Background-Orientated Schlieren (BOS) technique is variant of the schlieren technique that, in its simplest form, only needs a camera, a schlieren object, and a speckled background. Hence, the setup is simpler in comparison to the setup of the traditional schlieren technique. BOS was introduced around the same time by both Meier [58,59] and by Dalziel et al. [60,61]. However, the principle for this technique was already observed by Hooke and Schardin [5], and Schardin established that this technique is a schlieren technique that does not require a schlieren knife. This technique uses high resolution images of the background with and without a schlieren object between the camera and the background. The two images, also known as an image pair, are compared in order to reveal distortions in the background caused by the schlieren object. This post-processing of the images can be done with PIV software according to Hargarther and Settles [20]. Even though the technique itself has already been known for a long time, the recent developments in both hardware and software for computers and cameras have enabled a new use for the technique.

Figure 2.9 shows the arrangement for Schardin's schlieren method number one, which is also typical for the BOS technique [55]. This figure shows a single light-dark boundary for clarity instead of multiple light-dark boundaries which are common in real practice. In this case, light traveling through point p in the schlieren object is refracted by angle ϵ. This causes the background to look distorted as the point that is on the optical axis seems to be at point p". Usually, the image of the distorted background itself will not show features of the schlieren object. By comparing the distorted image to the reference image, the distorted areas and the amount by which these areas are displaced can be determined, hence revealing features of the schlieren object.

The sensitivity of the BOS technique depends on the distance between the background, the schlieren object, and the camera. Maximum sensitivity is achieved when the schlieren object

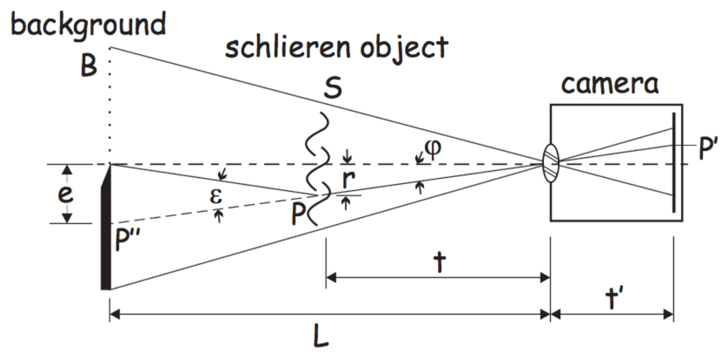

Figure 2.9: Schardins schlieren method number 1 [5]

is halfway between the background and the camera. However, both the background and the schlieren object need to be in reasonable focus for the BOS processing to succeed according to Hargarther and Settles [20]. Hence, the depth of field of the camera limits the set-up. The background needs to be composed of random patterns such that distortions can be traced back to one original position. These random patterns need to be clearly visible on the camera.

2.2.4 Differences Between the Shadowgraphy and Schlieren Techniques

The shadowgraphy and the schlieren techniques are based on same principles of light deflection. However, several important distinctions have to be made. First, the schlieren method requires a schlieren knife to cut off refracted light, while the shadowgraphy method needs no such cut off. Secondly, the schlieren object is in focus for the schlieren technique whereas the shadowgraphy technique is focused on a shadow. Finally, the illuminance levels for both methods correspond to a different relation of the refractive index. A schlieren image corresponds to $\partial n/\partial x$ and a schadowgraph corresponds to $\partial^2 n/\partial x^2$. Hence, the schlieren image represents the deflection angle whereas the shadowgraph shows the gradient of the deflection angle which is visible as the ray displacement as a result of the deflection [5].

The shadowgraphy technique has an advantage over the schlieren technique as far as simplicity is concerned. The shadowgraphy technique needs just three things namely, a light source, a schlieren object, and a screen to cast the shadow on, making it extremely easy to use. Due to this simplicity, shadowgraphs can often be observed in nature. For example, shadows caused by shock waves on the wing of an aircraft can sometimes be seen on the wing. In this case the sun acts as the light source, the shock wave as the schlieren object, and the wing as the screen on which the shadow is cast. The schlieren technique, on the other hand, works best in a laboratory environment because the lamps, mirrors and lenses need to be precisely aligned. Another advantage that shadowgraphy has over the schlieren technique is that it allows for a large field of view [13, 62].

The most important difference between the two techniques lies in their sensitivity. In general, shadowgraphy is less sensitive than schlieren. However, $\partial^2 n/\partial x^2$ can be much larger than $\partial n/\partial x$ for highly turbulent flows or flows with shock waves, making shadowgraphy a good technique to visualize them [5].

It should be noted that the BOS technique is actually closer to the shadowgraphy technique in comparison to the traditional schlieren technique. The BOS technique does not require a schlieren knife, which is artificially added by post-processing. The setup itself can be much simpler as a camera, schlieren object, and suitable background are needed, which is similar to what is needed for direct shadowgraphy. However, the most important difference between the BOS technique and the shadowgraphy technique remains, namely that the BOS technique measures $\partial n/\partial x$ and the shadowgraphy technique measures $\partial^2 n/\partial x^2$.

3. Literature Review

This chapter presents the literature that has been reviewed to determine the state of the art of the schlieren and shadowgraphy techniques when it comes to extracting quantitative information about the shock waves occurring on the wings of commercial aircraft during transonic cruise flight. This literature review has been performed to formulate the research questions for this thesis in a form that complies with the state of the art in the field.

First, some applications of shadowgraphy technique are presented, starting with the in-flight application of shadowgraphy. Since the use of in-flight shadowgraphy to obtain useful quantitative information about wing-bound shock waves does not seem to have been studied in detail yet, some examples illustrating the general use of the shadowgraphy are presented to show that the shadowgraphy technique is not commonly used for quantitative measurements. Shadowgraphy with a retroreflective screen is presented to show how shadowgraphy can be used outdoors to capture a large field of view and the simulated shadowgraphy technique is presented as this technique can allow one to extract quantitative information from shadowgraphs. Secondly, some laboratory and outdoor applications of the BOS technique are presented, including work where shock waves on supersonic aircraft have been visualized. Thirdly, the presented applications of the shadowgraphy and the BOS technique are compared and discussed to reveal a gap in the body of knowledge that will be filled by this M.Sc. thesis. Finally, the M.Sc. thesis subject and the research questions are presented.

3.1 Shadowgraphy Applications

3.1.1 In-Flight Shadowgraphy

In 1948, Cooper and Rathert Jr. presented a report about the visual observations of shock waves in flight [6]. Three different aircraft, unspecified in the report, were used for flight tests to produce visible images of the wing-bound shock waves on the wing itself, using the principles of the direct shadowgraphy technique. Cooper and Rathert Jr. stated that the conditions needed to visualize wing bound shock waves in-flight are basically the same as the conditions needed to create a shadowgraph of a pressure discontinuity. In other words, parallel light of sufficient intensity that travels through a varying density medium before striking a screen or viewing surface is needed. For the in-flight scenario, sun light was used to produce parallel light and the wing surface was used as the viewing screen. Figure 3.1 illustrates how parallel light rays from the sun are refracted when they pass through the shock wave, creating the dark and bright bands after the wing-shock wave intersection. It can be seen that the refraction of light near the surface is assumed to be greater since the shock wave is stronger near the surface. This interpretation of the shadowgraph on the wing surface, made by Cooper and Rathert Jr., was confirmed by the images taken of these shadow formations during their experiments. Figure 3.2 shows an image taken during one of the experiments where both the canopy shock wave and wing bound shock wave are visible. The greater width of the dark and bright bands corresponding to the canopy shock wave are, according to Cooper and Rathert Jr., caused by the conical shape of the shock wave and the larger distance between the shock wave and the wing.

Cooper and Rathert Jr. found that the shock wave shadowgraphs were most clear when the sun was near its zenith. Figure 3.3 shows the plane in which the sun was located for the best

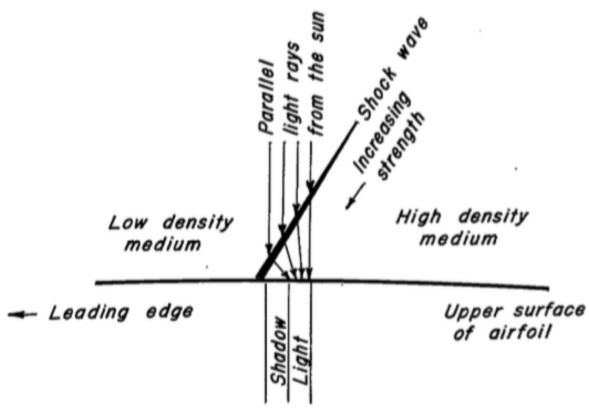

Figure 3.1: Shock shadow formation on wing surface [6]

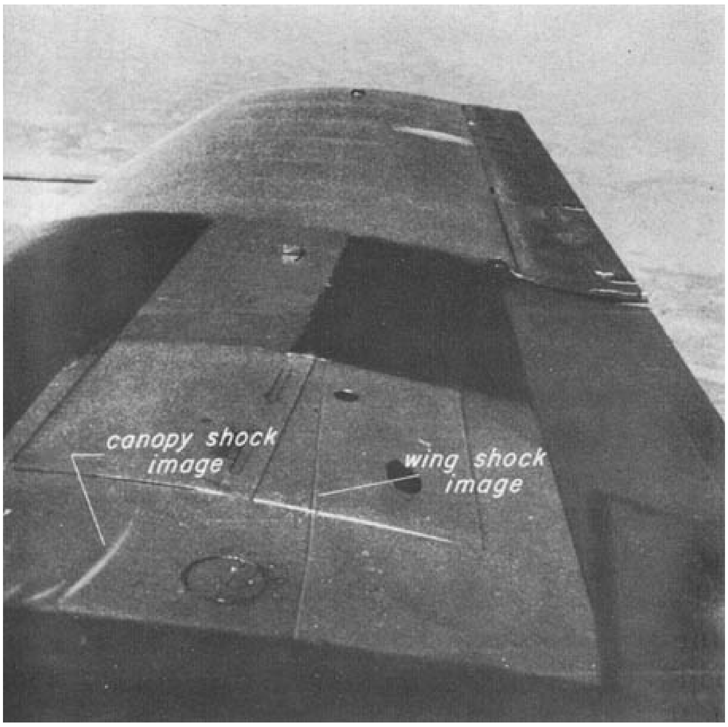

Figure 3.2: In-flight image of wing surface, visualizing both canopy and wing shock waves [6]

results during summer months. Visible shadowgraphs were obtained with the sun 20° forward or rearward of the wing, as shown by the 20° angle in Figure 3.3 which is defined in the xz-plane. It was also noted that the shock waves were approximately equally visible when looking into or away from the sun, which is indicated by the 45° angle defined in the yz-plane. Canopy shock waves, on the other hand, were only visible when looking away from the sun, i.e. visible on the down-sun wing. During winter months, Cooper and Rathert Jr. experienced problems with the shock visibility as a result of the low angle of the sun at its zenith. Cooper and Rathert Jr. also noted that the airplane attitude, required to obtain shock formations, needed to be taken into account. Hence, aircraft requiring a steep diving angle to obtain supersonic flow over the wings or supersonic flight had to dive, in some degree, towards the sun. On the other hand, aircraft that could obtain local supersonic flow or supersonic flight in level flight obtained the best results with the sun directly overhead.

The location of the viewer or the camera was also found to affect the visibility of the shock wave. The reference point for the camera positions was the pilot's head, which was positioned

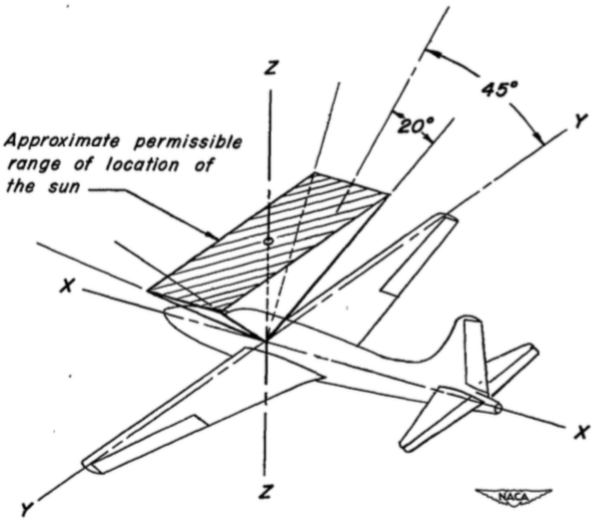

Figure 3.3: Orientation of the sun with respect to airplane axes [6]

on the line of the shock wave, if extended from one wing to the other. Camera's were located near the pilot's head, approximately 30 inches (76.2 cm) forward and 12 inches (30.48 cm) rearward. The best results were obtained if the pictures were taken with the camera directly in line with the shock wave. Both 16 and 35 millimeter motion picture cameras were used. To further increase the visibility, different background colors, i.e. colors of the wing surface, were tested. Out of dark blue, light gray, red, and polished aluminum, a red surface contributed to the best black and white photographs.

Cooper and Rathert Jr. found that shock waves were observed on both conventional and low drag airfoils, however, only photo's of the latter were obtained by them. Unpublished chordwise pressure distribution measurements were used to show that the shock wave location of the shadowgraphs agreed "quite well" with the pressure measurements. The pressure measurements were performed on similar aircraft at the Langley laboratory of NACA.

The movement of the shock waves was also analyzed by Cooper and Rathert Jr. They observed that the shock wave remains steady with constant Mach number and normal acceleration for Mach numbers below those at which severe buffeting occurred. For increasing Mach number and constant acceleration the shock wave location was found to progress smoothly rearward. For constant Mach number and increasing acceleration the shock wave location moved forward. It was also found that the shock wave location would begin to oscillate fore and aft with an amplitude of 2 to 3 inches when the test aircraft reached buffeting Mach numbers and the pull-out of a dive began. The general location of the shock was observed to follow the changes in Mach number and normal acceleration. Cooper and Rathert Jr. noted that the shock wave oscillations went hand in hand with severe buffeting of the airplane. On the two airplanes, on which the shock wave oscillations were observed, the pilots noted that they felt a relation between the frequencies of the oscillation and the buffeting. Cooper and Rathert Jr. did not obtain any quantitative measurements of this relation. When the Mach number was decreased, to cease buffeting, the shock wave would move forward steadily. With a further decrease in Mach number, to values below the critical Mach number, the visibility of the shock wave decreased until it ultimately disappeared.

Cooper and Rathert Jr. also found that the form of the shock wave image depended on the wing. For wings with a smooth and painted surface and no sudden changes in airfoil shape or wing twist, a smooth curve representing the shock wave was found in the shadowgraph image. On another wing that consisted of multiple sections, resulting in a less smooth and discontinuous wing surface, that was also unpainted, the shock wave appeared to be made up of several sections. In other words, the shock wave seemed to have varying shapes and strengths depending on the local wing shape. The form of the canopy shock wave was found to have lambda shock profile.

Figure 3.4: Photo of wingtip shock wave against air-cloud background [1, 7]

Cooper and Rathert Jr. also tried to visualize the shock wave by using a white painted wing with parallel dark lines painted on it. The idea was that the dark lines would look distorted when looking at them through the shock wave. However, even with the shock wave present, the lines did not seem distorted at the wing-shock wave intersection. A picture taken by Carla Thomas (NASA Dryden Research Center) proved that such a non-uniform background could be used to visualize a wing bound shock wave. The picture in question, presented in Figure 3.4, uses a cloudy sky as a background to visualize the shock wave by means of a distortion of the background [1, 7]. This image was taken during test flights with the L-1011 aircraft [1]. It should be noted that this manner of visualizing shock waves is very similar to the BOS technique presented in subsection 2.2.3. A picture, very similar to Figure 3.4, was obtained by Tauer et al. during a test flight with a F-16 flying at transonic speeds [8]. The picture was taken from the fuselage, looking through the shock wave on the wing, towards the background, which consisted of solar panels. The distortion of the solar panel array visualized the presence of a shock wave and revealed the position of the shock wave on the wing, as can be seen in Figure 3.5.

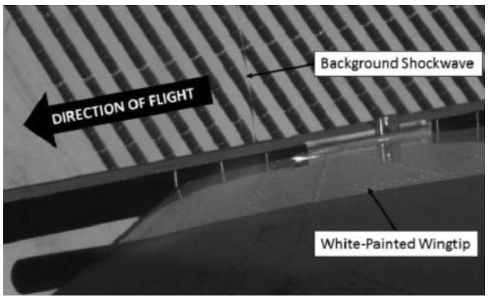

Figure 3.5: Shock wave on F16 wing visualization against solar panel back ground [8]

It was noted by Cooper and Rathert Jr. that one of the greatest advantages of this flight-shadowgraphy method is its simplicity as it needs few instruments and with little practice a "competent pilot" should be able to fly such that the shock waves are visible. They also said that this method should prove valuable in a further study of the relationship between the shock wave oscillations and buffeting. However, when both Crowder in 1987 and Fisher and Meyer Jr. in 1988 presented summaries of flow visualization techniques for in-flight experimentation, shadowgraphy was only mentioned briefly by Crowder [43, 47]. Crowder stated that the relative complexity of the schlieren, shadowgraphy, and interferometry techniques resulted in them not being used for application outside of the laboratory. Even though Crowder stated that sunlight shadowgraphy is an exception to this rule due to its simplicity, he found no systematic application of this shadowgraphy technique for validation of analytical solutions and wind-tunnel-to-flight correlations. Thereby concluding that the shadowgraphy technique has not been systematically used for in-flight purposes.

Crowder did mention a procedure that was developed to demonstrate the in-flight shadowgraphy technique [43]. The procedure consisted of flying in a shallow 360 degree turn at the desired Mach number. When the heading angle was such that the light rays from the sun were tangent to the shock wave, a visible shadowgraphy would occur on the wing surface. In 1998, Fisher et al. carried out experiments for NASA to determine the optimal sun angles and aircraft orientation needed to produce the most visible shadowgraphs on the wing of an aircraft [1]. The purpose of the paper of Fisher et al. was to document the sun elevation and azimuth angles for which the wing bound shock wave shadowgraphs are visible. They stated that the flight shadowgraph method was first described by Cooper and Rathert Jr. in 1948 for straight wing airplanes and that others, including Crowder, have discussed the method in the mean time but non described the required sun angles with respect to the wing. Hence the work of Fisher et al. continues on the work of Cooper and Rathert Jr. by determining the required sun angles for swept wings.

The Orbital Sciences Corporations's L-1011 aircraft was used by Fisher et al. for the experiments. The experiments were performed while flying between an altitude of 35,000 and 38,000 ft (10.7-11.6 km) at a nominal Mach number of 0.85. The first test flight was carried out in a summer month on August 10 of 1997 and the second test flight was performed during the winter on January 22 of 1998. Data were recorded on a nearly hourly basis when flying the aircraft in 360° or 540° turns banked at 20° to 30°. It should be noted that this procedure matches the procedure described by Crowder [43]. The test flights were performed between 30° and between 20° and 31.5° North latitude at approximately 119° East longitude [1].

An elaborate procedure to determine the orientation of the sun with respect to the aircraft at the time at which the shadowgraphs were imaged is described by Fischer et al. [1]. The results of the experiments are summarized in Figure 3.6. It can be seen that the shock waves are visible for a large range of azimuth angles when the elevation angle is large, i.e. when the sun is nearly exactly above the wing. It should be noted that shadowgraphs are only visible when the sun is forward of the quarter chordline when looking towards the sun whereas the sun can be both forward and aft the quarter chordline when looking away from the sun. The range of azimuth angles for which the shadowgraphs are visible decreases with decreasing elevation angle for both the looking towards and away from the sun cases. It should be noted, however, that for lower elevation angles, the shadowgraphs are most visible for azimuth angles that place the sun forward of the quarter chord when looking towards the sun. When looking away from the sun, azimuth angles that place the sun behind of the quarter chord results in the most visible shadowgraphs.

It can be deduced from Figure 3.6 that the shadowgraphs are only visible for low elevation angles when the sun is nearly aligned with the quarter chord line. Hence, the bright and dark lines in the shadowgraph on a certain spanwise position will not correspond to the shock wave at that spanwise position. In other words, some shock wave related data might be extracted

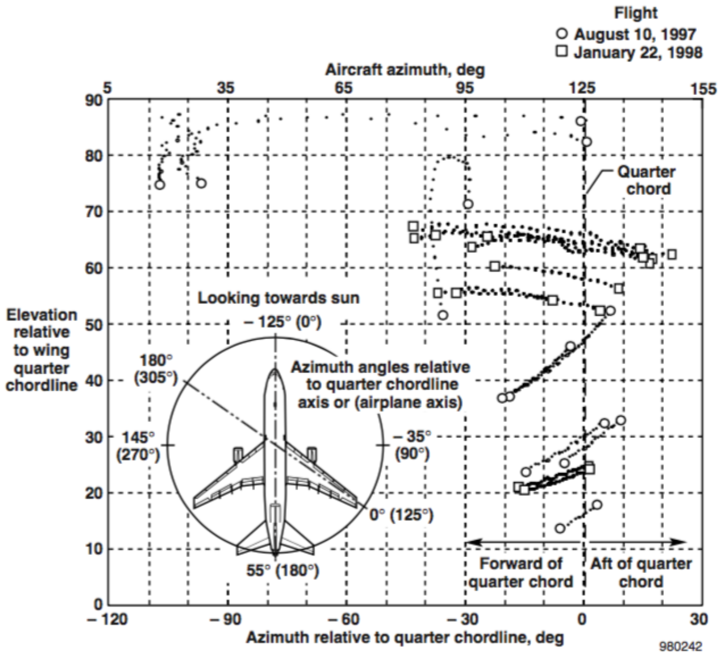

(a) Looking towards the sun

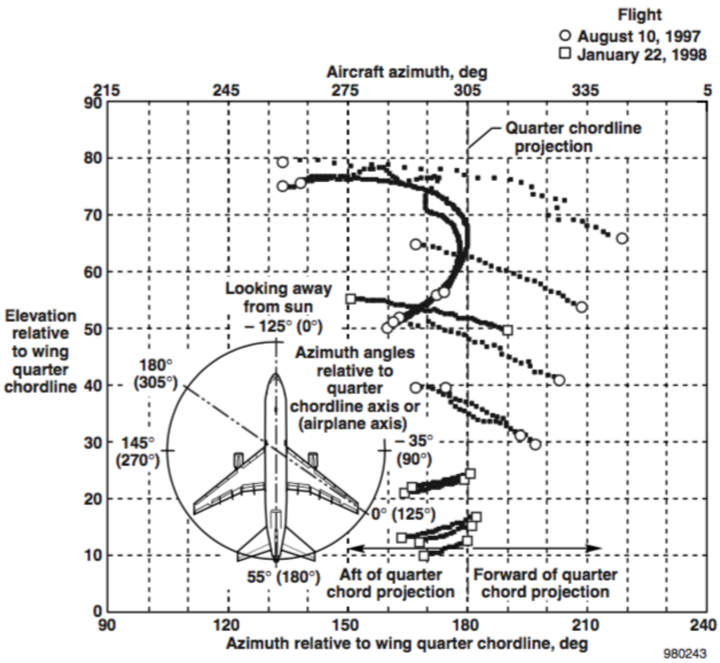

(b) Looking away from the sun

Figure 3.6: Sun elevation and azimuth angles for visible shock wave shadowgraphs on the wings of the L-1011 aircraft [1]

from the in-flight shadowgraph but it can never be linked to the correct position of the shock wave without information about the position of the sun. It can therefore be concluded that the position of the sun with respect to the wing will have to be known if quantitative data about a wing bound shock wave is supposed to be extracted from a in-flight shadowgraph.

3.1.2 General Use of Shadowgraphy

These days, shadowgraphy is still most used in laboratory setting to analyze flow related phenomena. In these settings, shadowgraphy is usually used as a qualitative tool to visualize a phenomena while other measurement techniques are used to obtain quantitative data about the phenomena. Hence, shadowgraphy is used to better understand certain flow phenomena as it can capture an entire flow field, but it is not used to quantify the phenomena. The papers presented in this section focus on the analysis of different flow types where shock waves occur. Although completely different flow types are analyzed in the different papers, the same use of shadowgraphy in combination with another quantitative measurement technique is found in the different papers. Hence, the following examples illustrate how the shadowgraphy technique is commonly used in combinations with other techniques that perform quantitative measurements when analyzing flow types where shock waves occur. It should be noted, however, that not the conclusions of these papers are presented but how shadowgraphy was used in combination with other measurement techniques.

In 2011, Disimile et al. performed experiments on the mitigation of shock waves within a liquid filled tank when a projectile was fired in such a tank [9]. This study was aimed to understand the pressure generated by a hydrodynamic ram event. To create such an event, a spherical projectile was fired into a 1000 gallon water tank, which was used to represent an aircraft fuel tank. Four different mitigation set-ups, consisting of triangular bars, were installed in the tank to mitigate the shock wave of internal pressure. Three pressure transducers were used to measure the pressure at the front wall, back wall, and at a position both in front of the mitigation arrangement and close to the "shot line" of the projectile. It was found that the pressure at the front wall, where the projectile entered the tank, was hardly affected by the inclusion of a mitigation arrangement. However, the pressure ratio between the back wall and the position close to the shot line, in front of the first mitigation members, was found to be affected by the different mitigation arrangements. In order to visualize how the mitigation arrangements affected the pressure levels across the tank shadowgraphs were made, as shown in Figure 3.7. In these images it can be seen that spherical reflected waves emanate from the first row of mitigation members as the initial wave reaches this row. Both the initial wave and the reflected waves propagate further and form a "secondary wave front", seen at 14.15 ms, where destructive interference takes place. Upon reaching the second row of mitigation members, the wave front is further reflected and distorted. Hence, shadowgraphy was used to qualitatively explain how the mitigation arrangement worked whereas pressure transducers where used to obtain quantitative results.

Lee et al. investigated the effect of a nozzle inlet configuration on under-expanded swirling jets [10]. The swirling jets were created by a convergent nozzle with four tangential inlets at the supply chamber. Different types of plug and needle combinations, which formed the back of the supply chamber, were used to alter the geometry of the supply chamber. Different supply pressures were used to obtain moderately to strongly under-expanded swirling flow at the nozzle exit. A pitot probe with an outer diameter of 0.8 mm, which was fitted onto a three-way traversing system, was used to measure the impact pressures of the supersonic swirling jet flow. Pressure measurements were taken along the jet axis to obtain quantitative data. However, shadowgraphy was used in order to visualize the entire flow field. The shadowgraphs enabled the comparison of the flow fields for different plug and needle combinations and different nozzle pressure ratios, and a better understanding of the flow field was obtained. Figure 3.8 shows the flow field for three different plug and needle combinations for two nozzle pressure ratios. The nozzle exit is at the left side of each image and it can be seen that the jets expand upon leaving the nozzle. The expansion is more severe for the cases where the nozzle pressure ratio is 7.0, which is as expected. For the FO case with a nozzle pressure ratio of 7.0, a large region of reverse flow is visible at the center of the jet. For the case S1-L and a nozzle pressure ratio of 7.0, a Mach disc is visible. In short, shadowgraphy was used during the experiment to visualize

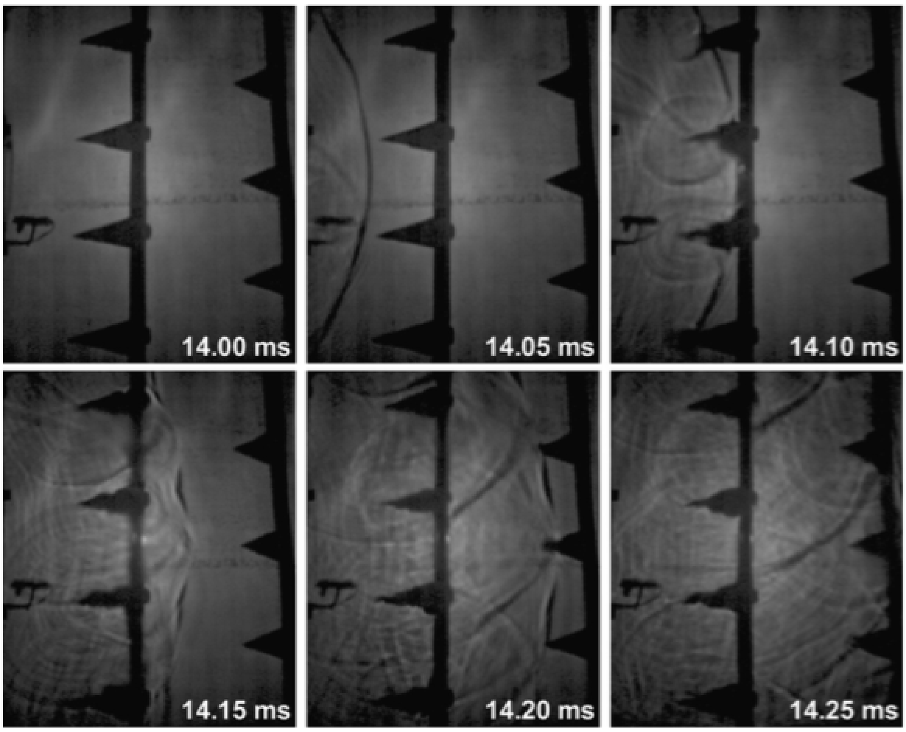

Figure 3.7: Shadowgraphs of initial shock interaction with mitigation arrangement [9]

the flow field and compare flow fields in a qualitative manner whereas pressure transducers where used to obtain quantitative results.

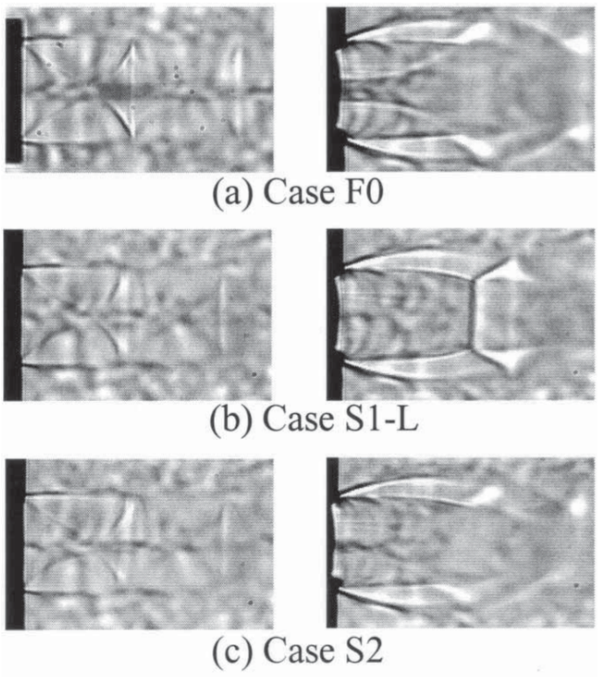

Figure 3.8: Shadowgraphs for three different nozzle supply chamber inlet configurations. Nozzle pressure ratio of 3.0 (left) and 7.0 (right) [10]

In 2003, Hafenrichter et al. studied a normal shock wave boundary layer interaction control technique, called mesoflaps, for aeroelastic recirculating transpiration [11]. This control technique was studied in a wind tunnel with an uniform Mach 1.37 flow. An array of small

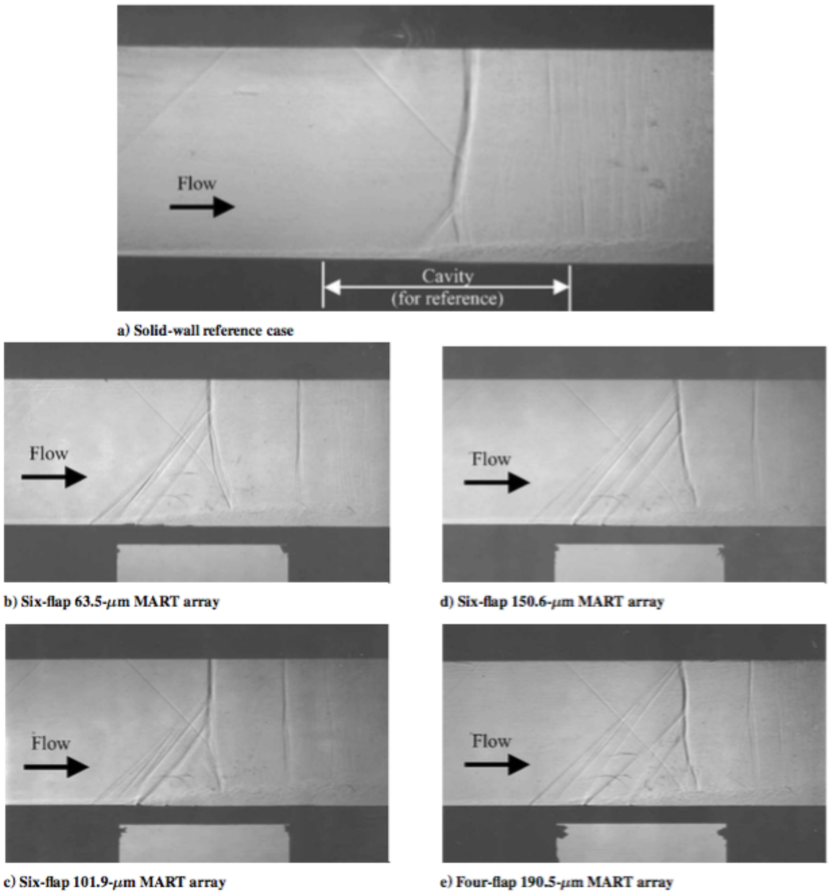

Figure 3.9: Shadowgraph visualization of flow field [11]

flaps is placed over a cavity which is located under the normal shock foot. Downstream of the shock wave, the flaps deflect downward as a results of the pressure increase along the shock wave. Hafenrichter et al. state that "this allows for removal of the low-momentum portion of the boundary layer in a fashion similar to conventional boundary-layer bleed." [11] Upstream of the normal shock, in the lower pressure region, the flaps deflect upward and the flow that was bled off through the downstream flaps is re-injected. This potentially energizes the boundary layer and oblique compression waves initiate from the upward deflected flaps, weakening the normal shock wave. Since the flap deflections are kept small, near tangential bleeding and blowing was achieved. Nine different mesoflap arrays and a solid wall case were investigated. Multiple measurement techniques were used by Hafenrichter et al. The flow at the surface on the bottom and on one of the sidewall windows was visualized by oil-streaks using a mixture of carbon black, STP oil treatment, and kerosene. The oil-streak surface-flow visualizations were used to determine in which regions separation occurred. 38 pressure taps were used along the test section spanwise centerline to measure surface pressures. 14 were placed upstream of the cavity, 13 on the cavity bottom, and 11 downstream of the cavity. It was found that pressure in the cavity was nearly constant and that the flaps performed as predicted. It was also found that six flap systems had a lower pressure than the solid wall case downstream of the cavity. Laser Doppler velocimetry was used to acquire centerline mean velocity profiles at several streamwise locations. Spark shadowgraphy was used to obtain images of the entire flow field, as can be seen in Figure 3.9. These shadowgraphs clearly imaged the oblique shock waves starting at the flaps and the weakening of the normal shock wave. In addition a secondary shock downstream of the cavity was also observed for the flap systems. In short, Hafenrichter et al. used shadowgraphy to visualize the entire flow field and oil-streaks were used to visualize the surface flow, whereas quantitative data was obtained by pressure taps and laser doppler velocimetry.

Kalkhoran et al. carried out an experimental study investigating the interaction of concentrated streamwise wing-tip vortices and normal shock fronts in a Mach 2.49 flow [12]. A semi-span wing with a diamond shape airfoil was used as the vortex generator. The vortex intensity was varied by changing the angle of attack of the semi-span wing. Downstream of the wing, a pitot-type inlet was used to generate normal shock waves. A wedge shaped block was used at the end of the pitot-type box to control the mass flow through the inlet, creating a normal shock wave by choking the flow. Both spark shadowgraphy and planar laser-sheet visualisations were used to examine the vortex-normal-shock interaction in a qualitative manner. Figure 3.10 shows two shadowgraphs and a sketch interpretation of the flow field. It was concluded from these, and unpublished shadowgraphs, that unsteady behaviour of the flow field led to the formation of conical shock structures that varied in size. The planar laser-sheet visualisation, which used smoke for the seed particles, confirmed that the sketch in Figure 3.10 was correct as little mixing between the supersonic outer flow and the subsonic central region occurred. Pitot-tube measurements were performed to obtain quantitative data about the frequency of the unsteadiness. It was found that the flow had a bimodal character, i.e. one mode where the pitot-tube was inside the conical structure and another mode for when the pitot-tube was outside this structure. These two modes were also visualised in shadowgraphs taken by Kalkhoran et al. In short, qualitative measurements were performed using shadowgraphy and planar laser-sheet visualisations while pitot-tube pressure measurements were used for quantitative measurements.

It should be noted that the shadowgraphy has already been used to obtain quantitative data about boundary and shear layers, as shown by Bowersox et al. [63]. However, these measurements were performed in laboratory settings where the distance between the camera film and the center of the test section, and the width of the test section were exactly known. Furthermore, the distance between the camera film in the test section could be controlled, which was needed to maintain an one-to-one relation between the shadowgraph and the index of refraction field. In other words, the distance between the test section and the camera film was minimized to avoid the crossing of light rays, which was mentioned in subsection 2.2.2 as a limiting factor when trying to quantify shadowgraph measurements. Hence, Bowersox et al. knew all the parameters needed to perform the double integration to quantify the density field. However, this technique would not work when using in-flight shadowgraphs because knowledge about the exact distances between the camera, the wings surface, and the shock wave are not known. Furthermore, the distance between an aircraft window and the wing surface is such that light rays are most likely to cross before reaching the camera, meaning that the one-to-one relation between the shadowgraph and the index of refraction field is lost. This technique is therefore not deemed useful for this work. It should also be noted that shadowgraphy has already been used in laboratory settings to obtain quantitative information regarding laser plasmas [64, 65]. However, this is not related to the research topic and will not be mentioned further.

3.1.3 Retroreflective Shadowgraphy Technique

In 2010 Hargather and Settles summarized the recent developments in Schlieren and shadowgraphy techniques of the last decade [20]. According to Hargather and Settles, the effect of the digital age on the schlieren and shadowgraphy techniques was and still is enormous. High-speed digital cameras, image-processing software, the use of computers to manipulate datasets, and electroluminescent light sources are mentioned as factors contributing to the development of the schlieren and shadowgraphy techniques in the last decade. Retroreflective shadowgraphy was mentioned as the development in shadowgraphy. The illumination that is reflected off the retroreflective screen back to the camera is, according to Hargather and Settles, orders of magnitude greater than the illumination that would be returned when using a diffusive screen. This

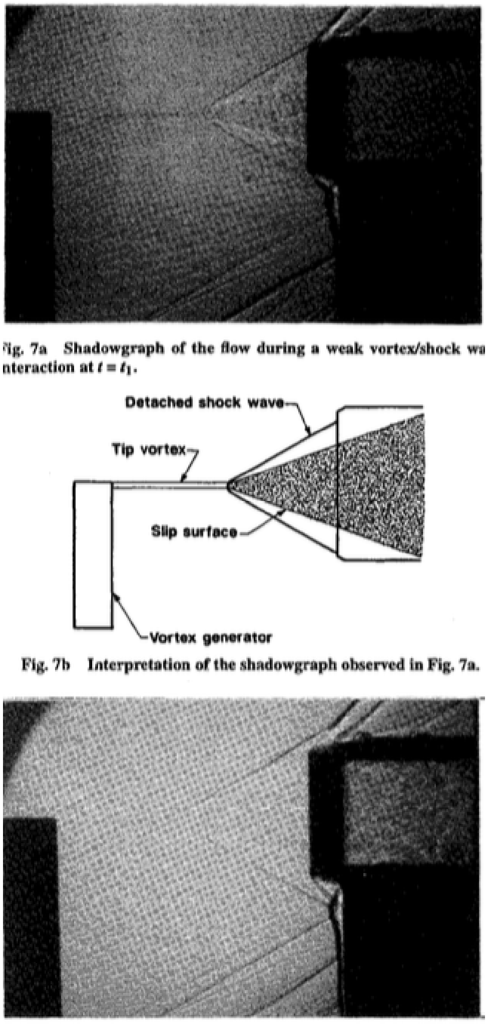

Figure 3.10: Shadowgraphs and interpretation of flow field [12]

greater illumination enables high-speed applications where microsecond and shorter exposures are desired, and outdoor experiments where interfering solar illumination is present.

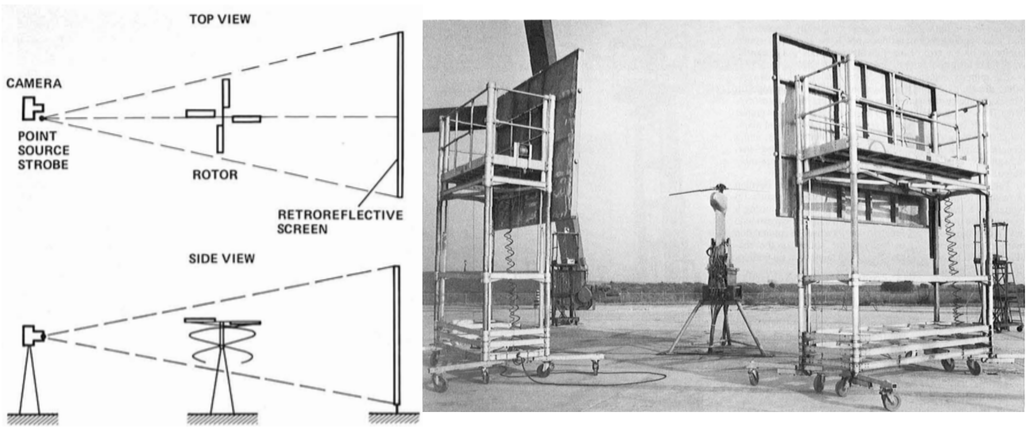

Figure 3.11: Shadowgraph setup using the retroreflective screen [13]

Among others, Norman and Light demonstrated the large field of view capabilities of the retroreflective shadowgraphy technique while studying helicopter rotor tip vortices outdoors [13]. They used a camera, a short duration high-intensity point-source strobe, a retroreflective screen, and the Ames rotor test rig with rotors. The largest rotor diameter used was just over one meter. Figure 3.11 shows a schematic of the used setup. It should be noted that the strobe and camera were located at approximately the rotor plane height and that the strobe and camera were located as close together as possible.

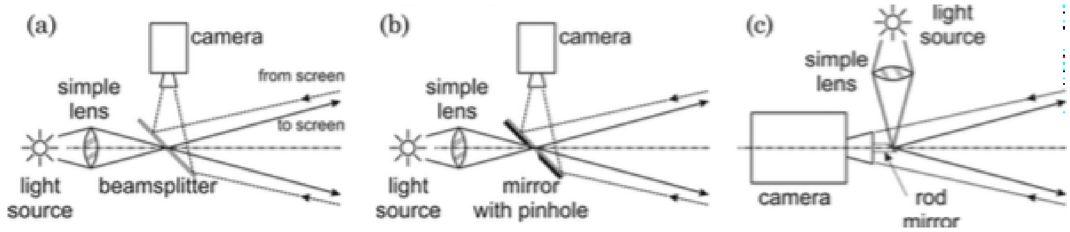

Figure 3.12: Diagrams of the coincident illumination setups for retroreflective shadowgraphy [14]

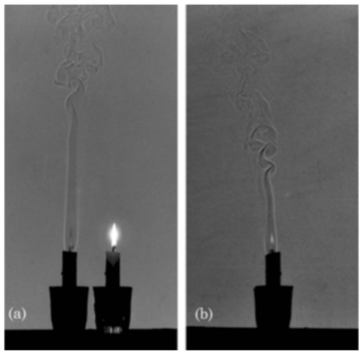

Figure 3.13: Shadowgraphs of a candle plum from (a) non-coincident setup and (b) coincident setup [14]

In 2009, Hargather and Settles modernized the technique with high-speed digital equipment, field portability, and advanced retroreflective screen material [14]. Coincident illumination setups, as shown in Figure 3.12, were used to align the physical object and its shadow. Figure 3.13 shows the effect of aligning the light source with the camera, i.e. removing the double image. This is also the reason why Norman and Light placed the strobe as close to the camera as possible, hence obstructing as little of the field of view as possible [13]. Hargather and Settles demonstrated their improved version of the technique in both laboratory and field experiments using explosives, firearms, and low-speed thermal plumes [14].

3.1.4 Simulated Shadowgraphy

Multiple studies [15–19] have been performed were shadowgraphs have been numerically simulated in order to compare them to experimentally obtained shadowgraphs to enable some quantitative analysis of the phenomena of interest. It should be noted that Thess and Orszag only discussed the possibility of experimental verification by producing simulated shadowgraphs [18]. Usually a simulated shadowgraph is created by calculating the light trajectory through a known density field and determining the illumination levels on the image screen. This section presents some studies that used this simulated shadowgraphy method.

In 1990, Hisley compared results from the BLAST2D, a gas dynamic code, to results of the SHARC and STEALTH codes [15]. These codes were used to simulate the interaction of a spherical blast wave with a compressive wedge. A Mach number of 2.12 and several different wedges angels were used for the simulation. An additional simulation of a shock impinging on a double wedge was performed using the BLAST2D code in order to compare the simulated shadowgraph to an experimental shadowgraph. The BLAST2D code was based on the 2D

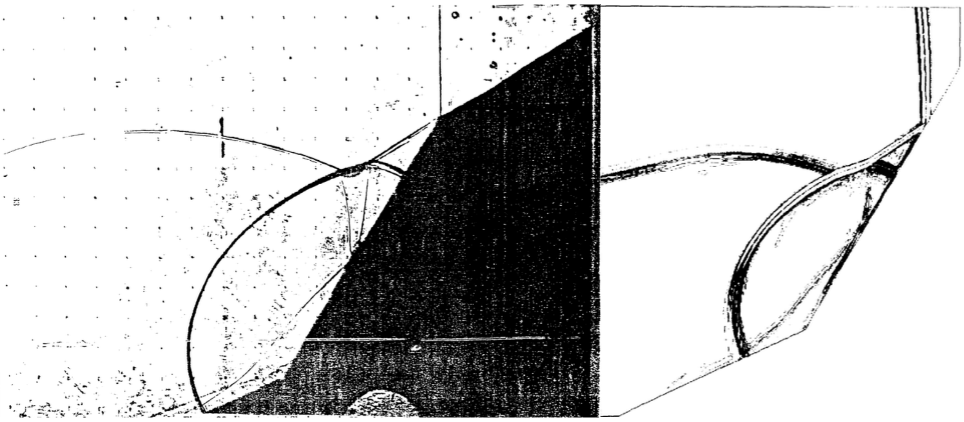

Figure 3.14: Experimental (left) and simulated (right) shadowgraphs of the double wedge flow [15]

unsteady Euler equations and a Finite Volume Scheme was used to solve the Euler equations on a uniform mesh. The physical coordinates were transformed to coordinates on the uniform mesh in the computational space. This saved computational time and the code could be applied to a variety of geometries. An upwind scheme was used for the discretization and a fully implicit scheme was used. In order to simulate shadowgraphs the following shadowgraph function was used: $f = \frac{\partial^2 \rho}{\partial x^2} + \frac{\partial^2 \rho}{\partial y^2}$. The double wedge had angles of 25° and 60°. First the density contour plot, produced by BLAST2D, was compared to the experimental shadowgraph. It was noticed that three slip lines that occurred in the experimental shadowgraph were not clearly indicated in the density contour plot. However, a density gradient contour plot did resolve two of the slip lines. When a simulated shadowgraph was produced, by plotting the contour lines of the solution of the shadowgraph function, all slip lines were resolved. Figure 3.14 shows the experimental and the simulated shadowgraphs. Hisley noted that the experimental shadowgraph does not give a good appreciation of the differing strengths associated with each discontinuity, but the simulated shadowgraph shows these differences through the distances between the contours.

In 1993, Yates described the CISS (Constructed Interferograms, Schlieren, and Shadowgraphs) code, which constructs images from ideal- and real-gas, 2D, axisymmetric, and 3D computed flow field solutions [16]. The computational grids can be structured or unstructured, and multiple grids can be used. This code reduces CPU time by eliminating the need for ray tracing as all image points are calculated and no interpolation between image points is required. Three steps are required to construct interferograms, schlieren images, or shadowgraphs from flow field solutions: 1) Identify and evaluate the appropriate functions of the refractive index. 2) Integrate these functions along lines of sight. 3) Post-process the integrals to obtain the desired image.

$$\delta\epsilon_x = \frac{1}{n}\frac{\partial n}{\partial x}, \qquad \delta\epsilon_y = \frac{1}{n}\frac{\partial n}{\partial y} \tag{3.1}$$

Yates used Equation 2.16 to determine the index of refraction from the flow field solution. Equation 3.1 was used to calculate incremental change in the angular deflection $\delta\epsilon$ at any point in the flow field. These functions were used for both schlieren and shadowgraphy to calculate the total angular deflections at the end of the computational flow field. However, for schlieren image simulation, part of the deflected light was cut off in order to simulate the effect of the schlieren knife. For the shadowgraph simulation, all light was used to form an image on the image plane. The simulated shadowgraph was constructed by using the distance to the image plane and adding the contribution of the deflected light beams at each point on the image plane. The advantage of using this distance to the image plane was that the thickness of the dark and bright regions could be controlled by altering this distance. This dependency on the distance between the schlieren object and the image plane was also mentioned by Settles [5]. In order to reduce computational time, computation of the actual light path, as it bends through the flow field solution and integrating the appropriate function of the refractive index along this path, was omitted. Instead, straight light paths perpendicular to the image plane were used. Yates stated that this should have minimal effect on regions without shocks, but this assumption may introduce errors for regions with shocks. Since the light paths are assumed to be straight throughout the flow field, the line integral to calculate the deflection of the light can be performed simultaneously for each computational cell, as the order of evaluation and summation has no effect on the final result. The shadowgraph is created by calculating the deflection of each square element of light that is projected onto the image plane. The angle that the light has with respect to the image plane, i.e. the total angular deflection, is also used to adjust the square size. Yates states that the error introduced by the presence of an infinitesimally thin shock, separating near vacuum from 1 atm, will result in a maximum deflection of approximately 0.02°.

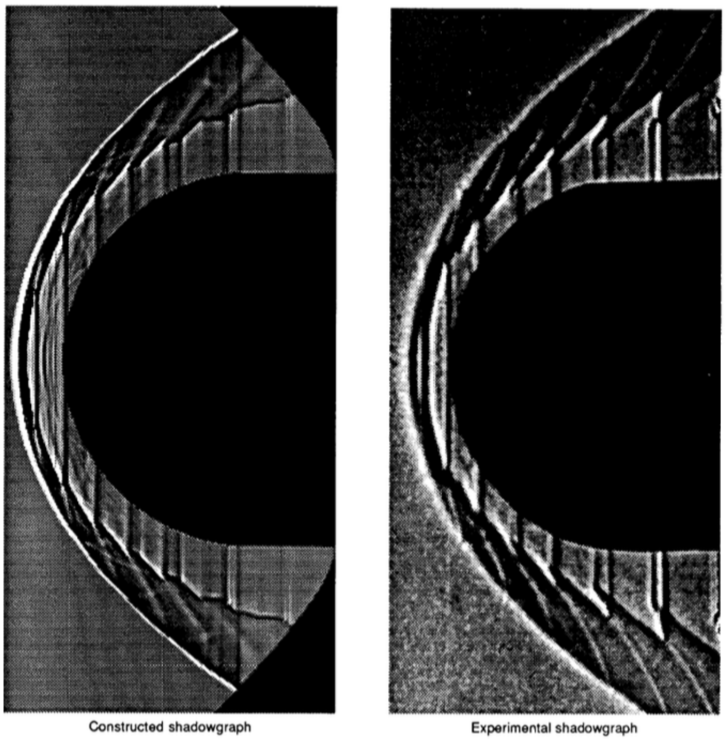

Figure 3.15: Simulated and experimental shadowgraphs of a ballistic range shot of a hemisphere cylinder into a combustible mixture [16]

Yates compared a simulated shadowgraph, created with an axisymmetric, real-gas, flow field solution of a ballistic range shot of a hemisphere cylinder into a combustible mixture, to an experimental shadowgraph, as shown in Figure 3.15. It was noted that the experimental shadowgraph was taken at slightly different test conditions in comparison to the simulation conditions. Yates stated that the flow was very complex and many features in the shadowgraph are three dimensional. However, it was found by Yates that the simulated shadowgraph represented most, if not all, of the features that were present in the experimental shadowgraph, hence allowing an one-to-one comparison.

Also in 1993, Bagai and Leishman presented a paper where they derived the general mathematical relationships between the schlieren and shadowgraph contrast profiles and the velocity profile for a series of 2D compressible vortices [17]. They also compared the results with actual shadowgraph contrast measurements performed on rotor tip vortices. This was done to extract information on both the vortex structure, and the extent and growth of the viscous core.

Bagai and Leishman also used Equation 2.16 to determine the index of refraction from the density field. For a radial symmetric flow, the contrast on a shadowgraph screen is defined in Equation 3.2 for spherical coordinates (r, θ, z). In this equation l stands for the distance from the vortex to shadowgraph screen, n_0 is the reference index of refraction, n represents the refractive index, ρ stands for the density, and l_1 to l_2 is the light path length through the density variation. Bagai and Leishman assumed inviscid, isentropic flow and chose a velocity profile for a stationary 2D vortex in order to calculate the density field. The chosen velocity profile, for the tangential velocity v_θ, is presented in Equation 3.3 for which three cases were considered: 1) the Scully vortex $n = 1$, 2) $n = 2$, 3) Rankine vortex $n = \infty$. Γ_∞ represents the strength of the vortex and r_c is the vortex core radius. Both a linearized small-perturbation thermodynamic approximation and a rigorous thermodynamic formulation were used to derive expressions for the density field and its derivatives from the chosen velocity model.

$$\frac{\Delta E_e}{E_e} = -\frac{l}{n_0} \int_{l_1}^{l_2} \left(\frac{1}{r} \frac{\partial n}{\partial r} + \frac{\partial^2 n}{\partial r^2} \right) dz = -\frac{lk}{n_0} \int_{l_1}^{l_2} \left(\frac{1}{r} \frac{\partial \rho}{\partial r} + \frac{\partial^2 \rho}{\partial r^2} \right) dz \tag{3.2}$$

$$v_\theta(r) = \frac{\Gamma_\infty r}{2\pi \left(r_c^{2n} + r^{2n} \right)^{1/n}} \tag{3.3}$$

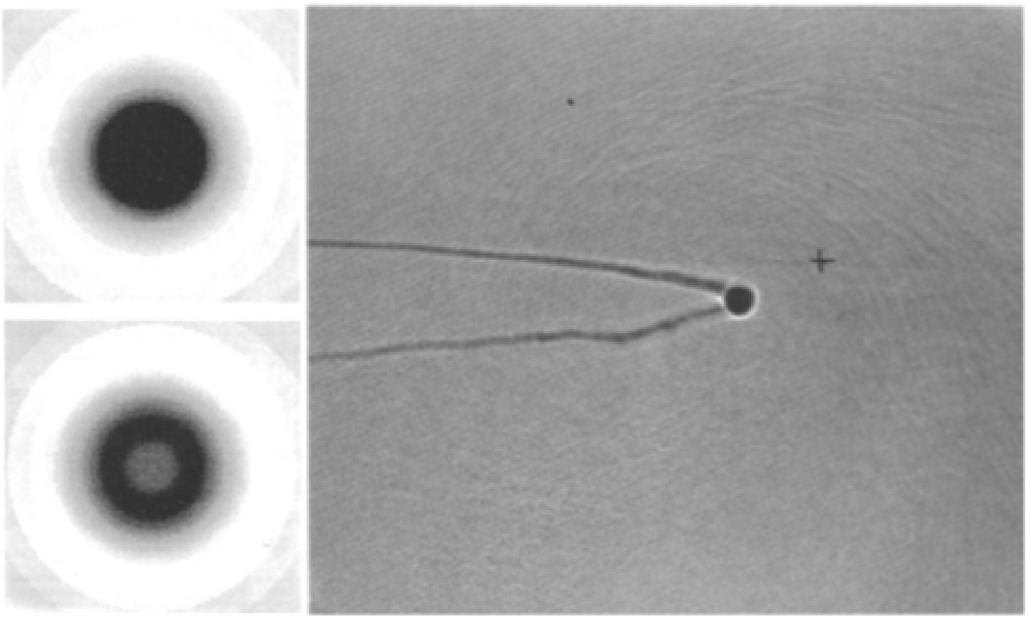

Figure 3.16: Simulated shadographs (left) n=1 (top) and n=2(bottom), and an experimental shadowgraph (right) of a rotor tip vortex [17]

When comparing the two models, Bagai and Leishman noted that the small-perturbation solution underestimates the density minimum. Although the small-perturbation solution underestimates the density minimum a little, it was found that the density profile has the same character as the solution of the rigorous thermodynamic formulation. The differences between the calculated shadowgraph contrast for the two models are, in the words of Bagai and Leishman, "fairly small". Hence, the small-perturbation solution was used to create simulated shadowgraphs. Figure 3.16 shows two simulated shadowgraphs as seen by an observer of a viewing screen mounted parallel to the $r - \theta$ plane. When Bagai and Leishman compared the simulated shadowgraphs to the experimental shadowgraphy, they stated that "the resemblance of the computed contrast to the observed contrast at the extreme edge of the shadowgraph is rather striking" [17]. Real shadowgraphs were further analyzed, converting them to an 8-bit gray scale and scaling them to reference points. This resulted in a contrast plot which could be compared to the shadowgraph contrast function. It was found that the experimental contrast was very similar to the shadowgraph contrast of the $n = 2$ case, but also had some characteristics of the $n = 1$ case.

In 1995, Thess and Orszag [18] studied surface-tension-driven convection in a planar fluid by means of numerical simulations. They discussed the possibility of experimental verification using shadowgraphs as the surface temperature itself is not easily accessible to measurements. Figure 3.17 shows a light beam that shines onto an isothermal layer of transparent fluid with a non-deformed surface. The beam is reflected at the bottom $z = 0$ and its image is recorded on a distant screen. Thess and Orszag used a calculation where the z-dependence of the temperature field was explicitly known. The trajectory of a light ray within the non-isothermal fluid is governed by the differential equations presented in Equation 3.4, where T stands for the temperature and n_0 is the index of refraction at the reference temperature $T = T_0$. For silicone oil $n_0 \approx 1.4$ and $dn_0/dT \approx 10^{-4}K^{-1}$. Since the distance between the image screen and the fluid surface is much larger than the thickness of the fluid layer, $s_1 \gg s_0$. The deflections s_1 and s_0 are both illustrated in Figure 3.17. An analytical expression for $\Delta E_e/E_e$ as a function of T can be obtained since $\|s_1\| \ll 1$, which in turn follows from $dn_0/dT \ll 1$. The smallness of dn_0/dT also permitted Thess and Orszag to treat $\partial_x T$ and $\partial_y T$ as functions of z only, evaluated at the entry point. As a result of these simplifications, the trajectory $1 \to 2 \to 3$ could be solved to obtain the direction of the light when exiting the fluid. This results in Equation 3.5 which describes the shadowgraph contrast on an image screen at a distance l from the schlieren object, which is the fluid layer in this case. The integral is performed over the thickness of the fluid layer and the deflection of light at the image screen is simply the distance l times the angular deflection of the light.

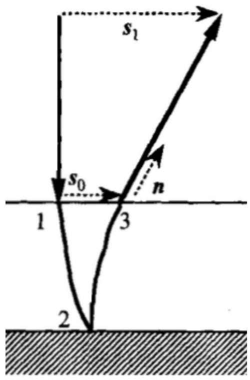

Figure 3.17: Deflection of a beam of light due to an inhomogeneous temperature distribution [18]

$$\frac{d^2x}{dz^2} = -\frac{1}{n_0}\left(\frac{dn_0}{dT}\right)\frac{\partial T(x,y,z)}{\partial x}, \qquad \frac{d^2y}{dz^2} = -\frac{1}{n_0}\left(\frac{dn_0}{dT}\right)\frac{\partial T(x,y,z)}{\partial y} \tag{3.4}$$

$$\frac{\Delta E_e}{E_e} = 2l\left(\frac{dn_0}{dT}\right)(\partial_x^2 + \partial_y^2)\int_{z=0}^{z=d} T(x,y,z)dz \tag{3.5}$$

It should be noted that Thess and Orszag only theoretically explained the possibility of a comparison between simulated and experimental shadowgraphs. It is also noticed that the $1/n_0$ seems to be omitted in Equation 3.5. Another thing that should be noted is that the index of refraction is related to the temperature in stead of the density, which would normally mean that the pressure is assumed to be constant. Although this assumption has not been specified by Thess and Orszag, it can assumed to hold as a liquid is used for the experiment in stead of a gas.

In 1996, Schopf et al. [19] used the shadowgraph method to visualize the 2D convective flow in a water-filled square cavity, which was differentially heated and cooled from the opposing vertical side walls. Since the temperature field could not be quantified from the experimental shadowgraphs, numerical solutions of the cavity flow were used to simulate shadowgraphs. The unsteady Navier-Stokes equations together with the energy equation were used compute the flow field and the calculated temperature field was used to calculate the index of refraction. By comparing the simulated and experimental shadowgraphs, an indirect comparison of the density fields can be made. This was found to lead to a clearer interpretation of the shadowgraph images because certain features in the shadowgraphs could be traced back to the numerical solution, resulting in a better understanding of the flow.

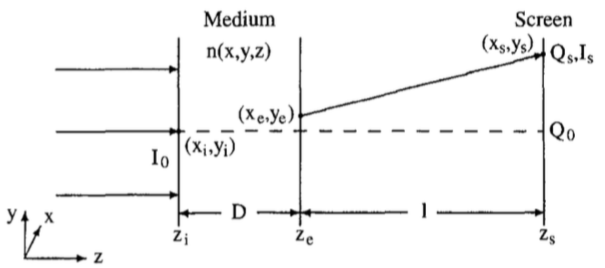

Figure 3.18: Simulated and experimental shadowgraphs of a ballistic range shot of a hemisphere cylinder into a combustible mixture [19]

Schopf et al. used Fermat's principle, that the optical path length between P_i and P_e has to be minimal, as can be seen in Equation 3.6 where the light path has been parameterized by z and $ds^2 = dx^2 + dy^2 + dz^2$. This results in $x(z)$ and $y(z)$ being functions of z. The primes denote differentiation with respect to z. Figure 3.18 illustrates how parallel light is refracted when it travels through an inhomogeneous flow field, leading to a displacement of light on the image screen. Figure 3.18 also shows the region over which the integral is performed. When the variational principle is applied to Equation 3.6, two coupled Euler-Lagrange equations which can be rewritten into Equation 3.7 are found. The four constants of integration, which are needed to solve these differential equations, are the location $(x(z_i), y(z_i))$ and the derivative $(x'(z_i), y'(z_i))$ of a light ray at the entry point. These differential equations were used to calculate the location of a light ray at the exit of the medium z_e and to calculate the deflection of the light between the medium exit point and the image screen by multiplying $(x'(z_e), y'(z_e))$ with l. The calculations were performed per light ray and the differential equations were discretized. A gray scale map of the illumination was created by counting and comparing the amount of pixels per each equal-sized cell on the computational image plain.

$$\delta\left(\int_{P_i}^{P_e} n(x,y,z)ds\right) = \delta\left(\int_{z_i}^{z_e} n(x,y,z)\sqrt{x'^2 + y'^2 + 1}dz\right) = 0 \tag{3.6}$$

$$x''(z) = \frac{1}{n}(1 + x'^2 + y'^2)\left(\frac{\partial n}{\partial x} + x'\frac{\partial n}{\partial z}\right), \qquad y''(z) = \frac{1}{n}(1 + x'^2 + y'^2)\left(\frac{\partial n}{\partial y} + y'\frac{\partial n}{\partial z}\right) \tag{3.7}$$

When it is assumed that a light ray only undergoes an infinitesimal deviation when traveling through an inhomogeneous flow field but has a non-negligible curvature on exit, the light ray will enter the medium at the same x- and y-coordinates where it entered but its derivative will not be zero. Under these assumptions Equation 3.7 would reduce to Equation 2.17. This results in Equation 3.8 which describes the changes in illumination on the image screen. According to Schopf et al., the assumption of infinitesimal deviations of the light within the medium is often justified by using very narrow experimental setups [19]. This was the case for Thess and Orszag, who used a slightly rewritten form of Equation 3.8 [18]. Schopf et al. also mention that the displacements can also become larger for larger density gradients.

$$\frac{\Delta E_e}{E_e} = \int_{z_i}^{z_e} \left(\frac{\partial^2}{\partial x^2} + \frac{\partial^2}{\partial y^2} \right) ln(n) dz \tag{3.8}$$

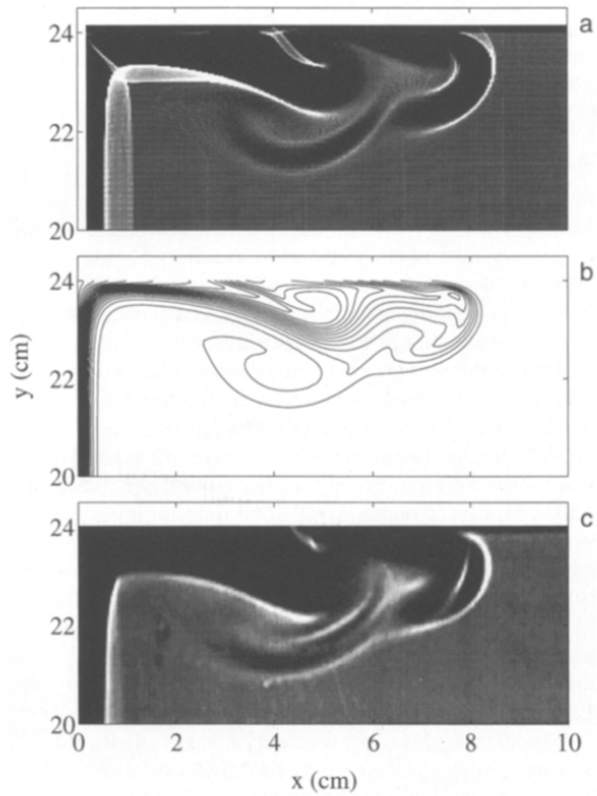

Figure 3.19: Top intrusion. a) simulated shadograph, b) calculated isotherms, c) experimental shadowgraph [19]

Figure 3.19 shows the top intrusion as it flows along the top wall into the isothermal fluid. Schopf et al. noted that the experimental and simulated shadowgraphs had essentially all the same features but some details were not exactly the same. For example, the bright "cusp" in the top left corner, in the simulated shadowgraph, is a result of the boundary conditions. The boundary condition changes abruptly from perfectly conducting to perfectly insulating in that corner whereas this change is less perfect in real life due to the finite thermal diffusivity of the insulating wall. Since the experimental and the simulated shadowgraph were in good agreement, Schopf et al. had good confidence that their numerical procedure accurately modeled the experimental system. This enabled Schopf et al. to identify the temperature structures which lead to certain features in the shadowgraph images, thus allowing some qualitative interpretation of the experimental images.

3.2 BOS Technique Applications

In 1994, Weinstein mentioned that shock waves, on aircraft flying at supersonic speeds, have been observed against a non-uniform background sky [44]. The shock waves were visible when the background became sufficiently distorted due to the light refraction caused by the shock waves. Weinstein stated that this technique was limited by its low sensitivity and the need for a non-uniform background sky. He therefore developed a method to use the schlieren technique to image shock waves around supersonic aircraft using an astronomical telescope, an opaque mask with a slit, film, and the sun as a light source [44,46]. Weinstein named this technique "schlieren for aircraft in flight". The schlieren images, obtained with this technique, were enhanced by means of image processing, revealing more details of the shock waves. A disadvantage of this technique was that the images could only be taken when the test aircraft flew through the small field of view. The aircraft had to fly in between the telescope and the edge of the sun, hence limited images could be obtained for each fly-by. The BOS technique, presented in subsection 2.2.3, can use more different backgrounds, allowing for more diverse applications. Some of these applications, that are used indoor and outdoor, are presented in this section.

3.2.1 BOS in Laboratory Setting

Hargather and Settles have demonstrated the BOS technique in the Penn State Gas Dynamics Laboratorys supersonic wind tunnel facility [20]. A simply cone model was placed in a Mach 3.0 flow, with nominal stagnation pressure and temperature of $6.9 \cdot 10^5$ Pa and 287 K respectively. A randomly dotted background was located 0.40 m away from the test section centerline. A Nikon D90 digital SLR camera was used and it was located 2.30 m away from the test section centerline on the opposite side of the test section. Hargather and Settles noted that this geometry does not result in the maximum sensitivity. However, the turbulent boundary layer and the oblique shock waves cause sufficient refraction of the light, hence the maximized sensitivity was not needed for this experiment.

Figure 3.20a shows an image that was taken during the wind tunnel test. The pixel shifts in an image were computed by comparing the image to a reference image, which was taken when the wind tunnel was not in operation. Figure 3.20b visualizes the vertical pixel shifts, corresponding to Figure 3.20a. A gray scale is used to quantify the pixel shift. This image resembles a typical schlieren image with a horizontal knife edge. Hargather and Settles also demonstrated that pixel shift contours can be presented with various color scales, as shown in the bottom two images. The images were taken with a shutter speed of 1/4000 s, which was insufficient to capture time-resolved information in the flow. As a result, the boundary layer structures were blurred, appearing as a continuous streak with a large pixel shift

Elsinga et al. assessed two quantitative schlieren methods, namely the calibrated color schlieren and the background-orientated schlieren [21]. Both techniques were used to measure the density of a 2D Prandtl-Meyer expansion fan and the results were compared to the theoretically calculated density and the density inferred from PIV velocity measurements. Figure 3.21 shows two color schlieren of flow over a 2D wedge-plate model. The left image shows the complete 2D wedge-plate model used for the experiments whereas the right image is zoomed in on the expansion fan at the top shoulder of the model, which is the expansion fan that was measured for the experiments. The solid white lines in the right image indicate the integration area and the dashed lines indicate the locations used for cross-plots. Elsinga et al. did not use the pixels that where close to the surface ($y < 9$ mm) because the deflection angles exceeded the range of the schlieren systems in that region. The experiments were performed in the transonic-supersonic wind tunnel of Delft University of Technology. A free stream Mach number of 1.96 was used with a stagnation pressure of 2.0 or 3.7 bar to study the influence of the density.

The BOS method was used in 'schlieren mode', meaning that parallel light coming from the test section was reflected by a collimating mirror after which it passed a diaphragm placed

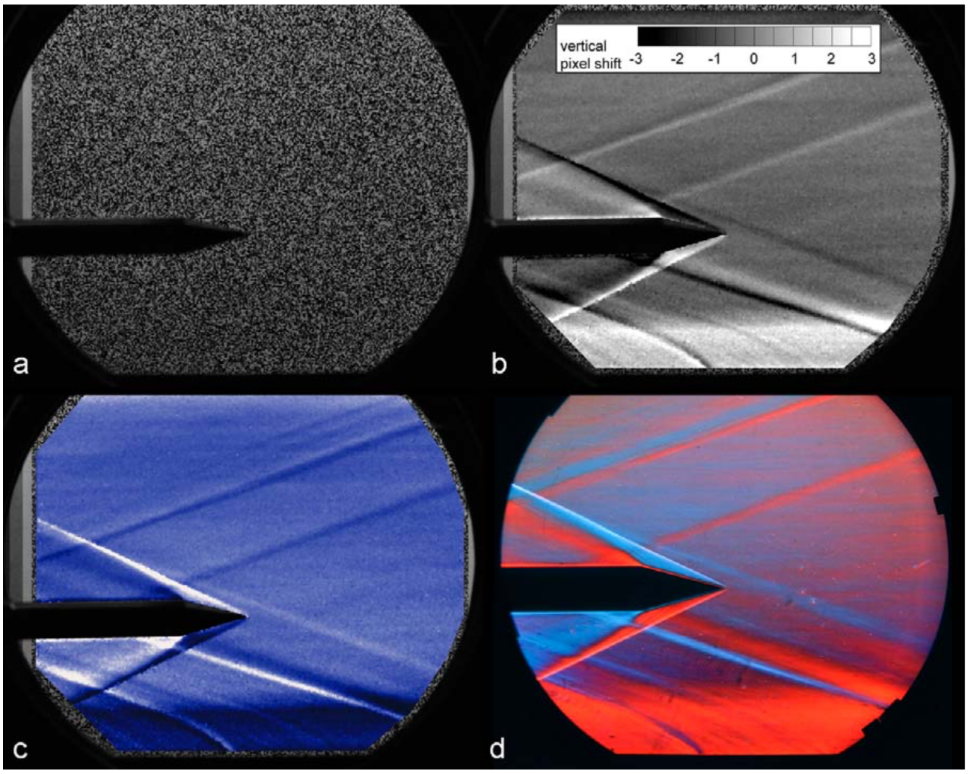

Figure 3.20: a) Original BOS image during supersonic wind tunnel operation, b) Processed BOS image with grayscale contours of vertical pixel shift, c) Blue-white color scale, d) Red-blue color scale [20]

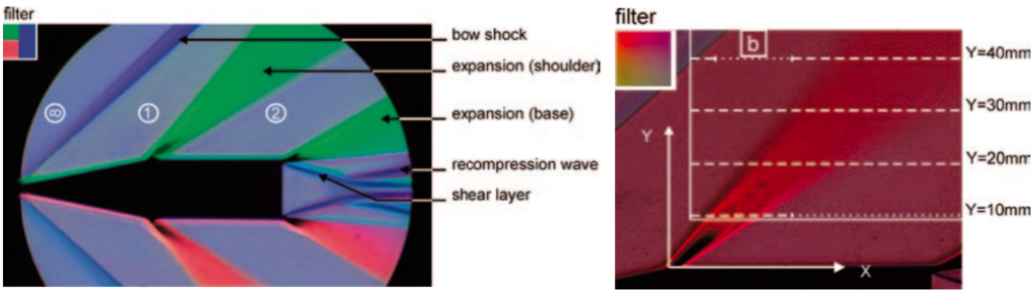

Figure 3.21: Color schlieren images of 2D wedge-plate model in Mach 2 flow [21]

at the focal length of the collimating mirror before reaching the CCD camera. A computer generated random dot pattern was used as the background, which was placed on the outside of the rear window of the test section. The measured deflection angle was related to the density gradient by $\epsilon \approx kW\nabla\rho$, where k is the Gladstone-Dale constant. W stands for the width of the schlieren object which equals the width of the test section in this case. The density gradient was spatially integrated to obtain the density field. Boundary conditions were applied at a small section of the integration area in the region upstream of the expansion fan. The final system of equations for the density calculation was over-specified and was solved using the iterative conjugate gradient method, a least square method.

It was found by Elsinga et al. that the accuracy of the BOS density measurement, with respect to the theoretical density, was around 3% (0% corresponds to complete agreement in this study). It was also found that the kinks in the theoretical density field, near the edges of the expansion fan, as seen in Figure 3.22, were attributed to shortcomings of the theoretical model. The kinks were rounded in both the results of the BOS, calibrated color schlieren, and

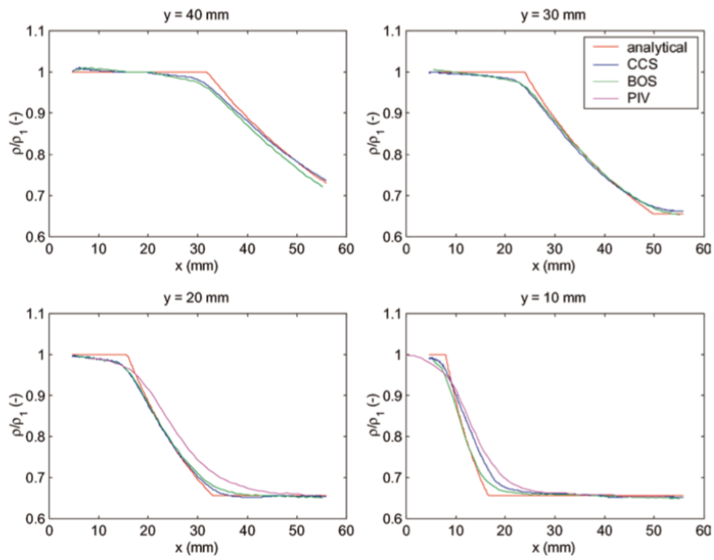

Figure 3.22: Density cross-plots comparing experiment I for BOS and calibrated color schlieren (CCS) on a Prandtl-Meyer expansion fan. PIV results are included for $y \leq 20$ mm [21]

PIV measurements. Hence, it was concluded that these round edges in the density profile were caused by the true 2D flow. Furthermore, it was found that the measurements were repeatable within 2%. It was noted that prior knowledge of the flow was needed to the achieve the attained level of accuracy because this method is very sensitive to wind tunnel or camera movement. During the calculations extra boundary conditions were needed to correct for the wind tunnel movement.

3.2.2 Outdoor BOS Applications

In 2000, Raffel et al. performed full-scale experiments on two different helicopters in hover flight using the BOS technique to visualize the blade tip vortices [22,66]. The first test was performed at the DLR centre Göttingen using an Eurocopter BK117 as the test helicopter. A CCD camera with a resolution of 1280 by 1024 pixels, shooting 8 frames per second, was located in a window of a nearby building at a horizontal distance of 32 m from the helicopter and 11.2 m above the ground. The random dot pattern background was created by splashing tiny droplets of white wall paint (between 1 and 10 mm diameter) with a brush onto the concrete ground. The best peak-fitting cross-correlation was achieved when using an iterative LevenbergMarquardt fit to a 10 x 10 pixel area, where the correlation values are weighted according to the Fisher transform. Figure 3.23 shows the displacement field around the blade in the image. Both the vortex that is created by the passing blade and the vortices produced by precious blades are visible in the image. The older vortices are still visible because the blade tip vortices do not dissipate or diffuse for many rotor revolutions according to Richard and Raffel. The zoomed view clearly shows the lines corresponding to a lower density, which were defined as the centers of the vortices.

A second experiment was performed at the NASA Ames research centre in California to study the blade tip vortex of a large US utility helicopter. The DLR and the Aeromechanics Branch US-Army/NASA Rotorcraft Division cooperated closely to investigate the interactions between the exhaust plume and the main motor during this experiment. This experiment was also performed to assess the feasibility of using a larger observation distance and a higher spatial resolution. During the tests, it was found that natural random or speckled backgrounds could be used. Figure 3.24 shows a BOS picture and the corresponding displacement field, which was calculated using a grass field, which was located 100 m behind the helicopter, as the

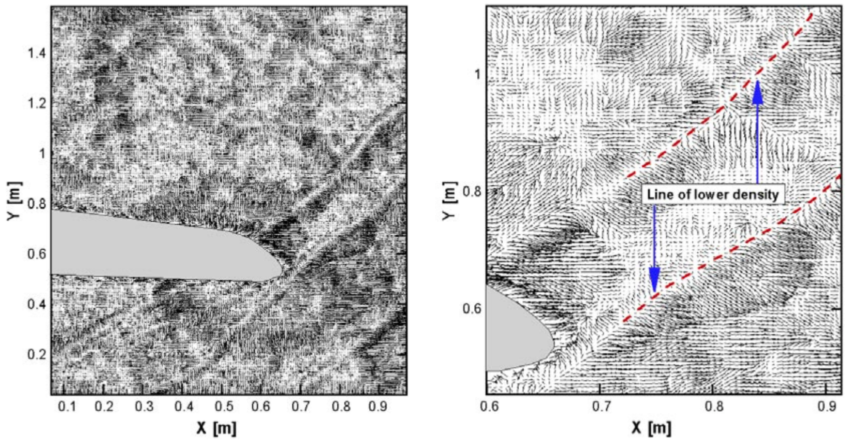

Figure 3.23: Displacement field, visualised with vectors proportional to $d\rho/dx$ and $d\rho/dy$. (Right) Zoom in on blade tip region [22]

background. The camera was focused on this grass field and the distance between the grass and the helicopter was sufficiently large to prevent the grass from moving due to the flow generated by the helicopter. One vortex between the two blades can be identified in the displacement field in Figure 3.24

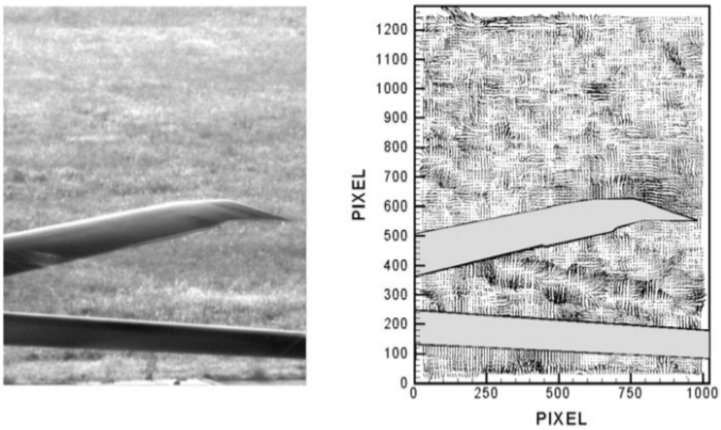

Figure 3.24: BOS pictures and displacement field using background grass [22]

In 2009, Hargather and Settles explored the suitability of natural backgrounds for BOS visualization [23]. A random dot pattern, a tree grove, a cornfield, and a corrugated silo were used as backgrounds for this experiment. The random dot pattern, which is not a natural background, was used as a reference. Cross correlations were performed between small interrogation windows, selected from within the image, and the entire image (381 x 191 pixels). The sides of the square interrogations windows were varied from 3 to 169 pixels and over 700 interrogation windows were randomly selected for each interrogation window size. Figure 3.25 shows the four different backgrounds and the cross-correlation effectiveness which is presented in the form of $1/\sigma^2$. For lower values of the standard deviation of the correlation values, the cross correlation is more effective and the $1/\sigma^2$ term increases. It was found that the random dot pattern always correlates best, which was expected since it is the ideal background with high contrast and unique features. The corrugated silo always correlates the worst because the background has a very periodic nature, i.e. there are many secondary correlation peaks. The cornfield and the tree grove fall in between the random pattern and the corrugated silo in terms of correlation performance. The decrease in the cornfield curve near 100 pixel window length is caused by the regular large scale pattern of the cornfield. Large structures of the tree trunks in the tree groove image contribute significantly to the correlation noise, hence limiting the correlation performance. Smaller tree branches would increase the performance as the background would be more random. The $A = ...$, shown in Figure 3.25 for each background, represents the average number of pixels for each distinct structure within each image. It was found that the correlation was more effective for low values of A when small interrogation windows were used.

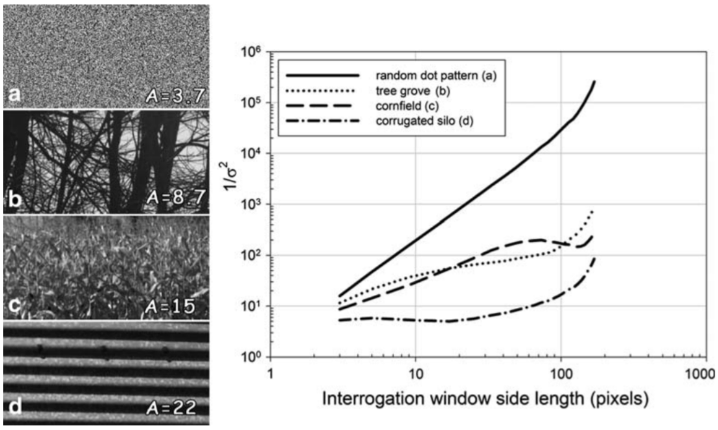

Figure 3.25: Background images and correlation results as a function of interrogation window size [23]

A torch plume, thermal plume of a hot truck, a 0.30-06 rifle discharge, and an explosion were used to create disturbances in the index of refraction for the experiments performed by Hargather and Settles. A black-white Photron APX-RS camera was used for the imaging of low-speed thermal plumes. This camera can record images up to 3,000 frames per second with a 1,024 x 1,024 pixel resolution. High speed images of gunshots and explosions were recorded at 15,000 frames per second with a pixel resolution of 1,024 x 192. The BOS background was sharply focused for all the experiments whereas the schlieren object was allowed to be slightly out of focus at times. This could result in the schlieren object not being properly imaged. However, when the background was out of focus, it was impossible to image pixel distortions within the background image. It was noted by Hargather and Settles that having the background in focus in stead of the schlieren object is the opposite of the philosophy used by Settles in 1999, where a sharply focused subject and a fuzzy background were used [7].

The shutter speed was set to $10\mu s$ for the test with the high-powered 0.30-06 rifle and images were obtained at 15,000 frames per second. The cornfield, illuminated by direct sunlight, was used as a background. The camera was placed at approximately 25 m from the cornfield and the rifle was located midway between the cornfield and the camera. Hargather and Settles used the cornfield for this test because its correlation effectiveness is relatively high for small interrogation windows. Figure 3.26 shows a image of the rifle discharge, the pixel intensity change of this image when compared to the reference image, the calculated horizontal pixel shift, and a schlieren image from a comparable laboratory experiment. The pixel shift image was found to reveal the muzzle blast well, however, the sensitivity was too low to capture the bullet and its oblique shock waves. It was noticed that shock wave blurring, of at least several mm, occurred due to the shutter speed being to slow. Finally, it was noted that the natural BOS images cannot compete with the schlieren image produced in the laboratory setting in terms of resolution, sensitivity, or visual appeal. However, Hargather and Settles mention that the costs of the natural BOS experiments are insignificant and incomparable to the cost needed to take the laboratory schlieren image as such a facility needs to be developed.

Hargather and Settles concluded that the natural background to be used in an experiment depends both on the phenomenon to be visualized and the image processing method to be used in data reduction. The size of the features in a background should be related to the strength

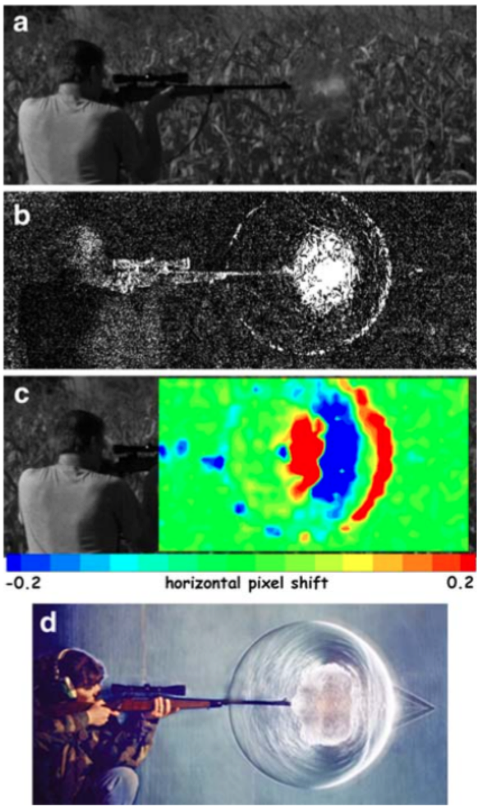

Figure 3.26: High-speed images of a 0.30-06 rifle discharge showing the muzzle blast and supersonic bullet. a) Raw image, b) Pixel intensity change, c) Horizontal pixel shift, d) Comparable laboratory experiment using the PSGDL Full-Scale Schlieren system [23]

of the schlieren object. Hargather and Settles recommend that the schlieren distortions should be about the same size as the background features. The distance between the object and the background should also be set to match the strength of the disturbance, i.e. a long distance is needed for a weak disturbance. Accordingly, the distance between the object and camera needs to be adjusted in order to keep both the schlieren object and the background in reasonable focus. The BOS system, like traditional schlieren, suffers from a compromise between high sensitivity and a broad measuring range. High speed applications can suffer from under illumination as short shutter speeds and high frame rates are required. Lastly, it was noted that natural BOS results do not have the same quality as the laboratory schlieren results. However, no refined optics are required and the natural BOS can be applied where traditional schlieren cannot be used. Overall, an ideal background should have small, random, and high contrast features.

Most recently, in August and September of 2015, Nasa has published two articles on their website about two different applications of the BOS technique [24, 25]. In one of these articles it is mentioned that "Ground-based systems, using the sun as a light source, have produced good results but because of the distances involved did not have the desired spatial resolution to resolve small-scale shock structures near the aircraft." This is most likely referring to the work performed by Weinstein et al. [44, 46] and the limitations of their schlieren for aircraft in flight technique. Hence, the desire to improve the quality of these schlieren or BOS images motivated the experiments performed by NASA.

In April 2011 the first air to air test, dubbed AirBOS 1, was performed using a F-18 as the test aircraft and a Beechcraft B200 King Air as the "photographer" aircraft. The F-18 was flown a several hundreds to a few thousand meters underneath the King Air in straight and level flight at velocities up to Mach 1.09. A high-speed camera on the underside of a King Air captured these passes, shooting 109 frames per second. A system consisting of a laptop with a frame grabber was used in combination with the natural desert vegetation, which was used as the speckled background pattern. It was mentioned in the article that the technique visualized not only the shock waves but all density changes including vortices and engine plume effects. In September and October 2014 new experiments were performed. On top of the equipment used during the previous test, two state-of-the-art high-definition, high-speed cameras were installed. It is said that the "images from the new cameras represented a dramatic improvement over those produced by the original system. The use of different lens and altitude combinations and knife-edge aircraft maneuvers by the pilot of the target aircraft provided the opportunity to obtain side-on images."

(a) Air-to-air BOS

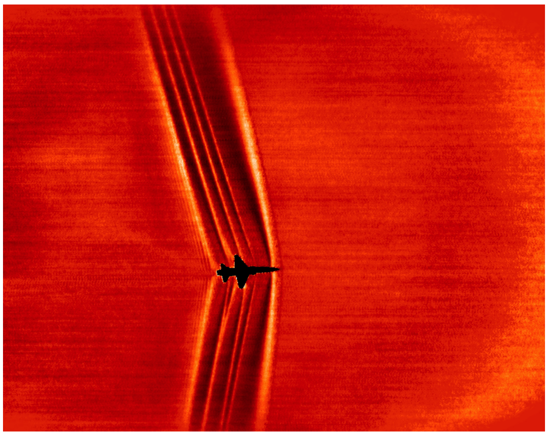

(b) BOSCO

Figure 3.27: Schlieren images obtained by NASA using the BOS technique [24, 25]

After the air-to-air BOS test, a new method was tested using the sky as a background. Bright and speckled light sources, such as the sun or moon, were used. The method was called Background-Oriented Schlieren using Celestial Objects (BOSCO). It was mentioned that by using a calcium-K (CaK) optical filter, the granulated texture of the suns chromosphere could be revealed, hence allowing the use of the sun as a speckled background. During an experiments, a supersonic T-38C was used as the target aircraft. It was found that the BOSCO technique showed not only the present shock waves, but also other density changes including wing vortices and engine plume effects. It was found that this ground-based method was significantly more economically feasible in comparison to the air-to-air method as only one aircraft is required.

Figure 3.27 shows two images that were obtained during the experiments performed by NASA. One image was obtained using the air-to-air BOS technique and the other image was obtained using the BOSCO technique. At the moment of writing, no technical reports or a papers in scientific journals about these experiments have been found. Nonetheless, these experiments do show new ways in which to use the BOS technique and are important to mention even though details about the experiments and the results are missing.

3.3 Discussion

From subsection 3.1.1 it can be concluded that shadowgraphy has been used for in-flight tests, however, all of the reviewed tests were qualitative. No work, describing a method of extracting quantitative information from in-flight shadowgraphy, has been found. It can also be concluded that in-flight shadowgraphy is not a common test method since it is not used very often. Cooper and Rathert Jr. were the first to record the use of in-flight shadowgraphy in 1948, but when flow visualization techniques, that were applied to full scale vehicles, were reviewed approximately 40 years later, shadowgraphy was only mentioned shortly [6, 43, 47]. In one of the two reviews, Crowder basically said that the in-flight shadowgraphy technique was not systematically used, acknowledging that the technique is not commonly used. In 1998, Fisher et al. presented an analysis of the the optimal sun angles and aircraft orientation for in-flight shadowgraphy, which was a continuation on the work of Cooper and Rathert Jr. [1]. This, once again, indicates how little has been done with in-flight shadowgraphy over long periods of time. In short, the optimal sun angles and aircraft orientation for in-flight shadowgraphy have been determined by Cooper and Rathert Jr. and in more detail by Fisher et al. However, in-flight shadowgraphy is only sporadically used to visualize the presence of a wing bound shock wave, but it has not been used to obtain quantitative information about a wing bound shock wave.

On the other hand, shadowgraphy is a commonly used non-intrusive experimental method to obtain flow related information in laboratory settings. It was found that shadowgraphy is mostly used to perform qualitative measurements in combination with another measurement technique that obtains quantitative information. From the reviewed work it can be concluded that shadowgraphy is used to visualize entire flow fields to gain a better understanding of the flow phenomenon of interest while quantitative measurements are performed locally with different measurement techniques. The shadowgraphs also allow one to discover some flow features that are missed by the local quantitative measurements. Quantitative measurements have also been performed using the shadowgraphy technique, however, these measurements were carried out in controlled laboratory environments to investigate boundary layers. These qualitative measurements have not yet been performed on shock waves outside of a laboratory setting.

One of the shadowgraphy methods that has been used in an outdoor environment to visualize flow fields is the retroreflective shadowgraphy technique. Norman and Light have demonstrated the large field of view capabilities of this method while investigating helicopter tip vortices [13]. This technique has also been used by Hargather and Settles to visualize the flow when a bullet was fired by a rifle [20]. Hence, demonstrating the outdoor and high speed capabilities of this technique.

Numerically simulated shadowgraphs have been used to compare calculated flow solutions to real experiments by means of shadowgraphs. Hisley did this mainly to verify the BLAST2D code, but others created the simulated shadowgraphs to extract more information from experimental shadowgraphs [15]. Both Hisley and Yates only made qualitative comparisons regarding the similarities between the simulated and experimental shadowgraphs [15, 16]. Bagai and Leishman compared simulated shadographs of rotor tip vortices for different velocity profiles to experimental shadowgraphs [17]. They were able to conclude that the experimental shadowgraph compared best to a certain velocity profile. Hence, they were able to extract quantitative information about the velocity profile of the rotor tip vortices from the experimental shadowgraphs. Schopf et al. stated that "A comparison of the simulated and experimental shadowgraph images represents an indirect comparison of the respective density fields. The method enabled the indentification of the temperature structures which lead to certain features in the shadowgraph images, thus allowing some qualitative interpretation of the experimental images" [19]. Even though no direct quantitative data in terms of flow fields was obtained, the reviewed works do show the potential of the method of comparing simulated shadowgraphs to experimental shadowgraphs when it comes to extracting more information from experimental shadowgraphs.

It should be noted that different assumptions were made to construct the simulated shadowgraphs depending on the flow of interest. Yates assumed that light rays only underwent infinitesimal deviations inside the inhomogeneous density field, hence only the curvature of the ray at the exit of the inhomogeneous density field and the distance to the image field were used to calculate the light deviations [16]. Both Yates and Schopf et al. stated that this assumption can lead to errors [16, 19]. Yates stated that this assumption should have minimal effect on regions without a shock, but Schopf et al. said that this assumption is only justified when using very narrow experimental setups. Yates did conclude that shock waves would introduce errors due to his assumption. Both Thess and Orszag and Schopf et al. concluded that the law of refraction is needed for discontinuities in the index of refraction, i.e. in case of shock waves or fluid interfaces [18, 19].

Another technique that has been used to visualise shock waves around aircraft is the BOS technique. Hargather and Settles labelled it as one of the recent developments in the schlieren technique [20]. Hargather and Settles have demonstrated the BOS technique by visualizing the around a simple cone model that was placed in a supersonic flow in laboratory settings. They showed that, with post-processing, images just like real schlieren images can be obtained. Elsinga et al. have assessed the performance of the BOS technique when it was used to perform quantitative measurements of a 2D supersonic flow over a wedge. They found that the accuracy of the BOS density measurements was around 3% when the results were compared to a theoretical density. They also found that the quantitative BOS technique is very sensitive to camera or wind tunnel movement. The advantage of the simple experimental set-up of the BOS technique, allowing outdoor experiments, where demonstrated by Raffel et al., Hargather and Settles, and NASA [22–25, 66]. Raffel et al. performed full-scale experiments on helicopters in hover flight to visualize the blade tip vortices using both man made backgrounds and a natural background. Hargather and Settles analyzed different natural backgrounds and analyzed how well they performed when different flow phenomena were investigated. NASA used natural backgrounds to visualize shock waves around supersonic aircraft, either making air to air photos or ground to air photos. In short, the BOS technique has already been used for quantitative analysis in laboratory settings and for qualitative analysis outdoors.

In comparison to in-flight shadowgraphy, that has been used since the late 1940s but has hardly been developed since then, the application of the BOS technique to full scale flight experiments is flourishing and new methods of application are currently being studied [24, 25]. At the moment of writing, NASA is using the BOS technique for supersonic flight, but nothing is mentioned about transonic flight. In-flight shadowgraphy, on the other hand, has been used to visualize the presence of shock waves in transonic flight. However, more than merely indicating the presence of a shock wave has not been done with the in-flight shadowgraphy technique. Therefore, both techniques could potentially be used to gather more information about wing bound shock waves occurring during transonic flight.

When the in-flight shadowgraphy technique and the BOS technique are compared to each other, the following advantages and disadvantages are found when both techniques are applied to obtain more information about the wing bound shock waves occurring on the wings of commercial aircraft during transonic flight: Firstly, Imaging shadowgraphs on the wing surface from within the aircraft itself is much cheaper than performing either the ground to air or air to air BOS experiments, as used by NASA. Secondly, the in-flight shadowgraphy technique can be used on any flight where these shadowgraphs on the wing surface become visible. For the BOS technique, on the other hand, test flights are needed. Thirdly, a less complex optical system is needed for the in-flight shadowgraphy technique to obtain an image of a certain resolution because the distance between the camera and the shadowgraph on the wing surface is usually several meters. Ground to air or air to air BOS techniques usually have a distance of at least several hundred meters between the wing of interest and the camera, hence a more complex optical system will be needed to obtain images of the same resolution. Another disadvantage of the BOS technique is that the aircraft itself can block part of the field of view. This might result in part of a wing bound shock wave not being visible on the BOS image. This is most likely to happen to the foot of the shock wave as this is located next to the wing surface. Lastly, the in-flight shadowgraphy technique has not been used to extract quantitative information about the wing bound shock waves from in-flight shadowgraphs and the technique does not seem to studied much over the past decades. The BOS technique, on the other hand, is currently being studied by NASA. Although the exact goal of the study by NASA is not known, there would be a risk of doing the same work if this topic is to be chosen for the M.Sc. thesis. Hence, studying the feasibility of using the in-flight shadowgraphy technique to extract quantitative data from in-flight shadowgraphs would therefore really be an addition to the body of knowledge and the technique itself is easier and cheaper to use.

It should be noted that real quantitative results will not be obtained directly from the in-flight shadowgraphs because the shadowgraph does not capture the shock wave itself. It is therefore impossible to use the method presented by Bowersox et al. [63]. Even if the shock wave itself was captured in the shadowgraph, uncertainty about the position of the shock wave would make the double integration impossible. A way to actually capture the shock wave in a shadowgraph during flight could be achieved by using the retroreflective shadowgraphy technique. In this case a camera and the light source should be placed on the wingtip, aiming towards the fuselage, and the fuselage should be covered in reflective material. In other words, the fuselage would be used as the retroreflective screen. This implementation would, however, have some important drawbacks since the wing moves during flight which results in camera movement and the fuselage is round which means not all light is reflected back to the camera. Even if this technique could be implemented successfully, it will completely discard the simplicity of the in-flight shadowgraphy technique where images are taken from the cabin. The most obvious solution is therefore to simulate the shadow formations that are formed on the wing surface and to compare these simulated shadow formations to the real in-flight shadowgraphs. This method will be very similar to the simulated shadowgraphy method presented in subsection 3.1.4, however, the shadowgraphs will not capture the shock wave itself. Therefore, the subject of the MSc thesis project will be the assessment of the feasibility of using simulated shadowgraphs to extract information regarding the wing bound shock waves from in-flight shadowgraphs by means of a comparative study between simulated and in-flight shadowgraphs. For the rest of this work, the term 'simulated shadowgraph' will refer to the numerically simulated shadow formations on the upper surface on a wing. The term 'in-flight shadowgraph' will be used to refer to the image, taken during flight, of shadow formations on the wing upper surface caused by wing bound shock waves.

3.4 Research Questions & Research Objective

The topic for the M.Sc. thesis project will be the assessment of the feasibility of extracting quantitative information, about wing-bound shock waves occurring on commercial passenger aircraft flying at transonic speeds, from in-flight shadowgraphs by means of a comparative study between simulated and in-flight shadowgraphs. A ray tracing algorithm will be developed to produce simulated shadowgraphs based on models of shock waves that commonly occur on the wings of commercial aircraft when flown at transonic speeds. A flow model that is able to represent transonic flows over supercritical airfoils will be used to generate flow fields which will be used by the developed ray tracing algorithm. If it turns out that it is not feasible to extract more information from the in-flight shadowgraphs by means of comparisons to simulated shadowgraphs, the M.Sc. thesis project will determine precisely why this information cannot be extracted and what additional data might be needed to make this feasible. If more information regarding the shock waves of interest can be extracted from the in-flight shadowgraphs by means of comparisons to simulated shadowgraphs, this method could be used to deepen the understanding of the shock dynamics. This better understanding could, in turn, be used to validate CFD or improve wing design to make flight more fuel efficient.

The MSc thesis project will aim to establish a relation between the certain shock wave characteristics and certain characteristics from the shadowgraphs. The characteristics of interest in the shadowgraph will be the positions and the illumination levels of both the dark and bright regions in the shadowgraphs. These characteristics are chosen as they are typical for wing bound shock wave shadowgraphs according to Cooper and Rathert Jr., and Fisher et al. [1, 6]. The shock wave characteristics of interest will be the shock wave position and the shock wave strength. The shock position is of interest for wing design improvements to mitigate these shocks and for flow control to alter the characteristics of these shock waves. The position of the shock wave and following the movement of the shock wave will also help the study of the dynamics of these shock waves. The shock strength is of interest because it dictates whether the shock is weak or strong, which strongly effects the flow behind the shock wave.

Research Questions

> Can simulated shadowgraphs, created by a ray tracing algorithm, be used to quantify the shock wave characteristics of shock waves on wings of commercial passenger aircraft flying at transonic speeds, by means of a comparative study between an in-flight shadowgraph and the simulated shadowgraphs?

The shock waves of interest in this study are the wing bound shock waves that occur on the wings of commercial passenger aircraft flying at transonic speeds, approximately 0.8-0.85 Mach, when the flow over the wing becomes supersonic locally. The shock wave characteristics of interest are the shock wave location on the wing and the shock wave strength. As mentioned before, the shock position is of interest because design improvements or flow control techniques have to be based on this position. The shock strength is of interest because it largely influences the degree of flow separation, i.e. a larger pressure rise is more likely to trigger flow separation.

In order to create the simulated shadowgraphs, information regarding the precise mechanism of the shadow formation will be needed. In this case, information about the transonic flow fields around supercritical airfoils, in which shock waves are present, is needed because light is refracted when traveling through such an inhomogeneous index of refraction medium. Information about the optical phenomena which are involved in the formation of a shadowgraph is needed as well in order to simulate shadowgraphs. Therefore, the following two sub-questions have been formulated:

> What do transonic flow fields around supercritical airfoils, with a shock wave standing on the surface of the airfoil, look like?

> In what way do optical phenomena form a shadow, in a shadowgraph created by direct shadowgraphy, on a surface?

The answers to these two sub-questions should provide sufficient information to develop a ray-tracing algorithm which can be used to simulate shadowgraphs by calculating the light intensity distribution on a surface. However, the in-flight shadowgraphs are images of the shadowgraph formed on the wing, taken by a camera. These images do not necessarily represent the same light distribution as the actual light intensity distribution on the wing surface. In order to compare the simulated shadowgraphs to an in-flight shadowgraph, it needs to be determined how a picture of shadow formations on the wing surface, taken by a camera, relates to the actual light distribution on the wing surface. Therefore, a third sub-question can be formulated:

> How does a camera capture the shadow image of a shadowgraph formed on a surface and what is the effect of the position of the camera on this captured image?

Research Objective

> The research objective is to assess the feasibility and the accuracy of extracting quantitative information about the shock waves of interest from in-flight shadowgraphs by means of a comparison with simulated shadowgraphs, which are created with a ray tracing algorithm, thus allowing a parametric study in terms of shock wave position and strength with respect to the shadow formation on a wing surface.

During the M.Sc. thesis project, knowledge to answer the three sub-questions will be gathered. This knowledge will be used to develop a ray tracing algorithm, which will be used to create simulated shadowgraphs. These simulated shadowgraphs will be used for a comparative study to determine whether an unique relation can be found between the shock characteristics of interest and the characteristics of interest of the shadowgraphs.

4. Shock Model

This chapter will start with brief a discussion about the Shock Wave-Boundary Layer Interaction, explaining how the shock wave and the boundary layer influence each other. This discussion will mainly focus on the effect that the SWBLI has on flow separation and at which Mach numbers the flow separation will most likely occur. Secondly, the transonic small disturbance potential flow model will be presented. The transonic small disturbance potential flow equations and the numerical Murman-Cole-Krupp scheme, used to calculate transonic flow fields, will be explained. The computed results will be compared to both numerical and experimental results and the limitations of the flow model will be discussed. Finally, the Bohning-Zierep model, which approximates the boundary layer on a curved wall in the vicinity of a shock wave, will be treated.

4.1 Shock Wave-Boundary Layer Interaction

Air traveling over the wing of an aircraft is usually locally accelerated. This can lead to local regions of supersonic flow over the wing, i.e. a wing in transonic flow. Depending on the back pressure or the change in the surface slope, shock waves may occur on the wing. These shock waves usually interact with the boundary layer that is present on the surface. The complex interaction between such a shock wave and the boundary layer determines the shock pattern, boundary layer characteristics, flow separation, etc. [37]. In turn, the mentioned phenomena have an effect on the efficiency and stability of an aircraft [35].

A flow is said to be transonic when there is both supersonic and subsonic flow outside the boundary layer. When a normal shock wave appears above an airfoil in transonic flow, it will interact and propagate through the boundary layer. When moving close to the wall, the Mach number in the boundary layer will decrease, hence weakening the shock, until the shock vanishes upon reaching the sonic line. Normally, the flow in front of a shock wave does not know about the pressure increase across the shock wave. However, information about the pressure increase across the shock wave is carried upstream by the subsonic part of the boundary layer. Hence, the pressure rise caused by the shock wave is perceived upstream of the point where the shock wave would meet the airfoil in a flow without a boundary layer. The boundary layer becomes thicker as it reacts to the increased adverse pressure gradient. The increased thickness of the boundary layer, in turn, results in the generation of compression waves. These compression waves, in turn, weaken the original shock wave [28, 37, 67]. In case of relatively high transonic Mach numbers, the compression waves meet before interacting with the normal shock wave. When this happens, the interaction between the compression waves results in an oblique shock wave in front of the normal shock wave, hence forming a lambda shock pattern, as can be seen in Figure 4.1.

Figure 4.1 shows a typical lambda shock pattern. Here the quasi-normal shock wave C_3 meets the oblique shock wave C_1 at the triple point I. Delery and Marvin use the term 'quasi-normal shock wave' to indicate strong oblique shock waves that are close to normal shock waves in terms of their angle with the flow and strength [28]. Hence, a strong oblique shock wave correspond to the strong solution of the θ-β-M relation [68]. The oblique shock is formed when the compression waves, generated by the thickening boundary layer, intersect with each other before they reach the quasi-normal shock wave. This oblique shock wave is weaker than a normal shock wave and the flow after the oblique shock wave is still supersonic. Since the states

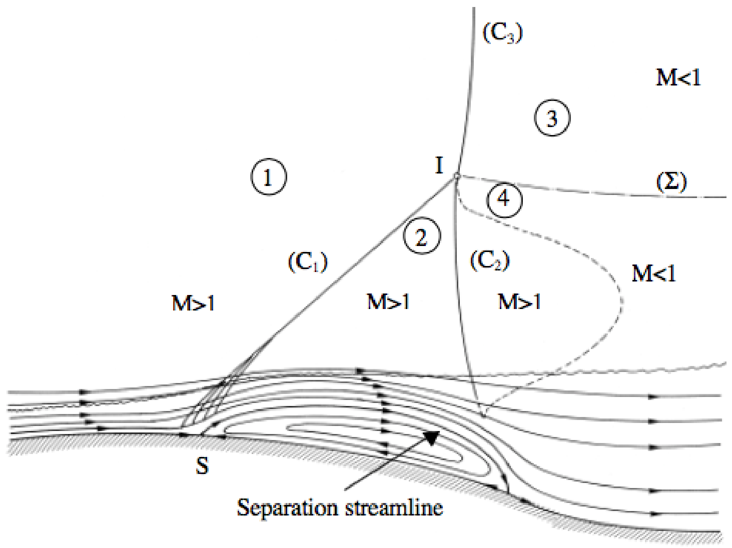

Figure 4.1: Lambda shock wave pattern on an airfoil [26]

behind C_1 and C_3 do not have the same pressure, a third shock wave C_2 is formed. The states after this third shock wave C_2 and the quasi-normal shock wave do have the same pressure but they are separated by a slip line because the velocities are different. It should be noted that the flow behind C_2 can be either supersonic or subsonic. If the flow is supersonic, the deceleration to subsonic velocities is most often isentropic [26]. It should also be noted that Figure 4.1 shows a separation bubble, which can occur depending on the flow field surrounding the airfoil.

Separation of a boundary layer depends mostly on the adverse pressure gradient and the velocity profile of the boundary layer. The interaction with a shock wave both thickens the boundary layer, making it more susceptible to an adverse pressure gradient, and it increases the shape factor H. The (momentum) shape factor is defined as the displacement thickness δ^* divided by the momentum thickness θ, as can be seen in Equation 4.3. The definitions for the displacement thickness and the momentum thickness are given in Equation 4.1 and Equation 4.2 respectively. As a result of the boundary layer thickening and the increased shape factor, the shock wave interaction with the boundary layer influences and promotes rear separation. However, the interaction between a shock and a boundary layer can also be beneficial for the boundary layer, according Delery, because the shock wave intensifies the turbulent mixing, which makes a boundary layer more resistant against adverse pressure gradients [37]. This means that the turbulent mixing, caused by the shock wave, might be so strong in certain cases that the boundary layer actually becomes more resistant against adverse pressure gradients after the interaction with the shock wave.

$$\delta^* = \int_0^\infty \left(1 - \frac{\bar{u}}{u_e}\right) dy \tag{4.1}$$

$$\theta = \int_0^\infty \frac{\bar{u}}{u_e}\left(1 - \frac{\bar{u}}{u_e}\right) dy \tag{4.2}$$

$$H = \frac{\delta^*}{\theta} \tag{4.3}$$

In 1955, Pearcey categorized the different types of shock-induced separation of turbulent boundary layers on airfoils in transonic flow [27]. Type A flows, the first of the two types, consists

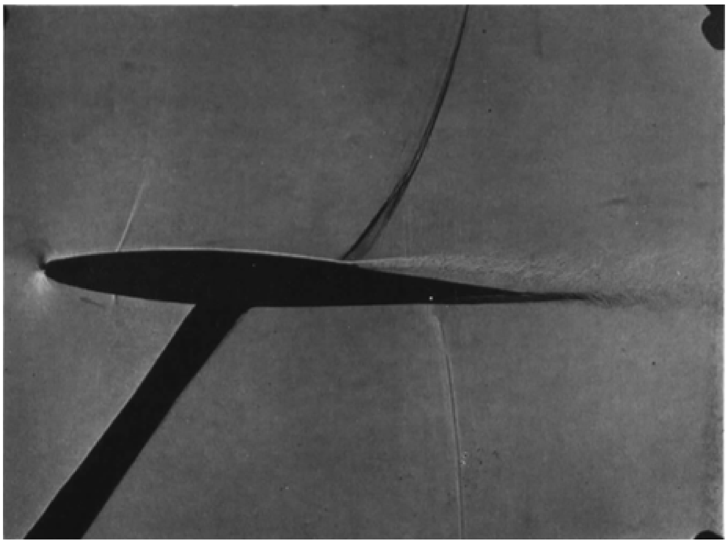

Figure 4.2: Schlieren photograph of severe separation on the upper surface near the trailing edge for $M_0 = 0.88$ and an angle of attack of 2° [27]

of a reasonably strong shock that causes the boundary layer thicken at and downstream of the interaction region. With an increasing free stream Mach number the shock becomes stronger and the boundary layer becomes thicker, eventually resulting in incipient separation at the shock foot. A further increase in the free stream Mach number results in the formation of a separation bubble at the shock foot that grows with increasing free stream Mach number. The separation bubble remains fixed at the shock foot and the reattachment point moves towards the trailing edge. This type A flow occurs when there is a moderate adverse pressure gradient downstream of the shock. Type B flows occur when the pressure gradient over the rear part of the airfoil is very strong, i.e. for rear-loaded airfoils like super critical airfoils. Rear-loaded airfoils are characterized by their nearly flat upper surface and the highly downward curved trailing edge which results in high pressure on the lower surface at the trailing edge. The difference between type A and B is that in addition to the separation bubble occurring at the shock foot, trailing edge separation also takes place for type B flows. When the free stream Mach number increases enough, the trailing edge separation and the separation bubble will merge, resulting in severe separation at the rear part of the airfoil. Figure 4.2 shows an example of severe separation of a type A flow. It can be seen that the bubble is closed rearward of the trailing edge when the two shear layers join.

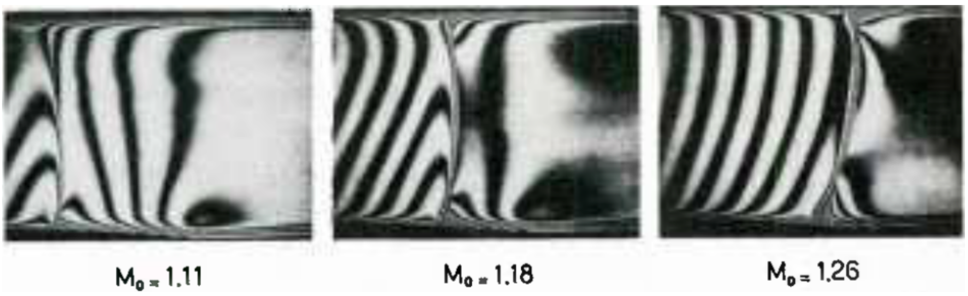

Figure 4.3: Interferograms of transonic interaction without separation [28]

Figure 4.3 shows the interferograms taken of two-dimensional transonic flow created using a bump on the lower wall while keeping the upper wall of the test section flat [28]. The Mach numbers under the interferograms in Figure 4.3 represent the upstream Mach numbers. According to Delery and Marving, the entropy rise across shocks in the transonic flows under investigation are sufficiently weak so that the flows can be considered to be irrotational with the exception of the boundary layer. Hence, the fringes of the interferograms represent constant density and also constant Mach number, constant pressure, etc. when isentropic flow is assumed. For the weakest shock, it was found that the shock wave penetrates deep into the boundary layer. For the higher upstream Mach numbers, compression waves were observed in the boundary layer. These compression waves seem to originate from near the wall and converged at the point where the quasi-normal shock wave seemed to start. It was concluded by Delery and Marving that flow separation did not occur for these flows with upstream Mach numbers up to 1.26.

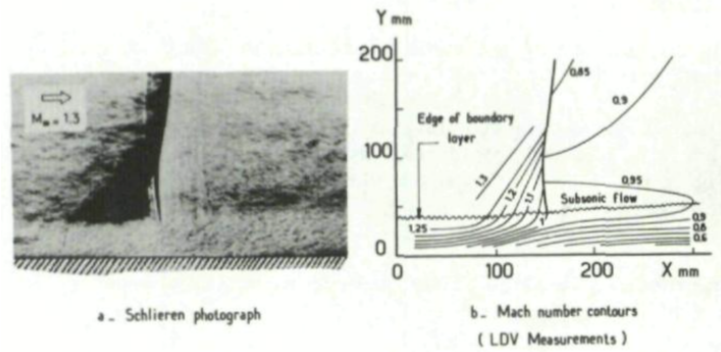

(a) $M_0 = 1.3$

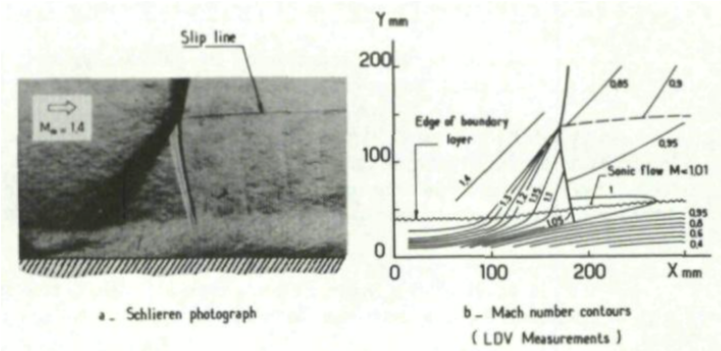

(b) $M_0 = 1.4$

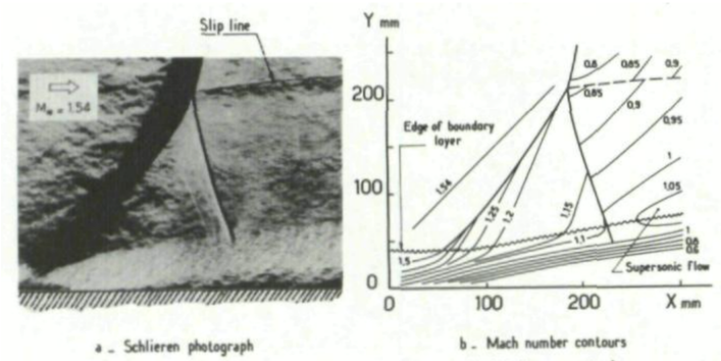

(c) $M_0 = 1.54$

Figure 4.4: Transonic shock wave boundary layer interaction [29]

In 1976, East published experimental results that clearly show how an increase in the upstream Mach number changes the flow field structure and the shock wave boundary layer interaction. The experiments were performed in a symmetrical test section of a wind tunnel and the shock wave formed after the first throat, i.e. the curved wind tunnel walls were used to represent an airfoil surface and no actual airfoil was placed in the wind tunnel. These experiments are thus comparable to the presented experiments by Delery and Marvin. The experiments were performed for upstream Mach numbers of 1.3, 1.4, and 1.54. The wind tunnel stagnation pressure was kept the same for all three test. The velocity fields were determined from laser Doppler velocimetry measurements and the flow field was visualized using the schlieren technique. The results are presented in Figure 4.4. The Reynolds number was nearly the same for the three test cases resulting in a practically identical incoming boundary layer thickness.

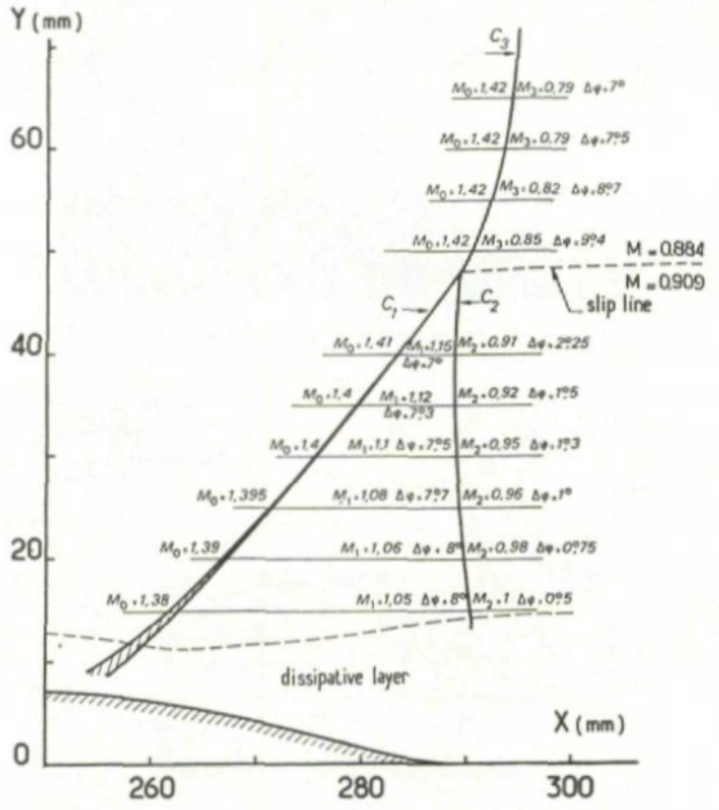

Figure 4.5: Details of the lambda shock pattern for $M_0 \approx 1.4$ [28]

It can be seen that for the $M_0 = 1.3$ case, incipient separation is not occurring. Compression waves, generated by the thickened boundary layer, are present and impinge on the quasi-normal shock wave. For the $M_0 = 1.4$ case, some compression waves converge and form a weak oblique shock wave in front of the quasi-normal shock wave, thus forming a lambda shock pattern. East found that flow separation occurred for this case. He also be noted that almost all the flow behind shock C_2 is subsonic, but that a small supersonic region is present near the boundary layer. For the $M_0 = 1.54$ case, the compression waves form the oblique shock wave C_1 closer to the edge of the boundary layer. In this case there is a significant portion of supersonic flow behind shock C_2 and it can be seen that the flow is accelerated behind the shock as a result of the after expansion. From these three experiments it was concluded that the triple point moves away from the wall and that the compression waves coalesce closer to the boundary layer for an increasing upstream Mach number. It was also concluded that flow separation did not occur for $M_0 = 1.3$, but that flow separation did occur for $M_0 = 1.4$.

Another similar experiment was performed by Delery and Marving for an upstream Mach number of approximately 1.4 [28]. Figure 4.5 shows details of the lambda pattern. Delery and Marving directly deduced the Mach numbers from field measurements using laser Doppler velocimetry and interferometry. The deflection angles were calculated using the oblique shock wave theory. It should be noted that the flow conditions in front of C_1 and C_2 are not constant as a result of the non-uniform incoming stream. It was concluded from Figure 4.5 that C_1 is a weak oblique shock wave, and C_2 and C_3 are strong oblique shock waves. The strength of C_2 decreases as it approaches the wall. It was noted that the Mach number of the flow downstream of C_2 is higher than the Mach number of the flow downstream of C_3. This difference is caused by the fact that a combination of an oblique shock and a normal shock wave can decelerate the flow more efficiently than a single normal shock wave. In other words, for the same pressure jump, a smaller entropy rise occurs, which means less energy is taken out of the flow, resulting in a higher Mach number. The result is that a slip line is present, separating the flow that crossed C_2 from the flow that crossed C_3. It was also found that the flow separation occurred for this upstream Mach number, thus agreeing with the results of East.

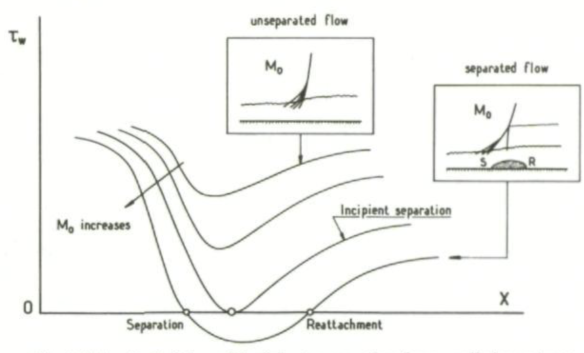

Figure 4.6: Definition of incipient separation based on wall shear stress [28]

Delery and Marving summarized the results of their own experiments and the experiments performed by East in Figure 4.6. This figure shows the definition of incipient separation which occurs when the minimum of the wall shear stress in the region near the shock interaction is equal to zero. The figure also shows that a lambda shock pattern starts to occur for increasing upstream Mach numbers and that a separation bubble starts to occur when a lambda shock pattern is formed. From the results by Delery and Marvin, and East it can be concluded that the lambda shock pattern does not occur for upstream Mach numbers up to 1.3. However, compression waves, caused by the thickening of the boundary layer, do start to occur for upstream Mach numbers between 1.18 and 1.26. It also was found that separation does not occur for these flow fields with an upstream Mach number up to 1.3. Hence, it can be concluded from these experiments that flow separation occurs when the $M_0 > 1.3$ and a lambda shock pattern occurs. The results by Pearcey, however, contradict this conclusion. Figure 4.2 shows the schlieren image of an experiment that used an airfoil in a wind tunnel where the upstream Mach number was subsonic. In this case, flow separation occurs but a lambda shock pattern is not present. Unfortunately, the Mach number of the flow at the boundary layer edge just upstream of the shock wave is not known, hence it is not possible to draw a quantitative conclusion from this experiment. It does, however, show that the absence of a lambda shock pattern does not guarantee that flow separation will not occur.

The flow solver, that will be presented in the next section, does not take the boundary layer or flow separation into account. Therefore, the Mach numbers at the edge of the boundary layer just upstream of the shock wave will be analyzed to determine whether flow separation is likely to occur. If such a Mach number is greater than 1.3 or a lambda shock pattern occurs in the flow, flow separation is likely to occur and the flow solution will not be valid anymore because the flow model cannot model this phenomena.

4.2 Transonic Potential Flow

By applying an expansion procedure to the Euler equations, the transonic small disturbance equation can be derived. Using the airfoil thickness ratio δ as the small parameter for the expansion, the flow quantities can be expanded, as can be seen in Equation 4.4. All the expanded terms consist of a free stream condition term and a first order disturbance term which is indicated by the superscript (1). Murman and Cole used Equation 4.4 to derive a transonic version of the continuity equation, as shown in Equation 4.5. They also derived that the flow is irrotational for the first and second order of the flow quantity expansions, i.e. $v_x - u_{\tilde{y}} = 0$ [30]. It should be noted that $\tilde{y}$, which stands for a scaled y-coordinate, is used instead of y. This scaled coordinate is used to take into account the tendency of the disturbances to spread laterally.

$$u = u_\infty(1 + u^{(1)} + ...), \quad v = u_\infty(1 + v^{(1)} + ...), \quad p = p_\infty + \rho_\infty u_\infty^2 (p^{(1)} + ...) \tag{4.4}$$

$$\left[Ku - (\gamma + 1)\frac{u^2}{2} \right]_x + v_{\tilde{y}} = 0 \tag{4.5}$$

According to Murman and Cole, shock waves that appear on thin airfoils in transonic flow are so weak that negligible vorticity is introduced. This matches with the fact that the flow is irrotational when the small disturbance equations up to the second order are used. Hence, a velocity potential can be introduced, i.e. $\bar{u} = \nabla\phi$. Using this velocity potential, the transonic equation can be rewritten to Equation 4.6, which is the transonic small disturbance equation. The derivatives of the velocity potential are denoted by the subscripts x or $\tilde{y}$, e.g. $\phi_{xx} = \partial^2\phi/\partial x^2$. The transonic similarity parameter is defined in Equation 4.7 and the scaled y-coordinate is defined in Equation 4.8. Using the definitions of the transonic similarity parameter and the scaled y-coordinate, the perturbation velocities in the normal, non-scaled, coordinate system, presented in Equation 4.9, can be derived. It should be noted that different versions of these equations have been used by different people. Krupp, Cole, and Murman have all used Equation 4.6 ignoring the $M_\infty^{2-3C_1}$ term and they used varying values for C_1 [30, 31, 69–71]. Ignoring the $M_\infty^{2-3C_1}$ term is justified by assuming the freestream Mach number is very close to one, hence the ignored term will be very close to one as well. Chattot describes the Murman-Cole-Krupp method, but does not use the scaled coordinate system, resulting in the same equations with $C_1 = 0$ [72]. Langley also describes the Murman-Cole-Krupp method and highlights the differences between the scaled and non-scaled systems [73]. In doing so, Langley pointed out some inconsistencies between work by different authors. Krupp, Cole, and Murman have used Equation 4.10 and set $C_1 = 1/2$ and $C_2 = 3/4$ to obtain results that agree the best with certain exact solutions. However, Collins and Krupp used $C_1 = C_2 = 2/3$ and Langely used $C_1 = 0.475$ and $C_2 = 0.75$ in combination with isentropic relations to compute the pressure coefficient [33, 73].

$$\left[K - (\gamma + 1)M_\infty^{2-3C_1}\phi_x \right] \phi_{xx} + \phi_{\tilde{y}\tilde{y}} = 0 \tag{4.6}$$

$$K = \frac{1 - M_\infty^2}{M_\infty^{2C_1}\delta^{2/3}} \tag{4.7}$$

$$\tilde{y} = M_\infty^{C_1}\delta^{1/3} y \tag{4.8}$$

$$u^{(1)} = \phi_x M_\infty^{-C_1}\delta^{2/3}, \qquad v^{(1)} = \phi_{\tilde{y}}\delta \tag{4.9}$$

$$u^{(1)} = \phi_x M_\infty^{-C_2}\delta^{2/3}, \qquad C_2 \neq C_1 \tag{4.10}$$

By substituting the expansions of Equation 4.4 into the Euler equations, it was found that $p^{(1)} = -u^{(1)}$. This relation was used by all the previously mentioned authors to derive Equation 4.11, which defines the reduced pressure coefficient. It should be noted that the different authors derived different, but matching, expressions for the expansion of the pressure, i.e. some authors multiplied $p^{(1)}$ with p_∞ whereas others multiplied $p^{(1)}$ with ρu_∞^2. The pressure expansion presented by Chattot is used in this work because it most resembles the definition of the pressure coefficient.

$$\bar{C}_p = -2u^{(1)} M_\infty^{C_1} \delta^{-2/3} = C_p M_\infty^{-C_1} \delta^{2/3} = M_\infty^{-C_1} \delta^{2/3} \frac{p - p_\infty}{0.5 \rho_\infty u_\infty^2} \tag{4.11}$$

The transonic small disturbance equation can be either hyperbolic or elliptic depending on the local solution. When $\phi_x > u^*$, the equation is hyperbolic and the flow is supersonic, and when $\phi_x < u^*$, the equation is elliptic and the flow is subsonic. The definition of the critical perturbation velocity u^* is given in Equation 4.12.

$$u^* = \frac{K}{(\gamma + 1) M_\infty^{2-3C_1}} \tag{4.12}$$

The method used here is the same as the method presented by Murman and Cole including the improvements made by Murman, i.e. a symmetrical non-lifting airfoil will be used for the calculations [30, 31]. The body shape of the airfoil is described by $y = \delta F(x)$. To comply with the tangent conditions, for the first and second order approximation according to Murman and Cole, the boundary condition as specified in Equation 4.13 is applied to the symmetry axis (y = 0). This boundary condition specifies that the vertical velocity component is equal to the local slope of the airfoil geometry. Equation 4.14 was derived by Murman and Cole for the far field boundary condition. This boundary condition is one of a doublet used to simulate a closed body. The doublet strength D depends on the solution, hence it will be updated every iteration. Following the example of Murman and Cole, the far field boundary is set at $x \approx \pm 6$ and $\tilde{y} \geq 7.5/K^{1/2}$ and far field coordinate stretching is used.

$$\phi_{\tilde{y}}(x, 0) = \begin{cases} F'(x) & |x| \leq 1 \\ 0 & |x| > 1 \end{cases} \tag{4.13}$$

$$\phi(x, \tilde{y}) \cong \frac{D}{2\pi K^{1/2}} \frac{x}{x^2 + K^{1/2} \tilde{y}^2} \tag{4.14}$$
$$\text{where: } D = 2 \int_{-1}^{1} F(\xi) d\xi + \frac{\gamma + 1}{2} \int \int_{-\infty}^{\infty} \phi_x d\xi d\eta$$

A different far field boundary condition for non-symmetric, lifting airfoils is presented by Krupp and Murman [71]. A slightly altered version is also used by Langley [73]. These methods make use of the circulation that is introduced by the airfoil and apply the Kutta condition. This boundary condition also depends on the solution and it introduces a ϕ jump on the $y = 0$ line. As the use of a non-symmetric, lifting airfoil complicates the solution procedure, requires more computational time, and will not create more realistic transonic flow fields for the intended purpose of this study, it was decided not to use this method.

4.2.1 Discretization Scheme

In order to solve Equation 4.6, the Murman-Cole-Krupp method uses relaxation methods to solve the finite difference equations at each mesh point depending on the flow type. Murman and Cole compare the elliptic form of Equation 4.6 to the Laplace equation where centered difference equations are used to represent the derivatives, as can be seen in Figure 4.7. These centered difference equations account for the fact that a point depends on all neighboring points. The hyperbolic form of the Equation 4.6 is compared to the wave equation, where points are only influenced by upstream points. Hence, a backward difference equation is used for the difference equation in the x-direction, as can be seen in Figure 4.7. However, both an explicit and implicit system can be used for the wave equation. When the explicit system is used, the step size in the x-direction is restricted to ensure that the domain of dependence of the difference equation contains that of the differential equation. The implicit system, on the other hand, does not have such a stability criterion. Hence, the implicit system is used by Murman and Cole and will be used throughout this work as well.

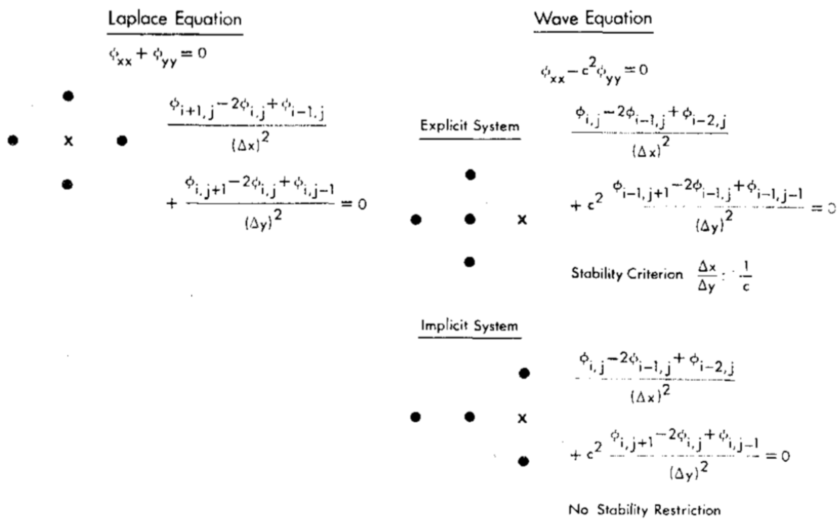

Figure 4.7: Difference equations of the Laplace and wave equations [30]

In order to select the correct finite difference scheme at each mesh point, the velocity is determined at each mesh point using Equation 4.15. The subscript n is used to indicate the number of the current iteration through the flow field and the subscripts c and b are used to indicate centered and backward finite difference schemes. The values of ϕ are solved per vertical line (x = constant) using a relaxation scheme. The relaxation scheme is specified in Equation 4.16, where ω is a relaxation parameter that is set to 0.95. The $\widehat{\phi}$ stands for the ϕ value that is calculated for the current vertical line, which will later be used in the relaxation scheme to calculate ϕ^{n+1}. Vertical lines are solved successively in the downstream direction (increasing x). New values of ϕ are used as soon as they become available, as can be seen in Equation 4.15 where the updated upstream ϕ values are used. Using this line by line relaxation scheme, the flow field is solved in an iterative manner. The term between the squared brackets in Equation 4.6 is replaced by B in the finite difference equations. Depending on the local velocity B depends on $\phi_{x,c}$ or $\phi_{x,b}$ as shown in Equation 4.17.

$$\phi_{x,c} = \frac{\phi^{n}_{i+1,j} - \phi^{n+1}_{i-1,j}}{2\Delta X}, \qquad \phi_{x,b} = \frac{\phi^{n}_{i,j} - \phi^{n+1}_{i-2,j}}{2\Delta X} \tag{4.15}$$

$$\Phi_i^{n+1} = \omega\widehat{\Phi}_i + (1-\omega)\Phi_i^n, \qquad \text{where: } \Phi_i = \begin{pmatrix} \phi_{i,1} \\ \cdot \\ \cdot \\ \phi_{i,j} \end{pmatrix} \tag{4.16}$$

$$\begin{aligned} B &= K - (\gamma+1)M_\infty^{2-3C_1}\phi_x \\ B_c &= K - (\gamma+1)M_\infty^{2-3C_1}\phi_{x,c}, \qquad B_b = K - (\gamma+1)M_\infty^{2-3C_1}\phi_{x,b} \end{aligned} \tag{4.17}$$

When $\phi_{x,c} < u^*$ and $\phi_{x,b} < u^*$, the flow is subsonic and Equation 4.18 is used. This is a second-order accurate difference equation suitable for the elliptic equation.

$$B_c\left(\frac{\phi_{i+1,j}^n - 2\widehat{\phi}_{i,j} + \phi_{i-1,j}^{n+1}}{\Delta x^2}\right) + \left(\frac{\widehat{\phi}_{i,j+1} - 2\widehat{\phi}_{i,j} + \widehat{\phi}_{i,j-1}}{\Delta\tilde{y}^2}\right) = 0 \tag{4.18}$$

When $\phi_{x,c} \geq u^*$ and $\phi_{x,b} \geq u^*$, the flow is supersonic and Equation 4.19 is used. This is a first-order accurate implicit backward difference equation with the positive x-axis as the propagation direction.

$$B_b\left(\frac{\widehat{\phi}_{i,j} - 2\phi_{i-1,j}^{n+1} + \phi_{i-2,j}^{n+1}}{\Delta x^2}\right) + \left(\frac{\widehat{\phi}_{i,j+1} - 2\widehat{\phi}_{i,j} + \widehat{\phi}_{i,j-1}}{\Delta\tilde{y}^2}\right) = 0 \tag{4.19}$$

There are two situations where the equation switches between elliptic and hyperbolic. Murman and Cole only used one equation for this situation where the jump conditions are not satisfied at the foot of a shock on a smooth profile [30, 72]. This was later fixed by Murman by adding a fourth operator, namely the shock point operator [31].

When $\phi_{x,c} \geq u^*$ and $\phi_{x,b} < u^*$, the equation switches from elliptic to hyperbolic. Hence, the flow accelerates from subsonic to supersonic and the corresponding mesh point is a sonic point. For this point $B = 0$, resulting in: Equation 4.20.

$$\left(\frac{\widehat{\phi}_{i,j+1} - 2\widehat{\phi}_{i,j} + \widehat{\phi}_{i,j-1}}{\Delta\tilde{y}^2}\right) = 0 \tag{4.20}$$

When $\phi_{x,c} < u^*$ and $\phi_{x,b} \geq u^*$, the flow decelerates and Equation 4.21 is used, which is the shock point operator. The difference equations in the x-direction are the sum of the elliptic and hyperbolic x-difference operators. According to Chattot, this scheme is not consistent with the transonic PDE, but the jump conditions are satisfied and the total flux of ϕ_y and $-0.5\phi_x^2$ in and out of the region of a mesh cell are conserved [72]. Hence, the choice was made that the conservation is important whereas consistency is not relevant at the shock discontinuity.

$$\begin{aligned} B_c\left(\frac{\phi_{i+1,j}^n - 2\widehat{\phi}_{i,j} + \phi_{i-1,j}^{n+1}}{\Delta x^2}\right) + B_b\left(\frac{\widehat{\phi}_{i,j} - 2\phi_{i-1,j}^{n+1} + \phi_{i-2,j}^{n+1}}{\Delta x^2}\right) + \\ \left(\frac{\widehat{\phi}_{i,j+1} - 2\widehat{\phi}_{i,j} + \widehat{\phi}_{i,j-1}}{\Delta\tilde{y}^2}\right) = 0 \end{aligned} \tag{4.21}$$

At $y = \tilde{y} = 0$, the boundary condition is specified as a $\phi_{\tilde{y}}$ value. Therefore, $\phi_{\tilde{y}\tilde{y}}$ at $y = \tilde{y} = 0$ is calculated with Equation 4.22. In order to use this equation, the mesh points for $j = 1$ are placed $0.5\Delta\tilde{y}$ away from the boundary ($\tilde{y} = 0$). The ϕ values at $\tilde{y} = 0$ are later calculated using an extrapolation formula.

$$\phi_{\tilde{y}\tilde{y}} = \frac{1}{\Delta\tilde{y}}\left[(\phi_{\tilde{y}})_{i,3/2} - (\phi_{\tilde{y}})_{i,1/2}\right] = \frac{1}{\Delta\tilde{y}}\left[\frac{\phi_{i,2} - \phi_{i,1}}{\Delta\tilde{y}} - (\phi_{\tilde{y}})_{\tilde{y}=0}\right] \tag{4.22}$$

The transonic equation is solved per line with Equation 4.23. Equation 4.18 through Equation 4.21, depending on the velocity per grid point, are rewritten to fit this equation. The column vector f contains the ϕ_{i+1}, ϕ_{i-1}, ϕ_{i-2} terms and A is a sparse matrix that is used to recreate all parts of the finite difference equations that contains ϕ_i terms.

$$A\widehat{\Phi}_i = f \tag{4.23}$$

Murman and Krupp determined that the convergence could best be measured by analyzing the surface pressure over 10 iterations, i.e. if the surface pressure did not change significantly (0.1 % is mentioned) over 10 iterations, convergence was obtained. [69]. During this study, convergence is checked by analyzing the ϕ values throughout the entire flow field and requiring that they would not change by more than 10^{-6} on the fine grid and $5 \cdot 10^{-6}$ on the coarser grid between iterations. The fine grid and the coarser grid have 501 and 201 points in the chordwise direction over the airfoil surface respectively. It should be noted that the values of ϕ range from approximately -1 to 1 over the entire flow field. Another difference between the methods used by Murman, Cole, and Krupp and this study is that the far field boundary conditions in this study are updated every iteration in stead of every 5 or 10 iterations. This continuous updating of the far field boundary conditions was also done by Langley, who reasoned that not updating the boundary conditions would, in the end, not result in lower computational time [73].

4.2.2 Results

The pressure coefficient that is calculated using the Murman-Cole-Krupp scheme is compared to the results presented by Krupp himself in Figure 4.8. It can be seen that the computed pressure coefficient matches the pressure coefficient that Krupp calculated using the fully conservative scheme, indicating that the Murman-Cole-Krupp scheme is correctly implemented [31]. Some very small difference between the calculated pressure coefficient and the fully conservative pressure coefficient presented by Krupp can be seen. These difference can be contributed to two factors. First, the mesh spacing used by Krupp for his calculations is not known, hence the solutions for two different grid point spacings are presented. Secondly, the plotted line corresponding to Krupp's data is extracted from the graph presented by Krupp. This extrapolation might have resulted in small errors. For these pressure coefficient calculations $C_1 = 1/2$ and $C_2 = 3/4$ were used to match Krupp's procedure. In Figure 4.8 it can be seen that the fully conservative scheme, which uses the shock point operator, yields a different result from the not fully conservative scheme, which uses the sonic point operator for both sonic points and shock points. For the fully conservative scheme, the shock is located further downstream and the shock is stronger in comparison to the shock in the not fully conservative scheme. Krupp explains that the computed shock Mach number of 1.29 is so high that the small-disturbance shock jump is 15% greater than the Rankine-Hugoniot jump. According to Murman, the discrepency between the two schemes was attributed to the smearing out of the re-expansion area after the shock when using the not fully conservative scheme. When the fully conservative scheme was used, this re- or after-expansion was well defined. From Figure 4.8, it can also be noted that the C_p calculated with the Murman-Cole-Krupp scheme deviates from the experimental data of Knechtel in the neighborhood of the shock wave. The data presented by Knechtel were obtained in a wind tunnel with a perforated wall [32]. Knechtel mentioned that the perforated wall interference at sonic speed may induce pressure gradients and blockage effects at the model location, as he already noticed deviations from theoretical results during his study in 1959. This partly explains the differences between the experimental and computed results. It should also be noted that the boundary layer in Knechtel's experiments was laminar.

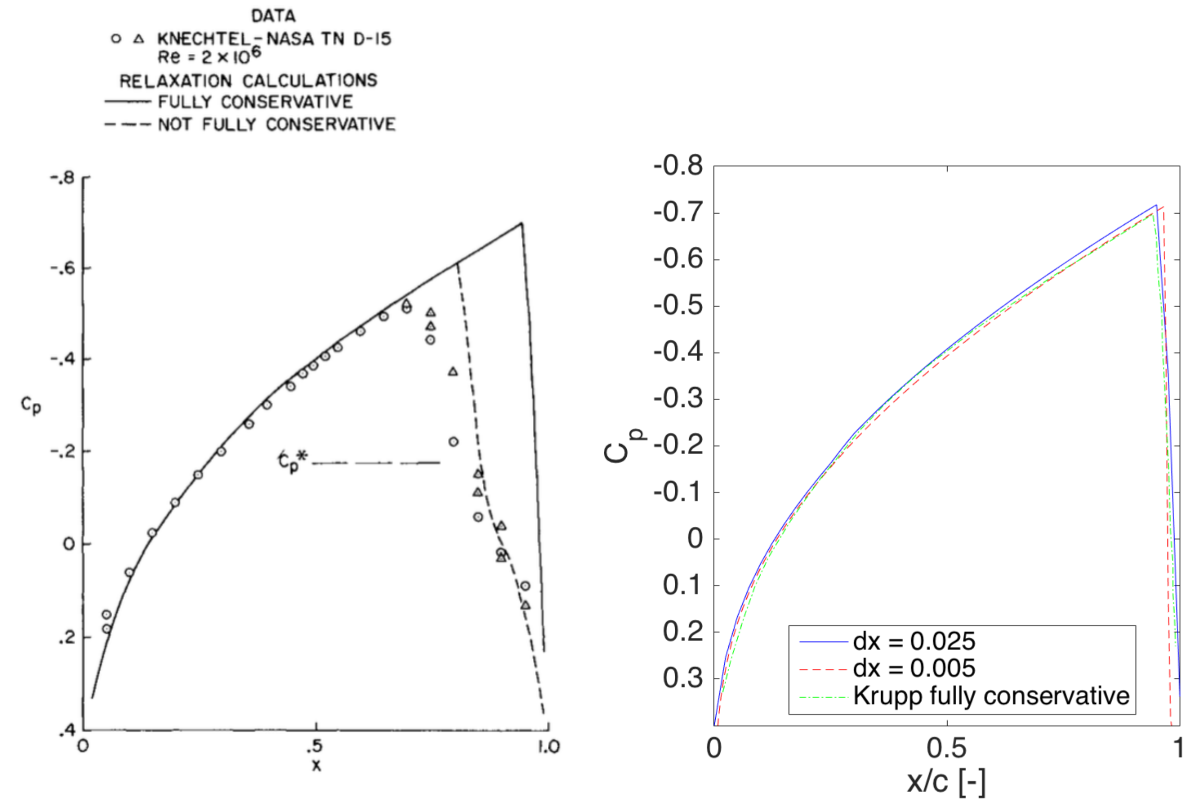

(a) Experimental and theoretical C_p (b) Computed C_p

Figure 4.8: Comparison of theory with data for a 6% parabolic arc airfoil, $M_\infty = 0.909$ [31, 32]

More than 10 years later, Collins and Krupp compared results of the Murman-Cole-Krupp scheme with experimental data again [33]. This time the measurements were performed in a closed wall wind tunnel where the velocity was set by adjusting the throat downstream of the test section. Collins and Krupp used $C_1 = C_2 = 2/3$ for the computational procedure. Figure 4.9 shows the experimental results for a 6% and 12% thick airfoils. The experimental results are scaled according to Equation 4.11 to obtain the reduced pressure coefficient. It was found that the agreement between the inviscid theory (transonic equation) and the experiments is within the three-percent difference range that exists between the two airfoil cases. It should be noted that the shock position in the experiments is at the same location as in the computational results, which was not the case when using the experimental data presented by Knechtel [32]. Since both the results for both a high and low value of transonic similarity parameter ($K = 1.36$ and $K = 5.12$) compare well to the theoretical results, it was concluded by Collins and Krupp that the scaling laws of Equation 4.7 and Equation 4.8 are valid for both flows where M_∞ is close to unity or M_∞ is considerably below one. The computed C_p compares well to the results of the inviscid theory presented by Collins and Krupp, once again confirming that the Murman-Cole-Krupp scheme is used correctly here. It should be noted, however, that differences in the computed solution can be seen for different mesh spacing. Collins and Krupp do not mention which Δx value they used for their computations, but the data for $\Delta x = 0.025$ seems to compare best to their results. It is therefore assumed that they used a similar or smaller spacing. In this case Δx represent the spacing of horizontal points on the airfoil surface for an airfoil running from $x = 0$ to $x = 1$.

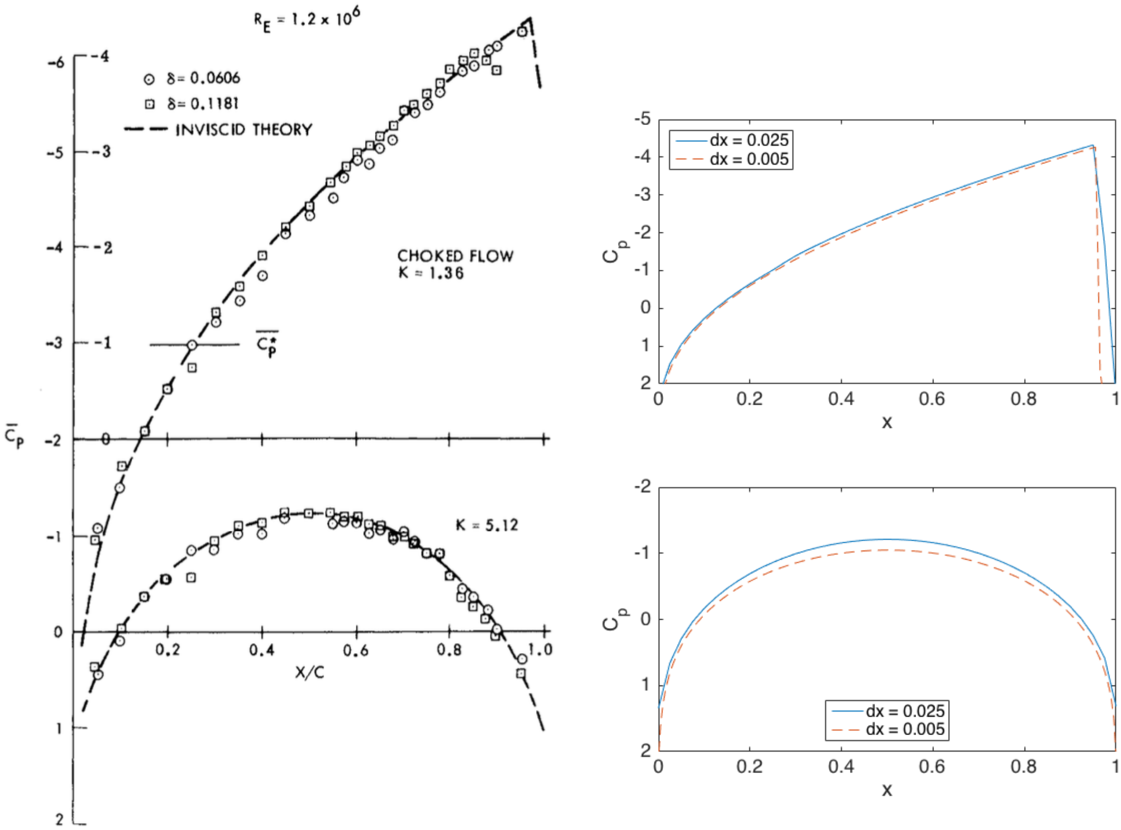

(a) Experimental and theoretical C_p (b) Computed C_p

Figure 4.9: Pressure distribution comparison of two parabolic arc airfoils to inviscid theory [33]

Till now, only the pressure coefficient at the airfoil surface has been used, however, in order to trace light rays through a flow the density field has to be determined. To do this, information about the atmospheric conditions are needed. The standard atmosphere, presented in Appendix A, is used to determine the total temperature, pressure, and density at the specified flight altitude. The speed of sound at both stagnation conditions and critical conditions can be calculated from the total temperature using Equation 4.24 [68]. The specified freestream Mach number is transformed to the characteristic Mach number with Equation 4.25 in order to determine the freestream velocity using $u_\infty = a_{cr} M^*_\infty$. The freestream temperature is determined with Equation 4.26. The freestream pressure is then determined using the isentropic relations, presented in Equation 4.27, which are valid in the far field and upstream as non-isentropic phenomena have not occurred there. The freestream density can be determined using either the isentropic relation or the perfect gas law, specified in Equation 4.28.

$$a_0 = \sqrt{\gamma R T_t}, \qquad a_{cr} = a_0 \sqrt{\frac{2}{\gamma + 1}} \tag{4.24}$$

$$M^2 = \frac{2}{\frac{\gamma+1}{M^{*2}} - (\gamma - 1)}, \qquad M^{*2} = \frac{(\gamma+1)M^2}{2 + (\gamma - 1)M^2} \tag{4.25}$$

$$\frac{T_t}{T} = 1 + \frac{\gamma + 1}{2} M^2 \tag{4.26}$$

$$\frac{p_1}{p_2} = \left(\frac{\rho_1}{\rho_2}\right)^{\gamma} = \left(\frac{\rho_1}{\rho_2}\right)^{\frac{\gamma}{\gamma-1}} \tag{4.27}$$

$$p = \rho RT \tag{4.28}$$

When the solution for ϕ has been found, the velocity components u and v and the pressure are determined using the flow quantity expansions from Equation 4.4. To determine u and v at all but the boundary locations, a centered scheme, similar to the one presented in Equation 4.15 is used. At the boundary locations, the velocities are determined using a first order accurate discretization, e.g. $u = (\phi_{i+1} - \phi_i)/\Delta X$. On the $y = 0$ boundary, the vertical velocity component is determined using the boundary condition, specified in Equation 4.13. The characteristic Mach number is then determined using $M^* = \sqrt{u^2 + v^2}/a_{cr}$. Using Equation 4.25, the Mach number at each location in the flow field can be determined. The temperature field is determined using Equation 4.26 because the entire field can be assumed to be adiabatic since a shock wave is adiabatic and viscous effects in the boundary layer are not taken into account by Murman-Cole-Krupp scheme. The density field is determined by substituting the calculated pressure and temperature values into the perfect gas law.

4.2.3 Remarks

It has to be mentioned that the symmetric small disturbance transonic equation, used to compute the transonic flow fields, is not the most accurate flow solver at the time of writing. However, in comparison to a RANS (Reynolds Averaged Navier Stokes), LES (Large Eddy Simulation), or DNS (Direct Numerical Simulation) method, the used method is much less computationally demanding and still yields realistic flow fields. A commercial flow solver, like the ANSYS Fluent package, could have been used as well. However, in order to use fluent for different airfoil geometries and varying Mach numbers, numerous meshes have to be produced. This is not needed when using the Murman-Cole-Krupp method, on the other hand. Another reason to choose the Murman-Cole-Krupp method was its relative simplicity, which could be translated into a good understanding of the shortcomings and assumptions of the method. Hence, the choice was made to use a simpler, computationally cheaper, but less accurate flow solver, which still yields realistic results. The computational cost argument was by far the most important factor for the trade-off as the computational resources were limited.

The symmetric small disturbance transonic equation does not take viscosity into account. Hence, the entire boundary layer is ignored. This could result in inaccurate predictions of the shock wave position and shock wave strength. However, experimental validation has shown that the Murman-Cole-Krupp method is still very accurate for a large range of values for the transonic similarity parameter. Another problem of ignoring viscosity is that separation phenomena are not being modeled. In cases where strong shock waves occur, i.e. high upstream Mach number (low K value), separation phenomena are to be expected. Therefore, it was decided not to use flow fields where a lambda shock pattern occurs. It was found that these only occur for high upstream Mach numbers and that local maximum Mach numbers exceeding 1.4 were present in front of the shock. According to Delery and Marvin, significant separation occurs under these conditions [28].

Another reason to no use the lambda shock patterns was the sometimes unrealistic position of the shock waves. It was found that the shock wave C_2 would not hit the airfoil surface in some cases, but instead it stood on the symmetry line after the airfoil. In this case, the symmetry condition makes it look like the symmetry line after the airfoil could be a flat plate. Since most airfoils used for commercial flight are not symmetrical and the shock waves have been found to be very dynamic, it is not very realistic that a lambda shock pattern on the upper and lower side of the airfoil would match perfectly.

Therefore, flow fields where significant separation phenomena are expected or flow fields where a shock stands on the symmetry line behind the airfoil are not used for the shadowgraph simulation. The flow fields that are used for the shadowgraph simulation, are the flow fields that were calculated with freestream Mach numbers below the freestream Mach number that resulted in a lambda shock pattern. For these flow fields, little to no separation is expected, hence the computed flow field will be more realistic when considering the inviscid density field. Since the aim of this study is to determine whether a relation between the transonic shock waves and the shadowgraphs on a wing surface exists, a realistic transonic flow field is needed to simulate shadowgraphs. However, realistic is by no means equal to the most precise and accurate solution and for this work the Murman-Cole-Krupp method will suffice for the purpose of simulating shadowgraphs. When a relation between shadowgraph features and some shock wave characteristics is found, more accurate flow solvers can be used to further refine the observed trends.

Another shortcoming of the symmetric small disturbance transonic equation is that pressure calculation at the stagnation point near the leading edge can be unrealistic. The manner in which the pressure is calculated has been validated and is realistic for the flow over the airfoil. However, when the velocity near the leading edge goes to zero, the small disturbance assumptions are violated. As a results, the pressure increases to values above the total pressure. This also results in too high density values at this location. However, these very low velocities are only present in a very small region in the vicinity of the leading edge. So the pressure and density are only too high in a very small region that is far away from the shock wave. Since the shock waves to be studied do not appear in the vicinity of the stagnation point, it can be concluded that the deflection of light rays that will form the dark and bright bands that are characteristic for shock wave shadowgraphs on a wing surface are not affected by this.

4.3 Bohning-Zierep Model

In the late 1970s, Bohning and Zierep developed a method to analyze the boundary layer on a curved wall in the proximity of a normal shock wave that is present in the transonic flow field [34, 74]. This analytic method will be used to model the density field in the boundary layer, which was not modeled by the Murman-Cole-Krupp scheme. The calculated density fields of the boundary layer will be used to calculate the light deflection that occurs in the boundary layer. In doing so, the error that is introduced by ignoring the boundary layer when tracing the light through the flow field can be estimated.

The model used by Bohning and Zierep divides the flow into three layers, as can be seen in Figure 4.10. The first layer represents the frictionless transonic flow outside the boundary layer. The second layer is the inviscid, compressible, outer boundary layer. Friction effects in this layer are prescribed by the velocity profile of the boundary layer upstream of the shock wave. The third layer describes the thin fully viscous and compressible inner boundary layer next to the wall. The Navier-Stokes equations were used by Bohning and Zierep to respresent this layer [74].

For the outer boundary layer, Bohning and Zierep assumed that both the dynamic viscosity and the thermal conductivity are constant. Furthermore, the Prandtl number was set to be one and the wall was assumed to be adiabatic. The dimensionless parameters, presented in Equation 4.29, where substituted into the governing equations. It should be noted that the dimensionless parameters in Equation 4.29 consist of a mean and a disturbance part, indicated with G for the 'Grundfeld' (mean) and S for the 'Störgrößen' (disturbance). The rewritten governing equations are presented in Equation 4.30 through Equation 4.33. It should be noted that the higher order terms are ignored and that the viscous terms are dropped because it is assumed that $Re_\delta = c^* \delta \rho^* / \mu \gg 1$. It should also be noted that $x = \hat{x}/l$ and $y = \hat{y}/\delta$ are the local dimensionless coordinates whereas $\hat{x}$ and $\hat{y}$ are the real coordinates. The parameters l and

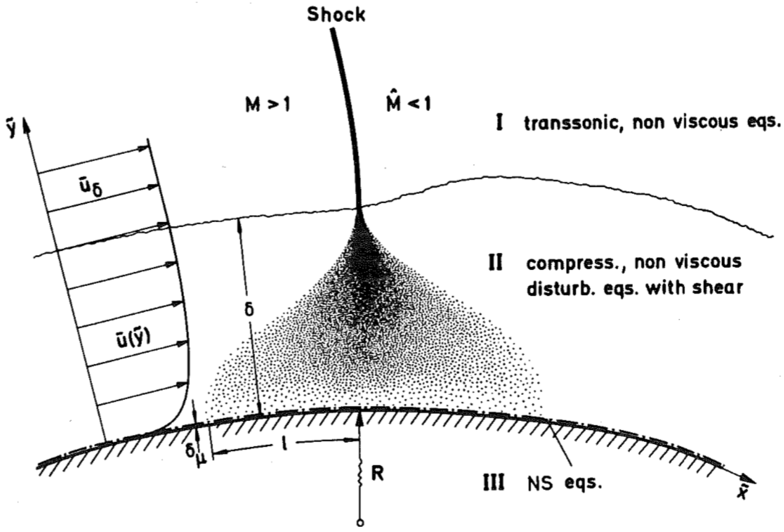

Figure 4.10: Schematic illustration of the flow model [34]

δ are the characteristic length scales in the x- and y-direction. For the derivations, Bohning and Zierep assumed that $l \sim \delta$.

$$\begin{aligned} M_G^* &= \frac{\bar{u}}{a_{cr}}, & v_G &= 0, & p_G &= \frac{\bar{p}}{p^*}, & \rho_G &= \frac{\bar{\rho}}{\rho^*}, & T_G &= \frac{\bar{T}}{T^*} \\ u_S &= \frac{u'}{a_{cr}}, & v_S &= \frac{v'}{a_{cr}}, & p_S &= \frac{p'}{p^*}, & \rho_S &= \frac{\rho'}{\rho^*}, & T_S &= \frac{T'}{T^*} \end{aligned} \tag{4.29}$$

$$\text{Continuity: } \rho_G \frac{\partial u_S}{\partial x} + \frac{\partial \rho_G v_S}{\partial y} + M_G^* \frac{\partial \rho_S}{\partial x} = 0 \tag{4.30}$$

$$\text{Momentum: } \rho_G M_G^* \frac{\partial u_S}{\partial x} + \rho_G v_S \frac{\partial M_G^*}{\partial y} = -\frac{1}{\gamma} \frac{\partial p_S}{\partial x}, \qquad \rho_G M_G^* \frac{\partial v_S}{\partial x} = -\frac{1}{\gamma} \frac{\partial p_S}{\partial y} \tag{4.31}$$

$$\text{Energy: } T_S + (\gamma - 1) M_G^* u_S = 0 \tag{4.32}$$

$$\text{Equation of State: } \rho_G T_S + \rho_S T_G = p_S \tag{4.33}$$

By means of substitution and elimination of variables, the equations can be reduced to Equation 4.34. The new equations are defined in terms of v_S and p_S only. When the coordinate transformation, defined in Equation 4.35, was used, it was found that $p_S = -\gamma \frac{\partial \phi}{\partial x}$ and $v_S = M_G^* \frac{\partial \phi}{\partial z}$. Hence, the equations can be rewritten to Equation 4.36, which is a second order differential equation. The first boundary condition of Equation 4.36 is dictated by the pressure of the outer transonic flow at the upper edge of the outer boundary layer. The second boundary condition states that the velocity normal to the wall at $z = z_0$, which is the boundary between the inner and outer boundary layer, has to be zero. The third boundary condition states that the vertical velocity component is zero far upstream and downstream of the shock wave. It should be noted that the z-coordinate does not correspond to a third-dimension but is used in analogy with the work by Bohning and Zierep.

$$\rho_G M_G^* \frac{\partial v_S}{\partial y} + \rho_G \frac{\partial M_G^*}{\partial y} v_S + \frac{1}{\gamma}(M_G^2 - 1)\frac{\partial p_S}{\partial x} = 0, \qquad \rho_G M_G^* \frac{\partial v_S}{\partial x} + \frac{1}{\gamma}\frac{\partial p_S}{\partial y} = 0 \tag{4.34}$$

$$z = \int_1^y M_G^2(\eta)d\eta \tag{4.35}$$

$$\phi_{zz} - \frac{M_G^2(z) - 1}{M_G^4(z)}\phi_{xx} = 0 \tag{4.36}$$

$$\begin{aligned}
&\text{B.C. 1: } \phi_x(x, z=0) = -\frac{1}{\gamma} p_S(x, z=0) \\
&\text{B.C. 2: } \phi_z(x, z=z_0) = 0 \\
&\text{B.C. 3: } \phi_z(-L, z) = \phi_z(L, z) = 0
\end{aligned}$$

The boundary value problem was solved for both the x- and y-part of the equation by separating the variables. The final solution is presented in Equation 4.37. It should be noted that the z-coordinate is replaced by the y-coordinate again, as the equation could not be solved in the z-coordinate form, according to Bohning and Zierep [74]. The y-part of the equation, $f_n(y)$, was solved using confluent hypergeometric differential equations. In these equations λ_n stands for the separation variable or eigenvalue and α is the exponent of the power law velocity distribution: $M_G^*(y) = y^\alpha$. This power law describes the mean velocity distribution in the outer boundary layer ($y_0 \leq y \leq 1$). The solution of the x-part of the equation was simplified by Bohning in 1978 by assuming that the far field boundaries $\pm L$ could be replaced by $\pm\infty$ because the mean velocity distribution is independent of x [75]. The simplified form of $g_n(x)$ is presented in Equation 4.39.

$$\phi(x, y) = \sum_{n=1}^{\infty} g_n(x) f_n(y) - \frac{1}{\gamma}\int_{-L}^{x} p_S(\bar{x}, 1)d\bar{x} \tag{4.37}$$

$$f_n(y) = e^{-\frac{\sigma_n}{2}y^\zeta}\left[y^{2\alpha+1}F_-(\sigma_n)F_+(\sigma_n y^\zeta) - F_+(\sigma_n)F_-(\sigma_n y^\zeta)\right] \tag{4.38}$$

$$\begin{aligned}
\text{where: } &\zeta = 2\alpha\frac{ln(2)}{ln(\alpha+1)} \\
&\beta = 4\alpha(\alpha+1)^{\frac{-(1+\alpha)}{\alpha}} \\
&p = \frac{2\alpha+1+\zeta}{\zeta} \\
&q_n = -\frac{\sqrt{\lambda_n\beta} - 2\alpha - \zeta - 1}{2\zeta} \\
&\sigma_n = \frac{2}{\zeta}\sqrt{\lambda_n\beta} \\
&F_+(\sigma_n y^\zeta) = {}_1F_1(q_n, p, \sigma_n y^\zeta) = 1 + \sum_{k=1}^{\infty}\frac{q_n(q_n+1)\cdots(q_n+k-1)}{p(p+1)\cdots(p+k-1)}\frac{(\sigma_n y^\zeta)^k}{k!} \\
&F_-(\sigma_n y^\zeta) = {}_1F_1(q_n - p + 1, 2 - p, \sigma_n y^\zeta)
\end{aligned}$$

$$g_n(x) = \frac{1}{2\gamma}\int_{y_0}^{1}\bar{\psi}(y)f_n(y)dy\left(\int_{-\infty}^{x}p_S(\bar{x},1)e^{\sqrt{\lambda_n}(\bar{x}-x)}d\bar{x} - \int_{x}^{\infty}p_S(\bar{x},1)e^{\sqrt{\lambda_n}(x-\bar{x})}d\bar{x}\right) \tag{4.39}$$

where: $\bar{\psi} = \dfrac{1-M_G^2(y)}{M_G^2(y)}$

The pressure and vertical velocity disturbance can be determined using Equation 4.40, where it can be seen that the solution is rewritten to be a function of y instead of z. The horizontal velocity disturbance term could be determined using the momentum equation and the solutions for p_S and v_S, as can be seen in Equation 4.41.

$$p_S = -\gamma\frac{\partial\phi}{\partial x}, \qquad v_S = M_G^*\frac{\partial\phi}{\partial y}\frac{dz}{dy} = \frac{M_G^*}{M_G^2}\frac{\partial\phi}{\partial y} \tag{4.40}$$

$$u_S(x,y) = -\frac{M_G^*}{\gamma M_G^2}p_S(x,y) - \frac{1}{M_G^*}\frac{dM_G^*}{dy}\int_{-\infty}^{x}v_S(\bar{x},y)d\bar{x} \tag{4.41}$$

Originally, Bohning and Zierep used a model for the inner boundary layer where the inner boundary layer thickness depended on the change in wall shear stress for different y_0 values [74]. For this layer, the governing equations were used with $v_S = 0$ and the viscous terms were not ignored this time by arguing that $1/Re_\delta \ll 1$. By manipulation of the equations, a definition for u_S was found which was used to calculate $\frac{\partial}{\partial y_0}\left(\frac{\partial \tau_{s,w}}{\partial x}\right) = \frac{\partial}{\partial y_0}\left(\mu\frac{\partial^2 u_S}{\partial x\partial y}\right) = 0$. Bohning and Zierep argued that this viscous layer would represent a laminar sublayer [34, 75]. Bohning, therefore, derived Equation 4.42. It can be seen that y_0 depends on the Reynolds number, hence the turbulent character of the flow is accounted for. According to Bohning and Zierep, Equation 4.42 also approximately takes the scaling effects, caused by the turbulent Reynolds stresses, into account. However, it is not mentioned how these scaling effects are accounted for. The assumed velocity profiles for both the inner and outer boundary layers are presented in Equation 4.43, which also presents a relation between α and Re_δ which was determined from measurements of turbulent boundary layers [75]. In this equation, $M_G^*(1)$ is the critical Mach number that appears just before the shock wave at the edge of the boundary layer.

$$y_0 = 1.14\left(\frac{1}{Re_\delta}\right)^{\frac{1}{2+\alpha}}, \qquad 5\cdot 10^3 \lesssim Re_\delta \lesssim 5\cdot 10^5 \tag{4.42}$$

$$\begin{gathered} M_G^*(y) = \begin{cases} M_G^*(1)y^\alpha & y_0 \le y \le 1 \\ M_G^*(y_0)\frac{y}{y_0} & 0 \le y < y_0 \end{cases} \\ \alpha = -0.023log_{10}(Re_\delta) + 0.25, \qquad 10^4 \lesssim Re_\delta \lesssim 10^6 \end{gathered} \tag{4.43}$$

This method by Bohning and Zierep is an iterative method which uses the solution of the boundary layer to adjust the outer transonic flow, which in turn is used to recalculate the boundary layer flow [34, 74, 75]. First, a pressure jump, corresponding to a normal shock wave, is imposed on the boundary layer, i.e. this pressure jump is used as a boundary condition for the boundary value problem. Secondly, the calculations for the inner and outer boundary layer are performed. Thirdly, v_S is used for the new calculation of the outer transonic flow field. The pressure found after this calculation is used to recalculate the boundary layer, i.e. to update the boundary layer. Koren and Bannink created a numerical scheme for this method that repeats these calculations until the solution converges, whereas Bohning and Zierep stopped the calculation after one iteration [76]. The outer transonic flow field was calculated with a method by Oswatitsch and Zierep which determines the shock wave curvature when impinged on a curved wall. Unfortunately, a very significant free parameter, which was said to match the outer transonic flow to the outer boundary layer flow, was unspecified. Bohning and Zierep did not specify this parameter and neither did Koren and Bannink. Information on this free parameter could also not be found in Zierep's original paper that described the vertical shock wave on a curved wall nor was it mentioned in Zierep's more recent paper, in which he discusses some questions and misunderstandings about his method [77, 78]. The influence of the free parameter on the solution of the outer transonic flow is clearly shown in Figure 4.11. Not only does the shock wave curvature change significantly, the post-shock wave flow is completely different for the different values of the free parameter. It should be noted that the x and y in these figures are the dimensionless coordinates. Hence, the shown flow field is six boundary layer thicknesses wide and 10 boundary layer thicknesses high. This also highlights the second issue concerning the outer transonic flow field model by Oswatitsch and Zierep, namely its region of validity. The model by Oswatitsch and Zierep is also based on an inviscid transonic potential flow model that was simplified to the point where it could be used analytically. Due to these simplifications, the model is only valid near the location where the shock wave intersects with the boundary layer.

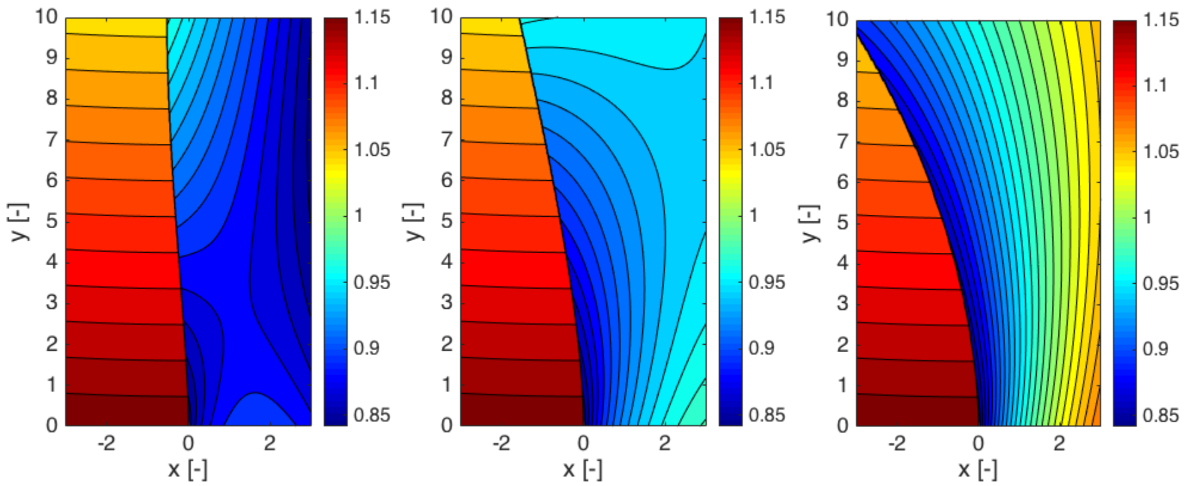

Figure 4.11: Outer transonic flow field Mach contours for different values of the free parameter (left to right -1, 0, 1)

To avoid the issues with the region of validity and the free parameter of the Oswatitsch and Zierep model, the use a different inviscid transonic flow model was preferred for this project. This other inviscid transonic flow model should replace the Oswatitsch and Zierep model for the pressure boundary condition for the outer boundary layer. In 1979, Bohning presented a solution for the flow behind the shock wave in a transonic flow field [79]. This model was inviscid and based on the transonic potential flow equation. The results of this model were compared to real experimental data, in a qualitative manner, and it was found that it modeled the after expansion realistically. The problem with this model was that one of the boundary conditions was based on the shock strength and hence the flow upstream of the shock. This information is not available for the present application, making it impossible to apply. Therefore, the choice was made to use the Murman-Cole-Krupp scheme which calculates the entire transonic flow field over an airfoil, including the after expansion that would sometimes occur after a shock wave in a transonic flow field [31, 34, 77, 79]. The pressure at the airfoil surface near the shock wave, calculated with the Murman-Cole-Krupp scheme, will be used as the boundary condition for the Bohning-Zierep model. However, the solution of the Bohning-Zierep model will not be used to update the outer transonic flow because this will change the boundary conditions for the the

Murman-Cole-Krupp scheme, which in turn will nullify the validation that has been done on the Murman-Cole-Krupp scheme, making the results questionable. Hence, the Murman-Cole-Krupp scheme will be used to calculate the entire inviscid transonic flow field around an airfoil and this solution will be used to approximate the boundary layer with the Bohning-Zierep model.

In 1981, Bohning and Zierep compared the calculated density fields corresponding to a flat and a curved wall to density fields that were experimentally obtained by means of interferograms [34]. They found that the fluid fields agreed very well even in fine details, especially the curvature of the isochoric lines near the walls were very similar. Hence, this model will approximate the boundary layer in the vicinity of normal shock well enough to get an approximation of the light deflection in the boundary layer. The density field can be calculated using Equation 4.32 and Equation 4.33 when the u_S, v_S, and p_S have been determined for the flow field.

5. Shadowgraph Simulation

In order to simulate shadowgraphs, a light source has to be modeled, light rays have to be traced, and the light intensity on the surface has to be calculated. This process of the ray tracing method will discussed first in this chapter. Secondly, an analysis of the accuracy of different functions used to model the light distribution per light ray will be presented. These functions are important as they will affect the light intensity on a surface. Finally, the iterative part of the shadowgraph simulation scheme will be discussed.

5.1 Ray Tracing

Ray tracing will be used to trace light rays from the light source, through a disturbance, to a surface. For this project the disturbance is a flow field over an airfoil where a wing-bound shock wave is present. The surface is the wing surface in this case, but can also be a camera film. For the purpose of this study, it will be assumed that the pixels measuring illumination levels are on the surface on which the light falls and not in a camera. By doing this, camera effects and the refraction of light when it travels from the wing surface to the camera are not considered. This will reduce the amount of factors that influence the formation of a shadowgraph. In turn, this will simplify the comparison between shadowgraph features and different flow fields.

For this study, the airfoil surface, on which the light is cast, is normalized for the ray tracing. The airfoil runs from $x/c = 0$ to $x/c = 1$, and the y-dimension represents the height above the airfoil. The leading edge, for all used airfoils, is placed at the origin. The ray tracing scheme, that will be discussed later, can also be applied to 3D situations, in which case the z-direction is parallel to the unswept wing span.

The first step in the ray tracing scheme is to obtain an index of refraction field, which can be deduced from one of the calculated flow fields. The density field of a known flow field is used to determine the index of refraction field using the Gladstone-Dale equation, which was defined in Equation 2.16. The index of refraction gradients $\partial n/\partial x$ and $\partial n/\partial y$ are calculated with the same discretization scheme used to determine the velocity components u and v, as shown in subsection 4.2.2. The only exception is the case for the $y = 0$ boundary where v is specified. In this case a first order forward discretization scheme is used to determine $\partial n/\partial y$. The index of refraction and both index of refraction gradients will be used by the ray tracing scheme.

The next sections will specify how the use of different light sources affects the light rays used during simulations. Secondly, the ray-tracing scheme will be discussed. Thirdly, the calculation of the radiant flux using different light distribution functions per light ray will be explained.

5.1.1 Light Sources and Light Rays

Two types of light sources will be used for the simulation of shadowgraphs, namely a point light source and parallel light. When using a point light source, the position of this light source will have to be specified. In the case of parallel light, the light source is assumed to be located at infinity. Hence, parallel light can be used to model sun light. It should be noted, however, that the sun is neither infinitesimal, nor at infinity. As a result, the circle of confusion should not be forgotten when, for example, simulated results are compared to real shadowgraphs. Another difference between the light sources is the variation in irradiance, which depends, among other things, on the optical path length between the light source and the surface. For parallel light, with a light source assumed at infinity, it will be assumed that the differences in irradiance are infinitesimal. This can be assumed since the difference in optical path length caused by the light ray refraction in the flow field near the wing are insignificant in comparison to the total optical path length from light source to wing surface. Hence the irradiance will be constant for parallel light.

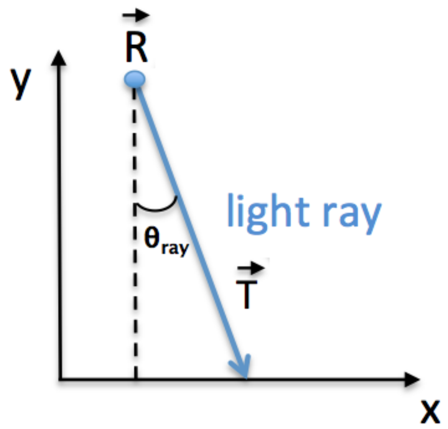

Figure 5.1: Starting position and light angle of a light ray

For the used ray tracing scheme, each light ray will have a location vector **R** and a direction vector **T**, which is also known as the optical ray vector. The initial values for the locations and direction of each light ray depend on the type of light source and have to be known in order to start the ray tracing scheme. During the ray tracing, the values of **R** and **T** will be updated. Hence, the first value of **R** is the location of the light source and later values will correspond to the light ray's location in the flow field. For a point light source, the initial location of all the light rays is equal to the position of the light source. The optical ray vector, however, is different for each light ray and depends on the light angle per ray θ_{ray}. Figure 5.1 illustrates the location of a light ray, the direction of the light ray if unaltered, and the light angle of the light ray at the current location. For a point light source, the initial light angles are determined such that the first ray will strike the leading edge and the last ray will strike the trailing edge if the light rays are not bent. This is illustrated in Figure 5.2 where the light rays corresponding to the minimum and maximum initial light angle are shown. The corresponding values of θ_{ray} are calculated with Equation 5.1, where the values of **R** correspond to the location of the light source in this case. In other words, R_x is the x-location of the light source and R_y is the y-location light source for Equation 5.1. The ray spacing depends on the amount of rays used for the simulation, n_r, and is defined in Equation 5.2. Hence, for a point light source, θ_{ray} will range from θ_{min} to θ_{max} with a spacing of $d\theta_{ray}$ between the light rays. It should be noted that n_r is actually the number of rays used minus one. For parallel light, the light angle is the same for all the rays, however, the initial locations of the light rays are not identical. In this case R_y is set to equal the upper edge of the calculated flow field and the values for R_x are chosen such that the first ray will hit the leading edge and the last ray will hit the trailing edge if the light rays are not bent. The corresponding values for R_x are calculated with Equation 5.3. The initial x-positions of the light rays will be spaced by $1/n_r$. Equation 5.4 shows how the optical ray vector is determined from the initial light angles. Equation 5.5 summarizes what the initial location and θ_{ray} values are for the two different light sources

$$\theta_{min} = \arctan\left(\frac{-R_x}{-R_y}\right), \qquad \theta_{max} = \arctan\left(\frac{1-R_x}{-R_y}\right) \tag{5.1}$$

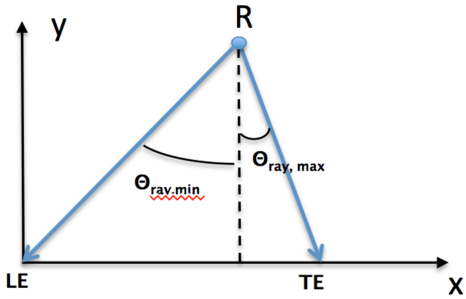

Figure 5.2: Minimum and maximum initial light angles for point light source

$$d\theta_{ray} = \frac{\theta_{max} - \theta_{min}}{n_r} \tag{5.2}$$

$$R_{x,min} = -R_y \tan(\theta_{ray}), \qquad R_{x,max} = 1 - R_y \tan(\theta_{ray}) \tag{5.3}$$

$$\mathbf{T} = \begin{pmatrix} \sin(\theta) \\ -\cos(\theta) \end{pmatrix} \tag{5.4}$$

$$\text{point source: } \mathbf{R} = \begin{pmatrix} x_{source} \\ y_{source} \end{pmatrix}, \quad \theta_{ray} = (\theta_{min}, \theta_{min} + d\theta_{ray}, \theta_{min} + 2d\theta_{ray}, ..., \theta_{max}) \tag{5.5}$$

$$\text{parallel light: } \mathbf{R} = \begin{pmatrix} R_{x,min} & R_{x,min} + 1/n_r & R_{x,min} + 2/n_r & ... & R_{x,max} \\ R_y & R_y & R_y & ... & R_y \end{pmatrix}, \quad \theta_{ray} = const.$$

If the starting position of a light ray is outside the domain of the known flow solution, the location where the light ray enters the flow field is calculated using the initial position of the light ray, the optical ray vector of the light ray, and the boundary conditions of the flow field. This is simply finding the intersection between lines, one being the optical ray vector that passes the initial ray position and the other being the flow field boundary. The distance that the ray has traveled between the old and new location can be calculated with Equation 5.6. The initial values of r are zero as the light rays have not covered any distance at their initial location. This is not necessarily true for parallel light, but the traveled distance is not relevant for the calculations for parallel light, hence no corrections will be made for this case.

$$r = r + \sqrt{(R_{x,old} - R_{x,new})^2 + (R_{y,old} - R_{y,new})^2} \tag{5.6}$$

Since light rays will be deflected by the changes in the index of refraction field, extra rays will be used on each side, meaning that extra rays will be used that would not strike the airfoil if they are not deflected. This is done for two reasons. First, to assure that even under deflection, rays will always reach the leading and trailing edge, hence covering the entire airfoil surface. This is to avoid unrealistic light representation at the edges of the airfoil in case of strong light deflection. Secondly, when a Gaussian distribution is used to represent the light distribution per light ray, a certain amount of Gaussian curves have to overlap in order to reach a uniform distribution. The light distribution functions per light ray will be discussed in more detail later. For a point light source, this means that the minimum and maximum values for θ_{ray} are stretched a bit, but the spacing between different rays remains unchanged. For parallel light, the minimum and maximum values for $\mathbf{R}_x$ will be stretched a little, but the ray spacing will also remain unchanged. Equation 5.7 and Equation 5.8 show how the light angle and the initial positions are altered for the point light source and parallel light cases respectively when using these extra rays. It should be noted that the total number or rays used for a simulation equals $n_r + 2n_{r,ext} + 1$.

$$\theta_{ray} = (\theta_{min} - n_{r,ext} \cdot d\theta_{ray},\ \theta_{min} + (1 - n_{r,ext})d\theta_{ray},\ \ldots,\ \theta_{max} + n_{r,ext}d\theta_{ray}) \tag{5.7}$$

$$\mathbf{R} = \begin{pmatrix} R_{x,min} - n_{r,ext}/n_r & R_{x,min} + (1 - n_{r,ext})/n_r & \ldots & R_{x,max} + n_{r,ext}/n_r \\ R_y & R_y & \ldots & R_y \end{pmatrix} \tag{5.8}$$

5.1.2 Ray Tracing Scheme

In order to trace the light rays through a flow field, the ray tracing scheme developed by Sharma et al. in 1982 and improved by Doric in 1990 will be used [80, 81]. This scheme numerically solves the ray trace equation in order to follow light rays through a graded-index medium. The ray equation, defined by Equation 5.9, where $\mathbf{r}$ is the position vector and ds is an element of an arc length along the ray, is rewritten using a new variable t which is defined in Equation 5.10. Using Equation 5.10, the ray equation can be rewritten to Equation 5.11. In this form the ray equation can be used for direct numerical integration. The optical ray vector, introduced earlier, can also be defined as a function of the position vector and the new variable t, as shown by Equation 5.12. Figure 5.3 shows both the location vector and the optical ray vector at the current location, which illustrates that the optical ray vector at a location is tangent to the light ray.

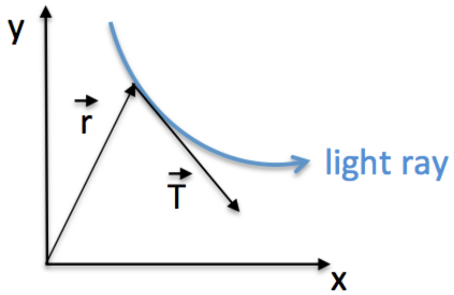

Figure 5.3: Ray tracing position and optical ray vector

$$\frac{d}{ds}\left(n(\mathbf{r})\frac{d\mathbf{r}}{ds}\right) = \nabla n(\mathbf{r}) \tag{5.9}$$

$$t = \int \frac{ds}{n}, \qquad dt = \frac{ds}{n} \tag{5.10}$$

$$\frac{d^2\mathbf{r}}{dt^2} = n\nabla n = \frac{1}{2}\nabla n^2 \tag{5.11}$$

$$\mathbf{T} = \frac{d\mathbf{r}}{dt} \tag{5.12}$$

According to Sharma et al., the refractive index is isentropic in most practical cases, hence ∇n^2 does not depend on the optical ray vector. As a result, Sharma et al. could use a Runge-Kutta method to solve the ray equation. Three vectors, defined in Equation 5.13, are used for this computational scheme. These are the location vector, the optical ray vector, and a vector representing the ray equation of Equation 5.11, i.e. $d^2\mathbf{R}/dt^2 = \mathbf{D}(\mathbf{R})$. When $\mathbf{R}$ and $\mathbf{T}$ are known as initial conditions, the equation $d^2\mathbf{R}/dt^2 = \mathbf{D}(\mathbf{R})$ can be used to successively calculate $(\mathbf{R}_1, \mathbf{T}_1)$, $(\mathbf{R}_2, \mathbf{T}_2)$, etc. Hence, a light ray can be traced through a medium using a Runge-Kutta scheme presented in Equation 5.14 and Equation 5.15 [80].

$$\mathbf{R} = \begin{pmatrix} x \\ y \\ z \end{pmatrix}, \qquad \mathbf{T} = \begin{pmatrix} \mathbf{T}_x \\ \mathbf{T}_y \\ \mathbf{T}_z \end{pmatrix}, \qquad \mathbf{D} = n \begin{pmatrix} \partial n/\partial x \\ \partial n/\partial y \\ \partial n/\partial z \end{pmatrix} \tag{5.13}$$

$$\mathbf{R}_{n+1} = \mathbf{R}_n + \Delta t \left[\mathbf{T}_n + \frac{1}{6}(A + 2B) \right] \tag{5.14}$$

$$\mathbf{T}_{n+1} = \mathbf{T}_n + \frac{1}{6}(A + 4B + C) \tag{5.15}$$

In Equation 5.14 and Equation 5.15 Δt stands for the incremental change in t, which can also be seen as the extrapolation distance for the scheme. The ray tracing scheme does not depend on the actual value of t, hence only Δt is used. By decreasing Δt, the accuracy of the ray tracing scheme is improved, however, this will also increase the computational cost. The matrices A, B, and C of the Runge-Kutta scheme are defined in Equation 5.16, Equation 5.17, and Equation 5.18 respectively.

$$A = \Delta t \mathbf{D} \left(\mathbf{R}_n \right) \tag{5.16}$$

$$B = \Delta t \mathbf{D} \left(\mathbf{R}_n + \frac{\Delta t}{2} \mathbf{T}_n + \frac{\Delta t}{8} A \right) \tag{5.17}$$

$$C = \Delta t \mathbf{D} \left(\mathbf{R}_n + \Delta t \mathbf{T}_n + \frac{\Delta t}{2} B \right) \tag{5.18}$$

It should be noted that the ray tracing for this project is performed in two dimensions whereas the ray tracing scheme by Sharma et al. is presented for three dimensions. This is to illustrate that the same ray tracing scheme can also be applied to 3D flow fields. For this work, the z-dimension will be ignored in order to perform the ray tracing in 2D, i.e. $\mathbf{R} = (x, y)^T$, $\mathbf{T} = (T_x, T_y)^T$, etc.

After each ray trace iteration the distance traveled by the ray is determined and added to the distance already traveled by that light ray using Equation 5.6. During each iteration, checks are performed to determine whether a light ray has reached the airfoil surface. If the y-component of $\mathbf{R}_{n+1}$ is smaller than zero and the y-component of $\mathbf{R}_n$ is larger than zero, the location on the optical path of the light ray where $y = 0$ is calculated by finding the intersection between the straight line connecting $\mathbf{R}_{n+1}$ and $\mathbf{R}_n$ and the line $y = 0$. If one of the locations for the intermediate Runge-Kutta steps (the terms between the brackets in Equation 5.16 to Equation 5.18) has a y-component that is smaller than zero, the location on the optical path of the light ray where $y = 0$ is determined by finding the intersection between $\mathbf{T}_n$ that passes through $\mathbf{R}_n$ and the line $y = 0$. The locations of the intersections of the light rays and the line $y = 0$, representing the airfoil surface, are stored in the vector $\mathbf{X}_w$. The angle that the light ray has when it crosses the line $y = 0$ is also calculated and stored as θ_s. The values for θ_s are calculated with Equation 5.19 where $\mathbf{T}_n$ is used if one of the intermediate Runge-Kutta steps has a y-component that is smaller than zero. If $R_{y,n+1} < 0$, a different value for $\mathbf{T}$ is used so that $\mathbf{T}$ corresponds to the straight line between $\mathbf{R}_{n+1}$ and $\mathbf{R}_n$, i.e. $\mathbf{T} = \mathbf{R}_{n+1} - \mathbf{R}_n$. When all rays have reached the $y = 0$ line, the ray tracing procedure has been completed.

$$\theta_s = \arctan\left(\mathbf{T}_x / - \mathbf{T}_y\right) \tag{5.19}$$

The assumption that the airfoil upper surface is equal to the line $y = 0$ for the ray tracing is justified by the following reasoning: First, the airfoils used for the flow field calculations have to be rather thin to comply with the flow solver assumptions. The thickest airfoil that will be used for this project is a 10% thick super critical airfoil. If a point light source placed at $y/c = 10$, which corresponds to the edge of the computed density field, the error in the traveled distance will be approximately 0.5 % at points of the maximum thickness. This error decreases if the light source is located further away from the airfoil and increases if it is placed closer to the airfoil. For parallel light, this error in distance is not problematic at all since the distance does not influence the irradiance levels. Secondly, the most important issue, when calculating the illumination levels at the airfoil surface, is the spacing between the light rays. For the thickest airfoil used during the calculations, the 10% thick super critical airfoil, the upper surface angles are never larger than 10° with the exception of the nose. If a simple trigonometric example is applied to this problem of ignoring the surface curvature, the following error can be calculated: If a 10° surface angle was added to a horizontal distance, the total distance of the hypotenuse would be 1.0154 times the horizontal distance. Hence the distance between two light rays will not differ more than 1.54% due to the ignored curvature of the airfoil. It should be noted that this example oversimplifies the problem since a straight surface under an angle is used instead of a curved surface. However, if a curved surface with a maximum curvature 10° is used, the straight line representing this curved surface will always have a smaller angle with the horizon. Hence, this simple example should give a good approximation of the approximate maximum error. It should be noted that the nose, which makes up the highly curved first 5% of the airfoil, is not a part of the airfoil where the transonic shock waves occur. Hence it is not an area of interest, and the larger errors in this area are therefore not crucial to the precision of this project. Furthermore, if a camera position were to be taken into account, light rays reflecting off the nose of the airfoil might not even reach the camera due to the high curvature of the nose. This also is not problematic as the nose of the airfoil is not an area of interest for the ray tracing in the project.

Shock waves are usually seen as irreversible discontinuities where flow properties change instantly when a fluid crosses the shock wave. However, it is impossible to have discontinuities in fluid properties, thus the normal shock is nearly discontinuous, meaning it has a finite thickness [82]. Shock waves in air have been measured to have a thickness of approximately 200 nm, which is roughly 4 times the mean free path of gas molecules [83]. It can be noted that this thickness is approximately 0.25λ to 0.5λ for visible light. Hence, according to subsection 2.1.2, a shock wave acts much like a discontinuity. This means that the law of refraction can be used to determine how the light is refracted when crossing a shock wave. This was also confirmed by Thess and Orszag, and Schopf et al. who stated that the law of refraction is needed when discontinuities in the index of refraction are present [18, 19]. Fox stated that several millions of g's are reached when the fluid is decelerated across the small thickness of a shock wave, and Delery and Marvin stated that "shock waves are viscous phenomena but on a microscopic scale in most usual situations" [28, 82]. Hence, shock waves can be treated as perfect discontinuities when performing flow calculations on a larger than microscopic scale. However, the chosen flow solver and the available computational power did not allow the use of a grid with an accuracy of 200nm or anywhere close to this scale. As a result, the shock could not be modeled as the very thin discontinuity that it actually is, hence the jump in flow properties is spread out over a larger area. Therefore, the choice was made to calculate the light deflection across the shock wave as gradually bending instead of using the law of reflection. It should be noted that the ray tracing scheme does allow for the use of the law of reflection if an accurate enough flow solution is available [80, 81].

5.1.3 Light Intensity at Surface

After the ray tracing scheme has been used to trace the light rays to the airfoil surface, the light intensity at the surface can be calculated. The positions where light rays strike the surface $\mathbf{X}_w$, the distance that light rays have traveled r, and the angles between the wing surface normal and the light rays θ_s will be used to determine the light intensity at the surface.

For parallel light, all light rays are evenly spaced and they represent square light beams with a cross-sectional area of $(1/n_r)^2$. It is assumed that the parallel light has uniform irradiance at the starting positions, hence all light rays have the same irradiance value at the start. For the point light source, each light ray represents a light beam with constant angles, i.e. a cone. Therefore, radiant intensity is used to represent the energy corresponding to a light ray. The irradiance corresponding to each light ray is determined later when the cross-sectional area of the light beams corresponding to the light rays can be computed. This can be done when the distance traveled by the ray is known, as the light beam corresponding to a light ray coming from a point source diverges. It is assumed that the radiant intensity is equal for all rays when leaving the light source, i.e. the light source radiates light evenly in all directions. Since constant angles are used for each light ray, a light beam has a square cross-sectional area. It should be noted that the cross-sectional areas are only squares if the surface on which the light beam falls is perpendicular to the light ray. If the light strikes the surface under an angle, the square form will be stretched. In short, equally spaced light rays representing light beams with equal cross-sections are used for parallel light. For a point light source, light rays with equal constant angles representing light cones are used.

To measure the illumination levels on the airfoil surface, pixels are used. In this manner, the radiant flux on the surface is determined by integrating the irradiance at the surface over the pixel areas. The area of a pixel divided by the average light beam cross-sectional area at the surface is used to determine the average amount of rays per pixel (RpP). This value will be used to determine how many rays are needed to obtain a radiant flux solution that is independent of the amount of light rays. For 2D simulations, i.e. a 1D surface with pixels, half of the projected area of a light beam on the surface is calculated with Equation 5.20 for a point light source and with Equation 5.21 for parallel light. It should be noted that this area is one-dimensional, so calling it the length or width of the light beam is more technically correct for the 2D simulation. Half the area, instead of the entire area, is calculated because this area is used determine the standard deviation for a Gaussian function later on.

$$A_r = \frac{r \tan(d\theta_{ray}/2)}{\cos(\theta_s)} \tag{5.20}$$

$$A_r = \frac{1}{2N_r \cos(\theta_s)} \tag{5.21}$$

The light distribution of one light beam corresponding to a light ray is represented by either a Gaussian function or a block created by step functions. Both are centered around the position where the light ray strikes the surface. Examples of a block, constructed with step functions, and a Gaussian distribution are shown in Figure 5.4. The 1D half area of the beam is either used to determine the width of a block created by step functions or the standard deviation for a Gaussian function, depending on which function is chosen to represent the light distribution per light ray. The standard distribution for the Gaussian function is defined in Equation 5.22, where w_g is a parameter that alters the width of the standard deviation of the Gaussian function.

$$\sigma = w_g A_r \tag{5.22}$$

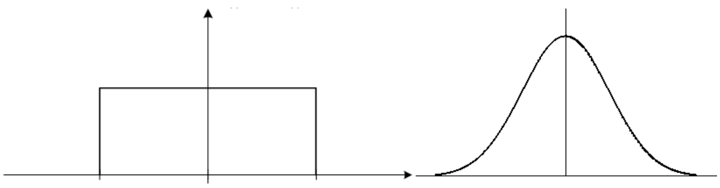

Figure 5.4: Block constructed with two step-functions (left) and a Gaussian distribution (right)

When a light distribution function is chosen to represent the light beam of each ray, these functions have to be integrated over the pixel areas in order to determine the radiant flux per pixel. Appendix B explains how the mean pixel intensity is determined, using 2D pixels and a 2D Gaussian distribution as an example. The information from Appendix B can be used to determine the radiant flux per pixel as the procedure is very similar to the one used to determine the mean pixel intensity. For the 2D simulation, the radiant intensity 'I_e' coming from the light source has to be translated to the irradiance 'E_e' at the surface where the pixel integration takes place. By integrating the irradiance over the pixel area, the radiant flux 'Φ_e' measured by each pixel is determined. The relation between the radiant intensity, irradiance, and the radiant flux is defined in Equation 5.23. The r^2 term represents the decrease in light intensity as a results of the light beam spreading out in the two directions perpendicular to the light propagation direction. This is a 3D effect that should also be modeled for 2D simulations in order to represent light correctly. It should be noted that the r^2 term is omitted for the parallel light cases as the variations in r^2 caused by the light refraction through the shock wave are negligible for this type of light, as discussed earlier.

$$\Phi_e = \int E_e dx = \int \frac{I_e cos(\theta_s)}{r^2} dx \tag{5.23}$$

When a Gaussian function is used to represent the light distribution per light ray, Equation 5.24 is used to calculate the irradiance on the pixel surface caused by one light ray. For parallel light, $a = 1$, as the differences in r do not alter the irradiance. For a point light source, the r^2 term is needed but only one r term is visible in Equation 5.24 as σ accounts for the other r term. So in this case, $I_e/a\sigma \propto I_e/r^2$. In this equation x_w represents the x-location where a light ray strikes the pixel surface. Hence x_w is one value from $\mathbf{X}_w$ corresponding to one light ray. It should be noted that the $\cos(\theta_s)$ term present in Equation 5.23 is accounted for by σ in Equation 5.24. Equation 5.24 can be integrated over the pixel area using the theory presented in Appendix B. This results in Equation 5.25 which represents the radiant flux measured by a pixel. This equation uses the error function for the integration of the Gaussian function. In this equation x_p represents the location of the pixel center of one pixel, hence it is one value from $\mathbf{X}_p$. The width of a pixel is depicted by dx_p, which is a constant as all pixels are equally sized.

$$E_e(x) = \frac{I_e}{a\sigma\sqrt{2\pi}} \cdot e^{-\frac{(x-x_w)^2}{2\sigma^2}}, \qquad a = \begin{cases} r & \text{point light source} \\ 1 & \text{parallel light} \end{cases} \tag{5.24}$$

$$\begin{aligned}
\Phi_p(x_p) &= \int_{x_p-dx_p/2}^{x_p+dx_p/2} \frac{I_e}{a\sigma\sqrt{2\pi}} \cdot e^{-\frac{(x-x_w)^2}{2\sigma^2}} dx, \qquad a = \begin{cases} r & \text{point light source} \\ 1 & \text{parallel light} \end{cases} \\
&= \frac{I_e}{a\sigma\sqrt{2\pi}} \cdot \frac{\sigma\sqrt{2\pi}}{2} \cdot \left[erf\left(\frac{x_p + dx_p/2 - x_w}{\sigma\sqrt{2}} \right) - erf\left(\frac{x_p - dx_p/2 - x_w}{\sigma\sqrt{2}} \right) \right] \\
&= \frac{I_e}{2a} \cdot \left[erf\left(\frac{x_p + dx_p/2 - x_w}{\sigma\sqrt{2}} \right) - erf\left(\frac{x_p - dx_p/2 - x_w}{\sigma\sqrt{2}} \right) \right]
\end{aligned} \tag{5.25}$$

When a block is used to represent the light distribution per light ray, unit step functions are used to create this block, as shown by Equation 5.26. The unit step function, also known as the Heaviside step function 'H', creates a unit jump at $x = x_w - A_r$ and a unit jump down at $x = x_w + A_r$, hence creating the block. The integral of the unit step function is the unit ramp function R. The ramp function is used to calculate the radiant flux measured by the pixel, as shown by Equation 5.27. Just as with the Gaussian distribution, the r^2 term is needed for the point light source and can be omitted for the parallel light source.

$$\text{block} = H(x - x_w + A_r) - H(x - x_w - A_r) \tag{5.26}$$

$$\begin{aligned}
\Phi_p(x_p) &= \int_{x_p-dx_p/2}^{x_p+dx_p/2} E_e \cdot [H(x - x_w + A_r) - H(x - x_w - A_r)]\, dx \\
&= \int_{x_p-dx_p/2}^{x_p+dx_p/2} \frac{I_e cos(\theta_s)}{a} \cdot [H(x - x_w + A_r) - H(x - x_w - A_r)]\, dx \\
&= \frac{I_e cos(\theta_s)}{a} \cdot [R\left(x_p + dx_p/2 - (x_w - A_r)\right) - R\left(x_p + dx_p/2 - (x_w + A_r)\right)] \\
&\quad - \frac{I_e cos(\theta_s)}{a} \cdot [R\left(x_p - dx_p/2 - (x_w - A_r)\right) - R\left(x_p - dx_p/2 - (x_w + A_r)\right)] \\
&\quad \text{where: } a = \begin{cases} r^2 & \text{point light source} \\ 1 & \text{parallel light} \end{cases}
\end{aligned} \tag{5.27}$$

Ideally, the light distribution corresponding to one ray would be integrated over each pixel area. However, it is known that the radiant flux caused by one light ray is limited to a certain area. Therefore, the integration to obtain the radiant flux measured by the pixels, is only performed for the pixels that lie within the area in which the radiant flux contribution of a light ray is non-zero. This is done to reduce the computational cost.

The radiant flux measured by the pixels is normalized with respect to the average radiant flux value of all the pixels. This normalization is performed to enable the comparison of different light distribution functions and to match the radiant flux levels if different ray spacings are used during refinement iterations. Such a refinement iteration would recalculate the illumination level of a certain area by using more light rays for the simulation in order to improve the accuracy of the solution in this area. However, the use of, for example, more closely packed Gaussian functions with smaller standard deviations results in different irradiance and radiant flux values. This would make the results obtained from the refinement very different from the results obtained earlier. By normalizing the results, solutions acquired by using different light distribution functions and RpP values can be directly compared.

5.2 Performance of Light Distribution Functions

In order to determine which light distribution function is most accurate when simulating shadowgraphs, a short comparative study has been performed. The light beams, discussed in the previous section, are used to create a continuous light field from the discrete light rays. This is done to convert the discrete rays to a more physically realistic continuous light distribution. For the shadowgraph simulation, gradients in the illumination levels need to be represented precisely in order to simulate the correct bright and dark regions. However, the use of as little rays as possible is also preferable as this will decrease the computational cost. In order to determine which light distribution function is most suited for this purpose, a comparative study for different illumination scenarios has been performed to determine which light distribution function is most accurate for different ray-to-pixel ratios. Two different illumination scenarios have been used and for each scenario three different variations have been tested.

Test case 1

The first test cases consist of a point light source that shines on a surface that runs from $x = 0$ to $x = 1$, which is identical to the airfoil surface. Figure 5.5 illustrates the test case for version a of test case 1, where the light source is placed at $(0, 5)$. The blue lines represent the light rays that travel from the source to the surface. This image clearly visualizes that the traveled distance is not equal for all light rays, which is exactly what will be modeled for test case 1. It also clearly shows that the distance between the light rays increases with increasing traveled distance. For all the test cases, light is measured using 1000 equally sized pixels that are located on the surface. Hence, the RpP value will be altered by changing the amount of light rays for the simulation.

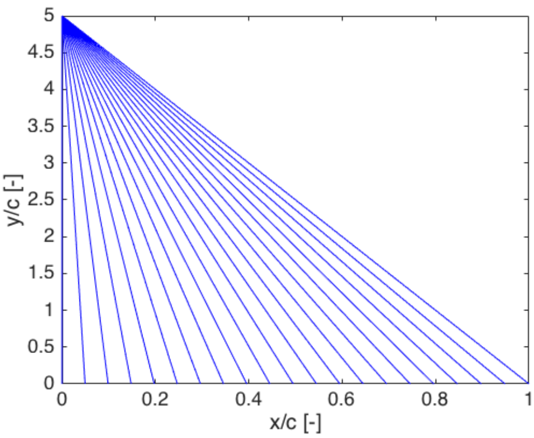

Figure 5.5: Light source, light rays, and pixel surface for test case 1a

The radiant intensity of the light source is constant and set to a value of one. Therefore, Equation 5.28 can be used to represent the irradiance at the surface. The distance from the light source to the surface can be written as $r^2 = y_l^2 + x^2$ and $\cos(\theta_s) = y_l/\sqrt{y_l^2 + x^2}$, where y_l represents the y-component of the light source location. Since $x_l = 0$, this term is omitted in the equations. The radiant flux Φ_e at the surface can be calculated by integrating the radiant intensity using the table of integrals presented by Stewart [84], resulting in Equation 5.29. The analytic reference value for the radiant flux at the surface, measured by each pixel, was determined by integrating the radiant intensity over each pixel using Equation 5.29.

$$E_e = \frac{I_e cos(\theta_s)}{r^2} = \frac{y_l}{\left(y_l^2 + x^2\right)^{3/2}} \tag{5.28}$$

$$\Phi_e = \int_{x_p - dx_p/2}^{x_p + dx_p/2} E_e dx = \int_{x_p - dx_p/2}^{x_p + dx_p/2} \frac{y_l}{\left(y_l^2 + x^2\right)^{3/2}} dx = \left[\frac{x}{y_l \left(y_l^2 + x^2\right)^{1/2}} \right]_{x_p - dx_p/2}^{x_p + dx_p/2} \tag{5.29}$$

Figure 5.6a and Figure 5.6b show the radiant flux at the surface that is determined using Gaussian light distributions for each light ray. It should be noted that the radiant flux is normalized with respect to the radiant flux value of the first pixel, which spans from $x = 0.000$ to $x = 0.001$. It can be seen that the Gaussian distribution with $w_g = 1$ does not yield an accurate representation of the radiant flux for a RpP value of 0.1. Figure 5.6b shows that the accuracy increases for $w_g = 1$ when the RpP is increased to one. However, the fluctuating behaviour is still visible. These fluctuations are a result of the spacing between the Gaussian distributions of each ray. For $w_g = 1$, the Gaussian distributions of each light ray do not overlap sufficiently to form a smooth function together. Both the Gaussian distributions for $w_g = 2$ and $w_g = 3$ represent the radiant flux well as the curves follow the analytical solution and have the same shape.

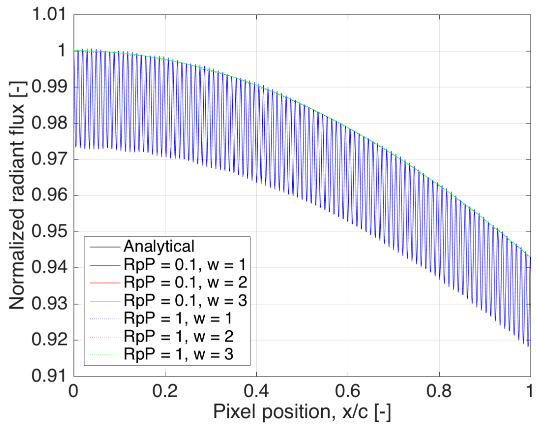

(a) Gaussian distribution, varying RpP and w_g

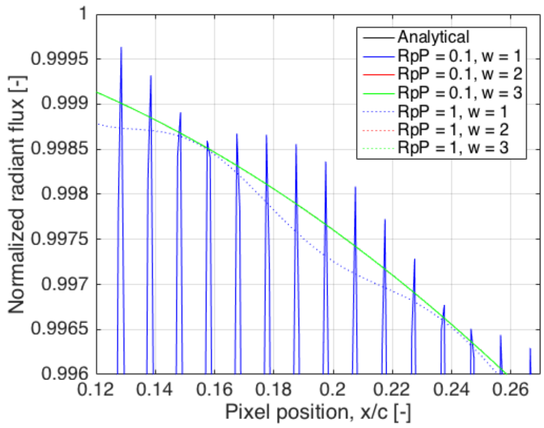

(b) Gaussian distribution, zoom-in

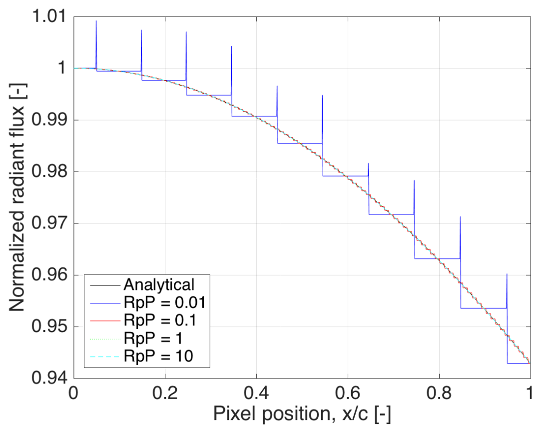

(c) Step function, varying RpP

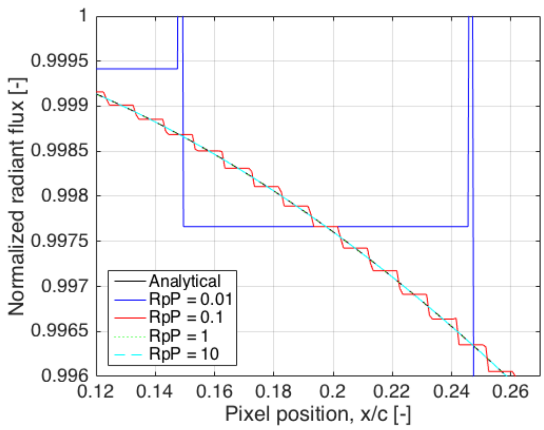

(d) Step function, zoom-in

Figure 5.6: Radiant flux at surface, measured using 1000 equal sized pixels

Figure 5.6c and Figure 5.6d show the radiant flux that is calculated when the step function is used to represent the light distribution for each light ray. For a RpP value of 0.01, the blocks by the step functions can clearly be seen and the spikes indicate that one block has not been terminated before the next one has started, i.e. the functions overlap slightly at their edges. For a RpP value of 0.1, the step function is still visible, but the overlap of step functions is not visible any more, indicating that the distance between two neighbouring step functions is very small. Hence, two neighbouring step functions might overlap or have a small distance between each other, but this gap or overlap is so small that it does not alter the radiant flux value of a pixel significantly. For RpP values of 1 or 10, the curves are not visibly different from the analytical curve. It should be noted that the overlap for low RpP values is a result of the discretization of light by light rays. With few light rays, the area of the light beam corresponding to a light ray is calculated for one position on the surface. Hence this area is correct for point x where the light ray hits the surface, but might be incorrect for point $x + \Delta x$ which is also within the area of the light beam. Hence, for low RpP values, each light ray has to represent light covering a relatively large area, which introduces discretization error. As expected, for higher RpP values, each ray represents a smaller light beam resulting in smaller errors.

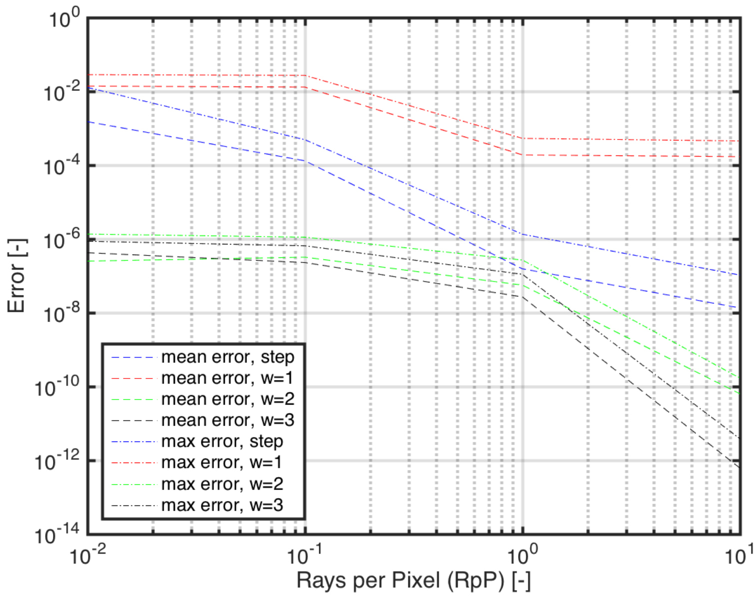

Figure 5.7: Mean and maximum errors for different light distribution functions for test case 1a

$$\epsilon_{rf} = \Phi_{e,ref} - \Phi_e, \qquad \bar{\epsilon}_{rf} = \frac{1}{N}\sum_{i=1}^{N} \Phi_{e,ref,i} - \Phi_{e,i} \tag{5.30}$$

The mean and maximum errors of the different light distribution functions, with respect to the analytical solution are presented in Figure 5.7. The errors are calculated according to Equation 5.30, where the reference is the analytical solution. Equation 5.30 gives the impression that an absolute error is calculated, however, the error is a relative error since all the radiant flux values have been normalized earlier. Figure 5.7 clearly shows that the Gaussian function with $w_g = 1$ has the lowest accuracy for this test. The Gaussian distributions with $w_g = 2$ and $w_g = 3$ have errors of approximately the same order for a RpP value up to 1. For a higher RpP value, the errors corresponding to the Gaussian distribution with $w_g = 3$ decrease more rapidly. Overall, the Gaussian distribution with $w_g = 3$ is most accurate. The errors corresponding to the step function fall in between the errors of the Gaussian function with $w_g = 1$ on one side and the Gaussian functions with $w_g = 2$ and $w_g = 3$ on the other side. It can be seen that the accuracy of the step function rapidly improves when the RpP value is increased from 0.1 to 1. However, this rapid increase in accuracy with increasing RpP values diminishes somewhat when the RpP value is increased above values of 1. Finally, it should be noted that the distance between the mean and maximum error curves is larger for the step function in comparison to the Gaussian functions. This means that the standard deviation of the error corresponding to the step function, measured over the entire surface, is larger in comparison to the Gaussian functions.

For version b of test case 1, the location of the light source has been changed to $(0, 2.5)$, i.e. the light is placed closer to the surface. Equation 5.28 and Equation 5.29 are once again used to determine the irradiance and the radiant flux measured at the surface by the pixels. Figure C.1 in Appendix C shows the results obtained using either the step function or the Gaussian function for the light distribution. The solution corresponding the the Gaussian distribution with $w_g = 1$ fluctuates, which was also noticed in test case 1a. Hence the Gaussian distributions of the different light rays do not overlap sufficiently for this test case either. The Gaussian distributions for both $w_g = 2$ and $w_g = 3$ follow the analytical solution accurately. For RpP values below 1, the step function solution clearly shows steps in the solution again. For RpP values of 1 or higher, the step function follows the analytical solution accurately.

Figure 5.8 shows that there are some slight differences in the errors when compared to test case 1a. The first thing that can be noted is that all the errors have increased slightly in comparison to test case 1a. Secondly, the error of the Gaussian distribution with $w_g = 1$ improves when the RpP is increased from 1 to 10, whereas it remained almost constant for test case 1a. Thirdly, the Gaussian distribution for $w_g = 2$ is significantly more accurate with respect to the $w_g = 3$ case for a RpP value of 0.01. It should be noted that the maximum error for the Gaussian distribution with $w_g = 2$ for a RpP value of 10 is much closer to the mean error when compared to the difference between the mean and maximum error for the Gaussian distribution with $w_g = 3$ for a RpP value of 10. Hence, the mean error of the Gaussian distribution with $w_g = 2$ for a RpP value of 10 might be larger in comparison to the $w_g = 3$ case, but the maximum errors are very similar. Therefore, it can be concluded that for case 1b, which consists of a gradual decrease in radiant flux over the pixel surface, the use of Gaussian light distribution with either $w_g = 2$ or $w_g = 3$ results in the most accurate solution, depending on which RpP value is used.

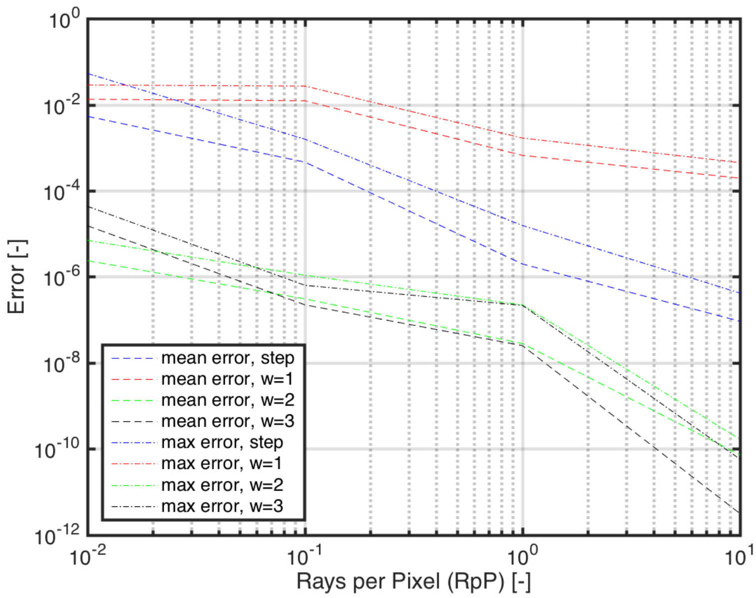

Figure 5.8: Mean and maximum errors for different light distribution functions for test case 1b

For version c of test case 1, the location of the light source has been changed to $(0, 1.0)$, i.e. the light is placed closer to the surface once again. Figure C.2 in Appendix C shows the results obtained using either the step function or the Gaussian function for the light distribution. The decrease in radiant flux over the surface is sharper for this version of test case 1. It can be seen that the angles between the light rays and the surface normal influence the size of the areas of each light beam. The step function clearly shows how the a light beam is smeared out over a larger area as it hits the surface under increasingly larger angles. Furthermore, the results corresponding to the test function show the same behavior as in the test cases 1a and 1b. The Gaussian distribution for $w_g = 1$, however, shows a little change in its behaviour. For a RpP value of 1, the fluctuations in the solution vanish shortly around $x = 0.5$ where the slope of the solution is steepest.

Figure 5.9 shows that the errors for all functions have increased. Most notable is the increase in the error for the Gaussian distributions with $w_g = 2$ and $w_g = 3$ for a RpP value of 0.01 in comparison to the previous test cases. When the RpP value is increased, the accuracy of the Gaussian functions with $w_g = 2$ and $w_g = 3$ rapidly increases. For a RpP value of 0.1, the Gaussian functions with $w_g = 3$ is slightly more accurate than the Gaussian function with $w_g = 2$. However, when the RpP value is further increased the Gaussian function with $w_g = 2$ becomes the most accurate solution. It should also be noted that the maximum error curve corresponding to the Gaussian function with $w_g = 3$ does not follow the mean error curve anymore when the RpP value is increased from 1 to 10. Hence, the use of the Gaussian function with $w_g = 2$ yields the most accurate solution for test case 1c.

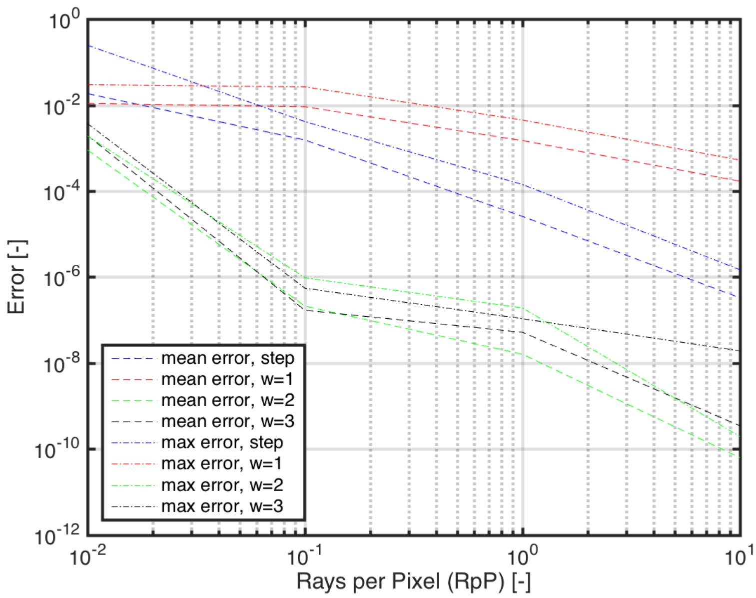

Figure 5.9: Mean and maximum errors for different light distribution functions for test case 1c

The conclusion that can be drawn from test cases 1a, 1b, and 1c is that the Gaussian distributions with either $w_g = 2$ or $w_g = 3$ result in the most accurate solution when the illumination levels slowly and steadily change over the surface. For higher rates of change in illumination levels over the surface, the Gaussian distribution with $w_g = 2$ becomes more accurate than the Gaussian distribution with $w_g = 3$. This indicates that a smaller standard deviation for the Gaussian distribution can follow larger changes in the radiant flux more accurately, however, the lower limit of the standard deviation still depends on the amount of overlap between the Gaussian distributions of the different light rays.

Test case 2

For test case 2, parallel light with non-uniform irradiance distribution was used. The irradiance values of the parallel light were varied along the chord length to determine how well the different light distribution functions can model abrupt changes in illumination for certain RpP values. The modeling of abrupt changes in illumination are important because the dark and bright zones in a shadowgraph usually start with either a strong decrease or increase in illumination. Equation 5.31 specifies the irradiance for each light ray, which varies depending on the starting location of the light ray. It should be noted that $\theta_{ray} = 0$ for this test case. The variables a and b mark the x-locations on the surface where the ramp function, which is used to create the decrease in irradiance, starts and ends. It can be noted that Equation 5.31 can also be written using the ramp function instead of using the step function, as shown by the second form of Equation 5.31. However, the second form is harder to integrate. Hence, the first form will be used to determine the radiant flux. The radiant flux at the surface for this test case can be calculated with Equation 5.32, where the integration boundaries are set to be the edges of the pixels. For test case 2a, $a = 0.1$ and $b = 0.9$.

$$\begin{aligned} E_e &= 1 - H(x_l - b) - \frac{x-a}{b-a} \cdot [H(x_l - a) - H(x_l - b)] \\ &= 1 - \frac{1}{b-a} \cdot [R(x_l - a) - R(x_l - b)] \end{aligned} \tag{5.31}$$

$$\begin{aligned} \Phi_e = \int_{x_p - dx_p/2}^{x_p + dx_p/2} E_e dx &= \int_{x_p - dx_p/2}^{x_p + dx_p/2} 1 - H(x_l - b) - \frac{x-a}{b-a} \cdot (H(x_l - a) - H(x_l - b))\, dx \\ = \left[\{1 - H(x_l - b)\} \cdot x - \frac{(x-a)^2}{2(b-a)} \cdot \{H(x_l - a) - H(x_l - b)\} \right]_{x_p - dx_p/2}^{x_p + dx_p/2} \end{aligned} \tag{5.32}$$

Figure 5.10a and Figure 5.10b show the results using the different Gaussian distributions. It can be seen that for a RpP value of 0.1, the $w_g = 1$ case shows the fluctuating behaviour, just as in the previous test cases. Furthermore, it can be seen that the Gaussian distributions have trouble to correctly model the kink in the radiant flux curve. It can be seen that higher values of w_g result in bigger errors in modeling the kink. It was also noted that the fluctuating behaviour of the Gaussian distribution with $w_g = 1$ was not present for this test case when the RpP value was equal to one. Figure 5.10c and Figure 5.10d show the results obtained using the step function. The same general step behaviour for low RpP values, as seen in the previous test cases, is visible for this test case as well. For a RpP value 1 or higher, the step function is capable of following the kinks in the radiant intensity curve precisely.

Figure 5.11 shows both the mean and maximum errors of the different light distribution functions, measured over the entire pixel domain. It can be seen that the mean errors are of approximately the same order of magnitude for a RpP value of 0.01. The mean errors corresponding to the Gaussian distributions with $w_g = 2$ and $w_g = 3$ decrease at a constant rate for increasing RpP. The average absolute errors corresponding to the Gaussian distribution with $w_g = 1$ and the step function hardly seem to decrease when the RpP value is increased from 0.01 to 0.1. However, the errors decrease drastically when the RpP value is increased from 0.1 to 1. For the RpP increase from 1 to 10, the step functions error increases slightly whereas the Gaussian distribution with $w_g = 1$ error keeps decreasing. It can also be seen in Figure 5.11 that the maximum errors are always larger than the average absolute errors, but that the difference between the average and the maximum error is significantly larger for the Gaussian distributions than for the step function. This is mostly likely caused by the inaccuracy of the Gaussian distributions near the kinks in the radiant flux curve.

In order to examine the accuracy of the different functions near the kinks in the radiant flux curve, from now on addressed as the left and right kink, the maximum and mean errors in the region near the kinks were determined. Figure 5.12a shows the errors in the regions near the left and right kinks. The regions near the kinks are defined as $x = a \pm 0.025$ and $x = b \pm 0.025$. It can be seen that the errors of all functions are comparable for RpP values of 0.1 or lower. However, for RpP values of one and up, the step function is by far the most accurate. Furthermore, it can be seen that the Gaussian distribution is more accurate when w_g is smaller for RpP values of one or higher. Figure 5.12b shows the errors in the region between the kinks, hence the region of the constantly decreasing radiant flux. It can be seen that for a very low RpP value or a higher RpP value, 0.01 and 10 respectively, all the functions

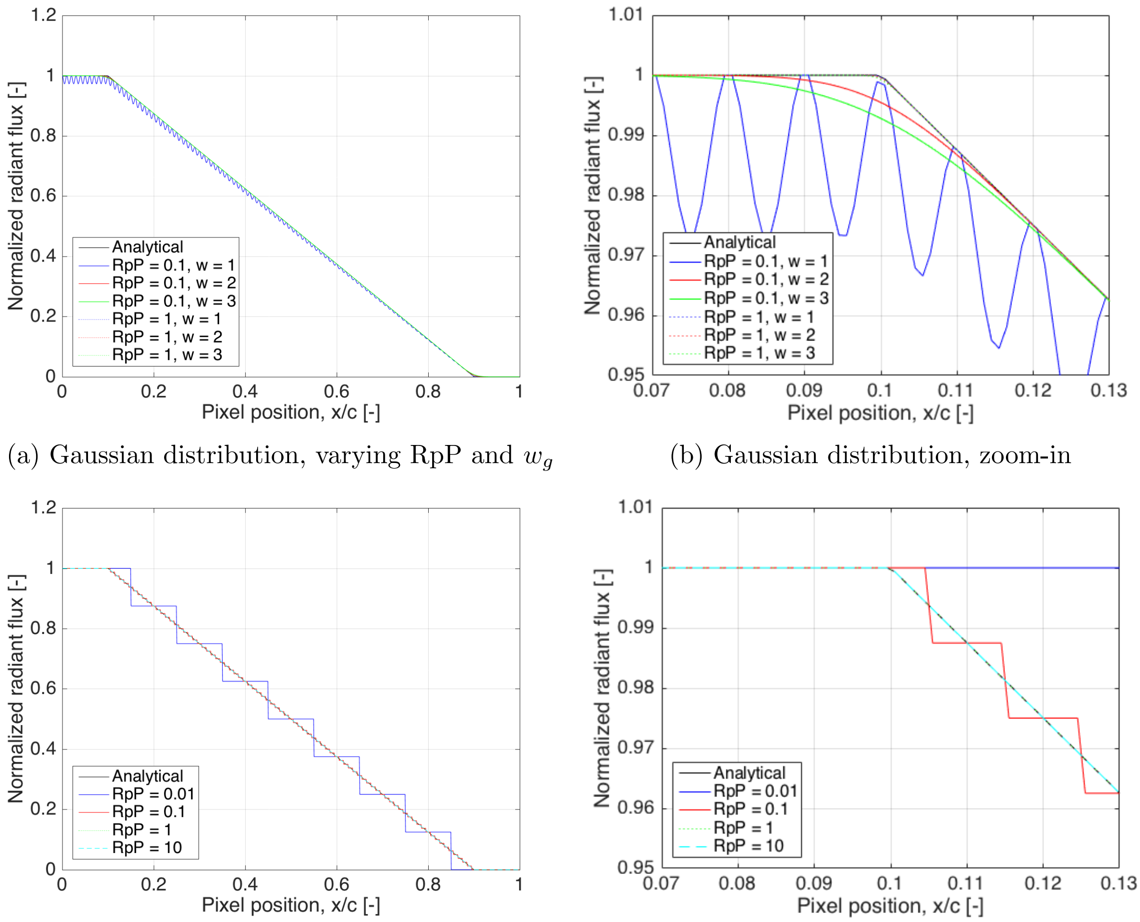

(a) Gaussian distribution, varying RpP and w_g

(b) Gaussian distribution, zoom-in

(c) Step function, varying RpP

(d) Step function, zoom-in

Figure 5.10: Radiant flux at surface, measured using 1000 equal sized pixels

have approximately the same error. As noticed before, the step function and the Gaussian distribution with $w_g = 1$ hardly become more accurate when increasing the RpP value from 0.01 to 0.1. However, the Gaussian distribution with $w_g = 2$ and $w_g = 3$ do improve for this increase in RpP. When the RpP is further increased to a value of 1, the errors of both the step function and the Gaussian distribution with $w_g = 1$ decrease dramatically, making them the most accurate functions. In short, it can be concluded that the step function is the most suited function to model sudden changes in the radiant flux curve, as both the kinks and the steep constant slope are more accurately modeled by the step function for RpP values of one and higher.

For version b of test case 2, $a = 0.3$ and $b = 0.7$, hence increasing the change in irradiance and radiant flux. Since only a and b are changed, Equation 5.31 and Equation 5.32 are still used to calculate the irradiance and the radiant flux for the analytical solution. Figure C.3 and Figure C.4 in Appendix C show the solutions obtained with the different light distribution functions per light ray and the mean and maximum errors calculated over the entire pixel domain. Both the obtained radiant flux curves and the errors for case 2b are very similar to case 2a. Figure 5.13 shows the errors in the regions near the kinks and the errors in the region of the decreasing radiant flux slope. It can be noted that these errors are also very similar to the errors found in test case 2a. Hence, the same conclusion regarding the accuracy of the different light distribution functions can be drawn as in test case 2a.

Test case 2c is identical to both test case 2a and 2b, but $a = 0.4$ and $b = 0.6$ in this case, hence increasing the change in irradiance and radiant flux even more. Figure C.5 and Figure C.6

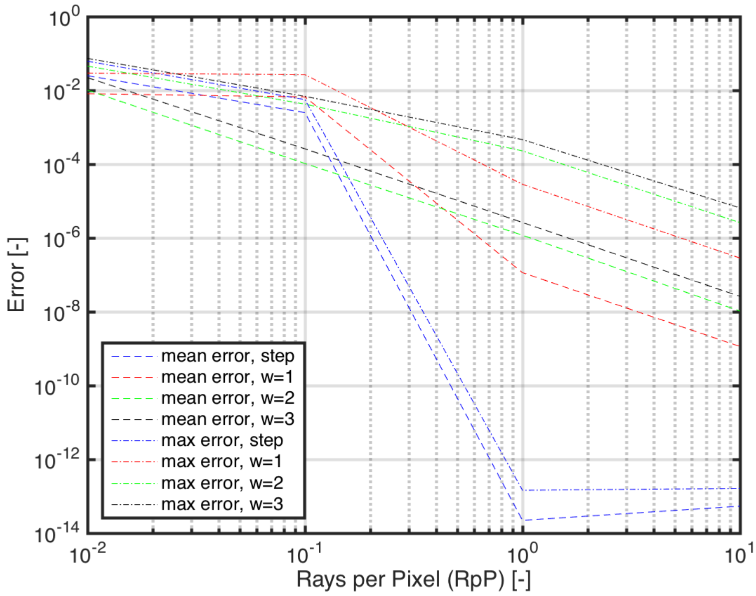

Figure 5.11: Mean and maximum errors for different light distribution functions for test case 2a

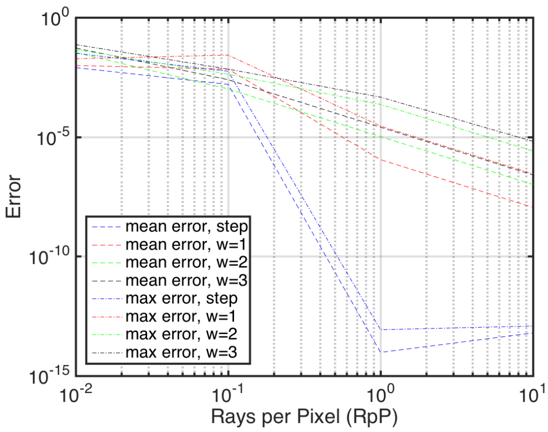

(a) Region around kinks

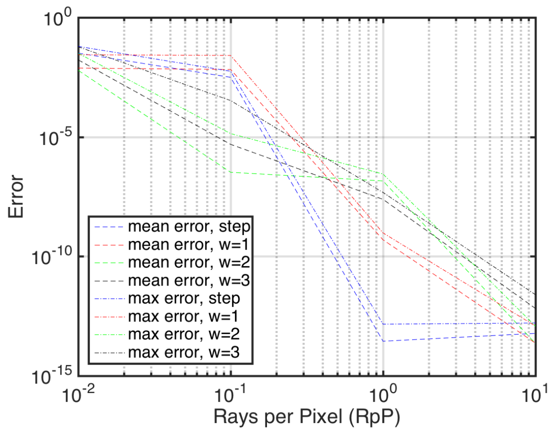

(b) Region of the slope

Figure 5.12: Mean and maximum errors in specific regions for test case 2a

in Appendix C show the solutions obtained with the different light distribution functions per light ray and the mean and maximum errors calculated over the entire pixel domain. Both the obtained radiant flux curves and the errors for case 2c are very similar to case 2a. Figure 5.14 shows the errors in the regions near the kinks and the errors in the region of the decreasing radiant flux slope. It can be noted that these errors are also very similar to the errors found in test case 2a. Hence, once again, the same conclusion regarding the accuracy of the different light distribution functions can be drawn as in test case 2a.

It can be concluded from test cases 2a, 2b, and 2c that the Gaussian distributions are not very accurate when a sudden change in the radiant flux occurs. For RpP values below 1, the step function is not much more accurate, but for RpP values equal to or above one, the step function accurately models these sudden changes in radiant flux. The constant slope of decreasing radiant flux is also best modeled using the step function with a RpP value of one.

From the performed test cases it can be concluded that a light distribution with sudden

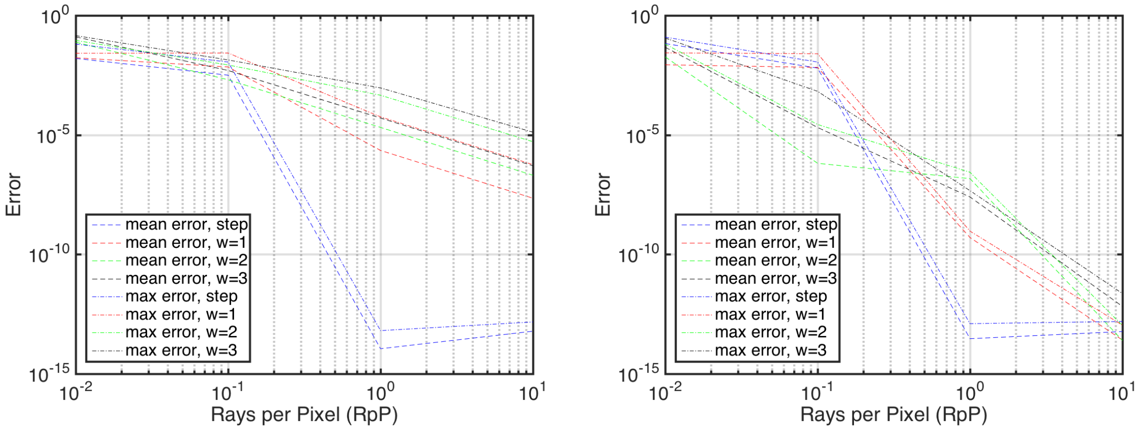

(a) Region around kinks

(b) Region of the slope

Figure 5.13: Mean and maximum errors in specific regions for test case 2b

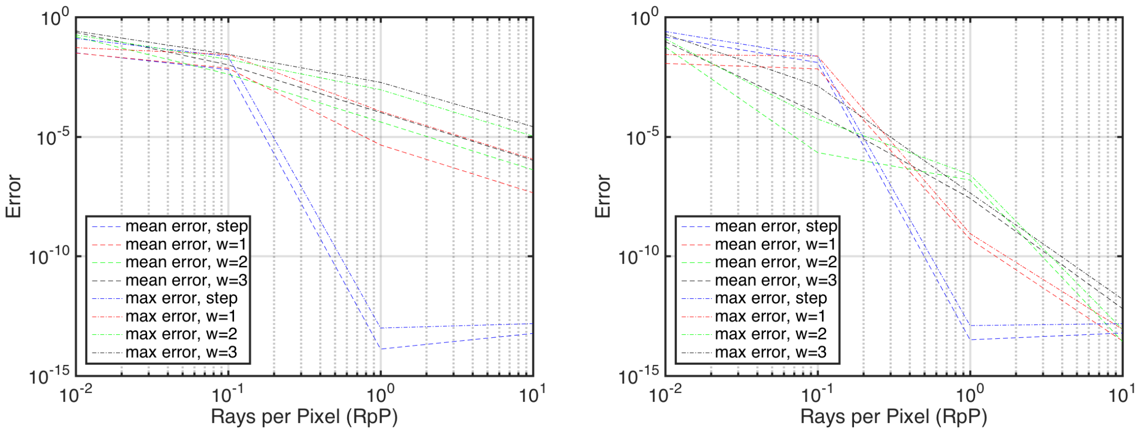

(a) Region around kinks

(b) Region of the slope

Figure 5.14: Mean and maximum errors in specific regions for test case 2c

changes in illumination levels can best be modeled with the step function. Functions with a continuous derivative are best modeled with the Gaussian distribution. A value of $w_g = 2$ for the Gaussian distribution will yield the best results as it is highly accurate for low RpP values and able to model radiant flux curves with steeper slopes in comparison to the Gaussian distribution with $w_g = 3$.

When local refinements are used to simulate the shadowgraphs, the best results would most likely be obtained by performing the first iteration or iterations, where the RpP value is low, with a Gaussian distribution with $w_g = 2$. When the regions with large changes in the radiant flux are refined, the step function should be used to model steep slopes and discontinuous derivatives.

5.3 Iterative and Adaptive Shadowgraph Simulation

In order to reduce the computational cost of the ray tracing scheme, an iterative and adaptive method is used. While using this method, less light rays have to be modeled to calculate the illumination levels measured on the surface. Not only does this method reduce the required computational time for the ray tracing procedure, it also allows the use of different light distribution functions to improve the accuracy of the scheme.

This method repeats the ray tracing procedure locally with higher RpP values depending on the radiant flux solution of the previous ray tracing procedure. For the first iteration, the procedure described in section 5.1 is used to calculate the radiant flux at the surface. This radiant flux solution is then analyzed to determine if an increase in the RpP value could locally improve the solution. If the solution is almost constant or changing at a constant rate (point light source), the use of more light rays will not result in an improved solution. However, if the radiant flux solution changes rapidly, forming either a shadow or a bright spot, the solution could locally be improved by using a higher RpP value. By analyzing the value, the first derivative, and the second derivative of the radiant flux solution, it is determined where the solution would benefit from an increase in light rays for the shadowgraph simulation. A second ray tracing iteration is then performed solely for these areas where the solution would benefit from an increased RpP value. The newly obtained local radiant flux solution is compared to the old solution to determine whether the refinement has resulted in an improved solution. If the solution has not changed significantly, increasing the RpP value is not deemed useful as it will not improve the accuracy. However, if the solution has changed significantly, another iteration with more light rays might improve the solution even more. Hence, iterations with increasing RpP values are performed locally until the radiant flux solution converges. Figure 5.15 illustrates how the iterative scheme is used in combination with the ray tracing procedure.

Since the radiant flux solution is known at the pixel locations, the areas that are marked for improvement are defined in terms of pixel locations. If it is known which pixels fall within the refinement area, it is determined which light rays fall on these pixels. Depending on the type of light source, the minimum and maximum light angles or starting positions of the light rays are determined. These new values for θ_{min}, θ_{max}, $\mathbf{R}_{x,min}$, and $\mathbf{R}_{x,max}$ are used to create the light rays for the next iteration using Equation 5.4 and Equation 5.5. The ray density or RpP value are increased tenfold for each new iteration. Hence, $d\theta_{ray} = 0.1 d\theta_{ray,old}$ and $n_r = 10 n_{r,old}$. Even though n_r is multiplied by ten, it does not mean ten times more light rays are used in total. It only means that the light ray density has increased tenfold for the region that will be refined. It should be noted that the transition areas on both sides of the refinement area are refined as well. This is done to ensure that the old and new solution still fit together.

For the first iteration, a RpP value of 0.1 is used. Therefore, the Gaussian distribution with $w_g = 2$ is used when calculating the radiant flux, as it was determined in section 5.2 that this light distribution function yields the most accurate results for this RpP value. For the second iteration, where the RpP value is set to one, the Gaussian distribution with $w_g = 2$ is used again. The Gaussian function with $w_g = 2$ is chosen over the step function for this iteration to most accurately improve the areas where only modest changes in radiant flux occur. The steep slopes in the radiant flux solution are solved in the third iteration where a RpP value of 10 is used and the step function is used for the light distribution per light ray. It was found that the solution does not change significantly between the second and third iteration for the shadowgraph simulation, hence three iterations are used for this scheme. This implies that there are no very sharp kinks followed by a long steady increase or decrease in the radiant flux solution.

In short, to obtain the most accurate and computationally least demanding radiant flux solution, the following procedure is used: First, the radiant flux at the entire surface is determined by tracing light rays, with a RpP value of 0.1, that strike the entire surface. Secondly, the radiant flux solution is analyzed to determine which areas have rapidly changing radiant flux values. Thirdly, the radiant flux for these areas is calculated once again. However, this time a RpP value of one is used and only the light rays that strike the areas marked for improvement are traced. For these first two iterations, the Gaussian distribution with $w_g = 2$ is used to model the light distribution per light ray. When the radiant flux solution has changed sufficiently between the two most recent iterations, another iteration is performed. This time a RpP value of 10 is used to trace light rays striking the areas where the solution between the previous two iterations

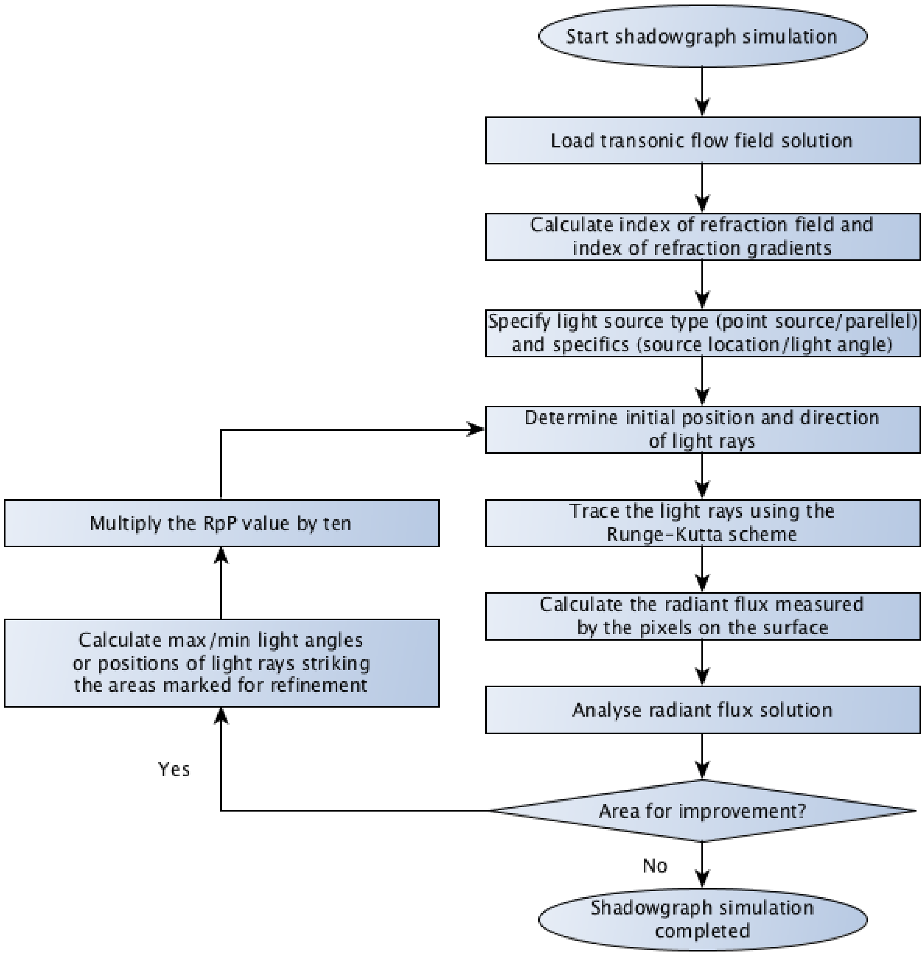

Figure 5.15: Flow chart of the iterative shadowgraph simulation scheme

has changed significantly. This time, the radiant flux is determined using the step function to represent the light distribution per light ray. Using this scheme, high amounts of light rays are only used locally where an increase in the RpP value actually results in an improved radiant flux solution, hence decreasing the computational time of the shadowgraph simulation.

6. Shock-Shadowgraph Relation

Before the simulated shadowgraphs will be discussed, the airfoils used for the flow field computations will be presented. The 6 % parabolic arc airfoil and the SC(2)-0410 super critical airfoil and the flow fields corresponding to these airfoils are presented first. A convergence problem that occurred during the flow field calculation is discussed as well.Secondly, the simulated shadowgraphs will be presented and discussed. Thirdly, several shadowgraph characteristics are analyzed and the relation found between the shadowgraph characteristics and the shock waves is presented. Fourthly, the ray deflection estimation for the boundary layer, using the Bohning-Zierep flow model, is discussed. This discussion explains which errors are introduced when the boundary layer is not accounted for during the ray tracing of the light rays to the wing surface. Finally, the possible implementation of the observed relation between the shadowgraph characteristics and the shock wave is discussed. This discussion also focuses on the limitations of this technique and will describe why this technique will or will not be suited for certain applications.

6.1 Airfoils and Flow Fields

In section 4.2, flow fields over symmetric parabolic arc airfoils were presented. Flows over these airfoils were calculated to compare the results with values from literature in order to validate the flow solver. However, these symmetric parabolic arc airfoils are not commonly used on commercial aircraft that fly at transonic speeds. Instead, super critical airfoil profiles are most commonly used. Therefore, a super critical airfoil profile has been used in addition to the parabolic arc airfoil profile to generate flow fields using the flow solver presented in section 4.2. The calculated transonic flow fields including shock waves have been used for the shadowgraph simulation.

For this study, the 6 % thick parabolic arc airfoil, which was also used in section 4.2, and the SC(2)-0410 airfoil were chosen. The upper surface of the 6 % thick parabolic arc airfoil is described by $y = 4\delta(x - x^2)$ (airfoil runs from $x = 0$ to $x = 1$). The SC(2)-0410 airfoil is a phase 2 super critical airfoil with a thickness ratio of 10 % and a design lift coefficient of 0.4. This airfoil is most commonly used on business jets according to Harris [35]. The SC(2)-0610 airfoil, which has a design lift coefficient of 0.6 is more common for transport and passenger aircraft. This airfoil is however less suited for the transonic flow solver used in this study, because the upper surface of the trailing edge of this airfoil has a negative y/c value. Since the flow solver assumes that the airfoils are symmetric, a negative y/c value on the upper surface would correspond to a symmetric airfoil that has zero thickness at one point that is not the leading or trailing edge of the airfoil. The SC(2)-0410 does not have negative y/c values for the upper surface and the upper surface is nearly identical to the SC(2)-0610 upper surface. Hence, the upper surface of this airfoil will serve as a good approximation of the upper surface of super critical airfoils used in modern commercial aviation. It should be kept in mind that the flow solver does not account for the lower surface of the airfoil, hence circulation effects are not taken into account. The calculated flow fields will therefore not represent the real flow exactly. However, they will still give a good representation of the shock formations over the upper surface of a super critical airfoil. The profile of the upper surface of the SC(2)-0410 airfoil is presented in Figure 6.1. The fitted curve is determined by the matlab function 'fit', using a piecewise cubic interpolation.

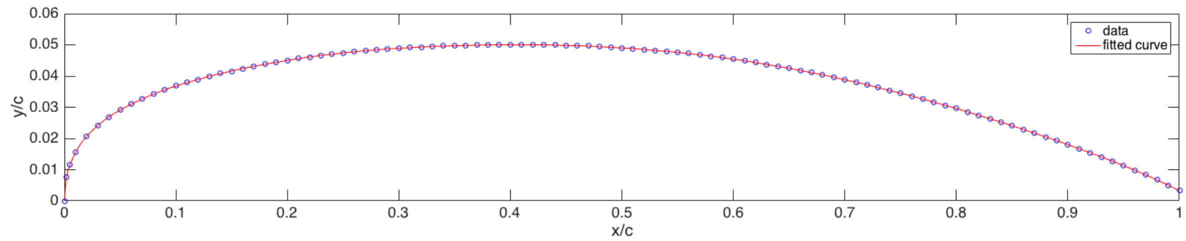

Figure 6.1: SC(2)-0410 upper surface profile. Data points and fitted curve [35]

The derivative of the upper surface profile of the SC(2)-0410 airfoil, which is used as a boundary condition for the transonic small disturbance potential flow solver, is presented in Figure 6.2. The data points in these figures represent the derivative of the airfoil upper surface, i.e. dy/dx. This derivative was calculated with a central scheme which used the locate data points presented in Figure 6.1. The fitted curve was determined with the matlab function 'fit', using a smoothing spline. The smoothing spline curve fit was chosen as it best followed the data points in the region where the derivative decreases in a step wise manner, as shown in the zoomed image of Figure 6.2. When using a piecewise cubic interpolation, the steps in the derivative resulted in an unrealistically wavy derivative curve. It can be seen that the first two data points, at the leading edge, are not used to calculate the fitting curve. These points are omitted for two reasons. First, the fitted curve ended up having unnatural kinks in the region of the leading edge when the first two points were taken into account. Secondly, the high value of the derivative at the leading edge caused an error to occur when it was used as a boundary condition for the transonic flow solver. This high value resulted in negative velocities at the leading edge stagnation point. By not taking the first two data points into account for the fitted curve, both the unnatural kinks in the fitted curve and the negative velocities at the stagnation point were resolved. In this case, a stagnation point with velocities close to zero was formed, which is physically realistic. These negative velocities that occurred earlier were most likely caused by a violation of the small disturbance assumption by having a very high derivative.

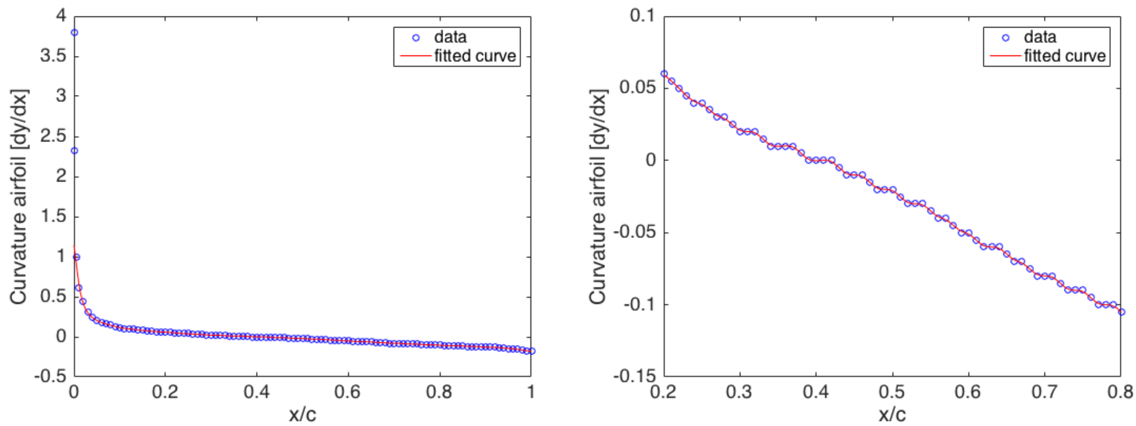

Figure 6.2: SC(2)-0410 upper surface profile curvature. Data points and fitted curve [35]

The calculated transonic flow fields with shock waves, for the SC(2)-0410 airfoil and the parabolic arc airfoil for various Mach numbers are presented in Appendix D and Appendix E respectively. The flow fields were calculated for a cruise altitude of 10 kilometers. All the flow fields corresponding to the parabolic arc airfoil have been calculated on a grid that has 501 equally spaced mesh point over the airfoil in the chordwise direction. Further away from the airfoil, the mesh has been stretched to decrease the computational cost, as was also done by Murman and Cole [30]. This grid was also used for the flow fields corresponding to the

SC(2)-0410 airfoil with free stream Mach numbers up to $M_\infty = 0.86$. However, for $M_\infty \geq 0.87$, convergence problems occurred when the fine grid was used. This was resolved when a grid with 201 equally spaced mesh points over the airfoil in the chordwise direction was used for the SC(2)-0410 airfoil and $M_\infty \geq 0.87$. From now on, the grid with 501 points in the chordwise direction over the airfoil surface will be referred to as the fine mesh and the grid with 201 points over the airfoil will be referred to as the coarser mesh. It should be noted that the flow fields were calculated in sequence, starting with a low free stream Mach number, and using the previous solution as the starting point for the new computation with a higher free stream Mach number. Thus following the procedure used by Murman and Cole [30].

Figure D.1 in Appendix D shows the Mach contour plots for the flow fields with a free stream mach number from $M_\infty = 0.83$ to $M_\infty = 0.86$ which were calculated on the fine mesh. Just as before, the x and y coordinates correspond to the flow solver coordinates, hence the airfoil runs from $x = -1$ to $x = 1$. A shock wave first occurs for $M_\infty = 0.83$. The shock wave is relatively far forward on the airfoil and it can be seen that the flow is accelerated to supersonic velocities again behind the shock wave. However, the second supersonic area is decelerated in a isentropic manner. For $M_\infty \geq 0.84$, there is only one region of supersonic flow which is terminated by a shock wave. It can be seen that the shock wave moves rearward and increases in strength for increasing free stream Mach numbers. This trend is also observed in Figure D.2, which presents the Mach contour plots for the flow fields with a free stream mach number from $M_\infty = 0.87$ to $M_\infty = 0.89$ which were calculated on the coarser mesh. It should be noted that the semi-stable shock position for $0.87 \leq M_\infty \leq 0.89$ was slightly more forward on the fine mesh in comparison to the stable shock position on the coarser mesh. The shock position on the fine mesh is called semi-stable because the position oscillated slightly due to the convergence problem. This difference in the shock position between the meshes indicates that the shock position for $M_\infty \geq 0.87$ might not be completely correct, i.e. it might be slightly too far rearward. This is taken into account for the shadowgraph simulation by also looking at light rays just rearward of the airfoil. It should be noted that the highest used upstream Mach number for the analysis is $M_\infty = 0.89$. For higher upstream Mach numbers, lambda shock patterns appeared in the computed solutions. It was also observed that the C_2 shock wave of the lambda pattern stood on the symmetry axis behind the airfoil. For reasons discussed in subsection 4.2.3, these flow fields are not used for the analysis in this work. The flow fields corresponding to the parabolic arc airfoil are shown in Figure E.1. It can be seen that the shock wave becomes stronger, moves rearward, and grows larger for increasing upstream Mach numbers. In this case, upstream Mach numbers greater than 0.91 resulted in flow fields with lambda shock patterns.

It was found that the solutions for the parabolic arc airfoil converged for $M_\infty \leq 0.89$. For higher values of M_∞, the shock position remained stable but some instabilities arose just in front of the shock foot. These instabilities caused small local changes in the flow field solution between iterations in the region just in front of the shock foot. Appendix F shows the flow field solutions for 10 consecutive iterations, clearly visualizing the changes that take place. Since these changes in the flow field are relatively small and very local, and since the shock position is not altered and its strength remains nearly the same, the light deflection will most likely not be significantly influenced by these small instabilities. It should be noted that the solutions for the flow fields with these instabilities were obtained after performing three times the amount of iterations in comparison to the amount of iterations needed to reach convergence for the $M_\infty = 0.89$ flow field.

The instabilities that occurred in the flow field solutions corresponding to the the SC(2)-0410 airfoil were larger in amplitude, covered a larger area of the flow field, and occurred for weaker shock waves. Hence, the flow fields were more significantly influenced by these instabilities. For $M_\infty \leq 0.86$, the instabilities were comparable to the instabilities that occurred in the flow fields corresponding to the parabolic arc airfoil, meaning that the shock wave was hardly influenced and the instabilities were restricted to a small area. However, for $M_\infty \geq 0.87$, the shock wave position and the shock wave strength were significantly influenced by the instabilities. Hence, the instabilities would in this case significantly alter the light path of the light rays, which would affect the simulated shadowgraphs. Therefore, the solutions that were obtained using a coarser grid, which did not suffer from these instabilities, will be used for these upstream Mach numbers. It should be noted that the convergence problems that were encountered in this study have not been mentioned in any of the papers by Murman, Cole, and Krupp [30,31,69–71]. Hence, the convergence problems might be the result of using a different convergence criterion in comparison to Murman and Krupp [69].

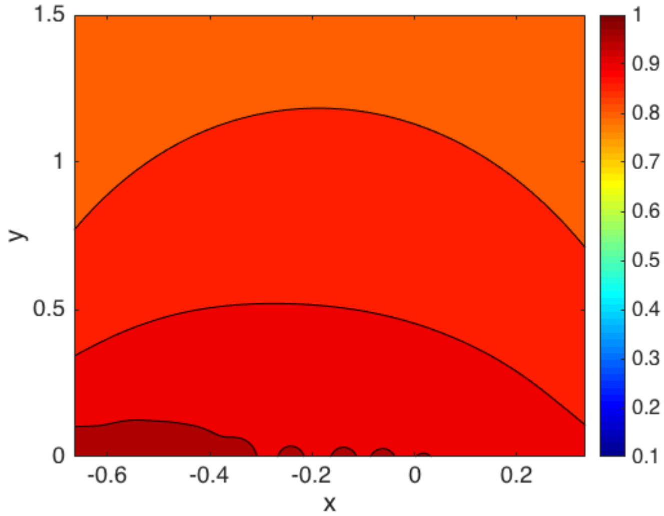

Figure 6.3: Mach number contour plot for $M_\infty = 0.79$, SC(2)-0410 airfoil

The instabilities mentioned earlier seemed to start at the airfoil surface, after which they traveled towards the shock wave over multiple iterations. Depending on the magnitude of the instabilities, the shock wave strength and position in the solution has been seen to change. At first, it was thought that these instabilities were caused by the discontinuous derivative of the SC(2)-0410 airfoil upper surface, which is the boundary condition at which the instabilities seem to originate. However, these instabilities also occurred when using the continuous derivative of the parabolic arc airfoil upper surface. Hence, it seems to be an inherent problem of the flow solver. In itself, this in not entirely unrealistic as the SWBLI is very dynamic. Even though a boundary layer is not present in this flow solver, the shape of the airfoil could still be such that a completely stable shock is not formed. Even though this might be an inherent flaw of the flow solver, it should be noted that the discontinuous boundary condition does promote the instabilities. Figure 6.3 shows the Mach contours in the region over the upper surface of the airfoil. It should be noted that the x and y coordinates still correspond to the flow solver coordinates, i.e. the airfoil runs from $x = -1$ to $x = 1$. A few small regions with higher velocities on the airfoil surface can be seen in Figure 6.3. The locations of these higher velocities correspond exactly to the location of the steps in the derivative curve. Hence, this figure clearly illustrates how these steps in the derivative of the airfoil surface influence the flow solution.

6.2 Simulated Shadowgraphs

Appendix G presents three figures that show how light rays deflect when they travel through a flow field with a varying index of refraction. The flow field over the upper surface of the SC(2)-0410 profile with an upstream Mach number of 0.86 has been used to calculate the light deflection for these figures. It should be noted that the density of this flow field has been multiplied by

200 to make the light deflection visible. If the normal density values and density gradient values had been used, the deflected and straight light rays would not have been discernible without zooming in to the extent that the flow field would not have been visible anymore. The straight black lines in the figures represent the straight light rays and the blue curved lines represent the deflected light rays. The background consists of the Mach number contour plot where warm colors correspond to high Mach numbers and lower density.

Figure G.1 shows the ray deflection when the light rays are initially parallel and have a light angle of 15°. It can be seen that all the light rays that strike the surface in front of the shock wave are deflected downward, i.e. bend towards the airfoil surface. In other words, they deflect towards the regions of higher density. The light rays that strike the surface after the shock wave are deflected away from the surface as they bend to the higher density regions further downstream of the shock. These deflections are strongest in the proximity of the shock wave, which results in a shadow followed by a bright spot. Figure G.2 shows the ray deflection when the initial light angle was 5°. Approximately the same flow deflections can be seen. However, the light angles are slightly different with respect to the flow field which results in a shadow and bright spot formation at a different, more forward location. It can also be seen that the light ray that runs nearly parallel to the shock wave deflects significantly more than the other light rays, highlighting the abrupt change in density that takes place across the shock wave. Figure G.3 shows the case where the initial light angle was $-5°$. The light deflects in the same manner as before, but the point where the light deflects more to the the right or to the left has shifted more upstream again. It can be seen that the light rays are deflected most when they cross the shock wave, which results in a bright spot just upstream of the shock wave.

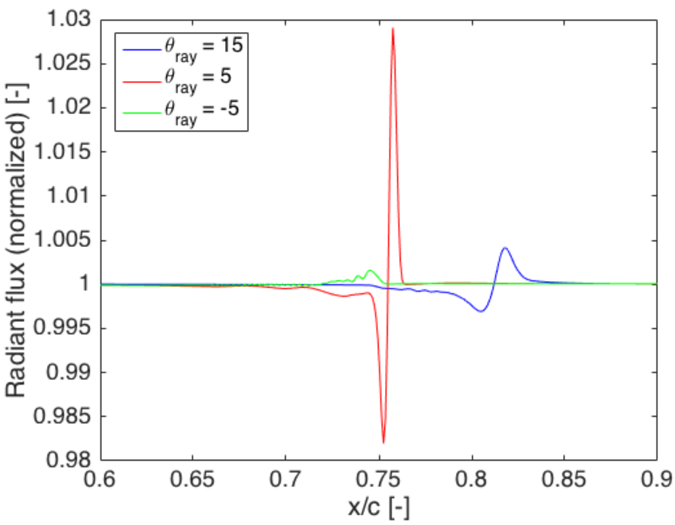

Figure 6.4: Normalized radiant flux measured at upper surface for the $M_\infty = 0.86$ flow field using parallel light with varying light angles

Figure 6.4 shows the radiant flux values that are measured by the pixels at the upper surface of the airfoil when parallel light travels through the flow field with an upstream Mach number of 0.86. These radiant flux values correspond to the ray deflection figures presented in Appendix G. However, this time, the density values were not multiplied by 200, which was only done to clearly visualize the ray deflections. A typical shadowgraph that is created by light traveling through a wing bound shock wave usually features a darker band followed by a light band. The dark band will be referred to as the shadow of the shadowgraph and the light band will be referred to as the bright spot of the shadowgraph from now on. It can be seen that the bright spot moves rearward for increasing initial light angles. It should be noted that the shadow, which is detected upstream of the bright spot, is not always present. From

Figure 6.4, it can be concluded that the shadow is hardly detectable if the initial light angle is negative. Furthermore, it can be seen that the radiant flux peaks corresponding to the bright spot and the shadow are significantly larger for $\theta_{ray} = 5$ in comparison to the other light angles. However, these radiant flux peaks for the shadow and bright spot are also more narrow or less spread out. It should also be noted that some small fluctuations can be seen in the solution for $\theta_{ray} = -5°$. These fluctuations are also seen in other simulated shadowgraphs and will be discussed at the end of this section.

Only parallel light will be used for the analysis that will determine whether a relation between certain shadowgraph features and shock wave features exists. Since the shock wave position changes for different upstream Mach numbers, a point light source would result in different light angles with respect to the shock wave when the point source location remains unchanged. It should also be noted that the radiant flux is measured from $x/c = 0$ to $x/c = 1.5$ instead of $x/c = 0$ to $x/c = 1$, which corresponds to the upper surface. This is done to account for the possible inaccuracies in the shock wave position. If, for example, a shock wave is modeled too far rearward by the flow solver, some shadowgraph features would not be visible on the wing. However, if the same shock wave would, in reality, occur at a more forward location on the airfoil, these shadowgraph features would be visible on the upper surface of the airfoil. It was therefore decided to also measure the radiant flux just after the airfoil in order to use these data when looking for a relation between shadowgraphs and shock waves. It should be noted that the pixel size has not been altered. Hence 1500 pixels are used over the area from $x/c = 0$ to $x/c = 1.5$ instead of 1000 pixels.

Appendix H presents the radiant flux values that are measured by the pixels at the upper surface of the two airfoil for different upstream Mach numbers and varying light angles. The flow fields presented in Appendix D and Appendix E were used for the ray tracing and shadowgraph simulation. A step distance or extrapolation distance of $\Delta t = 0.001$ was used for the ray tracing. This size was chosen because it is smaller than the smallest grid point spacing in the fine mesh, hence making full use of the information in the flow solution by not jumping over grid points. Initial light angles ranging from $\theta_{ray} = 20°$ to $\theta_{ray} = -15°$ were used. First, it should be noted that the radiant flux scale is different for the different figures. It can be seen that the radiant flux peaks, corresponding to the dark and bright bands in a shadowgraph, become larger for increasing upstream Mach number. In other words, the bright and dark spots become more visible in a shadowgraph when the shock wave becomes stronger. Secondly, it should be noticed that the magnitude of the radiant flux peaks vary for the different light angles. The radiant flux peaks are most detectable when the light angle is such that the light rays are approximately parallel to the shock wave at some distance from the surface. When the light rays are approximately parallel to the shock, maximum light deflection is achieved (see Snell's law, subsection 2.1.2). When this maximum light deflection occurs further away from the surface, the light deflection becomes more visible because the deflected light will have to travel further to the surface (see subsection 2.2.2). Hence, the light angle at which the maximum radiant flux peak occurs is related to the curvature of the shock wave away from the airfoil surface. Finally, it should be noted that there appears to be a small discrepancy between the radiant flux solutions that were calculated using either the fine or coarser mesh for the flow field solutions corresponding to the SC(2)-0410 airfoil. When the upstream Mach number is increased from 0.86 to 0.87, the radiant flux peaks in the solution decrease and they become wider. This indicates that the deflection of the light that travels through the shock takes place over a larger distance and that the deflection is less. This is in agreement with the flow solution of the coarser mesh because the shock wave is thicker in this solution, which means the density gradient is less severe. This indicates how much the shadowgraph simulation scheme depends on the accuracy of the flow field solutions.

It was noticed before that some fluctuations occurred in the solution for $\theta_{ray} = -5°$ in Figure 6.4. These fluctuations have also been seen in multiple other shadowgraph figures in

Appendix H. The fluctuations occur for higher upstream Mach numbers, in other words when the shock wave becomes stronger. They seem to appear first for the negative light angles, most notably for $\theta_{ray} = -10°$. The fluctuations appear around or just before the location of the shadow in the shadowgraph. Hence, the light rays that reach the surface at this location will have traveled through the shock wave and the area just upstream of the shock wave before reaching the surface. It therefore seems that there are two likely factors contributing to these fluctuations. First, the interpolation of the index of refraction field and its gradients is very sensitive to slight changes in position near the shock wave. Hence the discretization of the light rays and the steps in calculating its trajectory might result in small differences in the bending of light depending on the intermediate locations of the different light rays. It might be the case that some light rays spend 4 steps in the shock wave whereas other light rays only need 3 steps to cross the shock wave resulting in different bending of the light. Secondly, the instabilities that occur in the solution near the surface just upstream of the surface might contribute to these fluctuations in the radiant flux solution by bending the light in a different manner. For the analysis of the radiant flux solutions, shadows or bright spots that are part of these fluctuations and are not clearly a shadow or bright spot have been ignored.

It should be noted that the range of light angles that produce observable features in the shadowgraphs is smaller than the range of sun angles presented by Fischer et al. [1]. This difference is caused by the two-dimensional nature of this study. In the work presented by Fischer et al. the sun could be positioned in such a way that it was in line with the wing span. In that case, sunlight that passed through a shock wave would always fall on the wing, but the shadowgraph would be seen at different spanwise locations. Since shock waves on airfoils are studied in this work, these three-dimensional effects have not been taken into consideration, which results in a smaller range of light angles that produce observable features in the shadowgraphs.

6.3 Relation Between Shadowgraphs and Shock Waves

The characteristics of a shadowgraph that can be detected and quantified are the radiant flux values and the positions of the shadow and the bright spot. By using the method of Fisher et al., the light angle can be determined for in-flight shadowgraphs, hence the light angle will be treated as a known parameter during the analysis [1]. The goal of this study is to determine whether these parameters can be used to detect a relation between the shock position, the shock strength, shock curvature and shadowgraph features.

In the previous section, it was determined that the light angle, corresponding to the brightest peak in the radiant flux curve, is approximately parallel to the higher part of the shock wave, i.e. part of the shock wave that is further away from the airfoil surface. It was also observed that the radiant flux peaks, for both the shadow and bright spot, increase for increasing upstream Mach numbers. However, both the upstream Mach number and the light angle influence the radiant flux values. In this section, it will be determined whether a unique relation between the radiant flux values of the shadow and bright spot, the distance between the shadow and bright spot, and the light angle exists.

For this analysis, the detectable differences in the radiant flux values are defined as differences that can be measured on a 12-bit gray scale. Hence, the radiant flux value should deviate from the average with at least $1/2^{12} \approx 2.5 \cdot 10^{-4}$, i.e. shadows or bright spots are detectable when their radiant flux value falls below 0.99975 or rises above 1.00025. Figure 6.5 shows the radiant flux values corresponding to the bright spots in the shadowgraphs for different initial light angles of the parallel light. It should be noted that Figure 6.5 contains only radiant flux values that correspond to the parabolic arc airfoil. Figure 6.5 clearly shows that the radiant flux peak increases for increasing shock strength. The shift in light angle at which the maximum radiant flux is measured also shows that the curvature of the shock wave changes as the shock strength increases. It should be noted that not all the curves cover the entire light angle spectrum. If

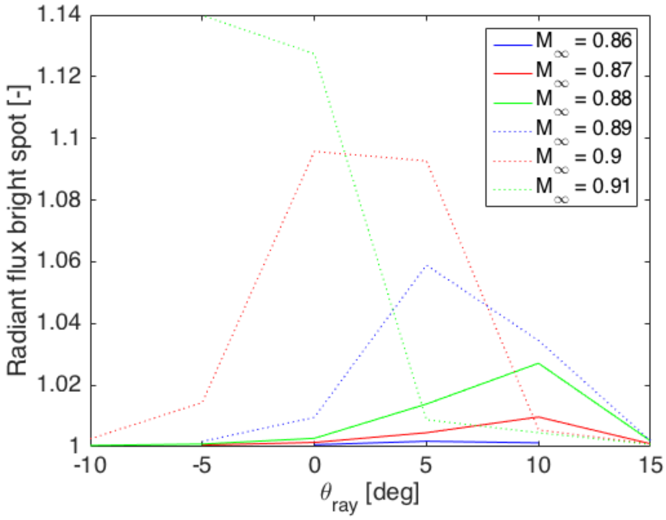

Figure 6.5: Peak radiant flux values corresponding to the bright spot in the shadowgraph for different light angles, parabolic arc airfoil

a curve does not appear for part of the spectrum it means that the radiant flux value of the bright spot for that light angle is too small to be measured on a 12-bit gray scale. It can be concluded from Figure 6.5 that a trend can be seen between the bright spot radiant flux and the increase in shock strength. However, a unique relation between the radiant flux value of the bright spot and the initial light angle cannot be established, which is indicated by the different curves crossing. Hence, when only the radiant flux value of the bright spot and the initial light angle are known, no unique relation can be established to determine the shock position or strength.

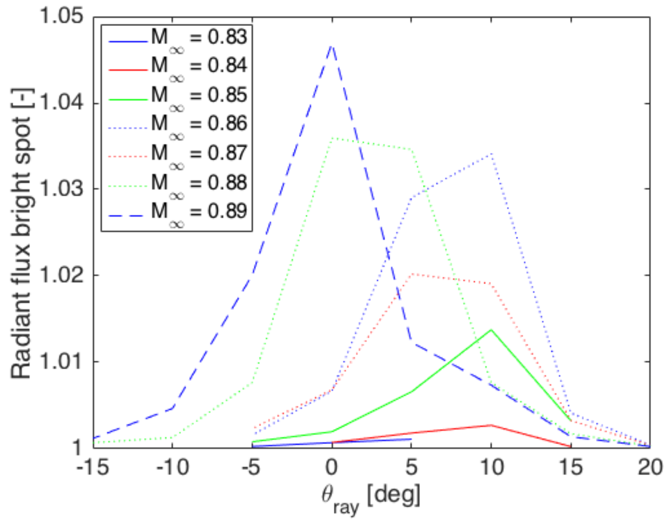

Figure 6.6: Peak radiant flux values corresponding to the bright spot in the shadowgraph for different light angles, SC(2)-0410 airfoil

The bright spot radiant flux values for varying initial light angles of the parallel light for the SC(2)-0410 airfoil are shown in Figure 6.6. Once again it can be seen that the radiant flux values increase for increasing upstream Mach number, i.e. stronger shock waves. The only exception is change in the radiant flux values when the upstream Mach number is increased from 0.86 to 0.87. This reduction in the maximum radiant flux value is caused by the use of different grids for the flow solution. The coarser grid, used for the flow field solution with $M_\infty \geq 0.87$, has a thicker shock, which results in a wider shadow and bright spot with less extreme radiant flux peaks. However, the use of different grids does not alter the shift in the light angle corresponding to the maximum radiant flux value between $M_\infty = 0.86$ and $M_\infty = 0.87$. This indicates the curvature of the shock wave is not significantly influenced by the use of different grids for the flow field solution. Since the different curves in Figure 6.6 cross, no unique relation can be established, using only the bright spot radiant flux values and the initial light angles, to determine the shock wave characteristics.

Figure I.1 and Figure I.2 in Appendix I show the relation between the light angle and the radiant flux values corresponding to the shadow in the shadowgraphs. It can, once again, be seen that the the shadowgraph feature becomes more distinguishable for increasing upstream Mach numbers. This means that the radiant flux values of the shadow decrease for increasing shock strength, i.e. the shadow becomes stronger, just like the bright spot becomes stronger for increasing shock strength. It can also be noted that the shift in light angle, at which the minimum radiant flux value is measured, also shows that the curvature of the shock wave changes as the shock strength increases. Again, this is similar to the relation between the light angle and the bright spot radiant flux values. Finally, it should be noted that the discrepancy between $M_\infty = 0.86$ and $M_\infty = 0.87$ for the SC(2)-0410 airfoil, caused by the use of different grids for the flow solver, is also visible in Figure I.2. Since the different curves cross, no unique relation between the shadow radiant flux values and the initial light angles can be established. Figure I.3 and Figure I.4 in Appendix I show the relation between the light angle and the distance between the shadow and bright spot in the shadowgraphs. This distance is nondimensionalized with respect to the chord length of the wing. It should be noted that a positive value for the distance between the shadow and the bright spot means that the shadow is upstream of the bright spot. It can be seen that the distance between the shadow and the bright spot is at its minimum for a certain light angle. The distance increases for both higher and lower values of the light angle. However, a unique relation between the light angle and the distance between the shadow and the bright spot cannot be established, as can be seen from the different curves crossing.

Although a completely unique relation is not found in Figure 6.5, Figure 6.6, or Appendix I, it should be noted that all these figures do show a general trend. This indicates that a general relation is present, even though this relation is most likely not unique when only one measured parameter is known. However, if multiple measured parameters are combined, a unique relation might be found. If the light angle is treated as a known parameter and is kept constant, the radiant flux values corresponding to the shadow and bright spot and the distance between the two can be used to obtain a unique relation. Such unique relations for a constant light angle are shown in Figure 6.7 and Figure 6.8.

Figure 6.7 relates the combination of the radiant flux value of the bright spot and the distance between the shadow and the bright spot to the distance between the bright spot and the location of the shock wave at the surface of the airfoil. It can be seen that, for a constant light angle, unique combinations of bright spot radiant flux values and distances between the shadow and bright spot exists for both airfoils. It is therefore possible to link this combination to the relative position of the shock wave at the airfoil surface with respect to the position of the bright spot. It should be noted that a positive value for the distance between the shock wave and the bright spot means that the shock wave is upstream of the bright spot.

Figure 6.8 relates the combination of the radiant flux value of the shadow and the distance between the shadow and the bright spot to the distance between the shadow and location of the shock wave at the surface of the airfoil. Just as in Figure 6.7, it can be seen that a unique combination exists for both airfoils for a constant light angle. Hence, it is possible to link the unique combination of the shadow radiant flux and the distance between the shadow and bright spot to the relative position of the shock. The position of the shock wave, at the airfoil surface,

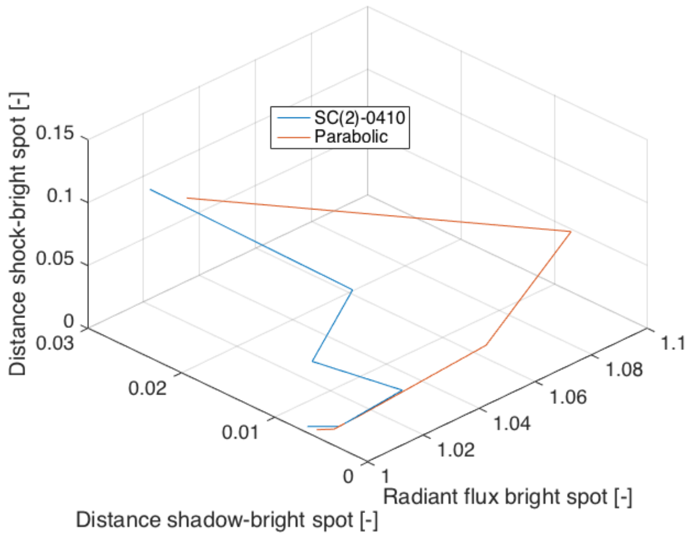

Figure 6.7: Relation between the bright spot radiant flux value, the distance between the shadow and bright spot, and the position of the shock wave with respect to the position of the bright spot for $\theta_{ray} = 5°$

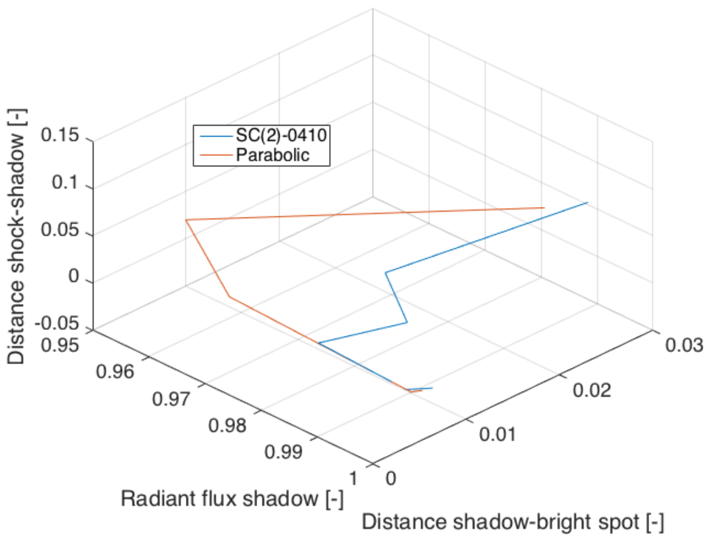

Figure 6.8: Relation between the shadow radiant flux value, the distance between the shadow and bright spot, and the position of the shock wave with respect to the position of the shadow for $\theta_{ray} = 5°$

is measured with respect to the position of the shadow and the distance is positive if the shock wave is upstream of the shadow.

Both Figure 6.7 and Figure 6.8 show that the curves for both airfoils follow the same trend. The biggest difference lies in the values corresponding to the radiant flux of either the bright spot or the shadow. It can be seen that the bright spot and the shadow have more extreme values for the parabolic arc airfoil. Another big difference is the kink that occurs in the SC(2)-0410 curve, i.e. the kink that makes the curves look a little like 'M' shapes. The points in both these curves that cause the kinks, are the points that correspond to the $M_\infty = 0.87$ case. This is corresponds to the first flow field solution that uses the coarser grid. It was already determined that this coarser grid results in less extreme radiant flux values for the shadow and the bright spot, and that both the shadow and bright spot are wider. This explains the decrease in the radiant flux values for the bright spot and the increase in the radiant flux values for the shadow and also explains the increase in distance between the shadow and bright spot.

Appendix J shows figures similar to Figure 6.7 and Figure 6.8 but for different light angles. It can be seen that the curves for both airfoils follow the same trend for $\theta_{ray} = 10°$ or $0°$. For $\theta_{ray} = 15°$ the curves follow nearly the same trend but the radiant flux values for the shadow and the bright spot are more extreme for the SC(2)-0410 airfoil. This is caused by the difference in shock wave curvature and strength for the two airfoils. From Figure 6.7, Figure 6.8, and the figures in Appendix J, it can be concluded that a unique relation can be established between shadowgraph characteristics and the shock wave position. When the location of the shadow and bright spot and their corresponding radiant flux values can be determined, the location of the shock wave on the airfoil can be determined. Not only the shock wave location can be determined in this manner, but the shadowgraph can also be linked to a certain shock wave, which enables the quantification of the shock wave strength and curvature. Basically, a shadowgraph and light angle combination can directly be linked to a certain flow field, hence revealing the the strength and curvature of the shock wave in that flow field.

Since the bright spot and shadow are not visible for every light angle and flow field combination, figures in Appendix J are only presented for $0° \leq \theta_{ray} \leq 15°$. It should also be noted that the shadowgraphs corresponding to the $M_\infty = 0.83$ flow field of the SC(2)-0410 airfoil have been omitted. This is done for two reasons. First, the shock wave is very weak and relatively far upstream on the airfoil in comparison to the other shock waves. On top of that, the flow after the shock wave is accelerated to sonic conditions again, making the flow field very different in comparison to the other flow fields. Secondly, the shadow and bright spot of these shadowgraphs are only visible for two light angles.

It can be concluded that a unique relation between the shadowgraph characteristics and the shock wave has been found, or rather between the shadowgraph characteristics and a certain flow field. However, it seems unlikely that the relation can be described with a general formula given the shape of the curve in figures like Figure 6.7. On top of that, the relation itself heavily depends on the airfoil under investigation and the light angle. The relation will therefore most likely be used in a the way a look-up table is used. Hence, when the light angle is known and the shadowgraph characteristics have been quantified by means of measurements, the graphs can be used to find the corresponding shock wave information by matching the correct values for shadow and bright spot radiant flux and the distance between the shadow and the bright spot.

6.4 Boundary Layer Estimation

The Bohning-Zierep model, presented in section 4.3, has been used to calculate the boundary layer flow field, which was needed to calculate the light deflection in the boundary layer. In turn, the calculated light deflection, that takes place in the boundary layer, has been used to determine the error that is introduced by ignoring the light deflection that takes place in the boundary layer.

In order to combine the Bohning-Zierep model with the transonic potential flow solution, an estimation of the boundary layer thickness had to be made. This was done using Equation 6.1, which approximates the turbulent boundary layer thickness as a function of the Reynolds number [68]. It should be noted that this equation is intended for a flat plate case with a zero pressure gradient. Since the boundary layer thickness, used for the nondimensionalization, is determined upstream of the shock wave where the pressure gradient is not too severe, this equation will give a good order of magnitude approximation of the boundary layer thickness.

$$\delta = \frac{0.37x}{Re_x^{0.2}} \tag{6.1}$$

If it is assumed that the chord of the airfoil, or wing, is five meters, the Reynolds number at an altitude of 10 km is $39 \cdot 10^6$. A chord length of five meters is a good approximation for commercial passenger aircraft as most mean aerodynamic chord lengths range between approximately 4 and 7 meters, depending on the range and size of the aircraft. Using this chord length and this Reynolds number, an approximate boundary layer thickness of 5.6 cm is obtained. It is found that $Re_\delta = 2.76 \cdot 10^5$ for this boundary layer thickness, which is within the domain of validity of Equation 4.42 and Equation 4.43.

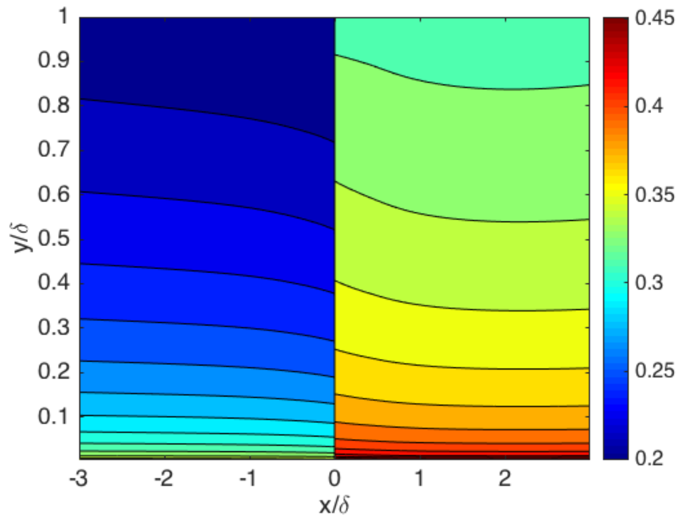

Figure 6.9: Boundary layer density field $[kg/m^3]$, Bohning-Zierep model coupled to the flow field solution of the 6% parabolic arc airfoil for $M_\infty = 0.89$

The flow field for $M_\infty = 0.89$, corresponding to the 6% parabolic arc airfoil, has been coupled to the Bohning-Zierep model by using the pressure at the airfoil surface as a boundary condition for the Bohning-Zierep model. This flow field was chosen because the Mach number just before the shock wave is 1.27, which is very close to the value of 1.28 that was used by Bohning and Zierep, hence making comparisons possible. The density field of the calculated boundary layer flow is presented in Figure 6.9. It should be noted that $T_t/T = 1 + 0.5(\gamma - 1)M^2$ was used to calculate the temperature throughout the flow field and the perfect gas law ($p = \rho RT$) was used to calculate the density. This deviates from the equations used by Bohning and Zierep, namely Equation 4.32 and Equation 4.33. When these equations were used, temperatures and densities were calculated that significantly exceeded the stagnation temperature and density. Since the viscosity terms are ignored in the governing equations when calculating the outer boundary layer, according to the Bohning-Zierep model, and since a shock wave is adiabatic the equation used to calculate the temperature can be used. The used equations resulted in more realistic results. It should be noted that both equations to calculate the temperature are derived from the same governing equations, however, the equation used by Bohning and Zierep uses disturbance terms which might cause the different behavior.

When the solution is compared to Figure 6.10, which shows the density field for both a flat and curved wall for a similar Mach number just upstream of the shock wave, it can be seen that the flow fields are not similar. It can be seen that the computed flow field changes abruptly at $x/\delta = 0$, which is the chordwise position of the shock wave. This change is much smoother in the solutions that were presented by Bohning and Zierep [34]. Hence, in the computed flow field it looks as if the shock wave is even present in the subsonic region of the boundary layer. In other words, it looks as if the viscous effects are not dominant enough to spread this change in conditions out over a larger region. This difference is probably caused by two things. First, the Bohning-Zierep model has, in this case, been coupled to a different flow solution for the outer transonic flow, hence the pressure boundary condition for the boundary layer has been changed. Secondly, Bohning and Zierep used iterations to come to a final solution, i.e. the solution of the boundary layer and the outer flow field were updated. This has not been done for the computed flow field. This lack of iterations between the boundary layer and outer flow is most likely the biggest cause of the lack of apparent viscosity in the solution.

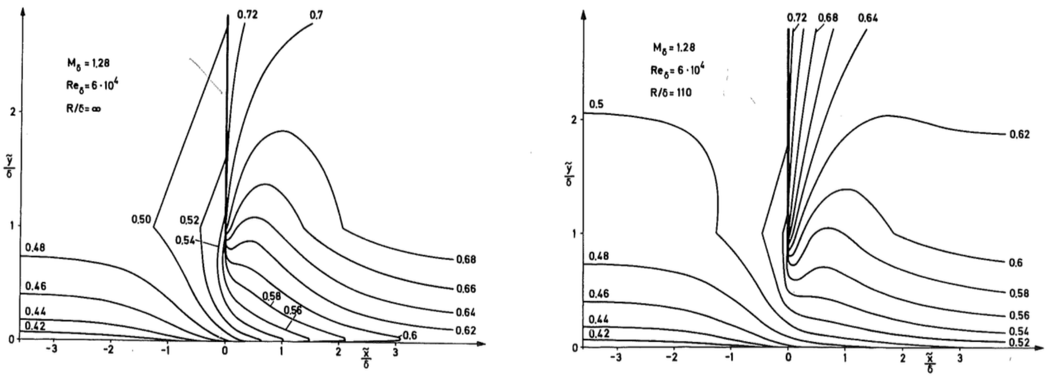

Figure 6.10: Boundary layer density field, contours present ρ/rho_0. Flat wall (left), curved wall (right) [34]

Even though the boundary layer flow field is not completely similar to the solutions presented by Bohning and Zierep, it can still be used in this case since it is only used to get an estimation of the light deflection in the boundary layer. It should be noted that the density contours follow a similar trend as the ones in the curved wall solution of Bohning and Zierep. They are actually quite similar if the part near the shock wave, approximately $-1 \leq x/\delta \leq 1$, of the solution by Bohning and Zierep is cut out. This part of the solution is basically the part where the effect of the shock wave is spread out by viscous effects. Furthermore, it should be noted that the effect of the shock wave does not reach very far up and downstream of the shock wave when the boundary layer flow field is compared to the length of the chord. Therefore, this model will approximate the light deflection throughout the boundary layer well enough for error estimation. Furthermore, the boundary layer flow solution does show an effect that the shock wave has on the boundary layer flow and since it is so abrupt the light deflection might even increase, which would result in a slightly higher error estimation of the light deflection.

When the light rays were traced through the boundary layer flow, using the method presented in chapter 5, and the trajectories were compared to straight trajectories, the following errors were found: For $\theta_{ray} = -45°$ the maximum difference between a straight and deflected light rays is $8.2 \cdot 10^{-5}$. For $\theta_{ray} = -30°,\ -15°,\ 0°,\ 15°,\ 30°,\ 45°$, the differences are $6.2 \cdot 10^{-5}$, $1.0 \cdot 10^{-4}$, $1.1 \cdot 10^{-3}$, $9.7 \cdot 10^{-5}$, $4.9 \cdot 10^{-5}$, $4.9 \cdot 10^{-5}$ respectively. It should be noted that these differences are defined in the local boundary layer coordinates. Furthermore, the relatively large difference for $\theta_{ray} = 0°$ is caused by the abrupt change in conditions which acts as an interface. Hence, the abrupt change in flow conditions results in more light deflection, which means that the error estimate might be a little too high. However, this can be seen as a safety factor due to some uncertainties regarding the boundary layer flow solution.

From this analysis it can be concluded that the maximum error in light ray deflection, when ignoring the boundary layer, is $1.1 \cdot 10^{-3}\delta$. Since the boundary layer is usually only a few centimeters thick, or in this case $\delta \approx 0.01c$, it can be assumed that the maximum error will be of the order $c \cdot 10^{-5}$. For the current project this means that the maximum error is approximately 0.1 of the pixel width. This error is not insignificant for the current analysis, however, this maximum error will only occur if a light ray goes through the part of the shock wave that is present in the boundary layer. Hence the error is confined to a very small region. Furthermore, it was already determined that the abrupt change in the boundary layer in the computed solution is an exaggeration of the real situation, which is more realistically presented by Figure 6.10. The real error in this small area will therefore most likely be smaller. Hence, ignoring the boundary layer when creating the simulated shadowgraphs will not significantly influence the solution. In the worst case scenario there could be a $10^{-5}c$ error in the determination of the shadow and bright spot location, which is already lower than the accuracy that is achieved with the used amount of pixels. This error is also smaller than the accuracy with which the shock wave position can be determined.

6.5 Limitations

This section will start by shortly describing how the relation that was found can be used to extract quantitative data about a wing bound shock wave from a shadowgraph. Secondly, both theoretical and practical limitations of the shock wave identification method will be discussed. Thirdly, the application of this method for CFD validation will be treated. Finally, the influence of the limitations on the results of the current study will be discussed.

From section 6.3, it can be concluded that the different curves, that describe the unique relations between shadowgraph characteristics and shock wave characteristics for a constant light angle, are hard to capture in a general formula. This is so difficult because the curves depend on both the light angle and the airfoil shape. It is therefore more obvious to use the data in the form of a look-up table or a look-up graph. For example, if the light angle, radiant flux value of the shadow or bright spot, and the distance between the shadow and bright spot are known, the table or graph will provide information about the shock wave. Hence, if the required shadowgraph characteristics can be determined for an in-flight shadowgraph, information about the wing-bound shock wave can be extracted from the in-flight shadowgraph using the look-up table or graph. The big shortcoming of such an implementation is that a large amount of data is needed to create a complete look-up table or graph. It should also be noted that this study has only analyzed two-dimensional flow fields and one-dimensional shadowgraphs, hence the application to three-dimensional flows and real in-flight shadowgraphs is only a theoretical possibility at this point. Further research is required to enable such an application.

6.5.1 Theoretical Limitations

The first thing that limits the technique of using shadowgraphs that use the wing surface as the imaging screen is that the information about an 'n'-dimensional flow field is stored in an 'n-1'-dimensional shadowgraph. For the current study, information about the two-dimensional flow field is stored in a one-dimensional shadowgraph. This differs from the more traditional application of the shadowgraphy technique, which creates two-dimensional shadowgraphs of two-dimensional flows. In this case the imaging screen is parallel to the two-dimensional flow field and the light that is used to form the shadowgraph travels in a direction perpendicular to the imaging screen and the plane of the two-dimensional flow. Examples of this application of the shadowgraphy technique can be seen in subsection 3.1.2. Only when three-dimensional flow fields are visualized using the more traditional application of the shadowgraphy technique will one dimension be lost.

Since one dimension is lost when the shadowgraph is made, it is very difficult to revert this one-dimensional shadowgraph back to precise information about the two-dimensional flow field. It becomes impossible, without extra information, to trace one detail in the shadowgraph back to the corresponding feature in the flow field. The only manner in which such a detail in the shadowgraph can be linked to a feature in the flow field is by extensive simulation of shadowgraphs for many different flow variations until the right flow field is found. However, there is no guarantee, that there is a one-to-one relationship between a flow field and a shadowgraph, i.e. several flow fields might result in the same shadowgraph.

The second limitation of this shadowgraphy technique is that it relies completely on the computed flow field solutions. If the CFD method is not accurate and does not represent the real flow, the simulated shadowgraphs, created using this CFD method, will differ from the real shadowgraphs. Hence, the level of accuracy of the CFD solver directly influences the accuracy of this shadowgraphy technique. To be very precise, the simulated shadowgraphy technique used during this study is basically a technique to visualize the CFD solution in a different manner.

In the event of a mismatch between the simulated shadowgraph and a real in-flight shadowgraph, it will be hard to determine exactly which part of the computed flow solution is the cause of the mismatch because the entire flow field influences the measured characteristics of the shadowgraph. However, it was found earlier that the shadow and the bright spot are most visible, i.e. the most extreme radiant flux peaks, when the light angle is approximately parallel to the part of the shock wave that is further away from the surface. It was also found that the shadow and bright spot, in general, become more visible for stronger shock waves. When the light angle is known, it can roughly be determined whether the shock wave in the computed flow field is upstream or downstream of the shock wave in the real flow. It can therefore be concluded that the exact cause of a mismatch between a simulated shadowgraph and a real shadowgraph can most likely not be found. However, it can be roughly determined whether the shock wave position, strength, and curvature are correct. It should be noted that simulated shadowgraphs for varying light angles and varying shock strengths, and real shadowgraphs with varying light angles are needed to carry out this error analysis.

6.5.2 Practical Limitations

The first practical limitation of this technique is the dependency of this technique on CFD solutions. In order to create a sufficiently large database, which is needed to create a reliable look-up table or graph, many CFD solutions and shadowgraph simulations are required. This will make this method computationally expensive. It should be noted that the dependency on the CFD solver is both a practical and theoretical limitation.

The second practical limitation lies in the accuracy of the measurement equipment. The determination of the positions of observable features in the shadowgraph is theoretically limited by the amount of pixels that a camera has. Since modern cameras have increasingly more pixels and can enlarge the object to be imaged several times, the position estimation is expected to be very precise. However, the radiant flux measurement depends on the gray-scale of the camera. If an 8-bit gray-scale is used, instead of a the 12-bit gray-scale used for this study, only a few shadows and bright spots will be visible. These shadows and bright spots would only be visible for the stronger shock waves at a very limited range of light angles. Furthermore, different noise factors could limit or disrupt the radiant flux measurements. Inhomogeneities in the wing surface, such as dents or dirt, could influence how light is reflected off the wing surface, hence effecting the measured radiant flux. Another possible noise factor is the light that can be reflected off the fuselage, causing extra illumination on the wing surface.

On top of the issues that might limit the radiant flux measurements, mismatches between the simulated shadowgraphs and the real shadowgraphs, caused by dynamic flow phenomena, could further limit possibility of comparisons between the two. In real life, the turbulent boundary layer is very dynamic, which will most likely result in smearing out of observable features of the shadowgraph. In other words, it is likely that the shadow and bright spot become wider at the cost of having a less extreme radiant flux value. Another effect that will also smear out the shadowgraph features is the circle of confusion, which is determined by the size of the light source and the distances between the light source, schlieren object, and the imaging surface (see subsection 2.2.2). Hence, both these factors will blur the observable shadowgraph features. In order to account for these effects, a calibration will most likely be needed to enable the comparison of simulated shadowgraphs and real shadowgraphs.

6.5.3 CFD Validation

Simulating shadowgraphs, the way it has been done during this study, can be used to validate CFD results by comparing them to shadowgraphs that are made in real flight conditions or during wind tunnel tests. Since wind tunnel tests that are used to create in-flight like shadowgraphs will most likely use spots as a light source, the shadowgraphy simulation algorithm developed in this study incorporates a point light source. This was done to enable the possibility of comparing wind tunnel shadowgraphy results to the simulated shadowgraphs for this study. Unfortunately, such wind tunnel results have not been obtained. Although CFD validation is possible using the shadowgraph simulation technique, it would most likely only indicate whether the computed flow field is correct or not since flow features cannot be linked to features in the shadowgraph in a direct and unique manner.

The simulated shadowgraph technique is not ideal for wind tunnel CFD validation because the flow field itself is not visualized nor quantified. If the shock wave position is to be validated, pressure tabs would be the most obvious and simple measurement devices to do so. Furthermore, if features in the flow field are to be validated, the PIV technique would be most suited because it can visualize and quantify the entire flow field.

Due to the complexity of visualizing flow fields over the wing during in-flight tests, the simulated shadowgraphy technique might be more feasible for CFD validation due to the method's simplicity. However, pressure tabs are still the more obvious choice when the shock position has to be determined. Furthermore, the practical limitations mentioned earlier will also limit the extent of the validation that can be done with the simulated shadowgraphy technique.

The conclusion to be drawn is that the simulated shadowgraphy technique can be used for CFD validation, but that other measurement techniques are, in most cases, more accurate, making them more suitable for CFD validation.

6.5.4 Limitations Current Analysis

The results obtained during this study are limited by the accuracy of the used flow solver. The circle of confusion of the sun and the dynamic behavior of the boundary layer have not been taken into account. Furthermore, the light reflection off the wing surface, which is needed in order to make the light reach the camera, and the camera effects have not been considered. This means that the simulated shadowgraphs represent the most undisturbed light deflection data that can be obtained, i.e. all the factors that results in shadowgraph blurring or deformation have not been included. In other words, the simulated shadowgraphs represent an ideal scenario in which all the shadowgraph feature can be measured without disturbance factors. However, the fact that the sun's visible light consists of multiple wave lengths has been ignored. During this study, the index of refraction has been kept constant for all the wave lengths of visible light. In real life, some wave lengths of the visible light deflect more than others, which could potentially influence a shadowgraph. However, the deviation of the index of refraction for different wave lengths is relatively small since the changes in the index of refraction have been very small in this study. It is therefore assumed that this has not influenced the results significantly, but further research should confirm this assumption.

7. Conclusion and Recommendations

The aim of this study was to assess the feasibility of extracting quantitative information about the shock waves on wings of aircraft flying at transonic speeds from in-flight shadowgraphs by means of a comparison with simulated shadowgraphs. The first step of this feasibility study was to obtain or create realistic transonic flow fields over a representative airfoil or wing profile. The transonic small disturbance potential flow equations were used to calculate the required two-dimensional flow fields. Secondly, an iterative ray tracing scheme was used to determine how light was deflected when it traveled through the calculated flow fields. Using the calculated light trajectories, simulated shadowgraphs were created. Finally, these simulated shadowgraphs were analyzed to determine if quantitative information about the shock wave could be extracted from the shadowgraph.

7.1 Conclusion

During this feasibility study, two of the three sub-research questions have been answered. The sub-question '*What do transonic flow fields around super critical airfoils, with a shock wave standing on the surface of the airfoil, look like?*', has been answered. Transonic flow fields over the upper surface of a SC(2)-0410 airfoil have been calculated using the transonic small disturbance potential flow equations. It was found that shock waves first appear on this airfoil for an upstream Mach number of 0.83. The shock wave is very weak and is located at approximately 0.4 chord lengths rearward of the leading edge. It was also found that the flow after this shock wave accelerated to supersonic velocities again. However, this second region of supersonic flow was decelerated in an isentropic manner, i.e. without shock waves. For increasing upstream Mach numbers, the shock wave was found to grow in strength and size, and it moved rearward on the airfoil. Furthermore, supersonic regions rearward of the shock wave have not been found for the increasing shock strength. However, post-shock expansion has still been observed, i.e. behind the shock wave flow has been found to accelerate locally.

The sub-question '*In what way do optical phenomena form a shadow, in a shadowgraph created by direct shadowgraphy, on a surface?*', has also been answered. A theoretical study revealed that changes in the index of refraction cause light to deflect when it travels through a medium with an inhomogeneous index of refraction field. It was found that light rays deflect towards regions with a higher index of refraction, i.e. light bends towards regions of higher density. This behavior was also observed during the shadowgraph simulation, which itself is based on the studied geometrical optics of light refraction. In the case of the transonic flow fields, it was found that the entire flow, and not just the shock wave, caused the light to refract towards regions of higher density. However, the light refraction has been observed to be strongest across a shock wave since the change in index of refraction is strongest across a shock wave. Shadows in a shadowgraph have been found at locations where light illumination levels have decreased due to light rays being deflected away from this region. Bright spots in shadowgraphs, on the other hand, have been observed at locations where the light is concentrated, i.e. light is deflected towards these regions. Hence, the light illumination is altered due to light refraction, resulting in shadows when light is deflected away and in bright spots when light deflects towards a region.

The knowledge that was obtained by answering the mentioned two sub-questions has been used to answer the main research question: *Can simulated shadowgraphs, created by a ray tracing algorithm, be used to quantify the shock wave characteristics of shock waves on wings* *of commercial passenger aircraft flying at transonic speeds, by means of a comparative study between an in-flight shadowgraph and the simulated shadowgraphs?* Flow fields, corresponding to a typical super critical airfoil and a thin parabolic arc airfoil, with varying upstream Mach numbers have been used for the shadowgraph simulation. Simulated shadowgraphs of the transonic flow fields with shock waves in them have been created for varying light angles. The simulated shadowgraphs have been analyzed and it was found that a unique combination of shadowgraph characteristics could be found for constant light angles. These shadowgraph characteristics consisted of the radiant flux values corresponding to the shadow and the bright spot of the shadowgraph and the distance between the shadow and the bright spot. When the distance between the shadow and the bright spot, the light angle, and the radiant flux of either the shadow or the bright spot are known, the shadowgraph in question could be coupled to a certain flow field, hence revealing quantitative information about the shock wave position and the shock wave strength and curvature. It should be noted that knowledge of the light angle is of the utmost importance when trying to extract data about a shock wave from these simulated shadowgraphs. During this study, the light angle was treated as a known parameter. However, in real life, the light angle has to be determined using the method that was presented by Fischer et al. [1]. It should be noted that this study has analyzed two-dimensional flow fields around airfoils and that the simulated shadowgraphs were one-dimensional.

Even though it has been found that quantitative information about wing bound shock waves could be extracted from shadowgraphs, some simplifications made during this study and experimental uncertainties might limit the practical use of the relation that has been found. First, the shadowgraph simulation is completely dependent on the CFD solutions. Hence, if the CFD solutions are inaccurate, the simulated shadowgraphs will not be representative and the the relation that is found will hold little value. During this study, a simple but reasonable accurate and validated flow model has been used for the shadowgraphs simulation. However, some flow characteristics, such as the boundary layer, have not been taken into account. Hence, the relation found during this study can be refined by using more accurate flow solvers. Furthermore, a large amount of shadowgraph simulations, and thus a large amount of flow fields, are needed to ensure that the relation between shadowgraph characteristics and a certain flow field are truly unique. It will therefore be computationally expensive to use this method to identify shock wave characteristics. Secondly, measurement inaccuracies, due to limited gray-scales of cameras or noise factors, could limit the comparability of real shadowgraphs to these simulated shadowgraphs, hence making it difficult to apply the theoretical relation that has been found to real-life applications.

It can be concluded that it is theoretically feasible to extract quantitative information about a wing bound shock wave from an in-flight shadowgraph formed on the airfoil surface by means of a comparison with simulated shadowgraphs. However, simplifications made during this study, measurement inaccuracies, and the fact that this study has not investigated three-dimensional flow fields makes the application of the relation that was found to real-life experiments questionable at this time.

7.2 Recommendations

The outcome of this feasibility study is that a theoretical relation between the shadowgraph characteristics and the wing bound shock waves exists. However, the flow model that was used was fairly simple. In order to further refine this relation, more realistic flow models which include the boundary layer should be used. Furthermore, the simulated shadowgraphs represent the light distribution at the airfoil surface, i.e. they represent the most 'clean' or undisturbed shadowgraph. In reality, the light that forms the shadowgraph on the wing should still be reflected off the wing surface towards the camera which images the wing. Therefore, the effects of the surface reflection and the effects that the camera has on the image should be investigated. Last but not least, the current study analyzed two-dimensional flow fields and the corresponding one-dimensional shadowgraphs. This analysis should be extended to three-dimensional flow fields and two-dimensional shadowgraphs before the method can be used for experimental applications.

All topics mentioned for further study are points of uncertainty at this point. Since so many different factors, both theoretical and practical, might cause errors, it seems unfeasible that this method can be used for in-flight determination of the shock wave position, strength, and curvature at this point in time. It is therefore very unlikely that the relation found between shadowgraph characteristics and wing bound shock waves can be of practical use before the number of uncertainties is reduced by further research.

Another possible method that could be studied is the application of the BOS technique to measure wing bound shock waves during flight. For this application, the wing surface should be used as the background and a camera aimed at the wing should make the BOS images. Light refraction caused by a shock wave should distort the background pattern that is painted on the wing, hence revealing the presence of the shock wave. In order to quantify light deflections, a 'clean' undistorted image of the background will be needed. This image will be hard to obtain because the wing itself will move and change shape during flight, hence affecting the BOS background. Being able to account for these wing deflections will therefore be key to the success of this method.

The following list summarizes the topics that are recommended for further study:

- The theoretical relation found between the shadowgraph characteristics and the shock wave should be refined by using more sophisticated flow solvers. Furthermore, the light sources, used for the shadowgraph simulation, should be extended. For example, the circle of confusion of the sun should be taken into account.
- The effect of a camera and its position on the observed shadowgraph should be investigated. In other words, how is the shadowgraph affected when light is reflected off the wing surface, when it travels through the flow field a second time (from wing surface to camera), and how does the camera affect the image (diffraction effects)?
- The shadowgraph simulation method presented in this work should be extended to three-dimensional wings. In order to do this a three-dimensional flow solver should be used.
- If it is found that the camera position significantly influences the observed shadowgraph, it should be investigated if the simultaneous use of multiple cameras could reveal more information about the shock. Triangulation of the different shadowgraphs could be used to, for example, determine the exact location of a shock wave on a three-dimensional wing.
- The feasibility of using a BOS technique, where the wing surface is used as the background, to extract information about shock waves that occur on the wing should be investigated. The wing surface should be painted such that it has a non-uniform speckled pattern. This pattern would look deformed when it is viewed through a shock wave. This study should focus on the possibility of extracting useful data from such an image that is taken with a camera overlooking the wing (camera attached to the fuselage).

References

[1] D. F. Fisher, E. A. Haering Jr., G. K. Noffz, and J. I. Aguilar, "Determination of sun angles for observations of shock waves on a transport aircraft," tech. rep., NASA, 1998. TM-1998-206551.

[2] E. Hecht, *Optics*. Addison-Wesley, 4th ed., 2002.

[3] M. Vaughan, "Optics," in *PY3101 - Optics*, University College Cork, 2004. University Lecture Notes.

[4] H. W. Jensen, S. R. Marschner, M. Levoy, and P. Hanrahan, "A practical model for subsurface light transport," in *Proceedings of the 28th annual conference on Computer graphics and interactive techniques*, pp. 511–518, ACM, 2001.

[5] G. Settles, *Schlieren and Shadowgraph Techniques*. Springer-Verlag Berlin Heidelberg, 2001.

[6] G. E. Cooper and G. A. Rathert Jr., "Visual observations of shock wave in flight," tech. rep., NACA, 1948. RM. No. A8C25.

[7] G. Settles, "Schlieren and shadowgraph imaging in the great outdoors," in *The 2nd Pacific Symposium on Flow Visualization and Image Processing*, Pacific Center of Thermal-Fluids Engineering, Tokyo, 1999. Honolulu, USA.

[8] T. Tauer, D. Kunz, and N. Lindsley, "Visualization of nonlinear aerodynamic phenomena during f-16 limit-cycle oscillations," *Journal of Aircraft*, vol. 53, no. 3, pp. 865–870, 2016.

[9] P. Disimile, J. Davis, and N. Toy, "Mitigation of shock waves within a liquid filled tank," *International Journal of Impact Engineering*, vol. 38, no. 2-3, pp. 61–72, 2011.

[10] K.-H. Lee, T. Setoguchi, S. Matsuo, and H.-D. Kim, "Influence of the nozzle inlet configuration on under-expanded swirling jet," *Proceedings of the Institution of Mechanical Engineers, Part G: Journal of Aerospace Engineering*, vol. 220, no. 2, pp. 155–163, 2006.

[11] E. Hafenrichter, Y. Lee, J. Dutton, and E. Loth, "Normal shock/boundary-layer interaction control using aeroelastic mesoflaps," *Journal of Propulsion and Power*, vol. 19, no. 3, pp. 464–472, 2003.

[12] I. Kalkhoran, M. Smart, and A. Betti, "Interaction of supersonic wing-tip vortices with a normal shock," *AIAA Journal*, vol. 34, no. 9, pp. 1855–1861, 1996.

[13] T. R. Norman and J. S. Light, "Rotor tip vortex geometry measurements using the wide-field shadowgraph technique.," *Journal of the American Helicopter Society*, vol. 32, no. 2, pp. 40–50, 1987.

[14] M. J. Hargather and G. S. Settles, "Retroreflective shadowgraph technique for large-scale flow visualization," *Appl. Opt.*, vol. 48, pp. 4449–4457, Aug 2009.

[15] D. Hisley, "Blast2d computations of the reflection of planar shocks from wedge furfaces with comparison to sharc and stealth results," tech. rep., US Army Ballistic Research Lab, Aberdeen Proving Ground, Maryland USA, 1990. Report BRL-TR-3147.

[16] L. A. Yates, "Images reconstructied from computed flowfields," *AIAA journal*, vol. 31, no. 10, pp. 1877–1884, 1993.

[17] A. Bagai and J. Leishman, "Flow visualization of compressible vortex structures using density gradient techniques," *Experiments in Fluids*, vol. 15, no. 6, pp. 431–442, 1993.

[18] A. Thess and S. Orszag, "Surface-tension-driven benard convention at infinite prandtl number," *Journal of Fluid Mechanics*, vol. 283, pp. 201–230, 1995.

[19] W. Schopf, J. Patterson, and A. Brooker, "Evaluation of the shadowgraph method for the convective flow in a side-heated cavity," *Experiments in Fluids*, vol. 21, no. 5, pp. 331–340, 1996.

[20] M. Hargather and G. Settles, "Recent developments in schlieren and shadowgraphy," in *27th AIAA Aerodynamic Measurement Technology and Ground Testing Conference 2010*, American Institute of Aeronautics and Astronautics, 2010. Chicago, Illinois, USA.

[21] G. Elsinga, B. van Oudheusden, F. Scarano, and D. Watt, "Assessment and application of quantitative schlieren methods: Calibrated color schlieren and background oriented schlieren," *Experiments in Fluids*, vol. 36, no. 2, pp. 309–325, 2004.

[22] H. Richard and M. Raffel, "Principle and applications of the background oriented schlieren (bos) method," *Measurement Science and Technology*, vol. 12, no. 9, pp. 1576–1585, 2001.

[23] M. J. Hargather and G. S. Settles, "Natural-background-oriented schlieren imaging," *Experiments in Fluids*, vol. 48, no. 1, pp. 59–68, 2009.

[24] P. Merlin, "Ground-based schlieren technique looks to the sun and moon." http://www.nasa.gov/feature/ground-based-schlieren-technique-looks-to-the-sun-and-moon, September 2015. Acccessed 26/Jan/2016.

[25] P. Merlin, "Schlieren images reveal supersonic shock waves." http://www.nasa.gov/centers/armstrong/features/shock_and_awesome.html, August 2015. Acccessed 26/Jan/2016.

[26] J. Delery and R. Bur, "The physics of shock wave/boundary layer interaction control: last lessons learned," in *European Congress on Computational Methods in Applied Sciences and Engineering, Barcelone 11-14 September 2014*, no. 181, OFFICE NATIONAL D ETUDES ET DE RECHERCHES AEROSPATIALES ONERA-PUBLICATIONS-TP, 2000.

[27] H. Pearcey, "Some effects of shock-induced separation of turbulent boundary layers in transonic flow past aerofoils," tech. rep., AERONAUTICAL RESEARCH COUNCIL REPORTS AND MEMORANDA, 1955. R. & M. No. 3108.

[28] J. Delery and J. Marvin, "Shock-wave boundary layer interaction," tech. rep., AGARD, NATO, 1986. AGARD-AG-280.

[29] L. East, "Application of a laser anemometer to the investigation of shock-wave boundary-layer interactions.," *AGARD Conf Proc*, no. 193, 1976.

[30] E. MURMAN and J. COLE, "CALCULATION OF PLANE STEADY TRANSONIC FLOWS," *AIAA JOURNAL*, vol. 9, no. 1, pp. 114–121, 1971.

[31] E. M. Murman, "Analysis of embedded shock waves calculated by relaxation methods," *AIAA Journal*, vol. 12, no. 5, pp. 626–633, 1974.

[32] E. D. Knechtel, *Experimental investigation at transonic speeds of pressure distributions over wedge and circular-arc airfoil sections and evaluation of perforated-wall.* National Aeronautics and Space Administration, 1959. Technical Note D-15.

[33] D. J. Collins and J. A. Krupp, "Experimental and theoretical investigations in two-dimensional transonic flow," *AIAA Journal*, vol. 12, no. 6, pp. 771–778, 1974.

[34] R. Bohning and J. Zierep, "Normal shock-turbulent boundary layer interaction at a curved wall.," No. 291, pp. 17. 1–17. 8, 1981.

[35] C. D. Harris, "Nasa supercritical airfoils: a matrix of family-related airfoils," tech. rep., NASA, 1990. NASA Technical Papers 2969.

[36] J. Westerweel, "Effect of sensor geometry on the performance of piv interrogation," in *Laser Techniques Applied to Fluid Mechanics*, pp. 37–55, Springer Berlin Heidelberg, 2000. Ninth International Symposium on Applications of Laser Techniques to Fluid Mechanics, Lisbon, Portugal, July 13-16, 1998.

[37] J. Delery, "Shock wave/turbulent boundary layer interaction and its control," *Progress in Aerospace Sciences*, vol. 22, no. 4, pp. 209–280, 1985.

[38] J. D. Anderson, *Introduction to Flight.* McGraw-Hill, 1978.

[39] L. Clancy, *Aerodynamics.* Pitman Aeronautical Engineering Series, Wiley, 1975.

[40] B. Dunbar, "Fact sheets: The supercritical airfoil." `http://www.nasa.gov/centers/dryden/about/Organizations/Technology/Facts/TF-2004-13-DFRC.html`, March 2008. Acccessed 12/May/2016.

[41] T. G. Ayers, "Supercritical aerodynamics worthwhile over a range of speeds.," *Astronaut Aeronaut*, vol. 10, no. 8, pp. 32–36, 1972.

[42] D. Dolling, "Fifty years of shock-wave/boundary-layer interaction research: What next?," *AIAA Journal*, vol. 39, no. 8, pp. 1517–1531, 2001.

[43] J. P. Crowder, "Flow visualization techniques applied to full-scale vehicles," in *14th Atmospheric Flight Mechanics Conference*, pp. 164–171, AIAA (American Institute of Aeronautics and Astronautics), 1987. Monterey, CA.

[44] L. M. Weinstein, "An optical technique for examining aircraft shock wave structures in flight," in *High-Speed Research: 1994 Sonic Boom Workshop*, pp. 1–17, NASA CP 3279, 1994.

[45] P. Doerffer, *UFAST Project – Unsteady Effects in Shock Wave Induced Separation*, pp. 345–347. Berlin, Heidelberg: Springer Berlin Heidelberg, 2010.

[46] L. M. Weinstein, K. Stacy, G. J. Vieira, E. A. Haering Jr., and A. H. Bowers, "Imaging supersonic aircraft shock waves," *Journal of Flow Visualization and Image Processing*, vol. 4, no. 3, pp. 189–199, 1997. NASA Langley Research Center.

[47] D. F. Fisher and R. R. Meyer Jr., "Flow visualization techniques for flight research," tech. rep., NASA, 1988. TM-100455.

[48] R. Kidd, J. Ardini, and A. Anton, "Evolution of the modern photon," *American Journal of Physics*, vol. 57, no. 1, pp. 27–35, 1989.

[49] A. Sommerfeld, *Optics.* Lectures on theoretical physics, New York: Academic Press, 1964.

[50] S. Nayar, K. Ikeuchi, and T. Kanade, "Surface reflection: physical and geometrical perspectives," *Pattern Analysis and Machine Intelligence, IEEE Transactions on*, vol. 13, pp. 611–634, Jul 1991.

[51] F. Pedrotti, L. Pedrotti, and L. Pedrotti, *Introduction to Optics*. Always Learning, Pearson Education, Limited, 2013.

[52] W. Smith, *Modern Optical Engineering, 4th Ed.* McGraw Hill professional, McGraw-Hill Education, 2007.

[53] R. J. Goldstein and T. H. Kuehn, "Optical systems for flow measurements - shadowgraph, schlieren, and interferometric techniques," in *Fluid Mechanics Measurements*, ch. 8, pp. 377–397, Berlin: Springer-Verlag, 1 ed., 1983.

[54] H. Jebsen-Marweder, ""shlieren" als wort, gebilde und begriffe," *Glastechniche Berichte*, vol. 33, no. 12, pp. 475–477, 1960.

[55] H. Schardin, "Die schlierenverfahren und ihre anwendungen," in *Ergebnisse der exakten naturwissenschaften*, vol. 20 of *Ergebnisse der Exakten Naturwissenschaften*, pp. 303–439, Springer Berlin Heidelberg, 1942. English translation available as NASA TT F-12731, April 1970 (N70-25586).

[56] F. Weinberg, *Optics of Flames: Including Methods for the Study of Refractive Index Fields in Combustion and Aerodynamics*. London: Butterworths, 1963.

[57] H. Hannes, "Über die eigenschaften des schattenverfahrens," *Optik*, vol. 13, no. 1, pp. 34–48, 1956.

[58] G. Meier, "Hintergrund-schlierenmeßverfahren," June 21 2000. DE Patent App. DE 199 42 856 A1.

[59] G. Meier, "Computerized background-oriented schlieren," *Experiments in Fluids*, vol. 33, no. 1, pp. 181–187, 2002.

[60] S. B. Dalziel, G. O. Hughes, and B. R. Sutherland, "Synthetic schlieren," in *Proceedings of the 8th International Symposium on Flow Visualization* (G. M. Carlomagno, ed.), no. 62, (Sorrento, Italy), 1998.

[61] B. Sutherland, S. Dalziel, G. Hughes, and P. Linden, "Visualization and measurement of internal waves by 'synthetic schlieren'. part 1. vertically oscillating cylinder," *Journal of Fluid Mechanics*, vol. 390, pp. 93–126, 1999.

[62] S. Parthasarathy, Y. Cho, and L. Back, "Wide-field shadowgraphy of tip vortices from a helicopter rotor," *AIAA journal*, vol. 25, no. 1, pp. 64–70, 1987.

[63] R. D. Bowersox, J. A. Schetz, and R. W. Conners, "Digital analysis of shadowgraph images for statistical index of refraction (density) turbulent fluctuation properties in high-speed flow," *Measurement*, vol. 15, no. 3, pp. 201 – 209, 1995.

[64] S. Minardi, A. Gopal, M. Tatarakis, A. Couairon, G. Tamošauskas, R. Piskarskas, A. Dubietis, and P. D. Trapani, "Time-resolved refractive index and absorption mapping of light-plasma filaments in water," *Opt. Lett.*, vol. 33, pp. 86–88, Jan 2008.

[65] A. Gopal, S. Minardi, and M. Tatarakis, "Quantitative two-dimensional shadowgraphic method for high-sensitivity density measurement of under-critical laser plasmas," *Opt. Lett.*, vol. 32, pp. 1238–1240, May 2007.

[66] M. Raffel, H. Richard, and G. Meier, “On the applicability of background oriented optical tomography for large scale aerodynamic investigations,” *Experiments in Fluids*, vol. 28, no. 5, pp. 477–481, 2000.

[67] E. Houghton, P. Carpenter, S. Collicott, and D. Valentine, *Aerodynamics for Engineering Students*. Elsevier Science, 2012.

[68] J. D. Anderson, *Fundamentals of Aerodynamics*. McGraw-Hill, 2006.

[69] E. M. Murman and J. A. Krupp, *Proceedings of the Second International Conference on Numerical Methods in Fluid Dynamics: September 15–19, 1970 University of California, Berkeley*, ch. Solution of the transonic potential equation using a mixed finite difference system, pp. 199–206. Berlin, Heidelberg: Springer Berlin Heidelberg, 1971.

[70] E. M. Murman, *Proceedings of the Third International Conference on Numerical Methods in Fluid Mechanics: Vol. II Problems of Fluid Mechanics*, ch. A relaxation method for calculating transonic flows with detached bow shocks, pp. 201–205. Berlin, Heidelberg: Springer Berlin Heidelberg, 1973.

[71] J. Krupp and E. Murman, “Computation of transonic flows past lifting airfoils and slender bodies,” *AIAA Journal*, vol. 10, no. 7, pp. 880–886, 1972.

[72] J.-J. Chattot, *Computational Aerodynamics and Fluid Dynamics: An Introduction*, ch. The Method of Murman and Cole, pp. 81–92. Berlin, Heidelberg: Springer Berlin Heidelberg, 2002.

[73] M. Langley, “Numerical methods for two-dimensional and axisymmetric transonic flows,” tech. rep., AERONAUTICAL RESEARCH COUNCIL CURRENT PAPERS, 1977. C.P. No. 1376.

[74] R. Bohning and J. Zierep, “Der senkrechte verdichtungsstoss an der gekrümmten wand unter bercksichtigung der reibung,” *Zeitschrift fr angewandte Mathematik und Physik ZAMP*, vol. 27, no. 2, pp. 225–240, 1976.

[75] R. Bohning and J. Zierep, “Bedingung fr das einsetzen der ablösung der turbulenten grenzschicht an der gekrmmten wand mit senkrechtem verdichtungsstoss,” *Zeitschrift fr angewandte Mathematik und Physik ZAMP*, vol. 29, no. 2, pp. 190–198, 1978.

[76] B. Koren and W. Bannink, “Transonic shock wave-boundary layer interaction at a convex wall.,” *Delft progress report*, vol. 9, no. 3, pp. 155–169, 1984.

[77] J. Zierep, “Der senkrechte verdichtungsstoss am gekrümmten profil,” *Zeitschrift für angewandte Mathematik und Physik ZAMP*, vol. 9, no. 5, pp. 764–776, 1958.

[78] J. Zierep, “New results for the normal shock in inviscid flow at a curved surface,” *ZAMM - Journal of Applied Mathematics and Mechanics / Zeitschrift fr Angewandte Mathematik und Mechanik*, vol. 83, no. 9, pp. 603–610, 2003.

[79] R. Bohning, *Recent Developments in Theoretical and Experimental Fluid Mechanics: Compressible and Incompressible Flows*, ch. Untersuchung der Nachexpansion hinter einem senkrechten Verdichtungsstoß an der gekrümmten Wand, pp. 39–47. Berlin, Heidelberg: Springer Berlin Heidelberg, 1979.

[80] A. Sharma, D. Kumar, and A. Ghatak, “Tracing rays through graded-index media: A new method.,” *Applied Optics*, vol. 21, no. 6, pp. 984–987, 1982.

[81] S. Dorić, "Ray tracing through gradient-index media: recent improvements," *Appl. Opt.*, vol. 29, pp. 4026–4029, Oct 1990.

[82] R. Fox, A. McDonald, and P. Pritchard, *Introduction to fluid mechanics*. Wiley, 6 ed., 2004.

[83] E. Doebelin, *Measurement Systems*. New York: McGraw-Hill, 4 ed., 1990.

[84] J. Stewart, *Calculus Early Transcendentals*. Thomson Brooks/Cole, 6 ed., 2008.

[85] NOAA, NASA, USAF, "Us standard atmosphere (1976)," *Washington DC*, 1976.

[86] C.-S. Guo, L. Zhang, Z.-Y. Rong, and H.-T. Wang, "Effect of the fill factor of ccd pixels on digital holograms: comment on the papers frequency analysis of digital holography and frequency analysis of digital holography with reconstruction by convolution," *Optical Engineering*, vol. 42, no. 9, pp. 2768–2771, 2003.

[87] R. Theunissen, "Improvements in hybrid piv/ptv algorithms and droplet sizing," msc thesis, Delft University of Technology, 2003. Graduation work performed at Von Karman Institute for Fluid Dynamics.

APPENDIX A. U.S. Standard Atmosphere

The U.S. standard atmosphere is used in this report to determine the total temperature, pressure, and density at the specified flight altitude [85]. Since the normal flight altitudes are normally within the troposphere (up to 11,000 m), only the calculations for the troposphere a used here.

The following procedure is used: First, the total temperature is determined at the specified flight altitude using Equation A.1, where 288.15 K is the reference temperature at sea level, a_{temp} is the temperature gradient, and h is the flight altitude. Secondly, the total pressure at the flight altitude is determined using Equation A.2, where 101325 Pa is the reference pressure at sea level, g is the standard gravity or gravitational acceleration at sea level, and R is the specific gas constant for dry air. Lastly, the total density is determined using the perfect gas law, as seen in Equation A.3.

$$T_t = 288.15 + a_{temp} * h = 288.15 + -0.0065 * h \tag{A.1}$$

$$p_t = 101325 \left(\frac{T_t}{288.15} \right)^{\frac{-g}{a_{temp} R}} = 101325 \left(\frac{T_t}{288.15} \right)^{\frac{-9.81}{-0.0065*287.05}} \tag{A.2}$$

$$\rho_t = \frac{p_t}{R T_t} \tag{A.3}$$

APPENDIX B. Pixel mean intensity

The intensity that a pixel measures is determined by the amount of light that falls on it, thus the size of the pixel and the illumination of the pixel determine the pixel intensity. However, it could be so that only part of a pixel is illuminated. Hence, an integration of the illumination over the pixel area has to be performed in order to determine the mean pixel intensity [86]. It should be noted, however, that not the entire area of a pixel is sensitive to light [36, 86]. Figure B.1 shows a zoom in of a pixel where the pixel area is defined as d_r^2 and the light sensitive area is defined as a^2. The pixel fill factor p_f is usually defined as the light sensitive pixel area divided by the total pixel area. However, Gou et al. [86] used fill factors for the two directions of the pixel. This notation will be followed, thus the pixel fill factor will be defined as $p_f^2 = a^2/d_r^2$ or $p_f = a/d_r$, assuming pixel has the same width and height and the same pixel fill factor ratios for the width and height.

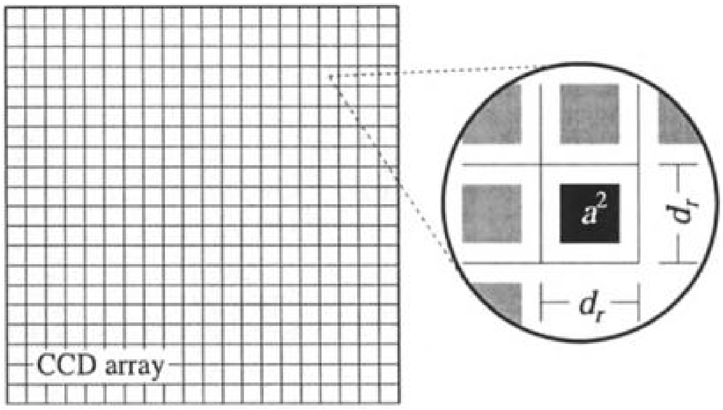

Figure B.1: Schematic representation of a CCD sensor array [36]

The mean pixel intensity can be determined with Equation B.1 where the light intensity over the light sensitive pixel area is integrated and divided by the light sensitive pixel area in order to obtain the mean pixel intensity. The light sensitive pixel area is defined as $A = p_f^2 dx_p dy_p$.

$$I_{pixel}(x_p, y_p) = \frac{1}{A} \int_{x_p - p_f \frac{dx_p}{2}}^{x_p + p_f \frac{dx_p}{2}} \int_{y_p - p_f \frac{dy_p}{2}}^{y_p + p_f \frac{dy_p}{2}} I(x, y) dy dx \tag{B.1}$$

Following the work of Theunissen [87], Equation B.1 can be written as Equation B.2 when a Gaussian with standard deviation σ and its center at (x_g, y_g) is used. The use of a Gaussian distribution for each light ray provides a good approximation to transform the light distribution from discrete rays to a continuous light distribution. Equation B.2 can be rewritten, using the error function defined is Equation B.3. Using the relation between t of the error function and x or y of the Gaussian distribution, defined in Equation B.4, and changing the integration limit as shown in Equation B.5, Equation B.2 can be rewritten to Equation B.6.

$$
\begin{aligned}
I_{pixel}(x_p, y_p) =& \frac{I_0}{A} \int_{x_p - p_f \frac{dx_p}{2}}^{x_p + p_f \frac{dx_p}{2}} \int_{y_p - p_f \frac{dy_p}{2}}^{y_p + p_f \frac{dy_p}{2}} e^{-\frac{(x-x_g)^2}{2\sigma^2}} e^{-\frac{(y-y_g)^2}{2\sigma^2}} dy dx \\
=& \frac{I_0}{A} \left[\int_0^{x_p + p_f \frac{dx_p}{2}} e^{-\frac{(x-x_g)^2}{2\sigma^2}} dx - \int_0^{x_p - p_f \frac{dx_p}{2}} e^{-\frac{(x-x_g)^2}{2\sigma^2}} dx \right] \cdot \\
& \left[\int_0^{y_p + p_f \frac{dy_p}{2}} e^{-\frac{(y-y_g)^2}{2\sigma^2}} dy - \int_0^{y_p - p_f \frac{dy_p}{2}} e^{-\frac{(y-y_g)^2}{2\sigma^2}} dy \right]
\end{aligned} \tag{B.2}
$$

$$
erf(x) = \frac{2}{\sqrt{\pi}} \int_0^x e^{-t^2} dt \tag{B.3}
$$

$$
t = \frac{(x - x_g)}{\sqrt{2}\sigma} \quad \Rightarrow \quad dt = \frac{dx}{\sqrt{2}\sigma} \tag{B.4}
$$

$$
\begin{aligned}
x = 0 \quad &\rightarrow \quad t = \frac{(-x_g)}{\sqrt{2}\sigma} \\
x = x_p + p_f \frac{dx_p}{2} \quad &\rightarrow \quad t = \frac{(x_p + p_f \frac{dx_p}{2} - x_g)}{\sqrt{2}\sigma}
\end{aligned} \tag{B.5}
$$

$$
\begin{aligned}
I_{pixel}(x_p, y_p) =& \frac{I_0}{A} \left(\sqrt{2}\sigma \frac{\sqrt{\pi}}{2} \right)^2 \left[erf\left(\frac{(x_p + p_f \frac{dx_p}{2} - x_g)}{\sqrt{2}\sigma} \right) - erf\left(\frac{(x_p - p_f \frac{dx_p}{2} - x_g)}{\sqrt{2}\sigma} \right) \right] \cdot \\
& \left[erf\left(\frac{(y_p + p_f \frac{dy_p}{2} - y_g)}{\sqrt{2}\sigma} \right) - erf\left(\frac{(y_p - p_f \frac{dy_p}{2} - y_g)}{\sqrt{2}\sigma} \right) \right]
\end{aligned} \tag{B.6}
$$

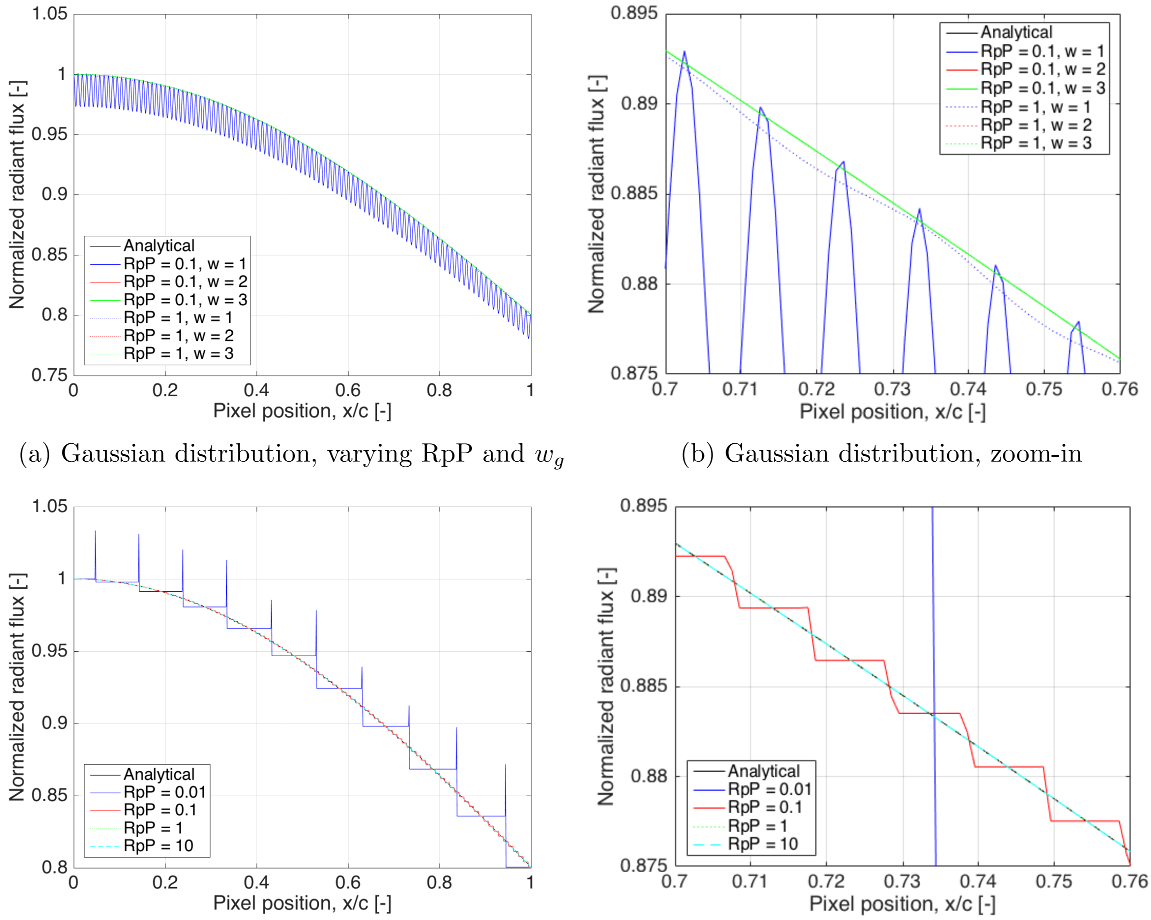

(a) Gaussian distribution, varying RpP and w_g

(b) Gaussian distribution, zoom-in

(c) Step function, varying RpP

(d) Step function, zoom-in

Figure C.1: Radiant flux at surface for test case 1b

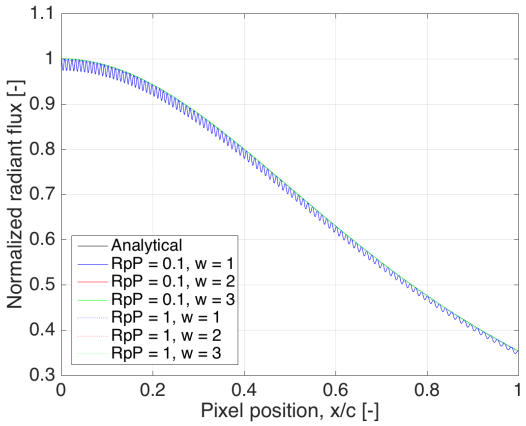

(a) Gaussian distribution, varying RpP and w_g

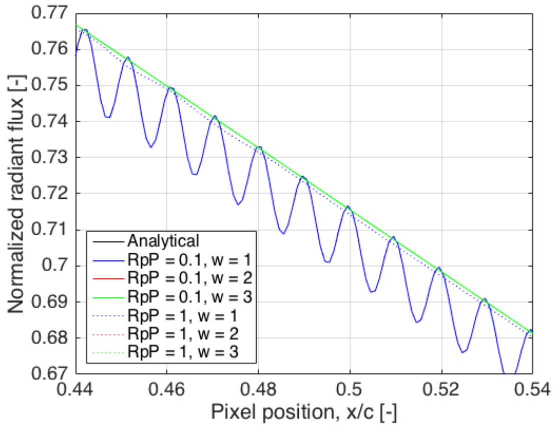

(b) Gaussian distribution, zoom-in

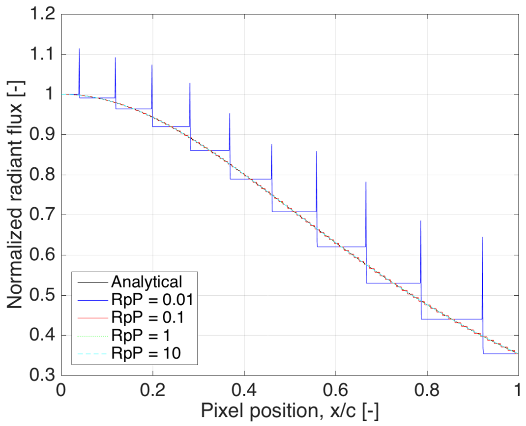

(c) Step function, varying RpP

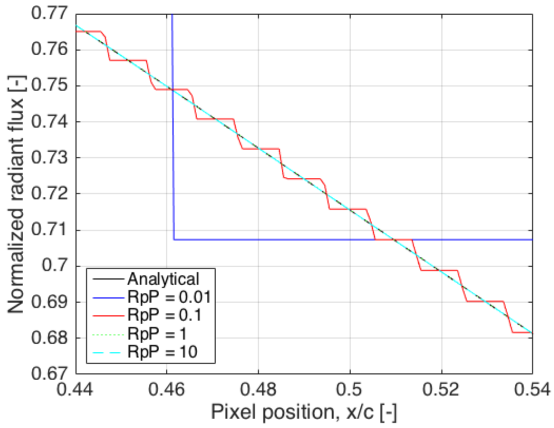

(d) Step function, zoom-in

Figure C.2: Radiant flux at surface for test case 1c

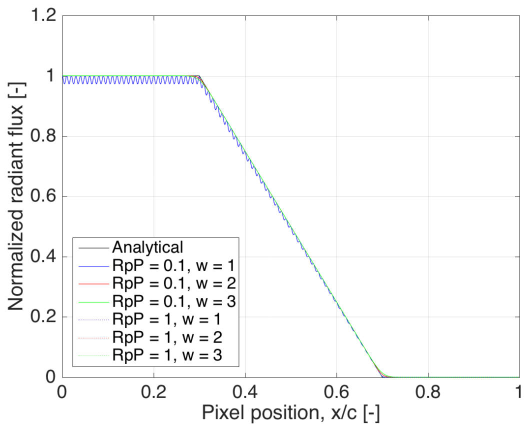

(a) Gaussian distribution, varying RpP and w_g

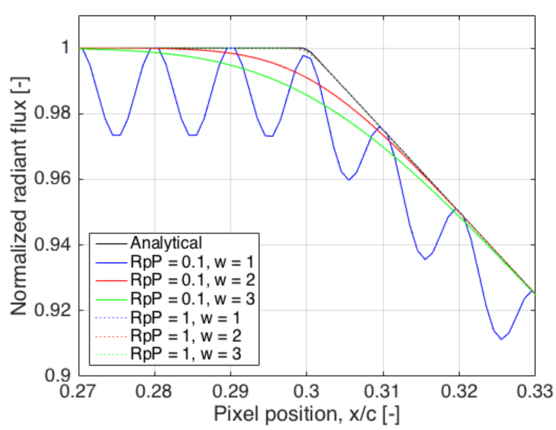

(b) Gaussian distribution, zoom-in

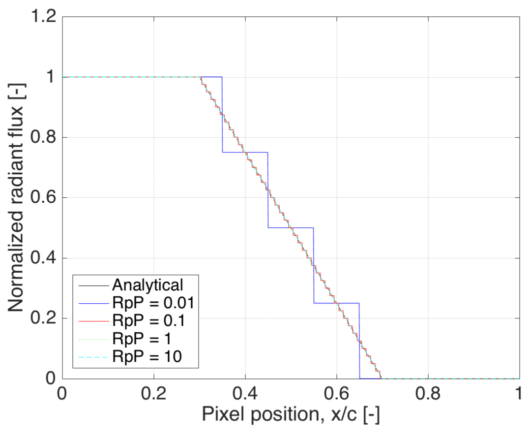

(c) Step function, varying RpP

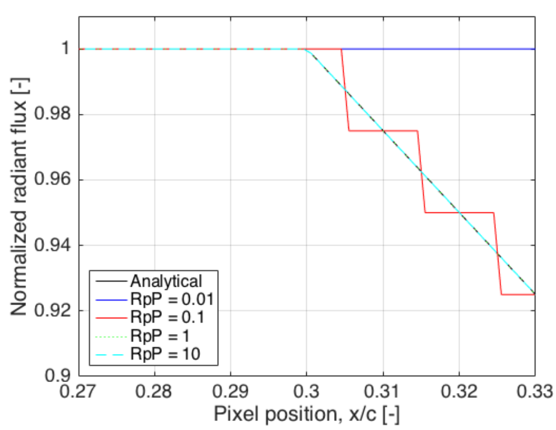

(d) Step function, zoom-in

Figure C.3: Radiant flux at surface for test case 2b

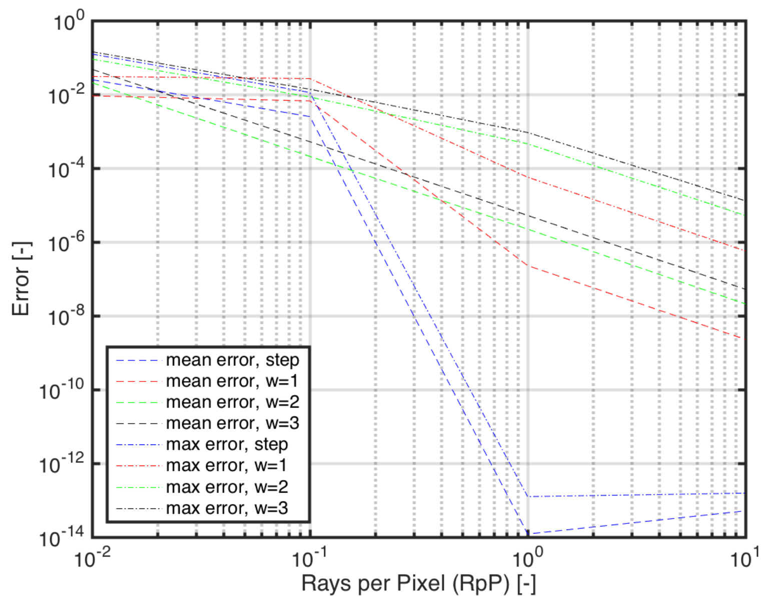

Figure C.4: Mean and maximum errors for different light distribution functions for test case 2b

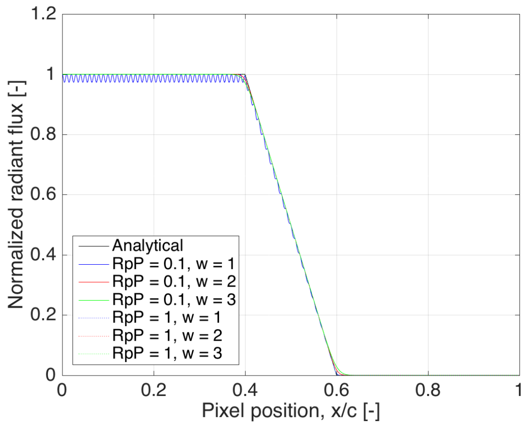

(a) Gaussian distribution, varying RpP and w_g

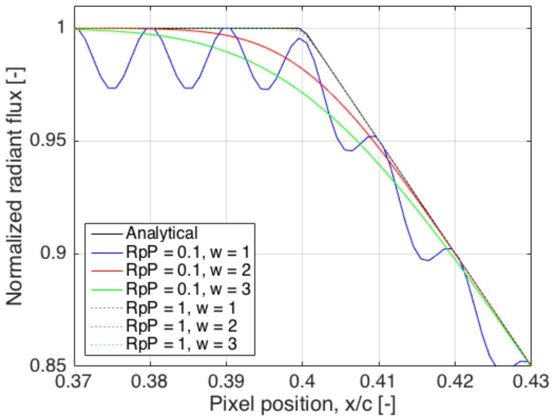

(b) Gaussian distribution, zoom-in

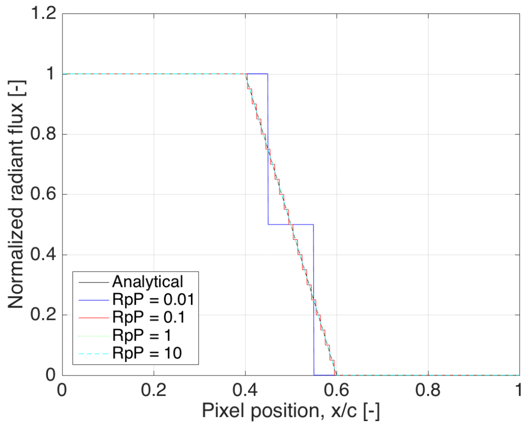

(c) Step function, varying RpP

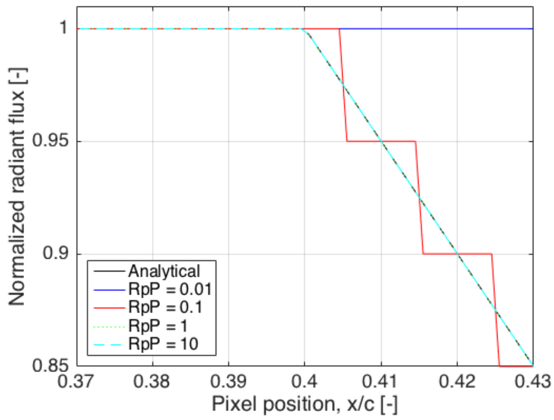

(d) Step function, zoom-in

Figure C.5: Radiant flux at surface for test case 2c

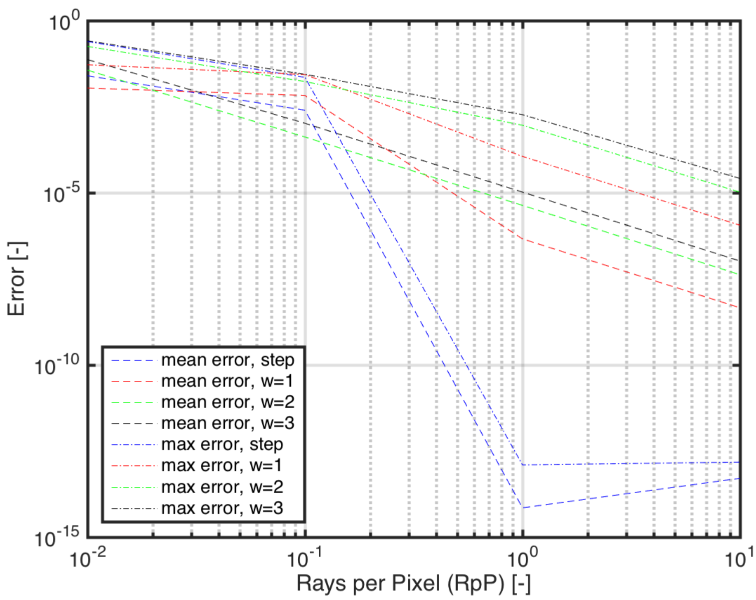

Figure C.6: Mean and maximum errors for different light distribution functions for test case 2c

It should be noted that the airfoil runs from $x = -1$ to $x = 1$ in the flow field graphs in both Appendix D, Appendix E, and Appendix F. This is in accordance with the method presented by Murman and Cole [30].

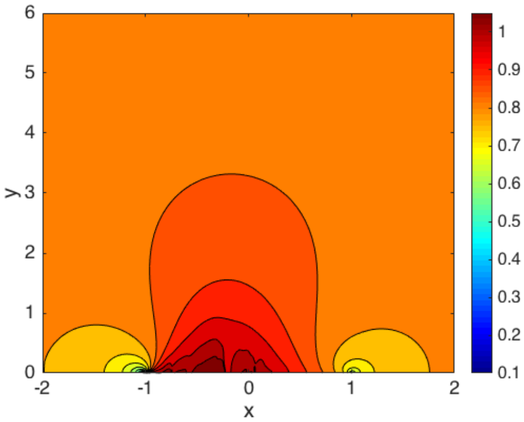

(a) $M_\infty = 0.83$

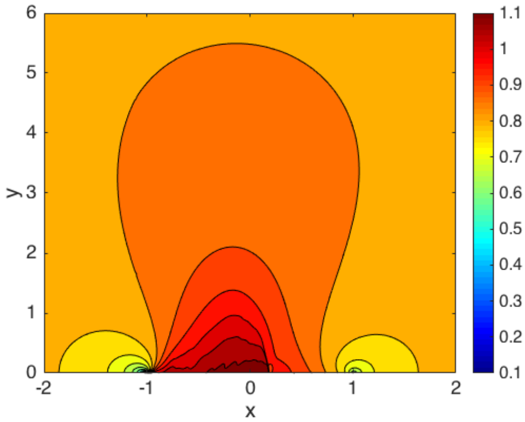

(b) $M_\infty = 0.84$

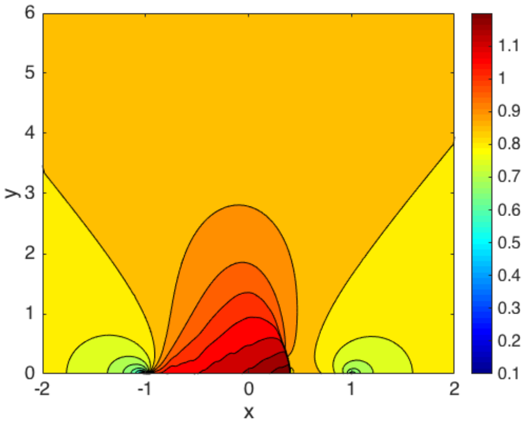

(c) $M_\infty = 0.85$

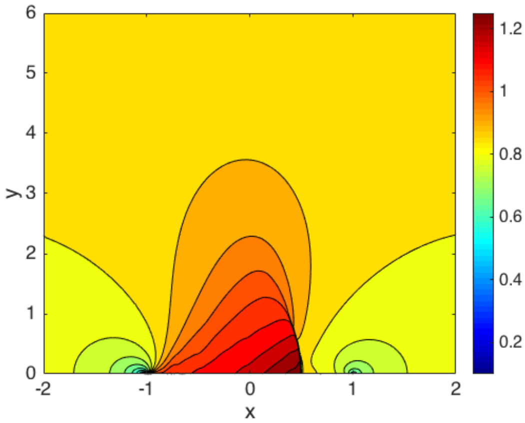

(d) $M_\infty = 0.86$

Figure D.1: Mach number contour plots, SC(2)-0410 airfoil, fine mesh

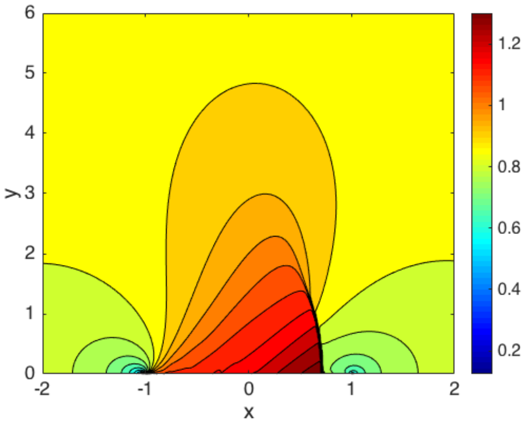

(a) $M_\infty = 0.87$

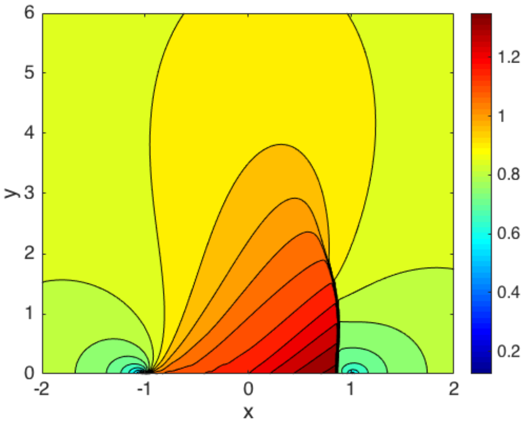

(b) $M_\infty = 0.88$

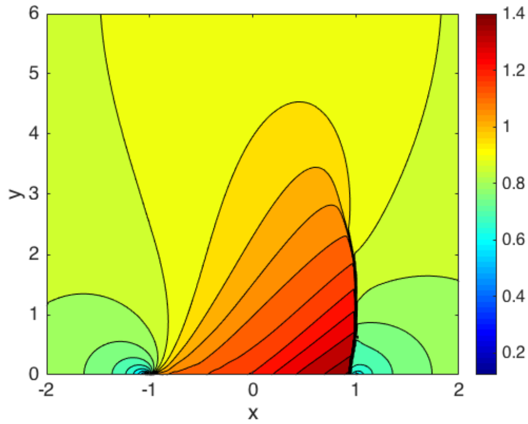

(c) $M_\infty = 0.89$

Figure D.2: Mach number contour plots, SC(2)-0410 airfoil, coarser mesh

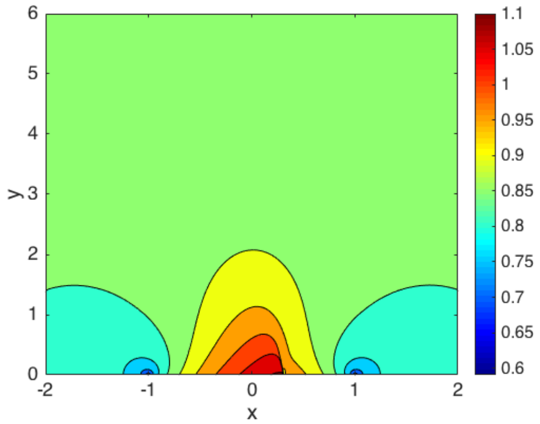

(a) $M_\infty = 0.86$

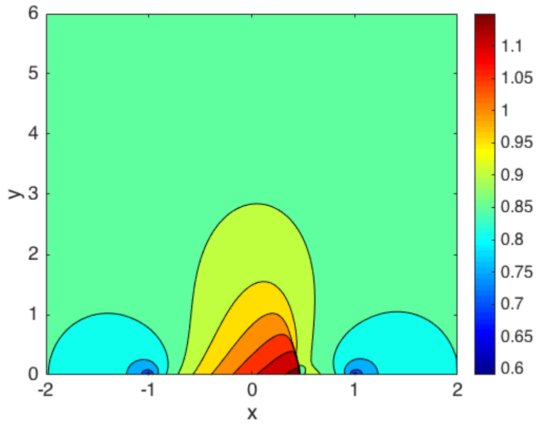

(b) $M_\infty = 0.87$

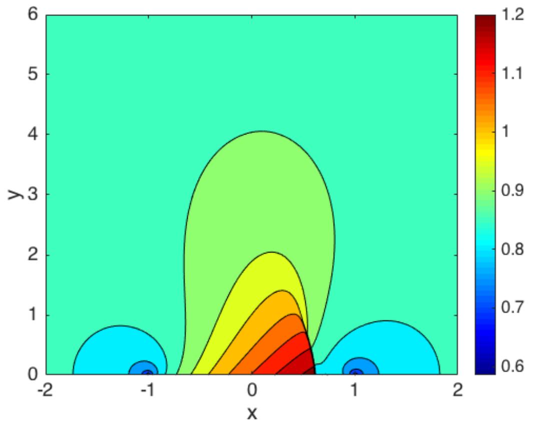

(c) $M_\infty = 0.88$

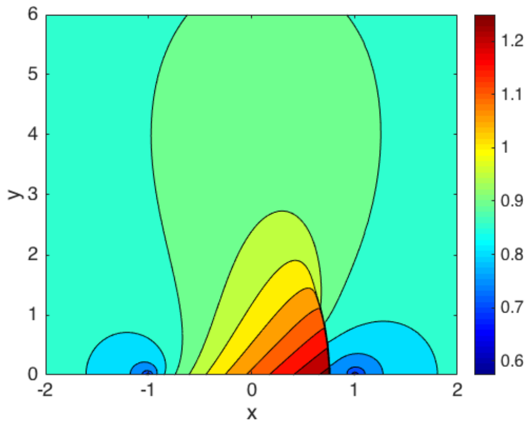

(d) $M_\infty = 0.89$

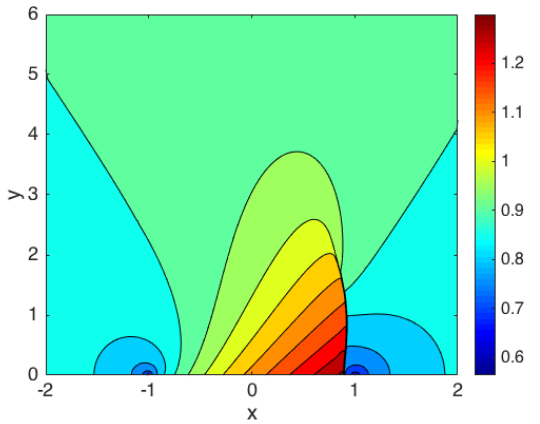

(e) $M_\infty = 0.9$

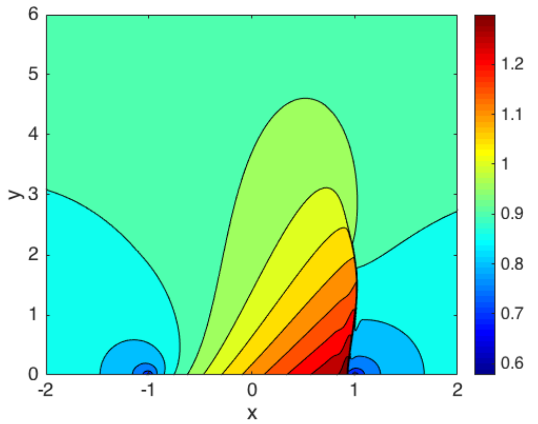

(f) $M_\infty = 0.91$

Figure E.1: Mach number contour plots, 6% parabolic arc airfoil, fine mesh

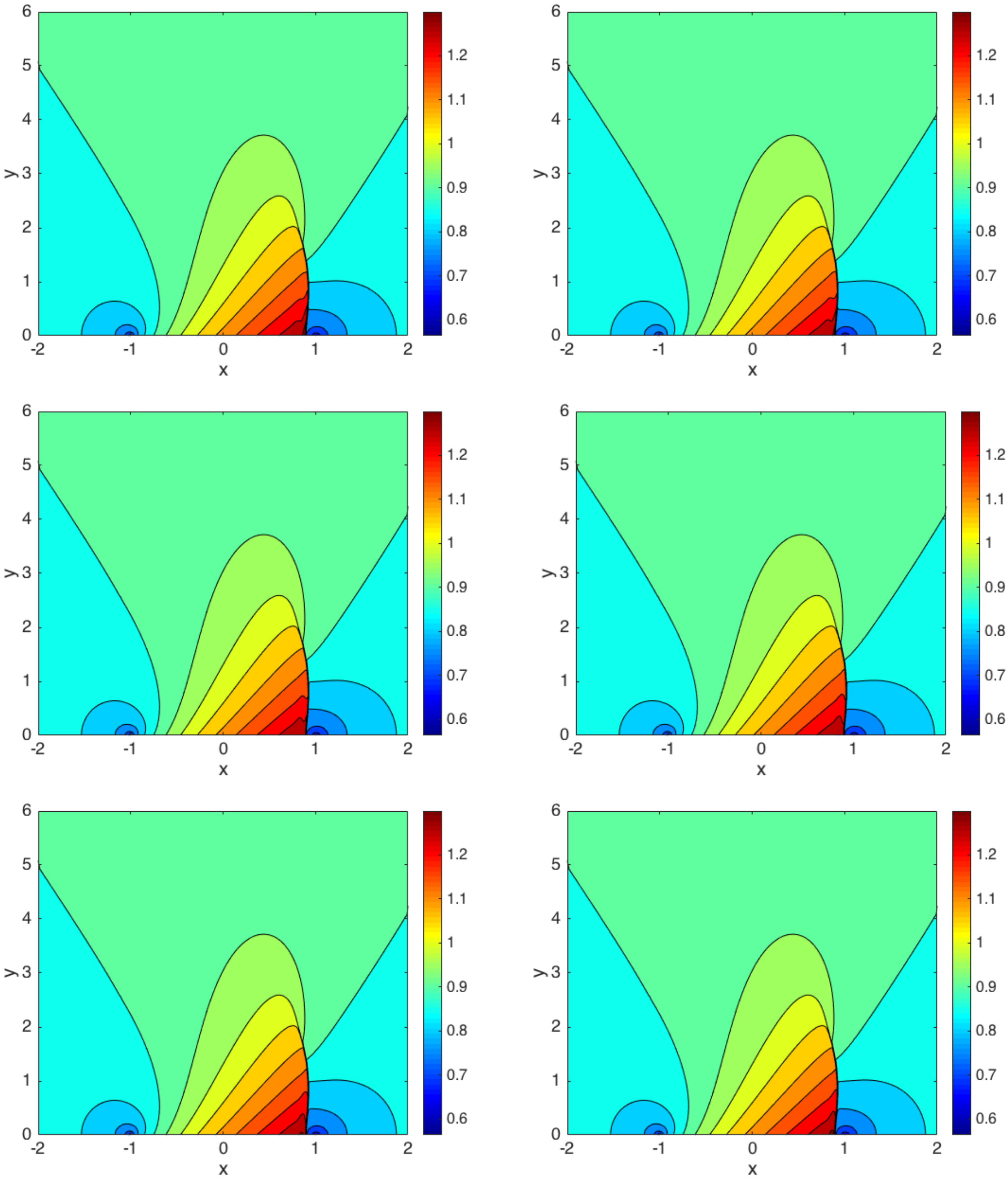

Figure F.1: Mach number contour plots for $M_\infty = 0.9$ flow fields with instabilities near the shock foot, 6% parabolic arc airfoil

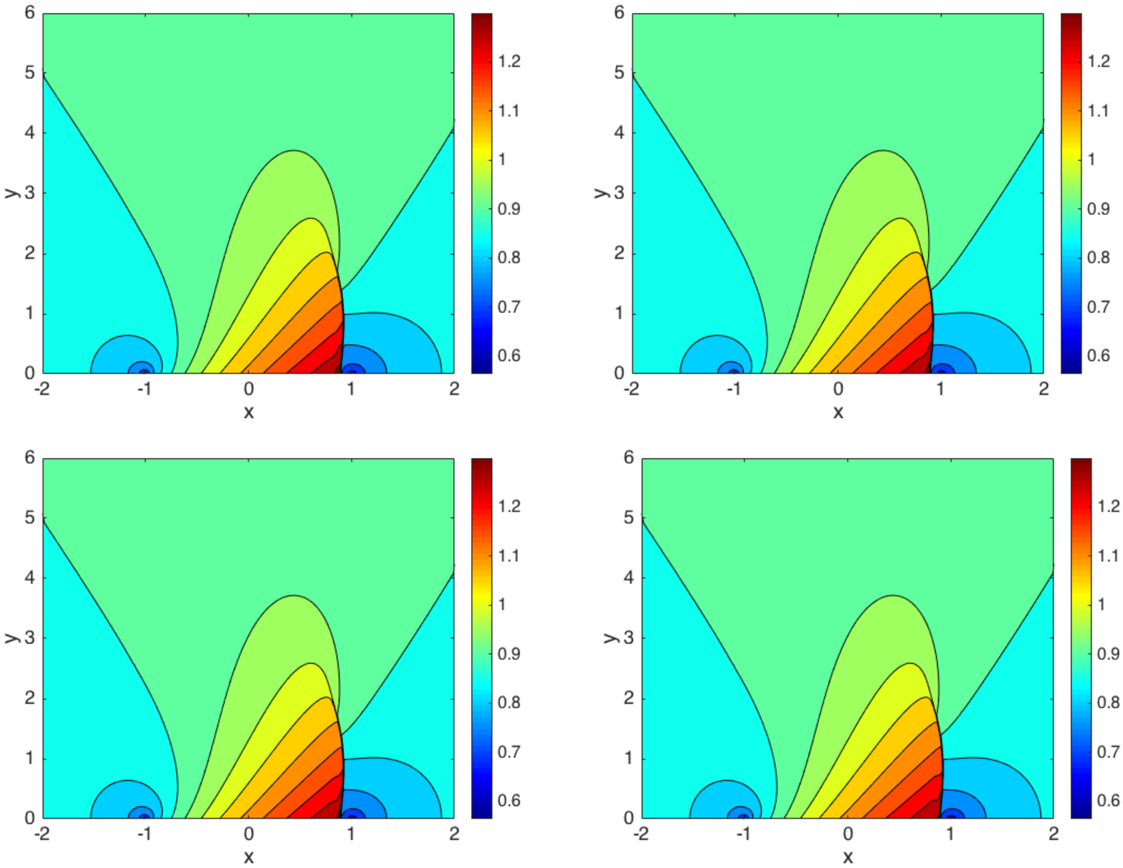

Figure F.2: Mach number contour plots for $M_\infty = 0.9$ flow fields with instabilities near the shock foot, 6% parabolic arc airfoil

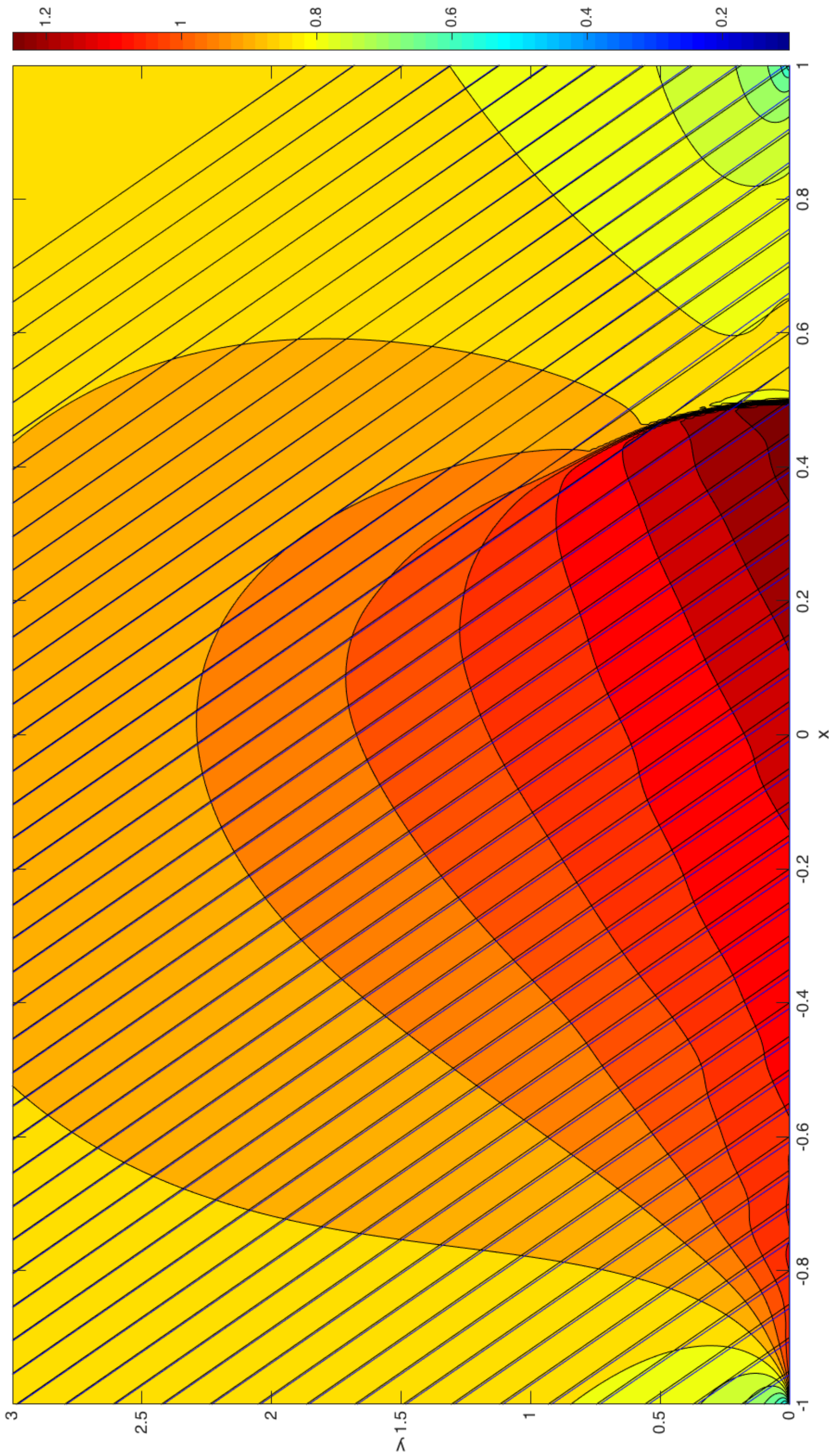

Figure G.1: Deflected and straight light rays for $\theta_{ray} = 15°$

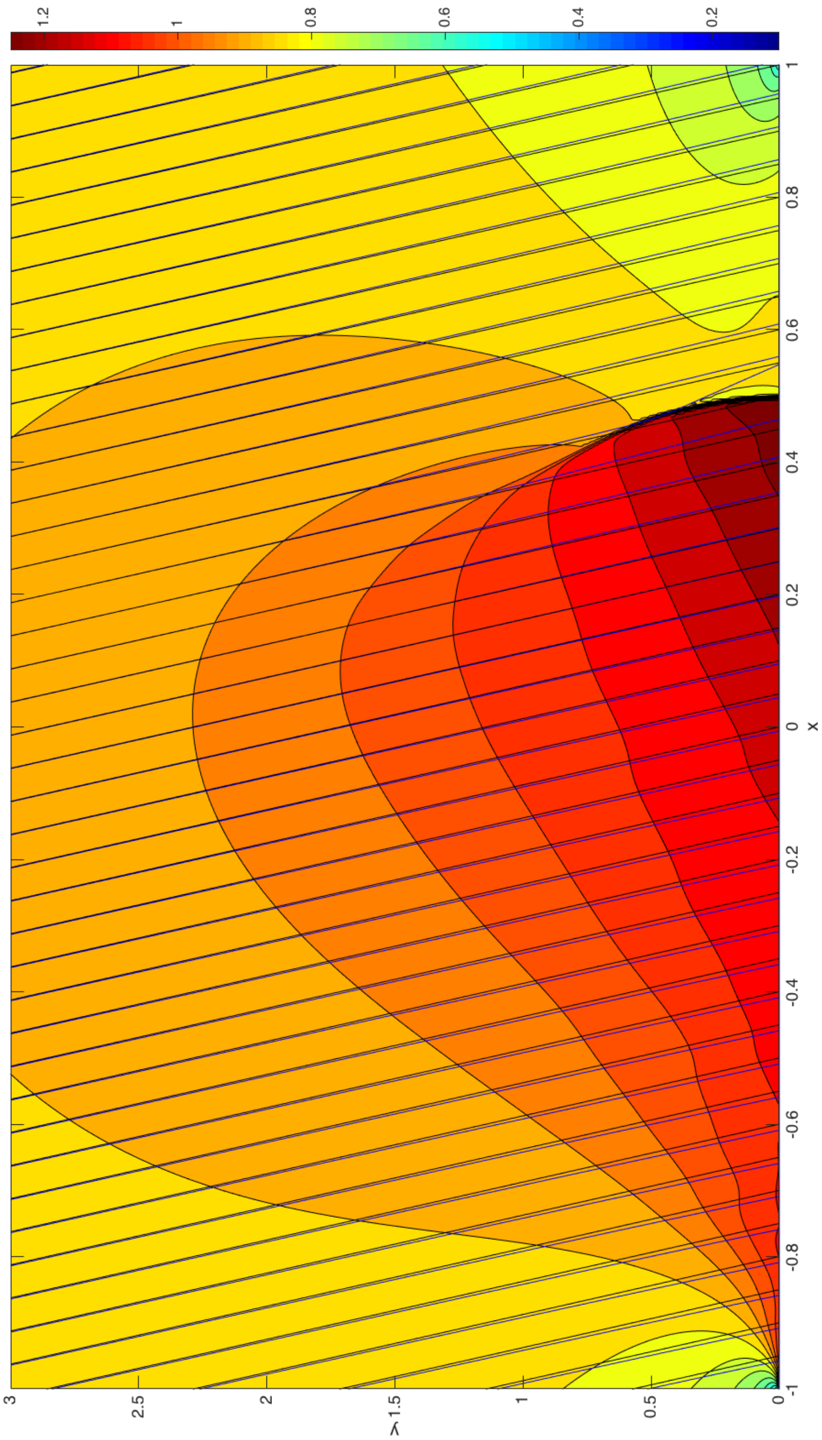

Figure G.2: Deflected and straight light rays for $\theta_{ray} = 5^{\circ}$

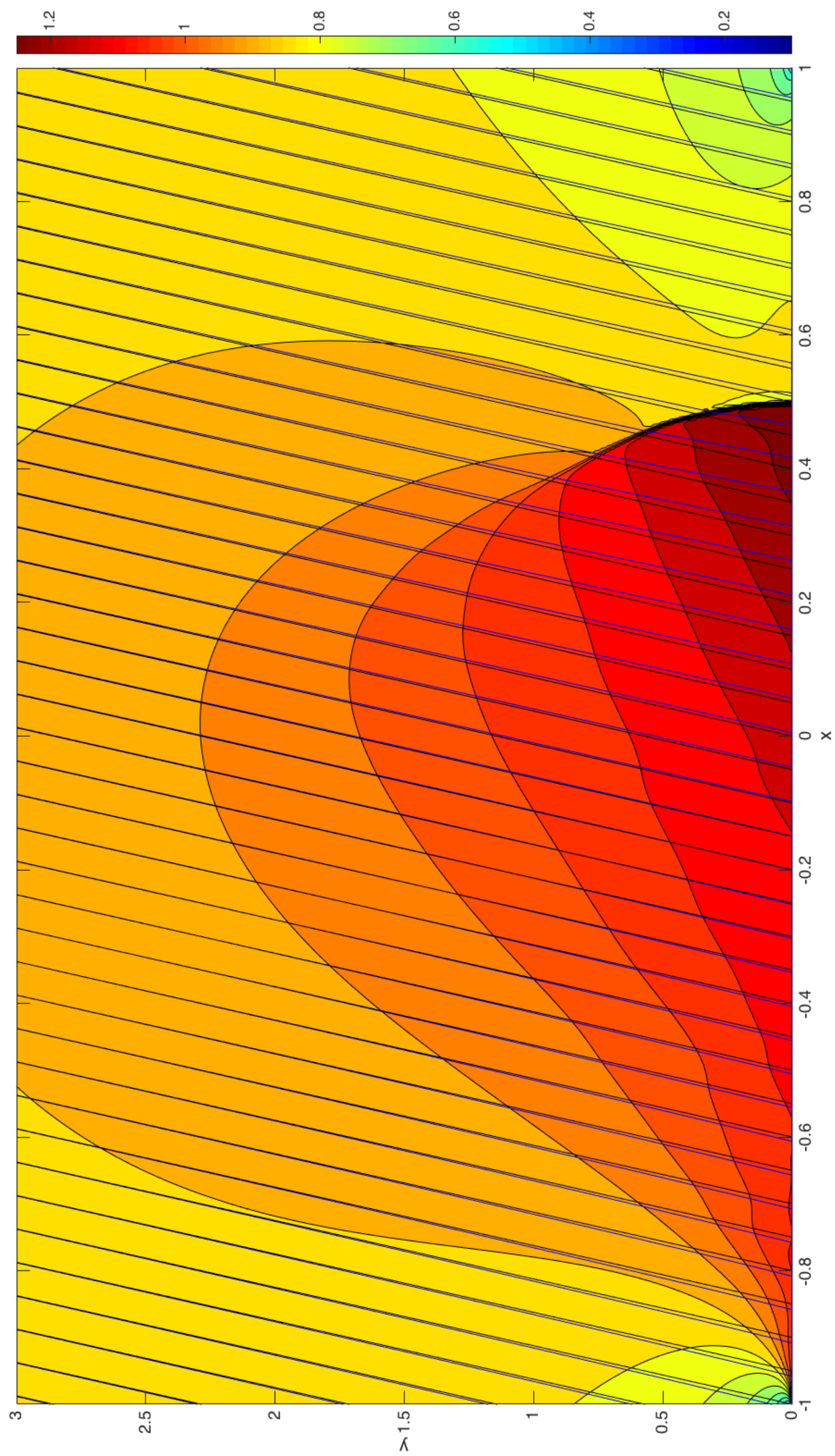

Figure G.3: Deflected and straight light rays for $\theta_{ray} = -5°$

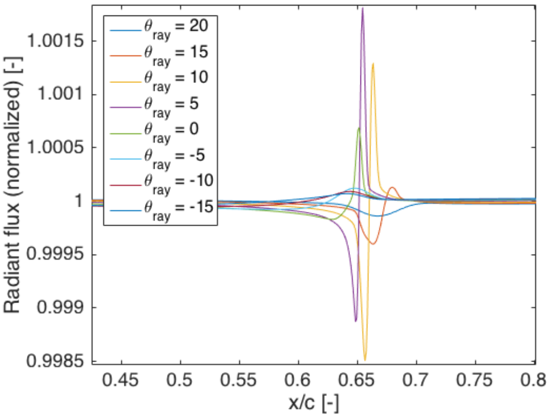

(a) $M_{\infty} = 0.86$

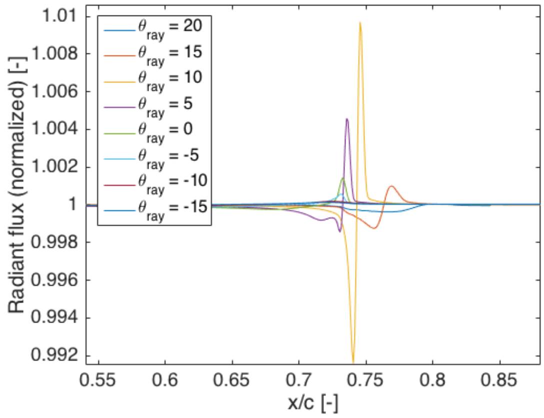

(b) $M_{\infty} = 0.87$

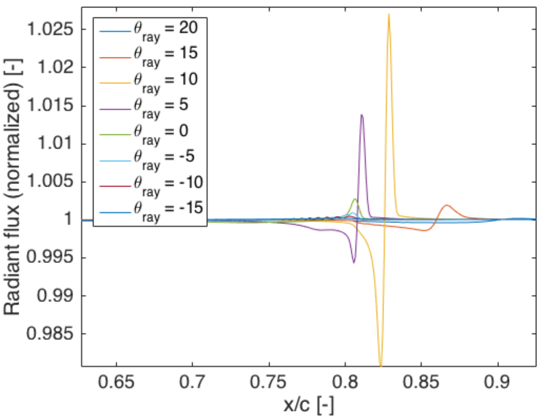

(c) $M_{\infty} = 0.88$

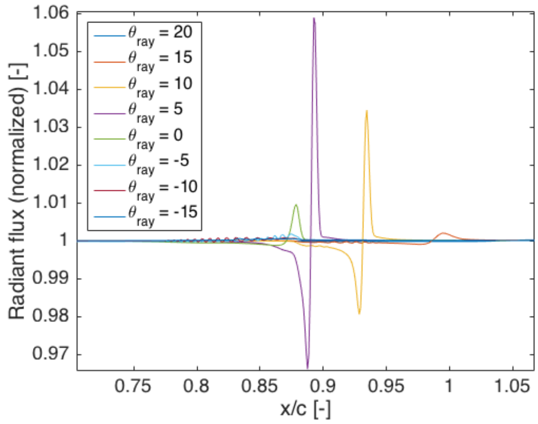

(d) $M_{\infty} = 0.89$

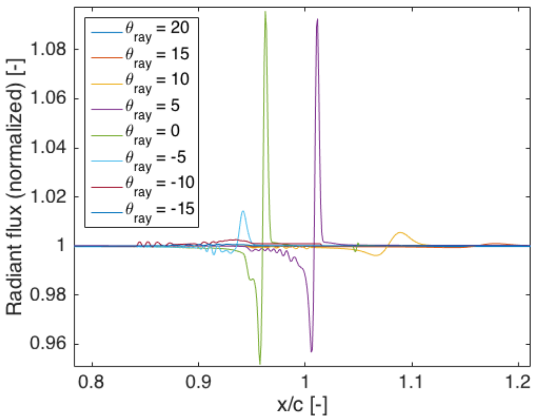

(e) $M_{\infty} = 0.9$

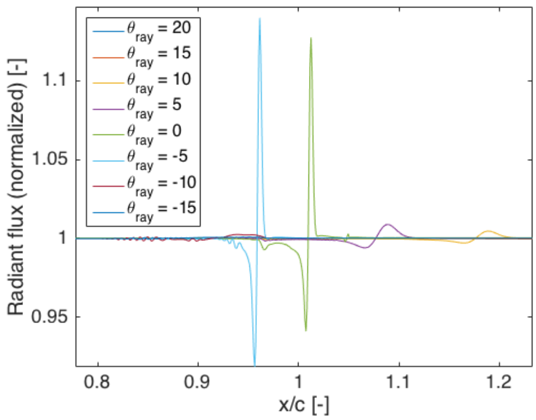

(f) $M_{\infty} = 0.91$

Figure H.1: Radiant flux measured at upper surface of 6% parabolic arc airfoil

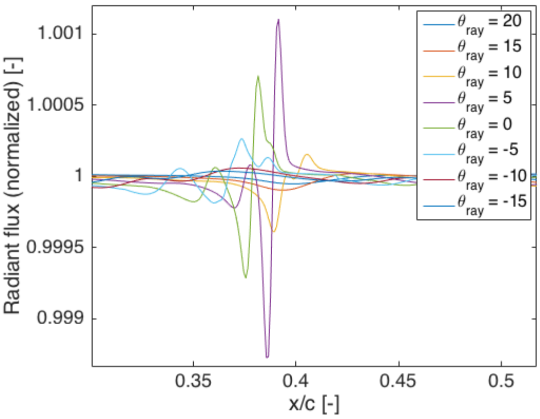

(a) $M_\infty = 0.83$

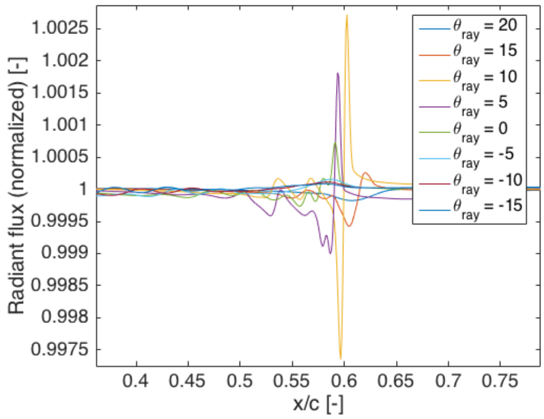

(b) $M_\infty = 0.84$

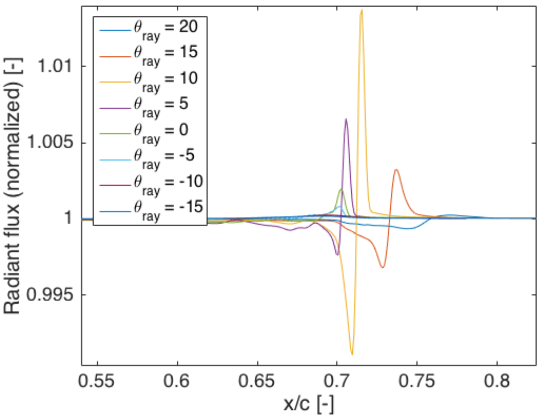

(c) $M_\infty = 0.85$

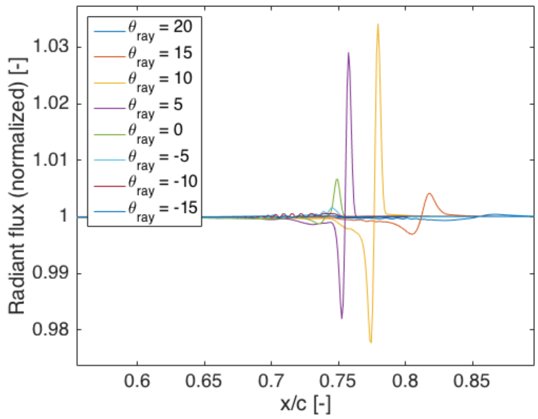

(d) $M_\infty = 0.86$

Figure H.2: Radiant flux measured at upper surface of SC(2)-0410 airfoil, flow field calculated using fine mesh

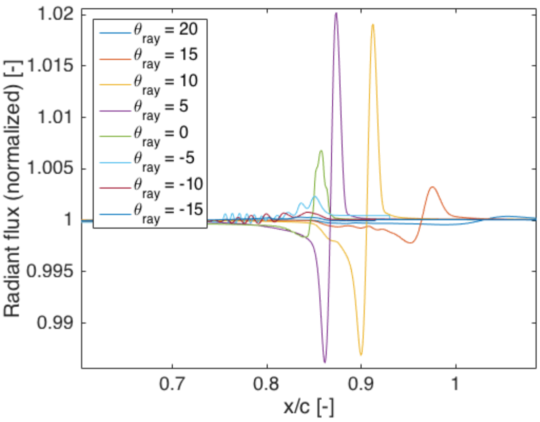

(a) $M_\infty = 0.87$

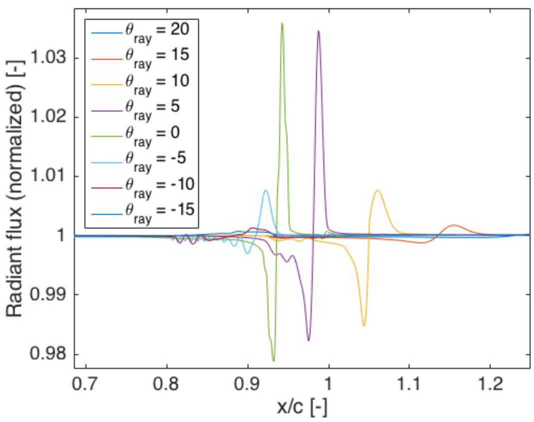

(b) $M_\infty = 0.88$

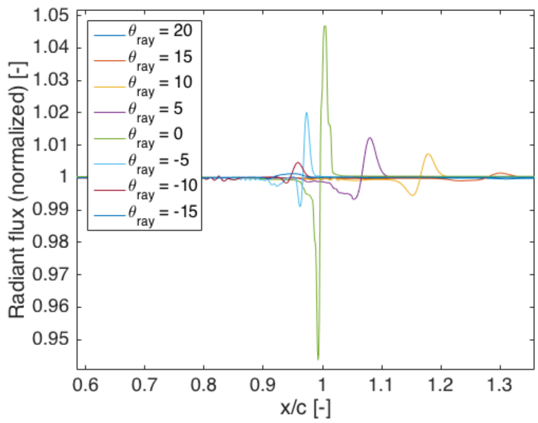

(c) $M_\infty = 0.89$

Figure H.3: Radiant flux measured at upper surface of SC(2)-0410 airfoil, flow field calculated using coarser mesh

APPENDIX I. Light Angle and Shadowgraph Characteristics Relations

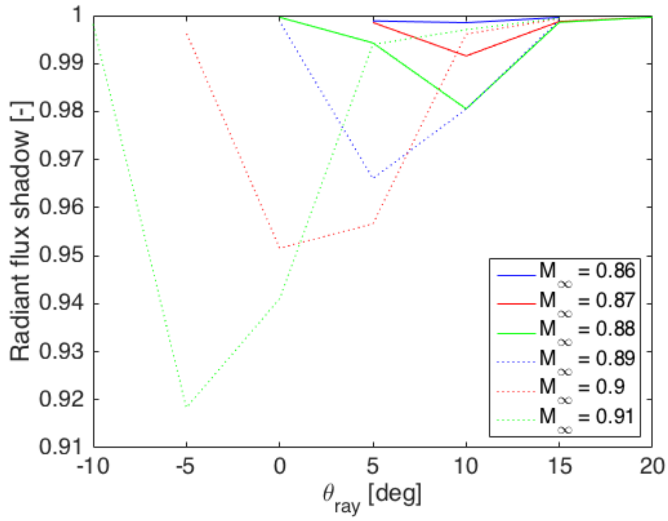

Figure I.1: Peak radiant flux values corresponding to the shadow in the shadowgraph for different light angles, parabolic arc airfoil

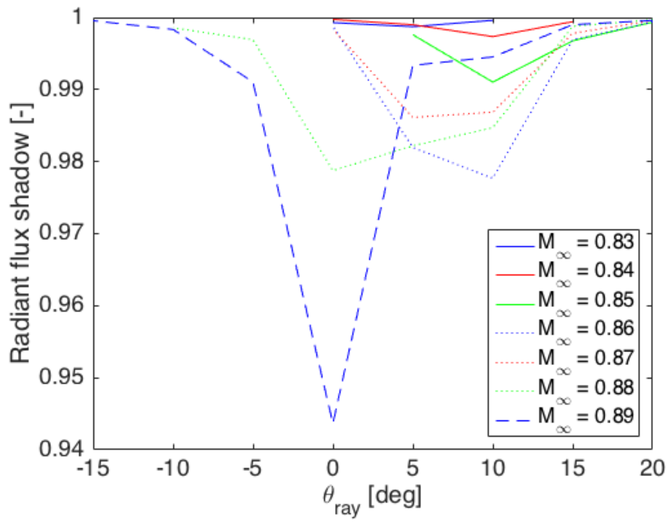

Figure I.2: Peak radiant flux values corresponding to the shadow in the shadowgraph for different light angles, SC(2)-0410 airfoil

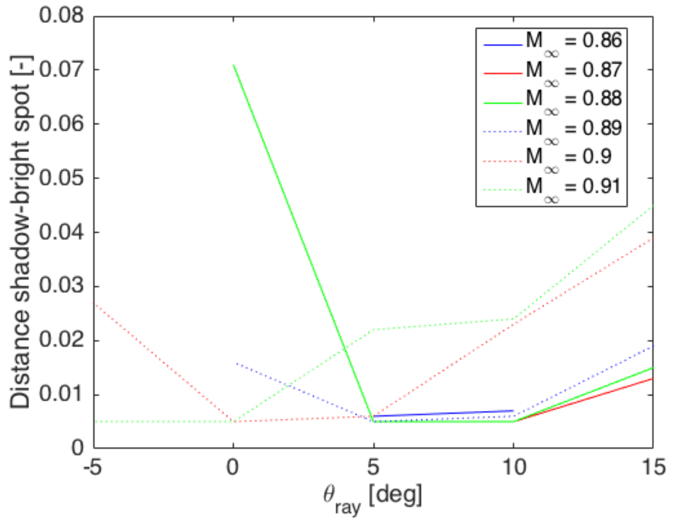

Figure I.3: Distance between shadow and bright spot in shadowgraph for different light angles, parabolic arc airfoil

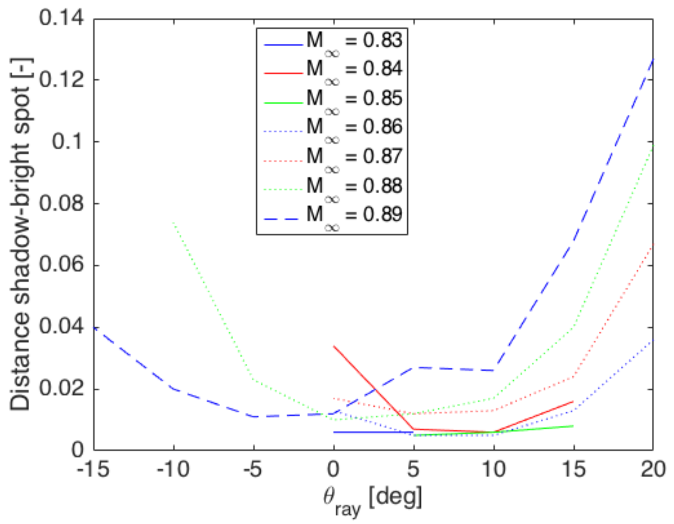

Figure I.4: Distance between shadow and bright spot in shadowgraph for different light angles, SC(2)-0410 airfoil

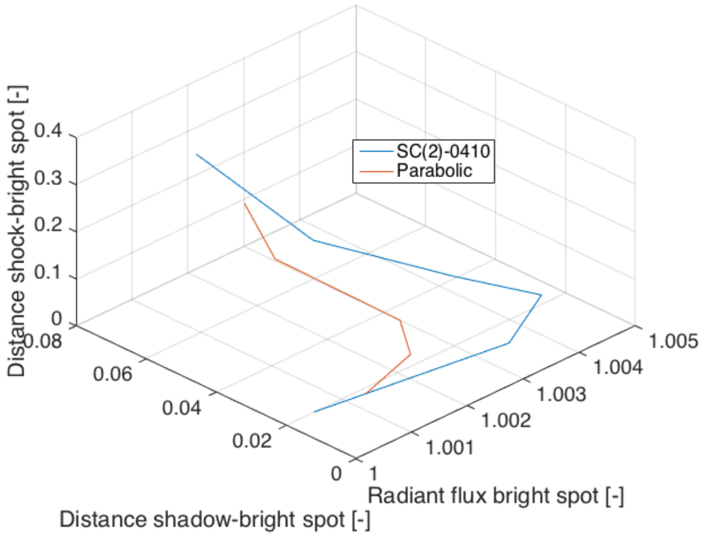

Figure J.1: Relation between the bright spot radiant flux value, the distance between the shadow and bright spot, and the position of the shock wave with respect to the position of the bright spot for $\theta_{ray} = 15°$

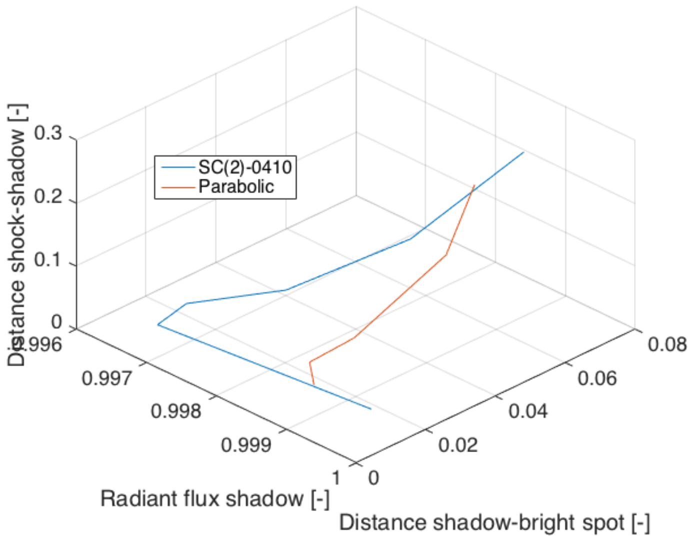

Figure J.2: Relation between the shadow radiant flux value, the distance between the shadow and bright spot, and the position of the shock wave with respect to the position of the shadow for $\theta_{ray} = 15°$

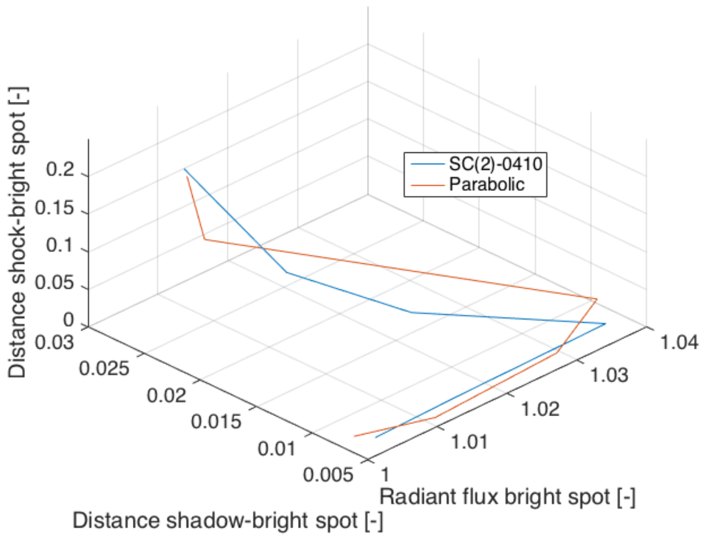

Figure J.3: Relation between the bright spot radiant flux value, the distance between the shadow and bright spot, and the position of the shock wave with respect to the position of the bright spot for $\theta_{ray} = 10°$

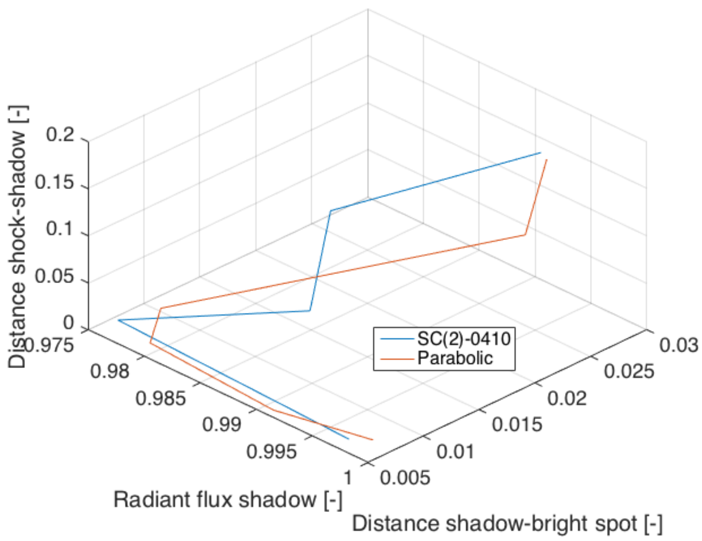

Figure J.4: Relation between the shadow radiant flux value, the distance between the shadow and bright spot, and the position of the shock wave with respect to the position of the shadow for $\theta_{ray} = 10°$

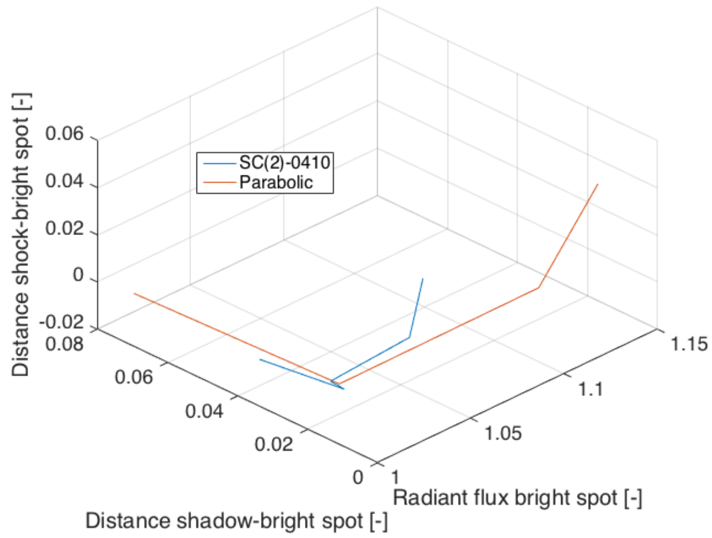

Figure J.5: Relation between the bright spot radiant flux value, the distance between the shadow and bright spot, and the position of the shock wave with respect to the position of the bright spot for $\theta_{ray} = 0°$

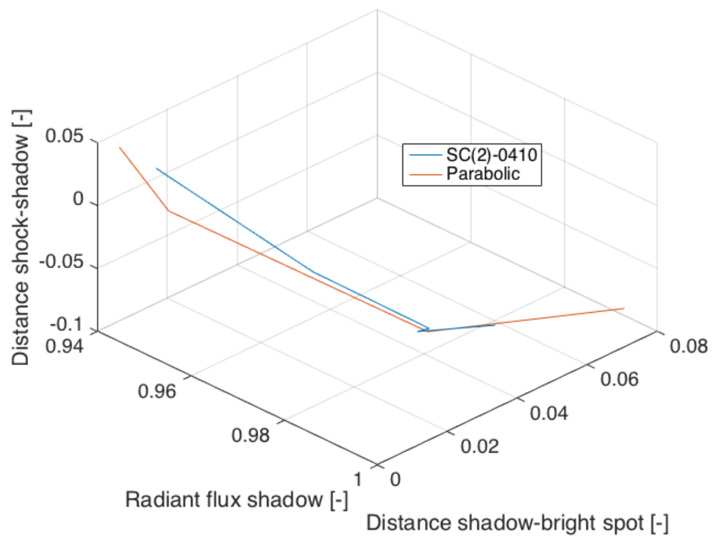

Figure J.6: Relation between the shadow radiant flux value, the distance between the shadow and bright spot, and the position of the shock wave with respect to the position of the shadow for $\theta_{ray} = 0°$